School of Chemistry

Cardiff University

Preparation and characterisation of gold and palladium based catalysts for the direct synthesis of hydrogen peroxide

Thesis submitted in accordance with the requirements of Cardiff University for the degree of doctor of philosophy by:

James Pritchard

2012

To my parents,

to those who have supported me over the years,

Abstract

The research presented in this thesis describes the direct synthesis of hydrogen peroxide from H_2 and O_2 using supported gold-palladium based catalysts. The direct synthesis process offers a green and sustainable approach compared to the anthraquinone autoxidation (AO) process, which is currently used on an industrial scale to produce >95% H_2O_2 worldwide. The work presented in this thesis is an attempt to examine the direct synthesis process in terms of determining optimum catalyst compositions for potential scale-up in the near-future. The primary aim of this investigation is centred on catalyst design and characterisation.

The first part of this work is a catalyst optimisation study for 2.5 wt% Au-2.5 wt% Pd/TiO_2, and involved changing the amount of water used in the catalyst preparation, in this case wet impregnation. It was found that the addition of small amounts of water resulted in approximately 100% enhancement in activity for TiO_2-supported catalysts but not for carbon-supported Au-Pd catalysts. The rate of Au/Pd uptake was contrasted and it was determined that the isoelectric point of the support was highly influential. While the activity can be enhanced for TiO_2-supported catalysts, both catalyst nanostructure and stability were detrimentally affected by the addition of water during the impregnation step.

The second part of this work is focussed on understanding the precise nature of the acid pre-treatment effect, where treatment of a carbon support in dilute nitric acid prior to the impregnation of Au and Pd precursors can result in the complete switching-off of sequential H_2O_2 hydrogenation activity over the catalyst. Characterisation and heat treatment studies gave an improved understanding of the relationship between Au/Pd and the carbon support.

The next part of the study addresses the use of a colloidal immobilisation method to pre-fabricate Au-Pd ‘designer’ nanoparticles onto supports and is accompanied by extensive advanced aberration corrected electron microscopy studies. The effect of acid pre-treating silica based supports is then considered for catalysts prepared by wet-impregnation, specifically the fact that acid pre-treatment of silica is required to induce synergy between Au and Pd metals for the direct synthesis of hydrogen peroxide. The final part of this work considers the effect of introducing a third metal into the catalyst design, specifically the addition of Pt to Au/Pd compositions. An extensive catalyst screening study is undertaken for Au-Pd-Pt/CeO_2 catalysts.

Acknowledgements

I would firstly like to thank my supervisor FRS Prof. Graham J. Hutchings for welcoming me into his group and onto a high profile and rewarding project. I appreciate the knowledge, encouragement and words of wisdom imparted to me throughout the degree and the positive impact it has had on my life. I am deeply indebted to my two co-supervisors: Dr. Jennifer Edwards for always believing in me and being a first class mentor throughout, and Dr. Albert F. Carley for his kindness and continual support with surface science aspects. A special gratitude must go to Prof. David Knight, Prof Gary Attard, Dr. Stuart Taylor, Dr. Damien Murphy and Dr. Alison Paul for their sound advice during my B.Sc. and Ph.D.

I would like to thank the team at Solvay® for their industrial expertise, friendliness and financial support from 2009-2011. The same gratitude is extended to Prof. Christopher J. Kiely and Dr. Qian He of Lehigh University for the high quality microscopy that has resulted from our collaboration and to Dr. Stewart F. Parker (ISIS/RAL, Oxford) for the technical expertise provided on MAPS and TOSCA instruments.

It has been a privilege to have worked in a large, diverse and talented group such as Cardiff Catalysis Institute. I value every moment that I have worked with Marco Piccinini – a once in a lifetime guy! A thank you to: Edwin, Nikos, Tony, Marco C, Simon's F & K, Greg, Adeeba, Yingyu, Ceri, Gareth, Cat, Peter, Gemma, Dave's E, M & S, James A & H, Ewa, Hasbi, Lokesh, Mike, Sarwat, Scott, Sivaram, Jon, Kieran, Nick, Rob, Rhys and Tom.

I would like to convey my gratitude to the technical staff: Steve Morris, Alun Davies, John Cavanagh, Richard Breeze and Mal Bryant, and the chemistry stores and general teams: Gary, Jamie, Sham, Simon, Steve, Steph, Matt, Trish, Terrie and Alison's R & T.

To my friends: Henry, Heulyn, James, Elliot, Alan and Jo - thank you for always being there. A thank you to the tutors who helped me before university: Mrs Williams, Mr Parfitt, Dr. Anderson, Dr. Hughes, Mrs Matthews, Mr Short, Mr Balshaw and Dr. Salmon.

I could not have succeeded without the unconditional love and support of my parents, grandmother and my aunt and uncle. This thesis is as much for you as it is for me!

Table of contents

Abstract I

Acknowledgements II

Chapter 1 – Introduction 1

1.1 Introduction 1

1.2 Hydrogen peroxide 11

1.2.1 Production of hydrogen peroxide 12

1.2.2 The direct synthesis of hydrogen peroxide from H_2 and O_2 using palladium based catalysts 17

1.3 Catalysis by Gold 23

1.3.1 CO oxidation 24

1.3.2 Hydrochlorination of acetylene 26

1.3.3 Alkene epoxidation 27

1.3.4 Alcohol oxidation 29

1.4 The direct synthesis of hydrogen peroxide from H_2 and O_2 using gold-palladium catalysts 31

1.5 Alternative technologies and theoretical studies 36

1.6 Aims of this study 41

1.7 References 42

Chapter 2 – Experimental 50

2.1 Outline 50

2.1.1 Catalyst precursors 50

2.1.2 Supports 51

2.1.3 Reagents 52

2.1.4 Gases 52

2.2 Catalyst Preparation 53

2.2.1 Catalyst synthesis by the wet impregnation method 53

2.2.1.1 Preparation of highly active Au-Pd/TiO_2 catalysts 53

2.2.2 Acid pre-treatment of catalyst supports 54

2.2.3 Catalyst synthesis by the deposition precipitation method 54
2.2.4 Catalyst synthesis by the sol-immobilization method 55
2.2.4.1 Au+Pd sol 55
2.2.4.2 Pd{Au} sol 56
2.2.4.3 Au{Pd} sol 57
2.2.5 Reflux method 57
2.3 Catalyst Testing 58
2.3.1 Hydrogen peroxide synthesis 58
2.3.1.1 Catalyst re-usability experiments 59
2.3.2 Hydrogen peroxide hydrogenation 60
2.4 Characterisation 61
2.4.1 UV-Visible Spectroscopy (UV-Vis) 61
2.4.2 Powder X-ray Diffraction (XRD) 62
2.4.3 Thermo-Gravimetric Analysis (TGA) 64
2.4.4 Temperature Programmed Desorption (TPD) 64
2.4.5 BET Surface Area and Porosimetry Measurements 65
2.4.6 Fourier Transform Infra-Red Attenuated Total Reflectance (FT-IR ATR) Corrected Spectroscopy 67
2.4.7 Atomic Absorption Spectroscopy (AAS) 69
2.4.9 Scanning Transmission Electron Microscopy (STEM) 71
2.4.8 Scanning Electron Microscopy (SEM) 74
2.4.10 X-ray Photoelectron Spectroscopy 75
2.4.11 Inelastic Neutron Scattering 77
2.5 References 79

Chapter 3 – Preparation of titania supported Au-Pd catalysts **80**
3.1 Introduction 80
3.2 Effect of wet impregnation parameters on H_2O_2 production and hydrogenation over bimetallic TiO_2-supported catalysts 83
3.3 Effect of wet impregnation parameters on H_2O_2 production and hydrogenation over monometallic TiO_2-supported catalysts 87
3.4 Effect of wet impregnation parameters on H_2O_2 production and hydrogenation over bimetallic carbon-supported catalysts 88
3.5 Catalyst Characterisation 90
3.5.1 Measurement of the uptake of Au and Pd compounds during impregnation using UV-Visible spectroscopy 90
3.5.2 X-ray Photoelectron Spectroscopy 92
3.5.3 Transmission Electron Microscopy 94
3.6 Evaluation of catalyst reusability 96
3.7 Discussion 97
3.8 The role of chloride in bimetallic Au-Pd/TiO_2 catalysts 99
3.9 Conclusion 109
3.10 References 110

Chapter 4 – Preparation of carbon supported Au-Pd catalysts **113**
4.1 Introduction 113
4.1.1 Experimental conditions 115
4.2 Characterisation of the carbon support 116
4.3 Effect of acid pre-treatment on the direct synthesis reaction 120
4.4 Characterisation of the carbon-supported Au-Pd catalysts 123
4.4.1 Electron microscopy characterisation 123
4.4.2 X-Ray photoelectron spectroscopy 128
4.5 Effect of calcination atmosphere on H_2O_2 synthesis and hydrogenation 133
4.5.1 Effect of heat treatment on activated carbon 136
4.5.2 Effect of oxidation and reduction cycles of Pd^{2+}/Pd^0 ratio 139
4.6 Discussion 141
4.7 Conclusion 144
4.8 References 145

Chapter 5 – Preparation of sol-immobilised Au-Pd catalysts **147**

5.1 Introduction 147

5.2 Electron Microscopy Characterization of Sol-Immobilized Catalysts 151

5.2.1 Au+Pd, Pd{Au} and Au{Pd} Colloids 151

5.2.2 Au+Pd, Pd{Au} and Au{Pd}/C and TiO_2 catalysts 152

5.2.3 The effect of sol-immobilisation on H_2O_2 synthesis and hydrogenation 155

5.3 The effect of heat treatment on catalyst structure 159

5.3.1 Characterisation of materials calcined at 200 ^oC 159

5.3.2 Characterisation of materials calcined at 400 ^oC 160

5.4 The effect of heat treatment on the direct synthesis of H_2O_2 163

5.5 The effect of Au:Pd ratio on catalyst structure and activity 165

5.5.1 UV-Visible spectroscopy of Au:Pd colloids 165

5.6 Characterisation of Au_xPd_y/C sol-immobilized catalysts 166

5.6.1 X-ray photoelectron spectroscopy 166

5.6.2 Electron microscopy characterisation 167

5.6.3 Effect of Au:Pd molar ratio on H_2O_2 synthesis and hydrogenation 170

5.7 The stability of sol-immobilized Au-Pd catalysts 173

5.8 Comment on reflux and reduction methods 176

5.9 Discussion 178

5.10 Conclusion 181

5.11 References 182

Chapter 6 – Preparation of silica supported Au-Pd catalysts **185**

6.1 Introduction 185

6.2 Effect of acid pre-treatment on H_2O_2 synthesis and hydrogenation activity 188

6.3 Catalyst reusability 189

6.4 Characterisation of the SiO_2 support 193

6.4.1 FT-IR ATR spectroscopy 193

6.4.2 Thermogravimetric analysis 194

6.4.3 Temperature programmed desorption 194

6.4.4 Inelastic neutron scattering 197

6.4.5 X-ray photoelectron spectroscopy 199

6.5 Characterisation of the Au-Pd/SiO_2 catalysts 199
6.5.1 Electron microscopy characterisation 199
6.5.2 X-ray photoelectron spectroscopy 202
6.5.3 Discussion 203
6.6 Comparison of different SiO_2 and Si-supports 204
6.6.1 Silicalite 204
6.6.2 Zeolites 206
6.6.3 Silicalit (Solvay ®) 209
6.6.4 Porous glass and other SiO_2 supports 210
6.7 Discussion 213
6.8 Conclusion 216
6.9 References 217

Chapter 7 – Preparation of trimetallic Au-Pd-Pt catalysts 219
7.1 Introduction 219
7.2 CeO_2-supported monometallic Pd catalysts for direct H_2O_2 synthesis 223
7.2.1 Effect of Au addition to CeO_2-supported Pd catalyst for the direct synthesis and hydrogenation of H_2O_2 224
7.2.2 Effect of acid pre-treatment of the CeO_2 support on the direct synthesis and hydrogenation of H_2O_2 225
7.2.3 Effect of calcination temperature on the activity of CeO_2-supported catalysts 227
7.2.4 Reusability of CeO_2-supported catalysts 230
7.2.5 Comparison of Au and Pd surface states as a function of heat treatment 231
7.3 Discussion 233
7.4 Development and optimisation of supported Au-Pd-Pt catalysts 235
7.4.1 Comparison of carbon-supported Au-Pd-Pt catalysts 236
7.4.2 CeO_2-supported mono and bimetallic Pt catalysts 237
7.4.3 CeO_2-supported trimetallic Au-Pd-Pt catalyst screening 239
7.4.4 The effect of 5 wt% Au-Pd-Pt/CeO_2 catalyst composition on both the rates of H_2O_2 synthesis and hydrogenation 241

7.5 XPS Characterisation 248
7.6 Effect of calcination temperature on 2.28% Au-2.28% Pd-0.45% Pt/CeO_2 250
7.7 Comparison of TiO_2-supported Au-Pd-Pt catalysts 253
7.8 Discussion 259
7.9 Conclusion 262
7.10 References 263

Chapter 8 – Conclusions **265**
8.1 Conclusions 265
8.2 References 275

Appendix **285**

List of Publications **294**

Chapter 1

1.1 Introduction

The term catalyst was first derived by Jons Jakob Berzelius in 1836 and describes a substance that can be added to a chemical reaction to accelerate its rate without itself being consumed[1, 2]. Berzelius commented:

"Many bodies have the property of exerting on other bodies an action that is very different from chemical affinity. By means of this action they produce decomposition in bodies, and form new compounds into the composition of which they do not enter. This new power, hitherto unknown, I shall call it catalytic power. I shall also call catalysis the decomposition of bodies by this force."

Some of the earliest studies were reported by Davy[3], Faraday[4] and Phillips[5], and concerned the application of Pt sponge as a combustion catalyst. An early application of catalysis was in the mining industry where the Davy lamp was used to warn miners of hazardous areas, leading to a reduction in the number of underground explosions and saving countless lives. The lamp comprised of Pt gauze casing, which would glow in the presence of a flammable gas such as methane, due to catalytic combustion processes taking place on the surface of the gauze.

In modern times, catalysts are used extensively with approximately 90% of chemicals produced today requiring a catalyst during one or more stages of their production. The fuel industry is powered by catalysts used for the 'cracking' and 'reforming' of oil into petrol and diesel. The synthesis of ammonia for use in the production of fertilisers along with polymerisation processes used to manufacture key chemicals and plastics are all facilitated by a catalyst and consequently, catalysis represents a vital component in everyday living and the world economy.

Catalysts work by providing an alternative reaction mechanism comprising a different transition state characterized by lower activation energy (E_a). As a result, more molecules possess sufficient energy to reach the transition state and overcome the energy activation barrier (corresponding to the peak maximum Gibbs free energy (ΔG) as shown in Figure 1.1). On entering the transition state, reactants experience such a degree of closeness and distortion that a small, further distortion will lead to the formation of products[6].

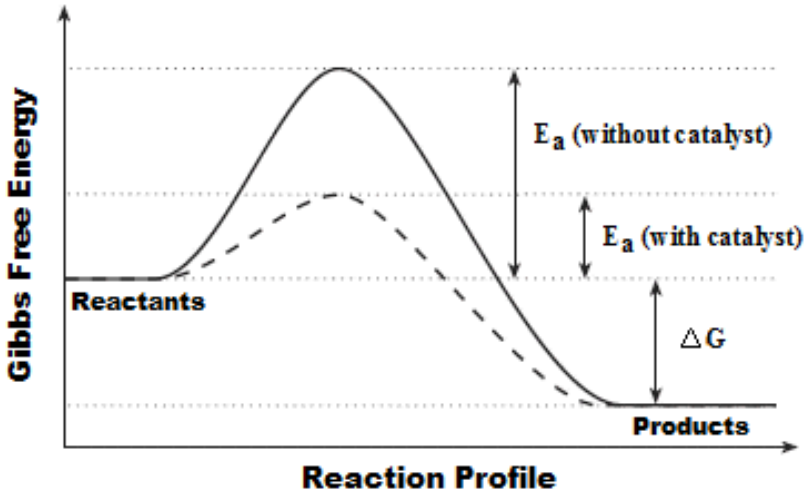

Figure 1.1 Reaction potential energy profile for both an uncatalysed (black line) and catalysed (black dash) reaction, showing a decrease in the activation energy barrier of the latter. The highest energy peak represents the transition state (T.S) for a given reaction.

The rate constant, *k*, which quantifies the speed of such a chemical reaction can be expressed using the Arrhenius rate law:

$$\boldsymbol{k = Ae^{(-Ea/RT)}} \qquad \textbf{(Equation 1.1)}$$

where $\mathbf{E_a}$ is the activation energy, **R** is the molar gas constant, **T** is the absolute temperature, **A** is the pre-exponential factor, and ***k*** is the rate constant. Specifically, the activation energy is defined as the minimum kinetic energy that reactants must possess in order to from products, while the fraction of collisions with a kinetic energy in excess of an energy, E_a, is given by the Boltzmann distribution as $e^{(-Ea/RT)}$. The pre-exponential factor, A, is a measure of the rate at which collisions occur irrespective of their energy, and therefore the product of A and the exponential factor, $e^{(-Ea/RT)}$, gives the rate of successful collisions.

There are three distinct types of catalysts: heterogeneous, homogeneous and enzymatic, which depend on the number of different phases present on the addition of a catalyst. For heterogenous catalysis, the catalyst is in a different phase to the reactants. For homogeneous catalysis, both the catalyst and reatants are in the same phase, whereas enzymatic catalysis exists between homogeneous and heterogeneous catalysts and is specific to biochemical reactions.

The majority of heterogeneous catalysts are solids, with the reactants in the gas or liquid phases. The reaction takes place on the surface of the catalyst material, with the performance of a heterogeneous catalyst typically measured in terms of: activity, selectivity and lifetime. The surface of catalyst provides free bonding states which are respnosible for observed catalysis by facilitating adsortion of reactants, transformation of reactants into products, and desorption of products *via* bond breaking/making and re-arrangment steps. An important example of a heterogenously catalysed process is the oxidation of carbon monoxide to carbon dioxide, which is described using a simple diagram in Figure 1.2.

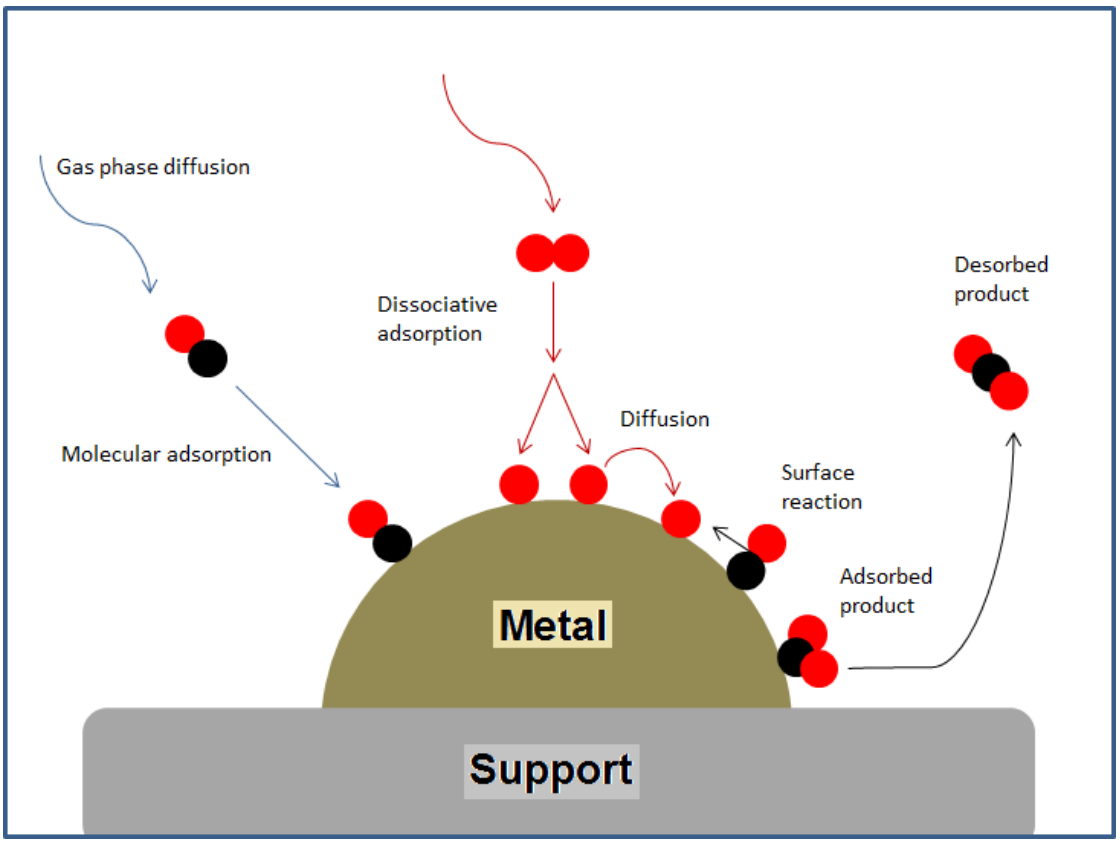

Figure 1.2 Schematic of molecular and atomic events taking place during a catalytic reaction[2].

Firstly, carbon dioxide molecules diffuse through the gas phase to the catalyst surface where molecules are molecularly adsorbed. This is followed by the possible surface diffusion and dissociation of molecules into atoms. For this reaction and based on the higher bond strength of the CO molecule with respect to O_2, only the oxygen molecule dissociates on the surface. As a result, oxygen atoms react with CO molecules to form carbon dioxide, CO_2, on the catalyst surface. The product then undergoes desorption from the surface to enter the gas phase. The specific sites on the catalyst surface responsbile for adsorption and reaction are referred to as 'active sites'.

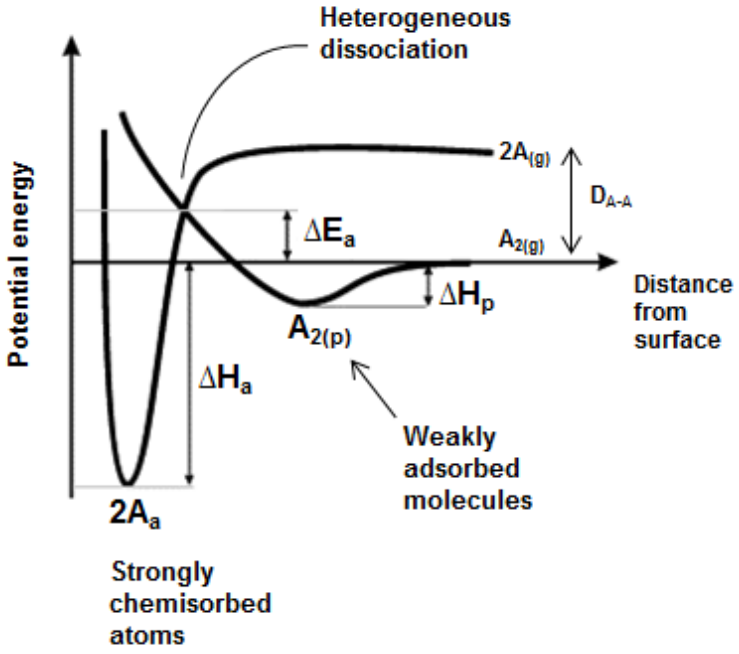

Figure 1.3 Lennard-Jones potential energy diagram describing the dissociation of a molecule as it approaches a surface. The molecule initially experiences an attractive energy minimum referred to as physisorption (ΔH_p), but can dissociate from that state. If the molecule possesses energy higher than the activation energy barrier, it can dissociate directly from the gas phase. For incoming atoms from the gas phase, there is only attraction until they are very close to the surface atoms, and a deep energy minimum for adsorption (ΔH_a)[6].

The performance of a catalyst is determined by the strength of the interactions exisiting between reactants and the solid surface. Specifically, Chemisorption is a term used to describe strong adsorption (of enthalpy >40 kJ mol^{-1}) and involves the breaking of bonds in reactants and the formation of bonds to the surface. It is the surface that stabilises reaction intermediates by bonding, satisfying valances and providing relatively stable configurations. For molecules that can undergo dissociaton, two states of adsorption are described in Figure 1.3.

Referring to Figure 1.3, as a molecule approaches the surface it begins to experience an attractive force due to Van der Waals and electrostatic polarisation effects between the molecule and the solid surface. On closer approach, the molecule begins to experience repulsion due to the increasing proximity of the outer electronic orbitals of the solid surface and the molecule, leading to an increase in potential energy. As a result, there is a minimum energy into which the molecule can be accomodated, known as the physisorbed state (physisorption) and characterised as a weak adsorption of low enthalhpy (20-40 kJ mol^{-1}). The average lifetime of a molecule adsorbed in this state on the surface can be estimeted using the Frenkel equation:

$$\tau = \tau_o e^{(\Delta Ha/RT)} \qquad \textbf{(Equation 1.2)}$$

where τ is the surface lifetime, τ_o is the lifetime of a surface vibration (10^{-13} s), and ΔH_a is the heat of adsorption. If a diatomic molecule is dissociated in the gas phase, it will be in a highly excited state and therefore bonding to a surface will lower its energy. In this instance its energy is lowered to the extent that it adsorbs into a stable, dissociatively adsorbed state, with a net exothermic reaction. As the atom is pushed closer than its equilibrium position to the surface, it experiences repulsion between electrons from the solid surface and its own non-bonding electrons due to Pauli exclusion. This bonding state is referred to as chemisorption and has a broad range of range of energies, ranging from 40 kJ mol^{-1} for weak, molecular chemisorption to 600 kJ mol^{-1} for the strongest binding atomic species. The overlap of the chemisorption and physisorption curves affords the possiblity of curve crossing (referred to as heterogeneous dissoication) of a molecule on close approach to the solid surface from the molecular to the dissociated state, providing that the molecule possesses sufficient energy to overcome the energy activation barrier.

For the adsorption of oxygen onto a metal surface, two barriers to adsorption from the gas phase exist. The first barrier is situated between physisorbed, $O_{2(p)}$, and molecularly chemisorbed states, $O_{2(a)}$, while the second barrier is between the latter and the dissociated state, $2O_{(a)}$. The probability for such a dissociative adsorption is strongly dependendent on the structure of the surface[2]. For heterogeneous catalysts, the nature of the top layer of atoms determines how fast a catalytic reaction may proceed. Different surface site morphologies can potentially be exposed, including kink, step and terrace sites and flat planes of atoms. These exposed morphologies have different co-ordination numbers, which in turn determines their

ability to bind and react with molecules. The surface is an abrupt termination of the bulk structure in which atoms are exposed in an asymetric environment, leaving free bonds at the surface that can interact with incoming molecules. In thermodynamic terms, the ability of such free bonding states to facilitate a catalytic reaction is represented by the surface Gibbs free energy, G_s.

For catalysts composed of highly dispersed, metal particles, very small particles (less than 3 nm in diameter) can significantly affect the reactivity and activation energies at each individual stage of a catalysed process. This is due to the splitting of the conduction band into discrete energy levels, at which point particles behave less like the bulk metal and more like individual atoms. If the metallic particles are dispersed over a support material, charge transfer between the catalyst particle and the support can take place depending on the size, stucture and nature of both the metal and the support[7].

Reactions on the catalyst surface may proceed either between adsorbed molecules (Langmuir-Hinshelwood mechanism), or directly between an absorbed molecule and molecules present in the gas or liquid phase (Eley-Rideal mechanism). If an oxide material is used as the catalyst, then lattice oxygen may participate in the reaction (Mars-van Krevelen mechanism). With regard to the adsorption step, the number of surface sites occupied by adsorbate molecules at equilibrium at a given temperature will depend on the gas pressure, P. An adsorption isotherm can be used to understand the dependence of the fractional coverage, θ, of adsorbate molecules on the gas pressure, P, at constant temperature[8]. The langmuir isotherm is the most common model used to interpret the equilibrium adsorption behaviour of a system and to determine the total surface area, S_A, of solid surfaces. The model assumes that:

(1) The solid surface is uniform and contains a number of equivalent sites, each of which may only be occupied by one molecule of adsorbate.

(2) A dynamic equilibrium exists between the gas (at pressure, P) and the adsorbed layer at constant temperature.

(3) Adsorbed molecules from the gas phase are continuously colliding with the surface. If they impact a vacant adsorption site, they form a bond with the surface and stick. If they strike a filled site, they are reflected back into the gas phase.

(4) Once adsorbed, the molecules are localized and the enthalpy of adsorption per site remains constant irrespect of coverage.

According to the second assumption, the associative adsorption of a molecule, M, in the gas phase onto a surface site, S, is described as:

$$M(g) + S \underset{k_d}{\overset{k_a}{\rightleftharpoons}} M{-}S \qquad \textbf{(Equation 1.3)}$$

where $\mathbf{k_a}$ and $\mathbf{k_d}$ are the rate constants for the adsorption and desorption steps. If P is the pressure and θ is the fractional monolayer coverage of the surface by adsorbate molecules, then:

$$\textbf{Rate of Adsorption} = k_aP(1-\theta) \qquad \textbf{(Equation 1.4)}$$

where **(1-θ)** is the fractional monolayer coverage of sites that are not occupied by adsorbate molecules. Equation 1.4 suggests that the rate of adsorption will be fast if $\mathbf{K_a}$ and **P** are large and **θ** is small. The rate of desorption is described as:

$$\textbf{Rate of Desorption} = k_d\theta \qquad \textbf{(Equation 1.5)}$$

and at equilibrium, both the rate of adsorption and desorption are equal:

$$k_aP(1-\theta) = k_d\theta \qquad \textbf{(Equation 1.6)}$$

Rearrangement of Equation 1.6 gives:

$$\theta = \frac{KP}{1 + KP} \qquad \textbf{(Equation 1.7)}$$

which is the Langmuir adsorption isotherm for assoicative adsorption (where $\boldsymbol{K = k_a/k_d}$) and predicts how the fractional monolayer coverage, θ, of adsorbate changes with P.

Using the same isotherm model, the dissociative adsorption of a molecule, M_2, in the gas phase onto a surface site, S, may be described as:

$$M_{2(g)} + 2S \underset{k_d}{\overset{k_a}{\rightleftharpoons}} 2(M{-}S) \qquad \textbf{(Equation 1.8)}$$

$$\textbf{Rate of Adsorption} = k_a P(1-\theta)^2 \qquad \textbf{(Equation 1.9)}$$

$$\textbf{Rate of Desorption} = k_d \theta^2 \qquad \textbf{(Equation 1.10)}$$

At equilibrium, both the rate of adsorption and desorption are equal:

$$k_a P(1-\theta)^2 = k_d \theta^2 \qquad \textbf{(Equation 1.11)}$$

Rearrangement of Equation 1.11 gives:

$$\theta = \frac{(KP)^{1/2}}{1 + (KP)^{1/2}} \qquad \textbf{(Equation 1.12)}$$

which is the Langmuir adsorption isotherm for dissociative adsorption (where $K = k_a/k_d$) and predicts how the fractional monolayer coverage, θ, of adsorbate changes with P.

During the twentieth century, the number and diversity of heterogeneously catalysed processes increased enormously to meet the demands of a rapidly growing population. Today, industrial catalytic processes are widespread and produce millions of tonnes of products per annum. Several important processes are listed in Table 1.1.

	Reaction	**Heterogeneous Catalyst**
1	Cracking of crude oil	Zeolites
2	Ammonia synthesis	Fe
3	Polymerisation of alkenes	Cr, $TiCl_x/MgCl_2$
4	Water-gas shift (WGS)	Fe (oxide), Cu-ZnO
5	Carbon Monoxide → Carbon Dioxide	$CuMnO_4$, Au/MO_X
6	Hydrocarbons, carbon monoxide and nitrogen oxides → carbon dioxide, water and nitrogen	Three way car exhaust catalyst Pt, Pd
7	Ethene → Ethylene Oxide	Ag
8	Methanol → Formaldehyde	Iron Molybdate, Ag

Table 1.1 Examples of important processes based on heterogeneous catalysts[9]. MO_x denotes the use of a metal oxide support, *e.g.* TiO_2, CeO_2.

The Haber process was first discovered in 1908 and to this day remains important for the production of ammonia from nitrogen and hydrogen gases, using a finely divided iron catalyst. A vast majority of the fuels and plastics available today are derived from the cracking and reforming of crude oil using zeolites, which are microporous, crystalline solids with well-defined structures. The cracking of long chain hydrocarbons into short chain length fuels takes place within the pores of zeolites, which allows for a greater degree of product control. The polymerization of alkenes, such as ethene and propene to form polyethene and polypropene, respectively, is important for the production of packaging and textile materials.

The water-gas shift (WGS) involves the reaction of carbon monoxide with water vapor to form carbon dioxide and hydrogen gases, and in industry is operated in conjunction with the steam reforming of hydrocarbons to produce high-purity hydrogen for the Haber process. Catalysis has also been used to address environmental problems such as the elimination of toxic gases from the atmosphere. The catalytic converter is an important material found in automobiles that is responsible for the vehicle emission control, converting three harmful compounds present in car exhaust emissions into less harmful compounds. The design of the catalyst (Pd and Pt metals dispersed on a metal oxide (*e.g.* Al_2O_3, SiO_2) support that is embedded into a ceramic monolith (CeO_2)) facilitates the oxidation of carbon monoxide and unburned hydrocarbons to carbon dioxide and water, and the simultaneous reduction of nitrogen oxides (NO_x) to nitrogen.

Reactions **7** and **8** in Table 1.1 are examples of selective oxidation processes, where the formation of other products in addition to the primary, desired product is possible. These could be in the form of side products, intermediates or the result of total oxidation to carbon dioxide and water. The choice of catalyst and its manufacturing process play an important role in determining both the conversion and the selectivity toward a desired product. The reaction conditions and the use of promoters are also very important factors. For the oxidation of ethene to ethylene oxide **(7)**, the addition of chloride ions to the reaction can improve the selectivity to ethylene oxide by poisoning surface sites on the Ag catalyst[10] responsible for the non-selective combustion of ethene to carbon dioxide and water.

For the commercial production of formaldehyde *via* the oxidative dehydrogenation of methanol **(8)**, an iron-molybdate catalyst is used, affording a 99% methanol conversion based on 92% selectivity to formaldehyde[11]. However, the iron-molybdate catalyst undergoes deactivation through the loss of molybdenum during the reaction. Consequently, the reaction must be stopped at intervals to allow recovery and either re-activation or replacement of the catalyst in order to maintain high performance.

The activity, selectivity and structural properties of a catalyst are the subject of continued research efforts aimed at improving the efficiency and viability of current, large scale processes, and in the development of new processes. The impact of catalysis on the environment has also been considered so that harmful products and waste are minimised, and to ensure that better, atom efficient reagents are used in catalysis, such as hydrogen peroxide.

1.2 Hydrogen Peroxide

Since its discovery in 1818 by Thennard[12], hydrogen peroxide has found extensive use in both the fine chemicals industry and environmental protection as a benign oxidant. This is due to the strong ability of hydrogen peroxide (50% active atomic oxygen content) in oxidising a large range of inorganic and organic compounds under mild conditions in the liquid phase, producing water as the sole by-product. Demand has steadily increased with 2005 worldwide production reaching approximately $4x10^6$ tonnes[13,14]. The pulp and paper bleaching industry accounts for approximately 40% of all manufactured hydrogen peroxide, with other uses including disinfectants and detergents, the high purity etching of silicon wafers for electronic applications and wastewater treatment[15]. The potential of utilising hydrogen peroxide in large volume chemical synthesises has been recognised with the advent of Titanium Silicate, TS-1 - a ZSM-5 type material[16] that is capable of effectively catalysing several different selective oxidation reactions including the epoxidation of propylene to propylene oxide (PO) and the ammoxidation of cyclohexanone to its corresponding oxime. In 2008, Dow Chemical and BASF opened a joint-venture pilot plant in Antwerp[17], based around the direct synthesis of hydrogen peroxide and its application as an oxidant for propylene epoxidation, referred to as the Hydrogen Peroxide Propylene Oxide (HPPO) process (Figure 1.4).

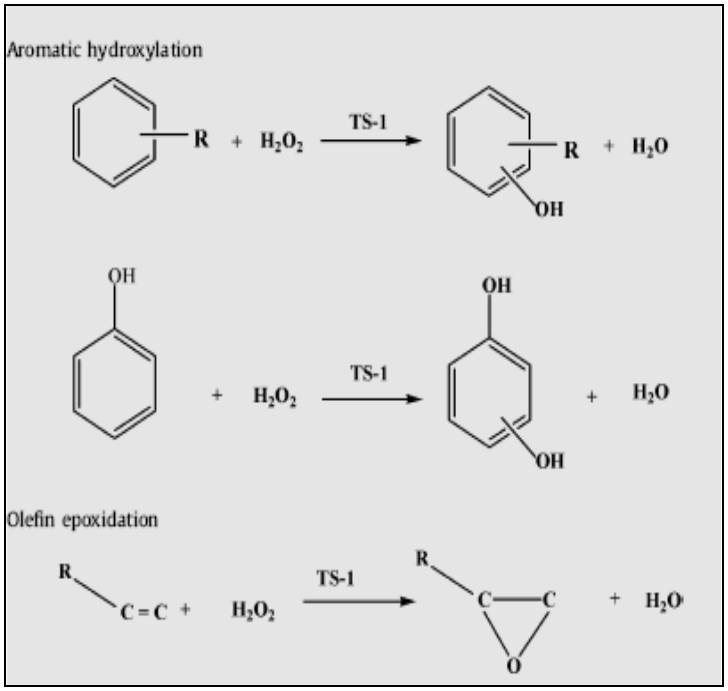

Figure 1.4 A selection of reactions performed using TS-1 catalysts and H_2O_2 as the oxidant[18].

Few stoichiometric processes are operated using molecular oxygen and instead are reliant on bulky non-atom efficient oxygen donors, for example, sodium percarbonate. One reason for this is because O_2 possesses a triplet ground state and so therefore does not require activation in comparison to singlet-state substrates, including molecular hydrogen, which must be activated *via* chemisorption on a catalyst surface in order to undergo reaction with a substrate. In addition, H_2 cannot be activated *via* radical pathways at relatively low temperatures, which are generally used for hydrogenation reactions. Consequently, significant demand exists for green, atom-efficient, singlet-state oxygen donors[19-21] (such as hydrogen peroxide) that are produced using economically viable synthesis routes to enable affordable and widespread applications.

1.2.1 Production of hydrogen peroxide

To date, three main industrial processes have been used to manufacture hydrogen peroxide. Both wet chemical and electrochemical processes[12, 22, 23] have been employed prior to the development of the auto-oxidation process at the beginning on World War II, which still accounts for >95% hydrogen peroxide production worldwide[24]. Hydrogen peroxide was first isolated by reaction of barium peroxide with nitric acid[12]. The yield of hydrogen peroxide was subsequently increased on addition of hydrochloric acid, with removal of barium chloride by precipitation with sulphuric acid (Scheme 1.1).

1.	$BaO_2 + 2HCl$	$\rightarrow$	$BaCl_2 + H_2O_2$
2.	$BaCl_2 + H_2SO_4$	$\rightarrow$	$BaSO_4 + 2\,HCl$
Overall	$BaO_2 + H_2SO_4$	$\rightarrow$	$BaSO_4 + H_2O_2$

Scheme 1.1 The production of H_2O_2 from reaction of BaO_2 with HCl **(1)**. $BaCl_2$ is then removed from solution by reaction with H_2SO_4 to form a $BaSO_4$ precipitate **(2)**.

An industrial process based on scheme 1.1 came online by around 1880 and remained operational until the middle of the 20th century, producing 2,000 tonnes of H_2O_2 per annum[25]. Although 3 wt% aqueous solutions of hydrogen peroxide were routinely produced, the process was expensive and resulted in a high end cost product that also contained impurities from the reaction, known to negatively affect hydrogen peroxide stability.

An electrolytic process was developed by Meidinger in 1853 based on the electrolysis of an aqueous sulphuric acid solution to produce hydrogen peroxide[22]. The reaction mechanism for this process was later established by Berthelot, who concluded that hydrogen peroxide was produced *via* formation of a peroxydisulphuric acid intermediate[23] (Scheme 1.2).

1.	$2\ H_2SO_4$	→	$H_2S_2O_8 + H_2$
2.	$H_2S_2O_8 + H_2O$	→	$H_2SO_5 + H_2SO_4$
3.	$H_2SO_5 + H_2O$	→	$H_2SO_4 + H_2O_2$
Overall	$2H_2O$	→	$H_2O_2 + H_2$

Scheme 1.2 The electrochemical production of aqueous hydrogen peroxide.

The electrochemical production of hydrogen peroxide was commercialised in 1908 and represented an improvement over the wet chemical process in terms of cost and efficiency[26]. The process was later upgraded to utilize ammonium sulphate instead of sulphuric acid, to produce ammonium peroxodisuphate, which is subsequently hydrolysed to H_2O_2. Using this approach, hydrogen peroxide production increased steadily, with the production level in 1950 standing at 35,000 tonnes H_2O_2 per annum[26].

Another industrial process was developed by Hans-Joachim Riedl and Georg Pfliederer in 1939 to meet the increasing demand for hydrogen peroxide (based on observations previously reported by Manchot[27] in 1901), known as the Riedl-Ffleiderer auto-oxidation (AO) process[24]. The process involves the sequential hydrogenation and oxidation of an R-alkyl anthraquinone (AQ) dissolved in an organic working solution.

A nickel or palladium based catalyst is used to hydrogenate a 2-alkylanthaquinone, (usually 2-ethyl, 2-tert-buyl or 2-amylanthraquinone) which is dissolved in a mixture of non-polar (C_9-C_{11} alkylbenzyl) and polar (usually trioctyl phosphate, tetrabutyl urea or diisobutyl carbinol) solvents to form the 'working solution' [28]. The hydrogenation is performed using a three-phase reactor (*e.g.* trickle bed/bubble column) at moderate temperature and pressure to form the anthrahydroquinone (AHQ). The AHQ is separated from the catalyst and oxidised in O_2/air to form the original anthraquinone and hydrogen peroxide (Figure 1.5).

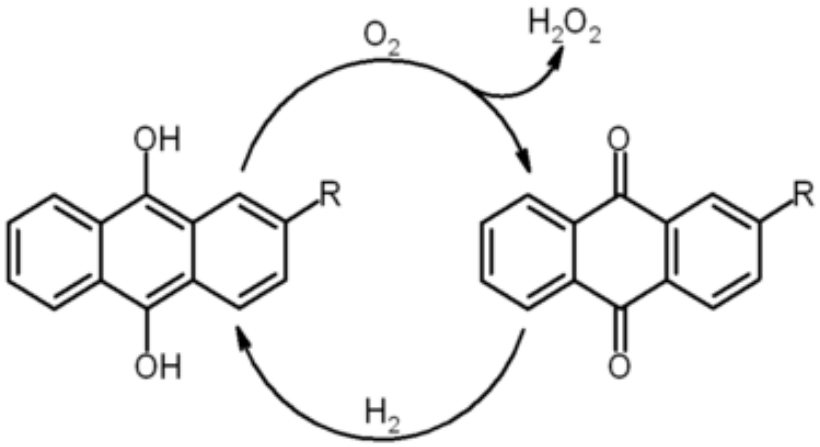

Figure 1.5 Reaction mechanism for the anthaqunione auto-oxidation (AO) process[29].

Hydrogen peroxide is subsequently extracted from the working solution by water to give approximately 30 wt% aqueous H_2O_2 solution, which can be concentrated to 70 wt% by distillation processes. As will be discussed later in chapter 1, high concentrations of hydrogen peroxide in particular are unstable with respect to temperature and the presence of base metal ions, and therefore storage at low temperatures and the addition of acid stabilizers (ppm level) are required.

Although the AO process has been employed for the last 60-70 years to manufacture >70 wt% aqueous H_2O_2 after distillation, it is only commercially viable on a large scale and entails many drawbacks including: high utility costs throughout the auto-oxidation process, side reactions and over-hydrogenation of AQ/AHQ compounds, necessitating the extraction and regeneration of very expensive compounds in the 'working solution'.

The selectivity of the hydrogenation catalyst toward the anthrahydroquinone product in some instances is limited, in particular for nickel catalysts, leading to formation of side products, some of which are presented in Figure 1.6. In addition, the stability of hydrogen peroxide in the presence of nickel represents a potential safety hazard, and therefore strict handling measures must be followed. The preferred choice of hydrogenation catalyst is palladium black, which is non-pyrophoric, affords improved anthrahydroquinone selectivity relative to nickel and can be easily recovered and re-activated. Because the anthraquinone is sequentially hydrogenated and oxidised, the auto-oxidation process overcomes the safety problems associated with mixing of hydrogen and oxygen gases.

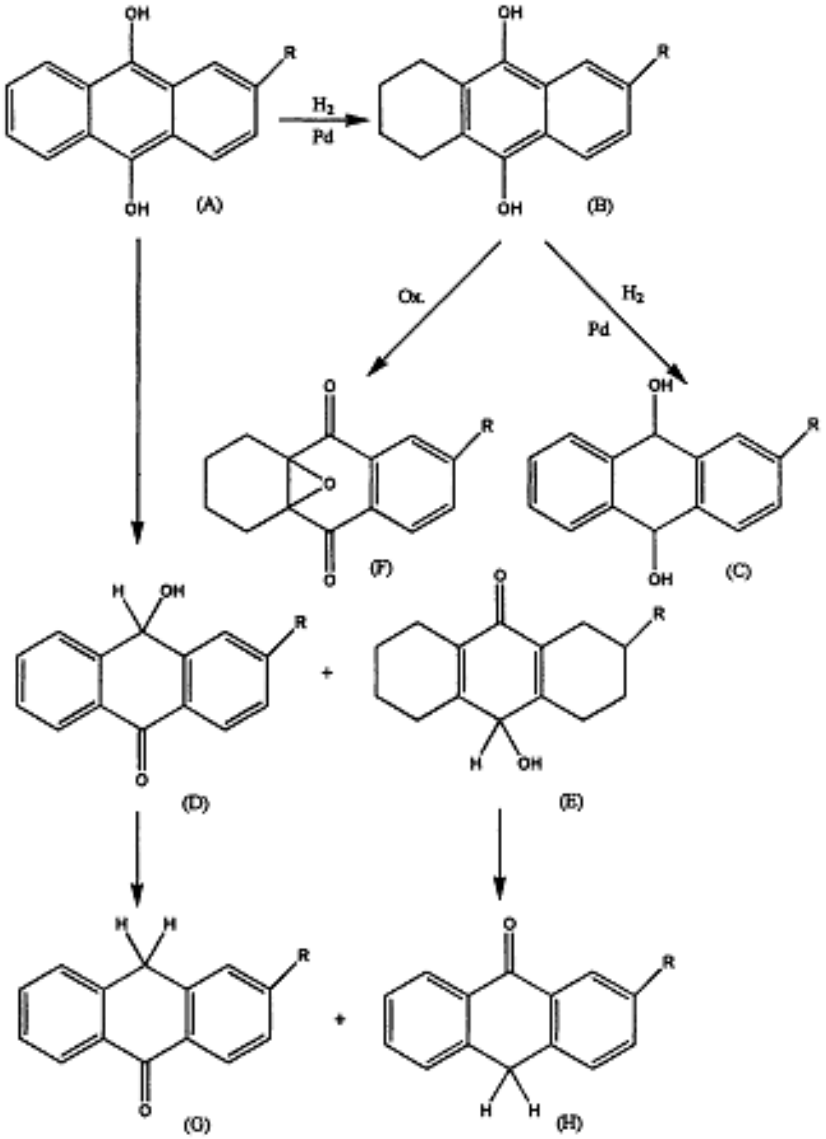

Figure 1.6 Side reactions taking place in the presence of 2-alkylanthraquinones[29].

Most importantly there are safety concerns associated with the transportation of an unstable product from a central site to point of use (therefore an acid stabilizer is therefore mandatory, *e.g.* H_3PO_4). The fact that an environmentally friendly oxidant is manufactured in a non-environmentally friendly manner when general applications require 3-8 wt% H_2O_2 has prompted research and development into small-scale and widespread synthesis routes with improved efficiency to manufacture hydrogen peroxide at a lower market value. As such, there exists considerable interest in the development of a direct synthesis process to produce H_2O_2 from H_2 and O_2 gases and catalysed using palladium based materials.

1.2.2 The direct synthesis of hydrogen peroxide from H_2 and O_2 using palladium based catalysts

Henkel and Weber were awarded the first patent[30] based on the direct synthesis of hydrogen peroxide from its elements using a palladium based catalyst in 1914. The reason why such a catalytic process has yet to be implemented on an industrial scale is primarily due to two factors. The first is that H_2/O_2 gas mixtures are explosive over a wide range of concentrations (5-95 vol% H_2 in O_2) and consequently for improved safety, hydrogen and oxygen can be diluted in "inert" gases, including CO_2 and N_2 in order to operate below the lower explosive limit[31, 32]. The second reason presents a direct challenge to scientists in that catalysts used to activate molecular hydrogen (reported as the rate limiting step)[33, 34] for the direct synthesis reaction also favour the parallel combustion and subsequent hydrogenation and decomposition pathways (all thermodynamically favoured) to form water, and therefore improvement in H_2 utilisation toward H_2O_2 and minimisation of subsequent hydrogenation/ decomposition pathways must be addressed in heterogeneous catalyst design (Figure 1.7)

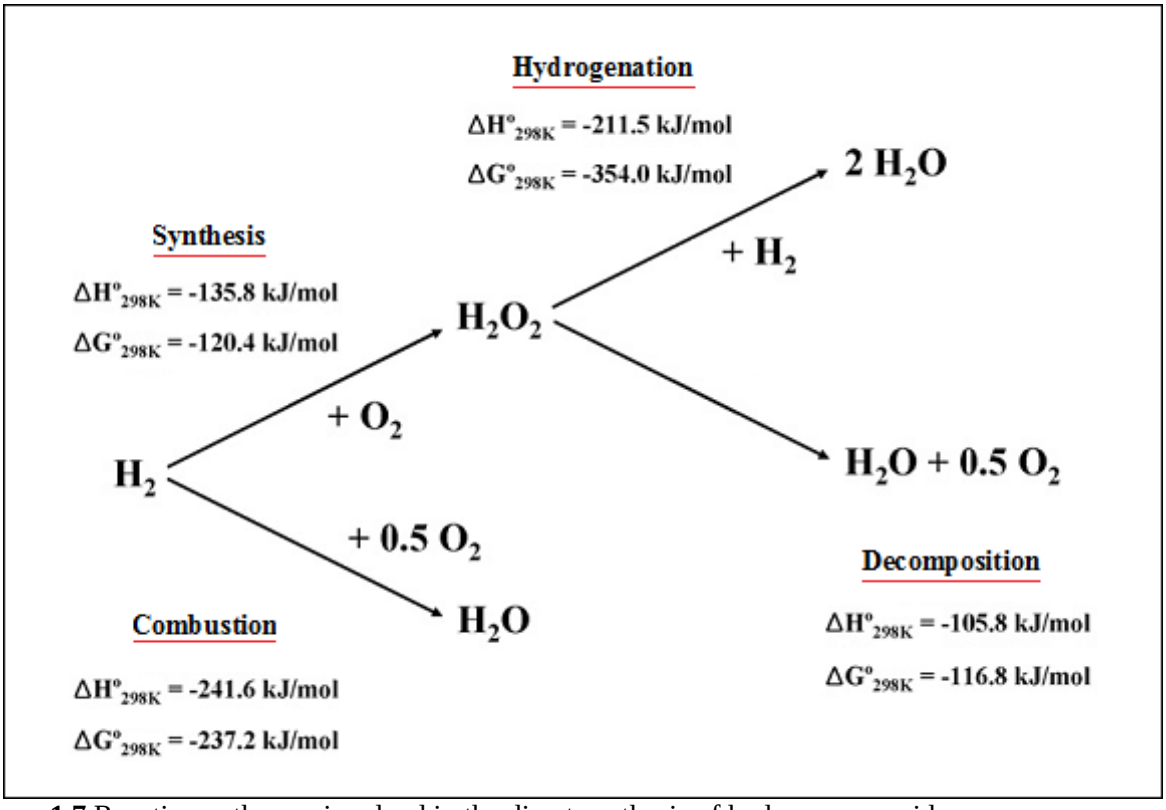

Figure 1.7 Reaction pathways involved in the direct synthesis of hydrogen peroxide.

In the literature it has been recognised that kinetic control is required to address this problem, with continued interest in developing a direct H_2O_2 synthesis process[16]. From a heterogeneous catalysis perspective, it is generally appreciated in theoretical and experimental studies that different active sites on a metal surface can be responsible for different chemical reactions[35, 36]. A three-phase (gas-liquid-solid) continuously stirred reactor system is normally used to study the direct synthesis reaction due to the minimisation/elimination of mass transport barriers[36], and while conditions vary between research groups with respect to catalyst synthesis and reaction setup, limiting the extent of true comparison, many general features of the reaction can still be seen throughout.

For catalysts prepared by impregnation and deposition precipitation routes, a heat treatment step (e.g. calcination or reduction) is determined as standard protocol in forming defined active sites on the catalyst surface in addition to influencing the oxidation state and stability of the metal surface (typically 0.5-5.0 wt% Pd loaded onto a support material and stabilized *via* metal-support interactions). Catalytic performance for direct H_2O_2 synthesis is measured by methods including volumetric titration and gas chromatography in order to determine the amount of reactant gases consumed/products formed.

Seminal studies by Pospelova *et al.* published in 1961 confirmed that the addition of acid (HCl, HNO_3) to supported Pd-catalysts is critical with respect to improving H_2O_2 yield, and is achieved by decreasing the base-catalysed decomposition of hydrogen peroxide[37-39]. These findings were extended by Choudhary and co-workers, who compared the effectiveness of a series of acids on the decomposition activity of a 5 wt% Pd/C catalyst in aqueous reaction medium[40]. Catalyst testing revealed that acids could be classified into two groups, with the nature of the associated anion also determined as being important (approximately one order of magnitude higher activity is achieved using halide acids), listed in the ascending order:

Oxyacids (moderate decomposition activity decrease) - acetic acid, phosphoric acid, sulphuric acid and perchloric acid.

Halide Acids (strongly suppressing acids with large activity decrease) - hydrochloric acid, hydrobromic acid and hydroiodic acid.

Phosphoric acid was identified as a suitable acid at low concentration (e.g. 0.03M), causing negligible leaching of Pd from the catalyst into the reaction medium. The effect of halide ion addition to either the reaction medium or catalyst structure (incorporated *via* pre-treatment) on H_2O_2 yield have been investigated in several studies[41-53] using a stirred glass reactor and ambient conditions for Pd supported on: ZrO_2, Ga_2O_3, CeO_2, SiO_2, H-Beta, ThO_2, BPO_4 and Pd/Al_2O_3 respectively. Results showed that both acid and halide additives were essential for improving H_2O_2 yield with results for halide incorporation (KF, KCl, KBr precursors) being similar in magnitude depending on whether the halide was present in the reaction medium or the catalyst structure. The nature of the halide ions in the reaction medium was found to influence H_2 conversion in the descending order:

KF > No Halide > KCl > KBr

The presence of iodide ions was detrimental to the catalyst with co-ordination to palladium resulting in surface poisoning and so was not included in the study, which indicated that while KF improved hydrogen conversion the most, the reverse effect existed for H_2O_2 selectivity in the descending order:

KBr > KCl > No Halide > KF

This confirmed that fluoride ions in fact promoted side and consecutive reaction pathways. The same sequence is reflected for hydrogen peroxide yield with bromide ions shown to be more effective than chloride ions on a molar basis (0.94 mmol/dm^3 KBr vs. 1.5 mmol/dm^3 KCl) and which is illustrated best by the decomposition pathway (previously hypothesised as being strongly dependent on H_2O_2 selectivity)[53].

It is acknowledged that even small amounts of halide additives can affect activity, with reduced decomposition observed using concentrations as low as 0.06 mmol-$Br/_{catalyst}$. Burch stated that this catalytic behaviour did not linearly correlate with electronegativity of the halide series[54] and suggested that the reason is due to sigma and pi donation effects, with the overall co-ordination ability increasing down group VII.

However results from separate studies by Burch[54] and Fan[55] contradict those of Choudhary who has shown reduced (Pd^0) catalysts in the absence of halides demonstrate both higher H_2 conversion and subsequent decomposition activity than their oxidised (PdO) counterparts, reducing the corresponding H_2O_2 selectivity by approximately one order of magnitude[41-53]. When compared to particle size and surface area, the bulk oxidation state of the catalyst is considered paramount in determining the observed catalytic activity, leading to suggestion that the oxidation state and halide type play a co-operative role since oxidised and reduced catalyst performances are influenced to different extents depending on the type of halide used[26-39].

This is best illustrated for bromide ions (Figure 1.8) in which X-ray photoelectron spectroscopy (XPS) studies indicated ions were either situated close to palladium particles or mobile on the catalyst surface during the reaction to have interactions with palladium[33]. The technique has been used by Fierro and Campos-Martin to confirm that Pd anchored on ion-exchanged resins functionalised with sulphonic acid groups was stabilised in the Pd^{2+} oxidation state (even after reductive heat treatment) to give improved hydrogen peroxide selectivity[56].

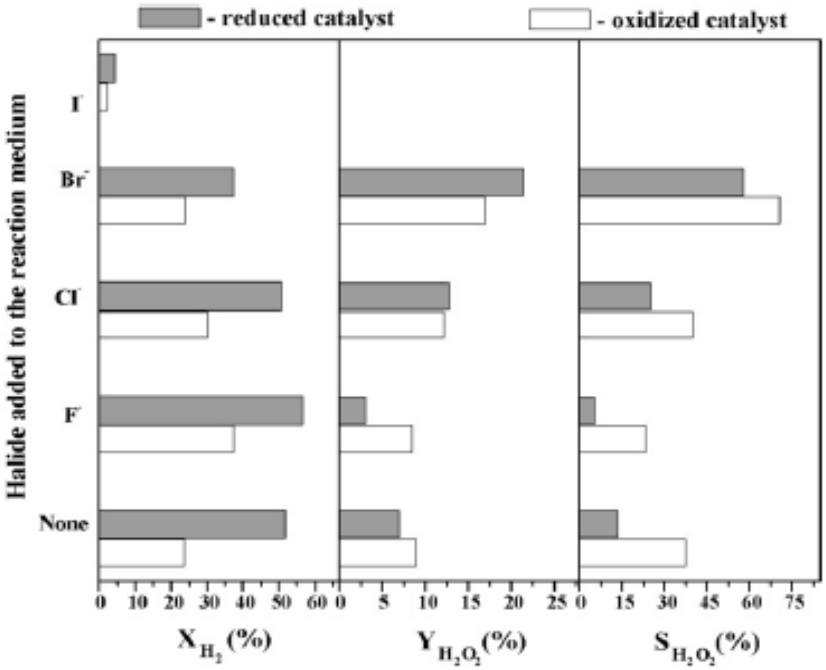

Figure 1.8 The effect of oxidation state and halide on the conversion (X), yield (Y) and selectivity of Pd/CeO_2 catalysts for direct H_2O_2 synthesis[53].

Lunsford and co-workers have presented evidence of colloidal Pd being active for the synthesis of hydrogen peroxide[34, 57-64]. Though use of a colloidal system on industrial scale would be extremely difficult to maintain, results from studies using different O_2/H_2 feed ratios introduced through a frit into an acidified solution (1M HCl) are of widespread significance. Addition of either $PdCl_2$ or Pd/SiO_2 to HCl resulted in oxidation of Pd^0 to form $PdCl_4^{2-}$ ions in solution, which are subsequently reduced back to metallic Pd by H_2, leaving some metal present as colloid (establishing a Pd^0/Pd^{2+} steady state) and confirmed by electron microscopy[57].

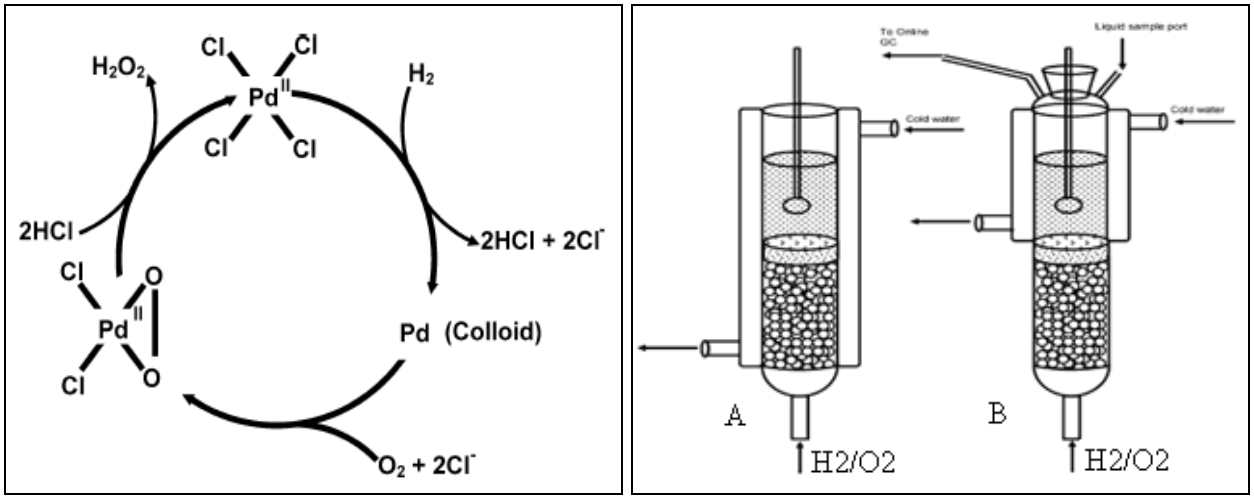

Figure 1.9 Schematic of colloidal system (left) and open **(A)** and closed **(B)** stirred testing reactors (right)[57].

A linear relationship between colloid concentration and H_2O_2 formation rate was observed during time on stream studies, while $^{16}O_2/^{18}O_2$ isotope experiments and Raman Spectroscopy confirmed that hydrogen peroxide is derived from molecularly adsorbed oxygen on the palladium surface[58], supporting the existence of a hydroperoxy intermediate species by Sivadinarayana[65]. The introduction of 0.01M Br^- ions in subsequent experiments saw increased product selectivity with H_2O_2 solutions nearing 2 wt%. Evaluation of different O_2/H_2 ratios (4 and 15) using the colloidal system indicated that the formation of hydrogen peroxide was first-order with respect to H_2 and zero-order with respect to O_2. The highest H_2 conversions were reported at low O_2/H_2 ratios, suggesting hydrogen activation as representing the rate limiting step[51].

In addition, the Lunsford group have proposed Pd^0 as the active phase for direct H_2O_2 synthesis over a Pd/SiO_2 catalyst in H_2SO_4/Ethanol slurry[66]. Pd^0/SiO_2 exhibited the highest activity at 10 ^oC, forming 0.16 wt% H_2O_2 after 2 h, and while PdO/SiO_2 was almost inactive for H_2O_2 synthesis, activity improved to an intermediate value after mild reduction. High Resolution Electron Microscopy (HREM) showed metallic Pd (d = 0.22 nm) decorated larger PdO (d = 0.26 nm) nanoparticles on silica with an amorphous boundary. It was concluded that both halide and acid promoters are required for the reaction to proceed, by preventing the development of surface oxide ions, leading to water formation[66].

Both Choudhary and Lunsford have investigated the effect of halide addition and concluded that bromide and chloride ions block surface sites responsible for catalysing the rapid decomposition of H_2O_2, with the sequential reaction of hydrogen peroxide instead directed through a slower hydrogenation pathway[16]. Given that decreased H_2 conversion is also evident with bromide/chloride it has been suggested that sites active for combustion are also blocked by Br^- and Cl^- ions, which for both site types inhibit cleavage of molecularly adsorbed oxygen to give water. Regarding the influence of oxidation state, Pd^0/Pd-H species are believed to act as an intermediate in the decomposition reaction[42] with halide addition preventing the homolytic fission of hydrogen peroxide to give hydroxyl radicals, leading to the formation of water[16].

The role of acid in the reaction medium have also been considered, concluding that acids facilitate the adsorption of halide ions onto the catalyst surface and reduce the base-catalysed decomposition pathway: phosphoric acid (0.03M) is effective without causing significant metal leaching[41-54]. Numerous studies have used methanol and ethanol as the reaction medium given the improved solubility of hydrogen and oxygen in these alcohols compared to water. This has been likened to the development of surface formate (methanol) and acetate (ethanol) species by reaction with oxygen on the Pd [110] surface, which prevent HO-OH bond breaking (HO-OH = 213 kJ mol^{-1}, H-O_2H = 369 kJ mol^{-1})[62, 63].

1.3 Catalysis by Gold

Catalysis by gold received worldwide attention after separate discoveries by Haruta[67] and Hutchings[68] of the unexpectedly high catalytic activity of supported gold nanoparticles for carbon monoxide oxidation and acetylene hydrochlorination respectively. Following these discoveries, there has been an exponential increase in the number of papers using supported Au catalysts for multiple applications (Figure 1.10), including: environmental catalysis (CO oxidation, NO_x reduction, oxidation of volatile alcohols and photocatalysis)[69-72], energy processing (the water-gas shift reaction)[73, 74] and chemical synthesis (selective hydrogenation and oxidation reactions, alkene epoxidation and the direct synthesis of H_2O_2)[75-78].

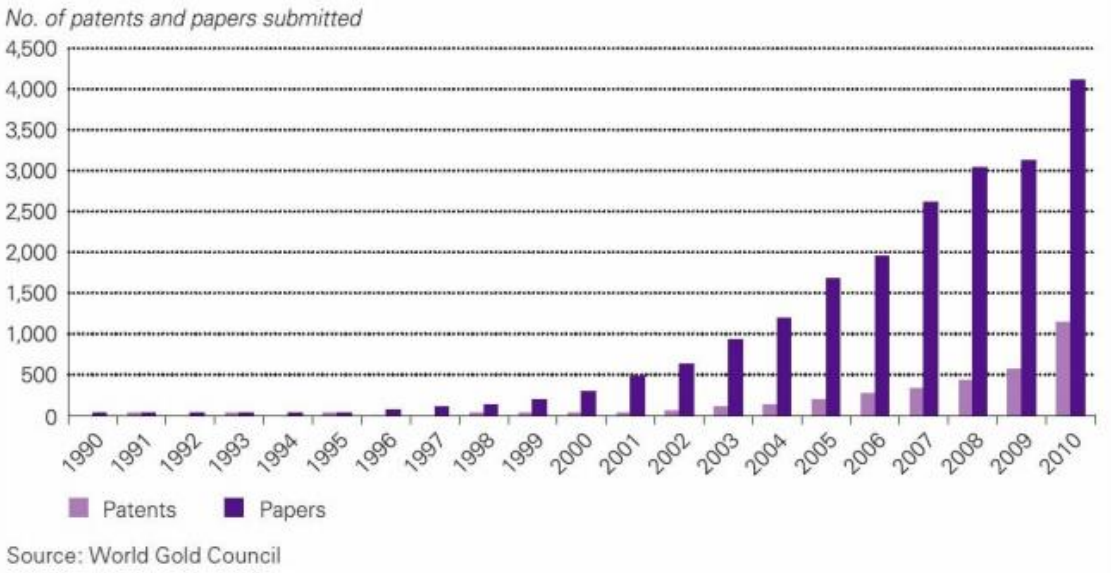

Figure 1.10 Summary of the number of papers and patents involving the application of gold catalysts as a function of time.

While bulk gold is one of the least reactive chemical elements that is solid under standard conditions, unique catalytic activity is present at the nanometre scale (<5 nm). The high catalytic activity of which has been suggested as correlating with relativistic effects in heavy metal elements, *i.e.* the contraction of 6*s* orbital across the transition metal series (which is greatest for Au and closely followed by Pt) and secondly the strength of the binding energy of the Au 6*s* electron, resulting in high electronegativity[79, 80]. Several important Au-catalysed reactions are discussed in the following sections.

1.3.1 CO oxidation

The oxidation of carbon monoxide at ambient temperature using supported Au catalysts represents one of the most significant breakthroughs in the field. In their initial studies[67, 70], Haruta and co-workers demonstrated that this reaction could be performed at temperatures as low as 203 K. There are many unresolved issues in the literature regarding CO oxidation over Au catalysts which are subject to continuing debate, including: the nature of the active site, the role of the catalyst support and lattice oxygen, the presence of moisture in the reaction[81, 82], the catalyst preparation method, and also deactivation effects. Several reaction mechanisms have been proposed[83-85], including the Bond-Thompson[83] model (Figure 1.11), in which Au atoms at the metal-support interface (an oxide support, *e.g.* TiO_2, Fe_2O_3, CeO_2) represent the active sites for CO oxidation.

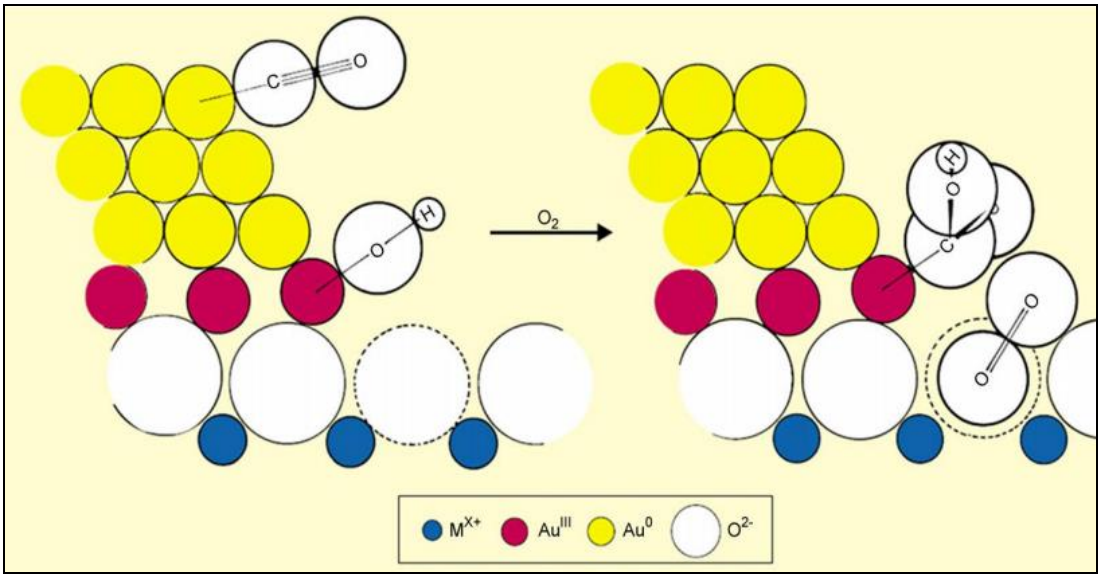

Figure 1.11 The Bond-Thompson model for the Au-catalysed oxidation of carbon monoxide[83].

Though a widely respected model, debate continues regarding the extent with which different Au oxidation states (Au^0/Au^{3+}) participate in the reaction[86-88]. X-ray photoelectron spectroscopy (XPS) characterisation of Au catalysts by Hutchings *et al.* showed a correlation between catalytic activity and Au($4d_{5/2}$) binding energy[89], identifying different Au oxidation states to be present in active catalysts, with the highest catalytic activity corresponding to the presence of cationic Au (for example, detection of Au^{3+} in Au/Fe_2O_3 catalysts).

Haruta pioneered the deposition precipitation (DP) method to synthesise Au catalysts in a carefully controlled manner (involving regulation of base, pH, temperature and light) to generate 2-4 nm Au particles, determined as critical to achieving high CO oxidation activity[70]. High Resolution Electron Microscopy (HREM) characterisation of Au/TiO_2 catalysts prepared using anatase and rutile phase TiO_2 supports concluded that different preferred orientations existed between Au nanoparticles and different TiO_2 phases, with the Au [111] plane parallel to TiO_2 [112] in anatase and TiO_2 [110] in rutile supports respectively[90], and corresponding to different observed activities for CO oxidation (Figure 1.12, left).

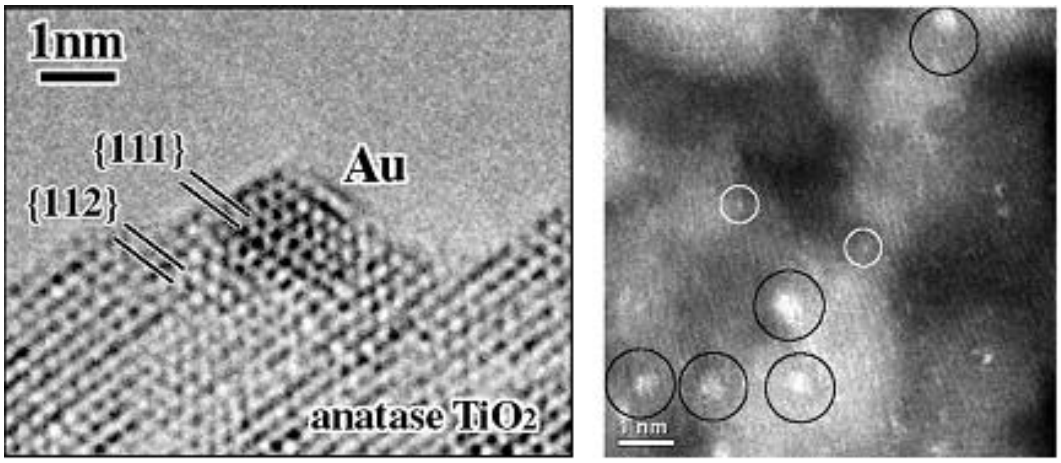

Figure 1.12 Transmission electron micrograph showing the Au/TiO_2 contact interface[90] for anatase TiO_2 (left), and High magnification aberration corrected STEM-HAADF images of the Au/FeO_x catalyst active for CO oxidation[91], using white circles to show individual atoms and black circles to show sub-nm Au clusters consisting of only a few atoms (right).

Application of advanced electron microscopy by Hutchings and Kiely[91] with respect to Au/FeO_x catalysts distinguished that sub-nm Au clusters of approximately 0.5 nm in diameter containing ~10 atoms were responsible for high CO oxidation activity (Figure 1.12, right). Theoretical studies also indicated the beneficial role of clusters with DFT calculations by Norskov *et al.* highlighting that the activation of CO molecules was energetically favoured on Au clusters containing 10 atoms[92], similar to calculations by Haruta *et al.*, which reported a strong interaction between negatively charged Au_{13} clusters and CO molecules respectively[93].

Goodman and co-workers[94] compared the activity of model Au/TiO_2 catalysts, showing that the turnover frequency (TOF) for CO oxidation reached a maximum for Au 'islands' of 3.5 nm in diameter and 3 atoms thick, corresponding to the point where Au partially loses its metallic character on transition from 'continuous' to 'discrete' band-gap energies, the transition of which has been suggested by the authors to correlate with catalytic activity. However, given this is a study of model catalysts, Haruta[95] stated that it is more reasonable that the ratio of the number metallic Au atoms on the surface of Au 'islands' relative to the number of Au atoms at the metal-support interface reaches an optimum at 3.5 nm average cluster diameter (Figure 1.13).

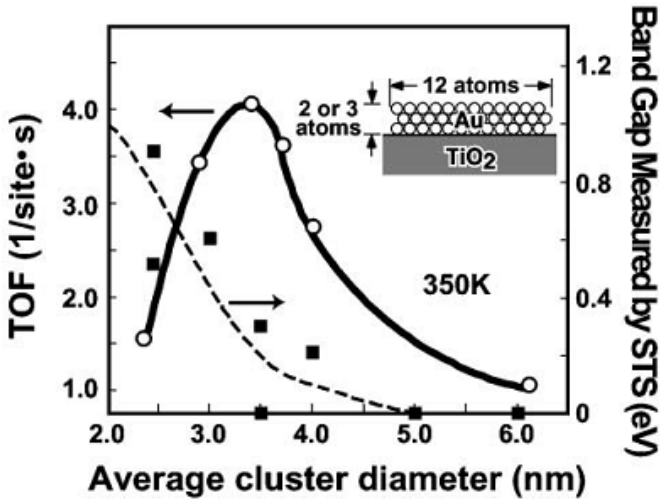

Figure 1.13 Turnover frequencies (TOF) and band-gap measured by STEM as a function of the diamter of Au islands depositied on TiO_2 [94].

1.3.2 Hydrochlorination of acetylene

Another milestone was the prediction by Hutchings[68] in the early 1980's that Au would be the best catalyst for the hydrochlorination of acetylene to vinyl chloride, an important industrial chemical used to produce the polymer polyvinyl chloride, a major plastics material[96-99]. One of the main industrial synthesis routes was based on acetylene hydrochlorination using mercuric chloride, $HgCl_2$, supported on carbon as the catalyst. Aside from the high toxicity associated with this catalyst, sublimation of the active component during reaction resulted in deactivation, prompting research and development of a stable, replacement material. A wide range of metal chlorides supported on carbon were evaluated for this reaction by Shinoda[100].

Hutching's subsequently plotted the activity of these catalysts (most of which were divalent) against the standard electrode potential of the cations to highlight a direct correlation, based on the reasoning that hydrochlorination was a two-electron process involving the 2π electrons of acetylene[68]. Based on these results it was predicted that $AuCl_3$ supported on carbon would be the best catalyst for this reaction, and incipient wetness impregnation with $HAuCl_4$ solution resulted in a catalyst three times more active than its $HgCl_2$/carbon counterpart, with >99.9% selectivity toward the vinyl chloride monomer.

While gold catalysts were more stable compared to mercuric chloride catalysts, slow deactivation was recognised and found to be dependent on temperature. At typical operating temperatures of around 180 ^oC, deactivation of the catalyst through reduction of Au^{3+} to Au^0 was determined using ^{197}Au Mossbauer spectroscopy[98], which could be countered by in-situ reactivation with NO.

1.3.3 Alkene epoxidation

The selective gas-phase epoxidation of propene to propylene oxide (PO) represents a major industrial target, as PO is the monomer used in the production of polyurethane and polyols. The epoxidation of C_3 alkenes is significantly more complicated (Figure 1.14) than that of ethene epoxidation, where >90% selectivity is currently achieved using Ag-based catalysts[101].

Figure 1.14 Reaction scheme for the epoxidation of propene[101].

Haruta and co-workers[102, 103] demonstrated that gold nanoparticles supported on TiO_2 were selective for the epoxidation of propene to propylene oxide in the presence of a sacrificial H_2 donor, albeit only at low conversion (~1%) at temperatures of 303-393 K. High selectivities based on very low conversions were widely reported in the literature, with the presence of H_2 in the reactant feed gas permitting the activation of O_2 at relatively low temperatures[104-107].

Characterisation of Au/TiO_2 catalysts prepared by deposition precipitation indicated that Au particle size was critical in determining H_2 selectivity for propene epoxidation, with Haruta suggesting high selectivity is attributed to hemispherical Au nanoparticles of 2-5 nm in diameter, with <2 nm particles likened to an increase in rate of propene hydrogenation to propane[108].

In addition to anatase and rutile TiO_2, the Ti-based materials: TS-1, TS-2, Ti-zeolite β, Ti-MCM-41 and Ti-MCM-48 were used to support Au, resulting in higher H_2 selectivities[109-111], which were attributed to changes in the co-ordination environment and hydrophobicity of the support material, leading to a reduction in the total oxidation of propene to CO_2. Propene conversion could be partially improved to 5% on increasing reaction temperature from 80 to 150 ^oC while maintaining H_2 selectivity >90%. However, time on-line deactivation was observed using all supports, due to accumulation of oxidised products on the catalyst surface[109-114]. This does not however eliminate the possibility of commercial application as catalysts can easily be reactivated, and while propene conversions reported in the literature do not exceed 7%, the H_2 efficiency/utilisation of the reaction stands at 40% [115, 116].

Chen and Nijhuis have demonstrated that high selectivities can be obtained using Au/TiO_2 catalysts prepared using low Au loadings[117, 118]. However, the formation of very small Au particles is these catalysts were found to be disadvantageous with high rates of propene hydrogenation to propane reported. The introduction of a small amount of carbon monoxide to the reactant feed gas was found to completely deactivate propene hydrogenation, and the presence of water in the gas feed reduced deactivation effect(s)[119]. Investigation of the reaction mechanism by the same authors determined that the formation of an active peroxy species on gold nanoparticles represents the rate determining step.

The sensitivity of the reaction to gold loading and Si/Ti ratio was noted by several authors, with high selectivity reported using a 0.01% Au/TS-1 catalyst (Si/Ti ratio = 500), suggested to improve the shape selectivity of catalysts and facilitate the release of PO away from the catalyst surface in order to limit the contribution of time on-stream deactivation effects[115].

1.3.4 Oxidation of alcohols and aldehydes

The selective oxidation of alcohols and aldehydes to form chemical intermediates of importance to the fine chemicals industry is a rapidly growing area, with key examples including the oxidation of glycerol to glyceraldehyde and the solvent-free oxidation of primary alcohols to aldehyde and acid products[120] (with hydroperoxy, OOH species considered to be a key intermediate in the selective oxidation of alcohols). Studies by Prati and co-workers[121-126] demonstrated that supported Au nanoparticles were effective for alcohol oxidation, with high activity and selectivity >98% toward the selective oxidation of polyols substrates such as 1,2-ethanediol and 1,2-propanediol. Catalysts were prepared by sol-immobilization (S_{Im}), a technique which involves the formation of metal colloid "sols" stabilised using a protective ligand[127], for example polyvinyl alcohol (PVA), before immobilisation onto a support material, *i.e.* carbon, CeO_2, TiO_2.

Following these initial discoveries, Christensen *et al.* [129] demonstrated that Au catalysts were effective for the oxidative esterification of polyols such as 1,2-propanediol and glycerol in the presence of methanol solvent to form dimethyl mesoxalate or methyl lactate products, respectively in high yields. Brett and co-workers have reported that using Au-Pd catalysts for this reaction lead to a significant enhancement in terms of activity and selectivity to methyl lactate, with high selectivity (70-75%) and >30% conversion using Au-Pd/CeO_2 catalysts. A mechanistic study showed that a primary pathway for methyl lactate formation proceeded *via* the oxidative esterification of hydroxyacetone or lactylaldehyde (Figure 1.15)[128]. Finally, by careful tuning of the catalyst support and Au/Pd molar ratio, the further oxidation of methyl lactate to methyl pyruvate was achieved for the first time in the literature.

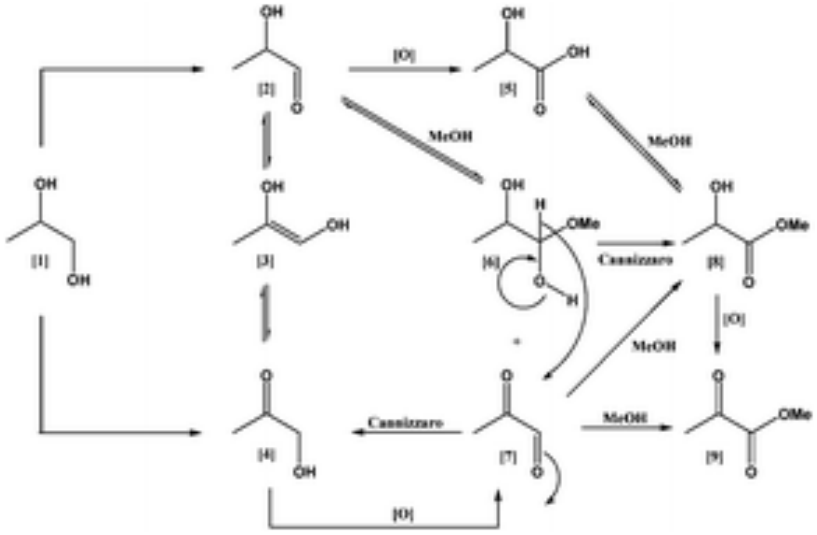

Figure 1.15 Reaction pathways for the oxidative esterification of 1,2-propanediol[128].

Glycerol is the main by-product in the production of biodiesel and is a sustainable raw material for which demand has significantly increased in recent years[130]. Hutchings *et al.* [131] demonstrated that the application of supported Au catalysts for the selective oxdaition of glycerol to glyceraldehyde resulted in >99% selectivities when using either carbon or graphite as the support, and performing the reaction under relatively mild conditions in glass-stirred reactors (60 ^{o}C, 3 bar) in the presence of NaOH, which is required for the first hydrogen abstraction in the reaction mechanism. Base-free conditions have subsequently been reported using Au-Pt and Au-Pd nanoparticles supported on $Mg(OH)_2$, resulting in enhanced glycerol conversion and selectivity toward C_3 products relative to monometallic counterparts[131].

Corma and co-workers demonstrated that high activity toward the selective oxidation of alcohols to aldehydes and ketones, and the oxidation of aldehydes to acids can be achieved using Au/CeO_2 catalysts[132-136]. A major breakthrough reported by these authors was that the reaction could be performed under solvent free conditions, without the requirement of a base to achieve high activity. Enache *et al.* [137] showed that bimetallic $Au\text{-}Pd/TiO_2$ catalysts were highly selective across a wide ride range of alcohol oxidation reactions under solvent free conditions, with turnover frequencies (TOF's) reported in excess of 270,000 in the case of 1-phenylethanol. These results were an improvement over those initially reported by Corma using monometallic Au and Pd catalysts[138], with the alloying of Au and Pd leading to an approximately 25 fold activity enhancement.

The selectivity for oxidation of benzyl alcohol to benzaldehyde (which has 5 possible side-products) using Au-Pd catalysts exceeded 90%, while further studies determined Au-Pd/ TiO_2 as the optimum catalyst for this reaction, which is operated at 100-160 ^oC [138]. Supported Au-Pd catalysts are versatile across a wide range of reactions and it was recently reported by the Hutchings group[139] that Au-Pd/C and TiO_2 catalysts were highly active and selective for the oxidation of C-H bonds in toluene, with a 95% toluene conversion and 96% selectivity to the benzyl benzoate product. This represents another significant result since benzyl benzoate, in addition to benzyl alcohol, is a valuable chemical intermediate used in the production of pharmaceuticals, dyes, solvents and plasticisers. Another recent discovery is the high activity and selectivity of supported Au-Pd catalysts for the direct synthesis of hydrogen peroxide in the absence of acid and halide promoters[78].

1.4 The direct synthesis of hydrogen peroxide from H_2 and O_2 using gold-palladium catalysts

In early work, Ishihara and co-workers reported that a 1 wt% Au/SiO_2 catalyst tested in the absence of halide promoters exhibited promising H_2O_2 synthesis activity (with 30% H_2 selectivity) compared to Pt, Pd or Ag/SiO_2 catalysts, for which no hydrogen peroxide was formed[140]. The rates of H_2O_2 synthesis and hydrogenation/decomposition were compared for monometallic Au catalysts and concluded that basic oxides such as MgO and ZnO were unsuitable supports (forming only water) while Au/SiO_2 performed the best. The addition of 1 wt% Pd to Au/SiO_2 gave improved rates of H_2O_2 synthesis, with a maximum yields reported when using a Pd:Au weight ratio of 82:18. The same group have also highlighted that Au is highly efficient in forming stable, hydroperoxy, OOH species (an intermediate in direct H_2O_2 synthesis) compared to Pd, which is highly efficient with respect to dissociating the oxygen-oxygen bond[141].

The promotional effect on addition of Au to Pd catalysts for the direct synthesis of hydrogen peroxide was first reported by Hutchings and co-workers, who have extensively studied the direct synthesis reaction using Au-Pd catalysts since 2002. The potential of monometallic Au catalysts were evaluated before advancing to Au-Pd nanoparticles[142]. Initial experiments were performed in a sealed stainless steel autoclave at 2 ^{o}C, 37.5 bar H_2/O_2 (1:2 molar) pressure and 100% methanol solvent, resulting in improved H_2O_2 yields based on higher H_2 selectivities upward to 53% when using an Au/Al_2O_3 catalyst[142]. To limit the influence of mass transfer effects during reaction, a 1200 rpm stirring speed was selected, with results for a 0.6 wt% Pd/sulfonated carbon catalyst[143] indicating that low temperature and shorter reaction times favoured hydrogen peroxide yield, with the rate of reaction being linearly dependent on pressure.

Further studies have been performed at 2 ^{o}C in a sealed, stainless steel autoclave (580 psi / 37.5 bar pressure, 1200 rpm) with CO_2-diluted 5% H_2 and 25% O_2 (1:2 molar) gases dissolved in a methanol/water (2:1 weight) solvent and catalyst (10 mg). Studies recognised that supported 2.5 wt% Au-2.5 wt% Pd catalysts evaluated for H_2O_2 synthesis in the absence of halide and acid promoters gave improved H_2O_2 productivities/synthesis activities relative to monometallic 5 wt% Au and Pd counterparts.

A series of supported Au-Pd catalysts prepared *via* wet-impregnation have been evaluated by the Hutching's group for direct H_2O_2 synthesis activity, including 2.5 wt% Au-2.5 wt% Pd/TiO_2, which after calcination in static air at 400 ^{o}C (3 h) demonstrated a high H_2O_2 productivity/synthesis activity of 64 $mol_{H2O2}kg_{cat}^{-1}h^{-1}$. This value corresponded to the formation of 0.12 wt% H_2O_2 in solution and represented a three-fold improvement in activity compared to previously evaluated $Au-Pd/Al_2O_3$ catalysts[144, 145]. A suitable reaction time was confirmed as 30 minutes, with a positive correlation found between H_2O_2 yield and catalyst mass (0-50 mg). The effect of calcination and reduction were investigated for $Au-Pd/TiO_2$ catalysts, with the uncalcined sample exhibiting the highest rate of H_2O_2 synthesis reported to date (H_2O_2 productivity = 202 $mol_{H2O2}h^{-1}kg_{cat}^{-1}$, 46% H_2 conversion and 89% H_2 selectivity), although significant catalyst deactivation was observed on subsequent reactions due to the leaching of Au and Pd from the catalyst, with ~90% metal content lost after the first reaction.

In comparison, catalysts calcined in static air at 400 ^{o}C retained 100% Au+Pd metal content on subsequent reactions, indicating that the calcination/heat treatment step serves as a compromise between catalyst activity and stability[144] (Figure 1.16, (left)).

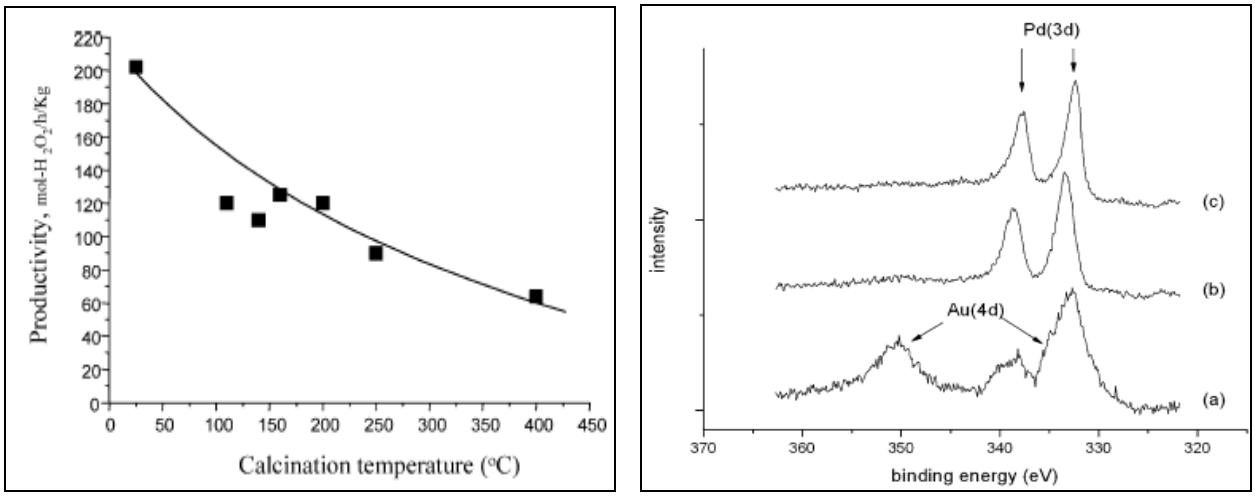

Figure 1.16 The effect of calcination temperature on $AuPd/TiO_2$ catalyst performance (left), and XPS analysis of uncalcined **(a)** and static air calcined 200 ^{o}C **(b)** and 400 ^{o}C **(c)** samples (right)[144].

XPS characterisation shown in Figure 1.16 (right) indicated the development of an $Au_{core}Pd_{shell}$ structure for Au-Pd particles supported on TiO_2 upon calcination in static air, reporting a high surface Pd/Au ratio with a dramatic decrease in the intensity of the Au(4d) signal after 400 ^{o}C calcination. Scanning Transmission Electron Microscopy (STEM) images concluded a bimodal distribution of small (2-10 nm) and large (35-80 nm) particle diameters with no small Au particles. This was likened to the improved surface mobility of Au relative to Pd particles (below 10 nm), resulting in sintering and formation of large, Au-rich particles upon calcination[144].

Subsequent evaluation of $Au\text{-}Pd/Fe_2O_3$ catalysts indicated an inverse relationship between CO oxidation and H_2O_2 formation (also reported for $Au\text{-}Pd/TiO_2$): specifically it was concluded that co-precipitation (CP) was the preferred preparation method of catalysts active for carbon monoxide oxidation, while catalysts most active toward hydrogen peroxide synthesis were prepared by wet impregnation, based on differences in both the nanoparticle composition and size distribution between methods[146].

The microstructural analysis of Au-Pd/C catalysts indicated a bimodal particle size distribution and the existence of homogeneous Au-Pd alloys in comparison to the Au-core Pd-shell morphologies characteristic of Au-Pd/TiO_2 and Al_2O_3 catalysts[147]. This is highlighted in the statistical analysis of X-ray energy dispersive spectroscopy (XEDS) maps leading to construction of red-green-blue, RGB images (Figure 1.17). For Au-Pd/C catalysts, the RGB image is aqua in colour and corresponding to the random mixing of Au (blue) and Pd (green) to form homogenous Au-Pd alloys (aqua), compared to the $Au_{core}Pd_{shell}$ nanoparticles clearly shown in RGB images for Au-Pd/TiO_2 and Al_2O_3 catalysts[147].

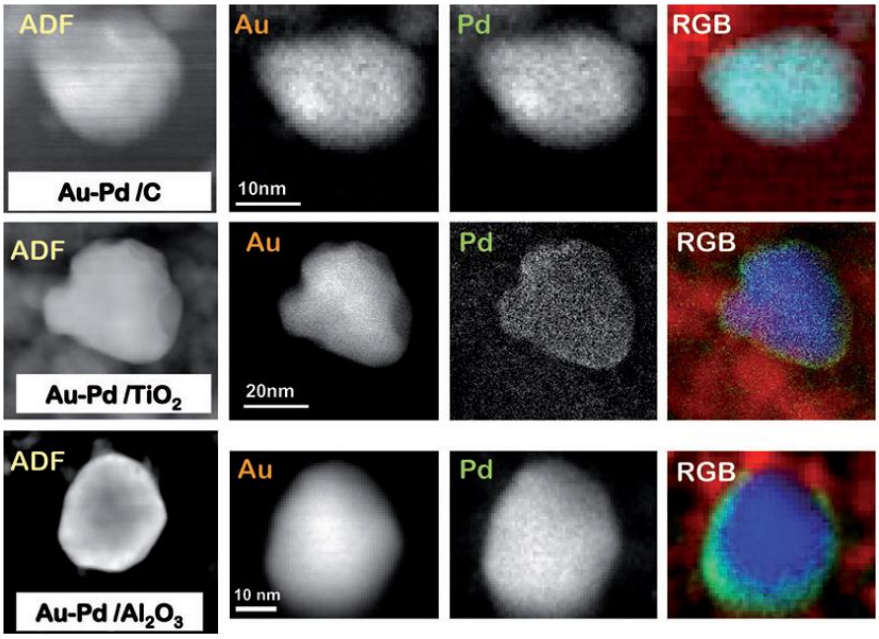

Figure 1.17 Comparison of High Angle Annular Dark Field (HAADF) images, Au and Pd maps and RGB (Au = Blue: Pd = Green) overlap maps for 2.5 wt% Au-2.5 wt% Pd/C, TiO_2 and Al_2O_3 catalysts prepared by wet impregnation and calcined in static air (400 ^oC, 3 h)[147].

The development of core shell morphologies has also been observed for Au-Ag nanoparticles contrary to phase diagrams for both bimetallic Au-Pd and Au-Ag systems predicting the formation of a complete homogeneous solid solution[148]. One reason as to why Pd is located at the nanoparticle shell/perimeter is due to the preferential formation of surface Pd-O bonds (confirmed by XPS analysis) during high temperature calcination in static air. A subsequent reduction step at high temperature >400 ^oC is required to observe an inversion of the $Au_{core}Pd_{shell}$ morphology, determined as detrimental to catalytic activity.

Taking into account the findings of an investigation into the effects of using different H_2/O_2 ratios and total reaction pressures, Hutchings and Moulijn proposed a kinetic scheme for the production of hydrogen peroxide (steps 1-5) and for the parallel combustion and consecutive hydrogenation/decomposition of hydrogen peroxide (steps 6-10, which consider the dissociative adsorption of O_2)[36].

1. $H_2 \rightarrow 2H_{(ad)}$

2. $O_2 \rightarrow O_{2(ad)}$

3. $H_{(ad)} + O_{2(ad)} \rightarrow OOH_{(ad)}$

4. $OOH_{(ad)} + H_{(ad)} \rightarrow H_2O_{2(ad)}$

5. $H_2O_{2(ad)} \rightarrow H_2O_2$

6. $O_2 \rightarrow 2O_{(ad)}$

7. $O_{(ad)} + H_{(ad)} \rightarrow OH_{(ad)}$

8. $OH_{(ad)} + H_{(ad)} \rightarrow H_2O_{(ad)}$

9. $H_2O_{(ad)} \rightarrow H_2O$

10. $H_2O_{2(ad)} \rightarrow H_2O_{(ad)} + O_{(ad)}$

Scheme 1.3 A proposed kinetic scheme describing the steps involved in the direct synthesis of hydrogen peroxide[36].

An important industrial target is to perform the direct synthesis reaction in the absence of acid and halide promoters, which are understood to inhibit dissociation of the O-O bond, thus reducing the activity of sequential H_2O_2 hydrogenation/decomposition reactions and increasing hydrogen peroxide yield. The presence of both acid and halide promoters in the reaction medium is disadvantageous in the development for a commercial application since acid/halide additives are detrimental when in contact with metal components, in particular stainless steel autoclaves where corrosion is noted as being a significant drawback[32]. There are also potential contamination issues and addition steps would be required to separate promoters during the extraction and purification of hydrogen peroxide.

The development of supported Au-Pd catalysts represents a potential means to overcome these drawbacks, and for Au-Pd/C catalysts it has been demonstrated by Edwards *et al.* that pre-treating the carbon support in dilute nitric acid prior to impregnating Au and Pd metals formed in a highly active catalyst with H_2 selectivity >98% due to the complete deactivation (switching-off) of the sequential H_2O_2 hydrogenation and decomposition activity over the catalyst[149].

This finding represents a first in the literature and the benchmark Au-Pd catalyst for direct H_2O_2 synthesis. Modification of Au-Pd particle composition and size distribution/ dispersion leading to 'blocking' of surface sites responsible for dissociating the O-O bond were proposed as the reasons behind enhanced activity. Further investigation into the effect of nitric acid-pretreatment represents the basis of chapter 4. Before outlining the aims of this thesis, some alternative direct H_2O_2 synthesis technologies and theoretical studies reported in the literature are presented in section 1.5.

1.5 Alternative technologies and theoretical studies

Zhou has reported that H_2/O_2 can be converted to H_2O_2 and water under ambient conditions when activated into non-equilibrium plasma inside a silent discharge reactor consisting of a pair of co-axial glass cylinders and two electrodes of which one was maintained at 12.8 kV[150]. The process requires H_2 and O_2 only, with no requirement for solvent and promoters to generate a stable 4.2 wt% H_2O_2 solution after 3 h discharge, the concentration of which increased linearly with time, forming 14.3 wt% H_2O_2 after 11 h discharge. Though scaling the reactor design up to $1m^3$ would result in formation of 30 wt% H_2O_2 solutions and represent a safe process, the non-adiabatic system is currently uneconomical to run with an energy consumption of 80 kWh per kilogram of H_2O_2 formed[150], outweighing the safety benefits and elimination of H_2O_2 extraction and purification steps[12].

Electrochemical studies by Yamanaka[151-154] based on the reduction of O_2 to H_2O_2 in an alkaline medium have shown that up to 8 wt% H_2O_2 solutions can be obtained with a 25% current efficiency (CE) when using an [AC(HNO_3) + VGCF/nafion] cathode, where AC = activated carbon, VGCF = vapour grown activated carbon. With recent improvements in fuel cell design and flexibility in alkaline medium selection, other reactions have employed electrolytes such as 2M NaOH to produce 7 wt% H_2O_2 solutions at 93% CE, with both the concentration and alkaline nature useful for pulp bleaching. However the reality with an electrochemical cell system is that the components are in many cases too expensive to scale up for an industrial processes and are difficult to maintain with time. Another direct synthesis technology investigated is the application of Pd membrane-based catalytic reactors[155-160].

The Pd membrane-based reactor in theory delivers a 100% reaction efficiency and involves feeding H_2 gas from an internal section of the membrane to an O_2 saturated solution, given the Pd membrane is permeable to hydrogen atoms but not molecular hydrogen (to give improved reaction safety by indirect mixing). Strukul *et al.* [155] identified that both the activity and selectivity of Pd catalysts are dependent on the type of support used and the surface Pd oxidation state, with 8 nm average particle size in particular producing favourable results. Work by Abate *et al.* [156] has indicated that defective surface sites on the Pd catalyst surface are responsible for parallel and sequential non-selective reactions taking place to different extents (and supported by kinetic studies) under adopted reaction conditions.

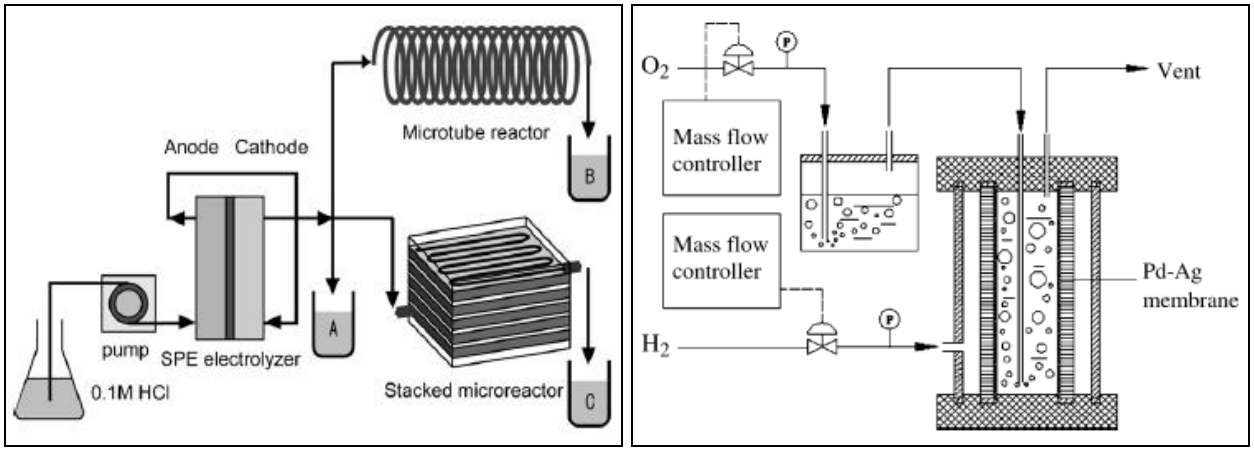

Figure 1.18 Schematic diagrams showing a typical microreactor set-up with hydrogen generation from the electrolysis of water[160] (left), and a catalytic membrane reactor based on a Pd-Ag composite porous membrane[159] (right).

Microreactor systems offer a less-energy intensive operation and allow safe study of O_2/H_2 mixtures within the explosive limit since as the microreactor channel width is less than the quenching distance of hydrogen and oxygen radicals, which consequently means that higher temperatures are required to initiate an explosion[161]. Microreactors also offer a degree of portability which would benefit the proposal of on-site small scale synthesis. Synthesis of 1.3 wt% H_2O_2 solutions have been achieved using a system packed with 2 wt% Pd/SiO_2 catalyst and though there was only 2% H_2 conversion, 100% H_2 selectivity was achieved posing the potential for a recycle system. The effect of steam flow velocity through the microreactor channel confirmed a kinetically controlled reaction with minimal mass transfer limitation[162].

Beckman has looked at the feasibility of synthesising H_2O_2 *in-situ* (for propene epoxidation) using a precious metal loaded TS-1 catalyst in compressed CO_2 which under optimal reaction conditions gave 32% H_2O_2 yield based on 56% H_2 selectivity [164]. However, both BASF/Dow Chemical and laboratory scale studies by Campos-Martin[164] have preferred a two-step process for Hydrogen Peroxide Propene Oxidation (HPPO) involving an on-site strategy where H_2O_2 synthesis occurs in a separate reactor, before being transported across site and used in an epoxidation reactor. This is based on different optimum conditions existing for both reactions including substrate/catalyst ratio, temperature and residence time.

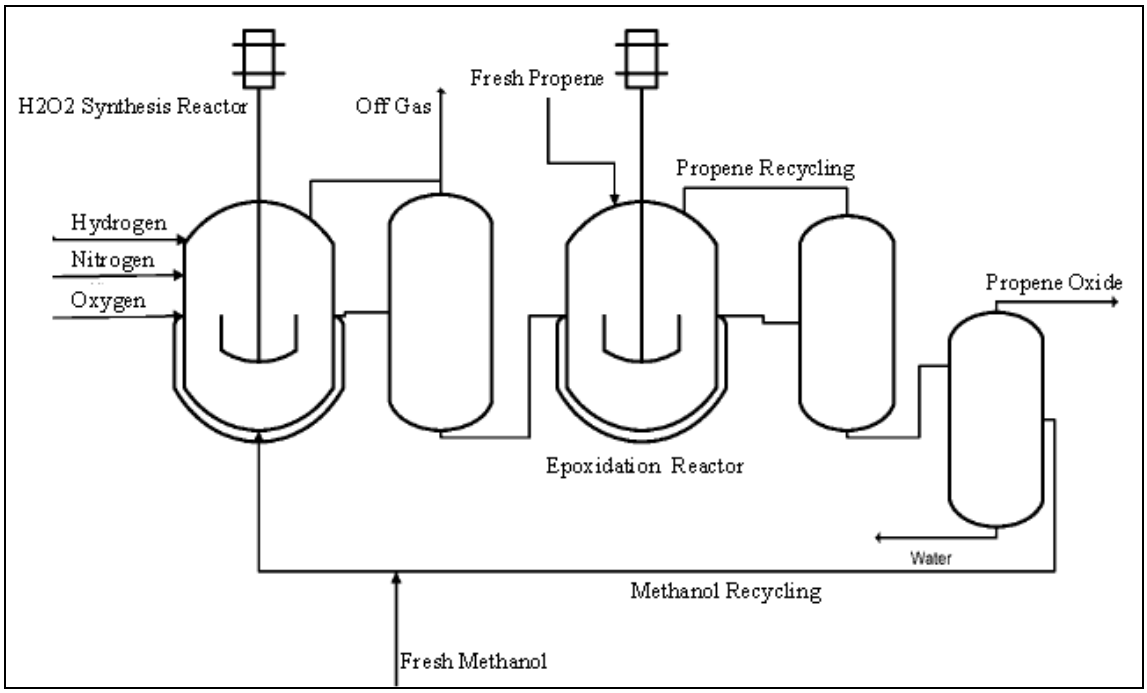

Figure 1.19 Schematic diagram of an integrated process for synthesizing propylene oxide (PO), based on the direct synthesis of hydrogen peroxide in neutral solutions[164].

The setup described in Figure 1.19 was used on a laboratory scale by Fierro and Campos-Martin with H_2O_2 synthesis performed using palladium anchored into ion-exchanged resins functionalised with sulphonic acid groups. A 9 wt% H_2O_2 solution was used in the TS-1 catalysed propene epoxidation which after 45 minutes at 343 K (H_2O_2/catalyst = 1:4, propene/catalyst = 1:25) resulting in a 95% H_2O_2 to Propylene Oxide selectivity based on a 96% H_2O_2 conversion, which decreased to 80% conversion after 135 h on-stream[164].

Hydrogen peroxide synthesis has formed the basis of numerous theoretical studies using DFT calculations *via* the elementary steps (Scheme 1.3) involving the formation of a hydroperoxy OOH intermediate - a process concluded as thermodynamically and kinetically favoured on AuPd and Pd_3 clusters[165].

Theoretical studies can discriminate between metallic and cationic Au states in an effort to determine the nature of the active site(s), for example, simulations of the formation of H_2O_2 over anionic Au clusters (Au_n^- where n = 1-4) revealed a high activation barrier for O_2 hydrogenation by Au^- (40.60 kcal/mol) influenced by cluster number[166], while calculations by Ishihara *et al.*, for Pd and Pd-Au systems revealed that the dissociation of the O-O bond, leading to the non-selective formation of H_2O on Pd [111] surfaces is blocked by the presence of Au atoms (Figure 1.20)[167]. Indeed from a theoretical viewpoint, there is agreement that arrangement of Au and Pd atoms on an alloyed Pd-Au surface significantly impacts both the selectivity and yield, with isolated Pd/Au atoms (contiguous sites[168-170]) found to improve the H_2 selectivity to H_2O_2 by inhibiting hydrogenation/decomposition reactions *via* scission of the O-O bond.

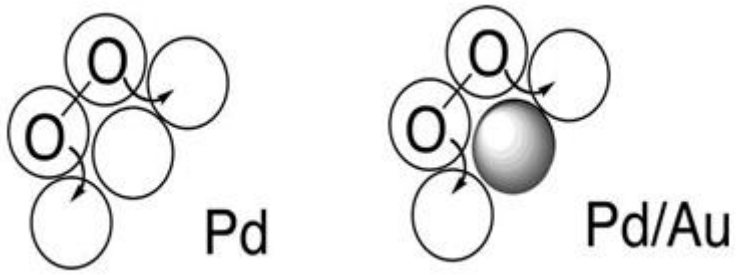

Figure 1.20 Schematic of O-O bond dissociation over Pd and Pd/Au surfaces[168].

In terms of the electronic structure of Au-Pd alloys, there is agreement in the literature that upon alloying, Au gains s, p electrons and loses d electrons, while Pd loses s, p electrons and gains d-electrons[171-174]. For late-transition metal elements, the d-character is more important than the s, p character in definining their chemisorption and catalytic properties. For Pd atoms, gaining d electrons shifts the d band away from the Fermi level, leading to a weaker interation between adsorbate and surface Pd atoms, with calculations showing that the Pd d-band for Pd monomers surrounded by Au is much lower in energy than that of either monolayer Pd or bulk Pd surfaces[175, 176].

In addition, the lattice mismatch between Au and Pd can also cause narrowing of the Pd d-band[177]. For instances in which Pd adopts the larger lattice constant of Au (which is 5% larger) upon alloying, the increase in Pd-Pd bond length causes the Fermi level within the Pd d-band to rise. This improves the atomic-like character of the Pd atoms, resulting in weaker interactions between the absorbate atoms and surface Pd-atoms. Consequently, it is understood that the synergistic effect manifested in Au-Pd alloys is due to Au weakening the binding strenth of Pd toward absorbate atoms and by perturbing its d-band structure. For direct H_2O_2 synthesis, a weaker interaction between oxygen atoms and surface Pd present in Au-Pd alloys could explain why a reduction in the rate of H_2O_2 hydrogenation/decomposition is observed relative to Pd-only catalysts. As such, whenever the term "synergy" is used in this thesis, it is related to the factors described in this paragraph and the preceding one.

1.6 The aims of this study

Using an autoclave reactor (a three-phase, stirred autoclave, operating under batch conditions), a range of Au, Pd, Au-Pd, Au-Pt, Pd-Pt and Au-Pd-Pt catalysts supported on carbon, ceria, silica and titania will be prepared, characterised and evaluated for the direct synthesis of hydrogen peroxide in the absence of acid and halide promoters. This study was undertaken in collaboration with Solvay®, the largest manufacturer of hydrogen peroxide using the auto-oxidation (AO) process, in an effort to determine suitable catalysts for the potential commercialisation of a direct H_2O_2 synthesis process.

1.6.1 Objectives

1 Optimisation of the wet-impregnation catalyst preparation method for carbon and TiO_2 supported Au-Pd catalysts for the direct synthesis of hydrogen peroxide, and study of the preparation of halide-free catalysts.

2 Achieving an improved understanding as to how the acid pre-treatment of carbon supports prior to Au-Pd impregnation generates highly active catalysts for the direct synthesis of hydrogen peroxide in which the non-selective H_2O_2 hydrogenation/ decomposition pathways are completely switched-off.

3 Development of the colloidal "sol" immobilisation methodology to prepare Au-Pd/C and TiO_2 catalysts with application of aberration corrected electron microscopy techniques to investigate the origin of the very high activity exhibited by these catalysts for the direct synthesis of hydrogen peroxide.

4 Investigation into the origin of synergistic effect(s) between Au and Pd supported on SiO_2 as a function of acid-pretreatment, using multiple characterisation techniques including Inelastic Neutron Scattering (INS).

5 Development of trimetallic Au-Pd-Pt catalysts for the direct synthesis of hydrogen peroxide, with an extensive catalyst screening study undertaken for Au-Pd-Pt/CeO_2.

1.7 References

1. J. J. Berzelius, *Edinburgh New Philosophical Journal*, **1836**, XXI, 223.
2. M. Bowker, The Basis and Applications of Heterogeneous Catalysis, *Oxford University Press, Oxford*, **1998.**
3. J. Z. Fullmer, Sir Humphry Davy's Published Works, *Harvard University Press, Cambridge, Massachusetts*, **1969**.
4. M. Faraday, *Phil Trans.*, **1834**, 124, 55.
5. Phillips, *GP6069*, **1831**.
6. P. Atkins, J. de Paula, Atkins' Physical Chemistry, *Oxford University Press, Oxford*, Seventh Edition, **2002.**
7. G. C. Bond, Heterogeneous Catalysis: Principles and Applications, *Oxford University Press, New York*, Second Edition, **1986**.
8. G. Attard, C. Barnes, Surfaces, *Oxford University Press, Oxford*, **1998**.
9. G. Ertl, H. Knozinger, F. Schuth, J. Weitkamp, Handbook of Heterogeneous Catalysis, *WILEY-VCH, New York*, Second Edition, **2008.**
10. C. T. Campbell, *App. Surf. Sci.*, **1984**, 19, 32.
11. H. Adkins, W. R. Peterson, *J. Am. Chem. Soc.*, **1931**, 53, 1512.
12. L. J. Thennard, *Ann. Chym. Phys.*, **1818**, 8, 306.
13. R. Hage, A. Lienke, *Angew. Chem. Pharm.*, **1853**, 88, 57.
14. C. W. Corti, D. T. Holliday, D. T. Thompson, *App. Catal. A. Gen.*, **2005**, 291, 253.
15. J. M. Campos-Martin, G. Blanco-Brieva, J. L G. Fierro, *Angew. Chem. Int. Ed.*, **2006**, 45, 6962.
16. P. Taramasso, G. Perego, B. Notari, US Patent No. 4,410,501, **1983**.
17. D. Kahlich, S. Hawkins, W. E. Russey, M. Pilkart-Muller, Ullmann's Encyclopedia of Industrial Chemistry, *VILEY-VCH, New York*, **2012**.
18. C. Samanta, *App. Catal. A. Gen.*, **2008**, 350, 133.
19. A. R. Vaino, *J. Org. Chem.*, **2000**, 65, 4210.
20. P. Wadhwani, M. Mukherjee, D. Bandyopadhyay, *J. Am. Chem. Soc.*, **2001**, 123, 12430.
21. S. Lee, P. L. Fuchs, *J. Am. Chem. Soc.*, **2002**, 124, 13978.
22. H. Meidinger, *Ann. Chem. Pharm.*, **1853**, 88, 57.
23. H. Bethelot, C. R. Hebd, *Seances Acad. Sci.*, **1878**, 86, 71.
24. H. J. Riedl, G. Pfleiderer, US Patent No. 2,215,883, **1940**.

25. C. W. Schumb, R. L. Satterfield, Hydrogen Peroxide, *Rheinhold Publishing Company, New York,* **1955.**
26. W. M. Weigert, H. Delle, G. Kabisch, *Chem. Ztg.*, **1975**, 99, 101.
27. W. Manchot, *Liebeigs Ann. Chem.*, **1901**, 314, 177.
28. W. Eul, A. Moeller, N. Steiner, Hydrogen Peroxide, *Kirk-Othmer Encyclopedia of Chemical Technology*, John Wiley & Sons, Inclusive, **2001**.
29. C. W. Jones, Applications of Hydrogen Peroxide and Derivatives, *RSC Publishing*, **1999**.
30. H. Henkel, W. Weber, US Patent No. 1,108,752, **1914**.
31. L. W. Gosser, J. A. T. Schwartz, US Patent No. 4,772,456, **1988**.
32. J. K. Edwards, A. Thomas, A. F. Carley, A. A. Herzing, C. J. Kiely, G. J. Hutchings, *Green. Chem.*, **2008**, 10, 388.
33. V. R. Choudhary, C. Samanta, P. Jana, *App. Catal. A. Gen.*, **2007**, 332, 70.
34. S. Chinta, J. H. Lunsford, *Abstracts of Papers of the American Chemical Society*, **2004**, 227, U229-U299.
35. R. Todorovic, R. J. Meyer, *Catalysis Today*, **2011**, 160, 242.
36. M. Piccinini, E. Ntainjua N., J. K. Edwards, A. F. Carley, J. A. Moulijn, G. J. Hutchings, *Phys. Chem. Chem. Phys.*, **2010**, 12, 2488.
37. T. A. Pospelova, N. I. Kobozov, *Zhurnal Fizicheskoi Khimii*, **1961**, 35, 1192.
38. T. A. Pospelova, N. I. Kobozov, E. N. Eremin, *Zhurnal Fizicheskoi Khimii*, **1961**, 35, 298.
39. T. A. Pospelova, N. I. Kobozov, *Zhurnal Fizicheskoi Khimii*, **1961**, 35, 535.
40. V. R. Choudhary, C. Samanta, T. V. Choudhary, *J. Mol. Catal. A. Chem.*, **2006**, 260, 115.
41. V. R. Choudhary, C. Samanta, *J. Catal.*, **2006**, 238, 28.
42. V. R. Choudhary, C. Samanta, T. V. Choudhary, *App. Catal. A. Gen.*, **2006**, 308, 128.
43. V. R. Choudhary, C. Samanta and P. Jana, *App. Catal. A. Gen.*, **2007**, 332, 70.
44. V. R. Choudhary, P. Jana, *App. Catal. A. Gen.*, **2007**, 329, 79.
45. V. R. Choudhary, C. Samanta and P. Jana, *App. Catal. A. Gen.*, **2007**, 317, 234.
46. V. R. Choudhary, C. Samanta, T. V. Choudhary, *Catal. Comm.*, **2007**, 8, 1310.
47. V. R. Choudhary, P. Jana, *J. Catal.*, **2007**, 246, 434.
48. V. R. Choudhary, P. Jana, *Catal. Comm.*, **2008**, 9, 2371.
49. C. Samanta, V. R. Choudhary, *Catal Comm.*, **2007**, 8, 2222.
50. C. Samanta, V. R. Choudhary, *App. Catal. A. Gen.*, **2007**, 326, 28.
51. C. Samanta, V. R. Choudhary, *Catal. Comm.*, **2007**, 8, 73.

52. C. Samanta, V. R. Choudhary, *App. Catal. A. Gen.*, **2007**, 330, 23.
53. C. Samanta, V. R. Choudhary, *Chem. Eng. J.*, **2008**, 136, 126.
54. R. Burch, P. R. Ellis, *App. Catal. B. Env.*, **2003**, 42, 203.
55. Y. F. Fan, J. H. Lunsford, *J. Catal.*, **2005**, 230, 313.
56. G. Blanco-Brieva, E. Cano-Serrano. J. M. Campos-Martin, J. L. G. Fierro, *Chem. Comm.*, **2004**, 1184.
57. S. Chinta, J. H. Lunsford, *J. Catal.*, **2004**, 225, 249.
58. D. P. Dissanayake, J. H. Lunsford, *J. Catal.*, **2002**, 206, 173.
59. D. P. Dissanayake, J. H. Lunsford, *J. Catal.*, **2003**, 214, 113.
60. Y. F. Fan, J. H. Lunsford, *J. Catal.*, **2005**, 230, 313.
61. Q. S. Liu, J. H. Lunsford, *App. Catal. A. Gen.*, **2006**, 314, 94.
62. Q. S. Liu, J. H. Lunsford, *J. Catal.*, **2006**, 239, 237.
63. Q. S. Liu, J. C. Bauer, R. E. Schaak, J. H. Lunsford, *App. Catal. A. Gen.*, **2008**, 339, 130.
64. J. H. Lunsford, *J. Catal.*, **2003**, 216, 455.
65. C. V. Sivadinarayana, T. V. Choudhary, L. L. Daemon, J. Eckert, D. W. Goodman, *J. Am. Chem. Soc.*, **2004**, 126, 38.
66. Q. Liu, K. K. Gath, J. C. Bauer, R. E. Schaak and J. H. Lunsford, *Catal. Lett.*, **2009**, 132, 342.
67. M. Haruta, T. Kobayashi, H. Sano, N. Yamada, *Chem. Lett.*, **1987**, 16, 408.
68. G. J. Hutchings, *J. Catal.*, **1985**, 96, 292.
69. T. V. Choudhary, D. W. Goodman, *Top. Catal.*, **2002**, 21, 25.
70. M. Haruta, N. Yamada, T. Kobayashi, S. Iijima, *J. Catal.*, **1989**, 115, 301.
71. G. C. Bond, D. T. Thompson, *Catal. Rev. Sci. Eng.*, **1999**, 41, 319.
72. M. Haruta, M. Date, *App. Catal. A. Gen.*, **2001**, 222, 427.
73. Q. Fu, H. Saltsburg, M. Flytzani-Stephanopoulos, *Science*, **2003**, 301, 935.
74. P. Landon, J. Ferguson, B. E. Solsona, T. Garcia, A. F. Carley, A. A. Herzing, C. J. Kiely, S. E. Golunski, G. J. Hutchings, *Chem. Comm.*, **2005**, 27, 3385.
75. A. Corma, H. Garcia, *Chem. Soc. Rev.*, **2008**, 37, 2096.
76. A. Corma, P. Serna, *Science*, **2006**, 313, 332.
77. C. Della Pina, E. Falletta, L. Prati, M. Rossi, *Chem. Soc. Rev.*, **2008**, 37, 2077.
78. J. K. Edwards, G. J. Hutchings, *Angew. Chem. Int. Ed.*, **2008**, 47, 9192.
79. G. C. Bond, *Catalysis Today*, **2002**, 72, 5.
80. G. C. Bond, *Catal. Rev. Sci. Eng.*, **1999**, 41, 319.

81. M. Date, M. Haruta, *J. Catal.*, **2001**, 201, 221.
82. M. Date, M. Okumura, S. Tsubota, M. Haruta, *Angew. Chem. Int. Ed.*, **2004**, 43, 2129.
83. G. C. Bond, D. T. Thompson, *Gold Bull.*, **2000**, 33, 41.
84. C. K. Costello, J. H. Yang, H. Y. Law, Y. Wang, J.-N. Lin, L. D. Marks, M. C. Kung, H. H. Kung, *App. Catal. A. Gen.*, **2003**, 243, 15.
85. G. C. Bond, M. A. Keane, H. Kral, J. A. Lercher, *Catal. Rev. Sci. Eng.*, **2000**, 42, 323.
86. G. Frelicke, G. von Holden, D. B. Meijer, B. Pederson, D. M. Simard, J. Rayner, *J. Am. Chem. Soc.*, **2005**, 127, 8416.
87. Z.-P. Lui, P. Hu, *J. Am. Chem. Soc.*, **2002**, 124, 14770.
88. L. D. Socaciu, J. Hagen, T. M. Bernhardt, L. Woste, U. Heiz, H. Hakkinen, U. Landman, *J. Am. Chem. Soc.*, **2003**, 125, 10437.
89. G. J. Hutchings, M. S. Hall, A. F. Carley, P. Landon, B. E. Solsona, C. J. Kiely, A. A. Herzing, M. Makkee, J. A. Moulijn, A. Overweg, J. C. Fierro-Gonzalez, J. Guzman, B. C. Gates, *J. Catal.*, **2006**, 242, 71.
90. M. Haruta, M. Date, *App. Catal. A. Gen.*, **2001**, 222, 427.
91. A. A. Herzing, C. J. Kiely, A. F. Carley, P. Landon, G. J. Hutchings, *Science*, **2008**, 321, 1331.
92. N. Lopez, J. K. Norskov, *J. Am. Chem. Soc.*, **2002**, 142, 11262.
93. M. Okumura, Y. Kitagawa, M. Haruta, K. Yamaguchi, *Chem. Phys. Letts.*, **2001**, 346, 163.
94. M. Valden, X. Lai, D. W. Goodman, *Science*, **1998**, 281, 1647.
95. M. Haruta, M. Date, *App. Catal. A. Gen.*, **2001**, 222, 427.
96. B. Nkosi, N. J. Coville, G. J. Hutchings, *J. Chem. Soc., Chem. Comm.*, **1988**, 1, 71.
97. B. Nkosi, N. J. Coville, G. J. Hutchings, *App. Catal.*, **1988**, 43, 33.
98. B. Nkosi, N. J. Coville, G. J. Hutchings, M. D. Adams, J. Friedl, F. E. Wagner, *J. Catal.*, **1991**, 128, 366.
99. B. Nkosi, M. D. Adams, N. J. Coville, G. J. Hutchings, *J. Catal.*, **1991**, 128, 378.
100. K. Shinoda, *Chem. Lett.*, **1975**, 3, 219.
101. C. L. Bracey, A. F. Carley, J. K. Edwards, P. R. Ellis, G. J. Hutchings, *Catal. Sci. Technol.*, **2011**, 1, 76.
102. M. Haruta, *Chem. Record*, **2003**, 3, 75.
103. T. Hayashi, B. L. Han, S. Tsubota, M. Haruta, *Ind. Eng. Chem. Res.*, **1995**, 34, 2298.

104. G. Mul, A. Zwijnenburg, B. van der Linden, M. Makkee, J. A. Moulijn, *J. Catal.*, **2001**, 201, 128.
105. A. Zwijnenburg, M. Saleh, M. Makkee, J. A. Moulijn, *Catalysis Today*, **2002**, 72, 59.
106. E. E. Stangland, K. B. Stavens, R. P. Andres, W. N. Delgass, *J. Catal.*, **2000**, 191, 332.
107. M. Haruta, *Catalysis Today*, **1997**, 36, 153.
108. C. Qi, M. Okumura, T. Akita, M. Haruta, *App. Catal. A. Gen.*, **2004**, 263, 19.
109. Y. A. Kalvachev, T. Hayashi, S. Tsubota, M. Haruta, *Stud. Surf. Sci. Catal.*, **1997**, 110, 965.
110. B. S. Uphade, M. Okumura, N. Yamada, S. Tsubota, M. Haruta, *Stud. Surf. Sci. Catal.*, **2000**, 130, 833.
111. B. S. Uphade, M. Okumura, N. Yamada, S. Tsubota, M. Haruta, *App. Catal. A. Gen.*, **2000**, 190, 43.
112. T. Hayashi, K. Tanaka, M. Haruta, *J. Catal.*, **1998**, 178, 566.
113. M. Haruta, B. S. Uphade, S. Tsubota, A. Miyamoto, *Res. Chem. Intermed.*, **1998**, 3, 329.
114. T. A. Nijhuis, B. J. Huizinga, M. Makkee, J. A. Moulijn, *Ind. Eng. Chem. Res.*, **1999**, 38, 884.
115. A. K. Sinha, S. Seelan, S. Tsubota, M. Haruta, *Angew. Chem. Int. Ed.*, **2004**, 43, 1546.
116. A. K. Sinha, S. Seelan, M. Okumura, T. Akita, S. Tsubota, M. Haruta, *J. Phys. Chem. B.*, **2005**, 109, 3956.
117. T. A. Nijhuis, T. Q. Gardner, B. M. Weckhuysen, *J. Catal.*, **2005**, 236, 153.
118. T. A. Nijhuis, T. Visser, B. M. Weckhuysen, *Angew. Chem. Int. Ed.*, **2005**, 44, 1115.
119. T. A. Nijhuis, B. M. Weckhuysen, *Chem. Comm.*, **2005**, 48, 6002.
120. A. S. K. Hashmi, G. J. Hutchings, *Angew. Int. Chem. Ed.*, **2006**, 45, 7896.
121. L. Prati, G. Marta, *Gold Bull.*, **1999**, 32, 96.
122. F. Porta, L. Prati, M. Rossi, S. Coluccia, G. Marta, *Catalysis Today*, **2000**, 61, 165.
123. F. Porta, L. Prati, M. Rossi, G. Scari, *J. Catal.*, **2002**, 211, 464.
124. S. Biella, L. Prati, M. Rossi, *Inorg. Chim. Acta.*, **2003**, 349, 253.
125. M. Comotti, C. Della Pina, M. Rossi, A. Siani, *App. Catal. A. Gen.*, **2005**, 291, 204.
126. C. L. Bianchi, P. Canton, N. Dimitratos, F. Porta, L. Prati, *Catalysis Today*, **2005**, 102, 203.
127. N. Dimitratos, F. Porta, L. Prati, *App. Catal. A. Gen.*, **2005**, 291, 210.
128. E. Taarning, A. T. Marsden, J. M. Marchetti, K. Egeblad, C. H. Christensen, *Green Chem.*, **2008**, 10, 408.

129. G. L. Brett, P. J. Miedziak, N. Dimitratos, J. A. Lopez-Sanchez, N. F. Dummer, R. Tiruvalam, C. J. Kiely, D. W. Knight, S. H. Taylor, D. J. Morgan, A. F. Carley, G. J. Hutchings, *Catal. Sci. Technol.*, **2012**, 2, 97.

130. S. Meenakshisundaram, E. Nowicka, P. J. Miedziak, G. L. Brett, R. L. Jenkins, N. Dimitratos, S. H. Taylor, D. W. Knight, D. Bethell, G. J. Hutchings, *Faraday Discuss.*, **2010**, 145, 341.

131. G. L. Brett, Q. He, C. Hammond, P. J. Miedziak, N. Dimitratos, S. Meenakshisundaram, A. A. Herzing, M. Conte, C. J. Kiely, D. W. Knight, S. H. Taylor, G. J. Hutchings, *Angew. Chem. Int. Ed.*, **2011**, 50, 10136.

132. A. Abad, P. Conception, A. Corma, H. Garcia, *Angew. Chem. Int. Ed.*, **2005**, 44, 4066.

133. S. Carrettin, A. Corma, M. Iglesias, F. Sanchez, *App. Catal. A. Gen.*, **2005**, 291, 247.

134. A. Corma, M. E. Domine, *Chem. Comm.*, **2005**, 4042.

135. A. Abad, C. Almela, A. Corma, H. Garcia, *Chem. Comm.*, **2006**, 3178.

136. A. Abad, A. Corma, H. Garcia, *Chem-A. Euro. J.*, **2008**, 14, 212.

137. D. I. Enache, J. K. Edwards, P. Landon, B. E. Solsona, A. F. Carley, A. A. Herzing, M. Watanabe, C. J. Kiely, D. W. Knight, G. J. Hutchings, *Science*, **2006**, 311, 362.

138. O. Casanova, S. Iborra, A. Corma, *ChemSusChem*, **2009**, 2, 1138.

139. L. Kesavan, R. Tiruvalam, M. H. Ab-Rahim, M. I. bin Saimon, D. I. Enache, R. L. Jenkins, N. Dimitratos, J. A. Lopez-Sanchez, D. W. Knight, S. H. Taylor, C. J. Kiely, G. J. Hutchings, *Science*, **2011**, 331, 195.

140. T. Ishihara, Y. Ohura, S. Yoshida, Y. Hata, H. Nishiguchi, Y. Takita, *App. Catal. A. Gen.*, **2005**, 291, 215.

141. A. Staykov, T. Kamachi, T. Ishihara, K. Yoshizawa, *J. Phys. Chem. C*, **2008**, 112, 19501.

142. P. Landon, P. J. Collier, A. J. Papworth, C. J. Kiely, G. J. Hutchings, *Chem. Comm.*, **2002**, 2058.

143. P. Landon, P. J. Collier, A. F. Carley, D. Chadwick, A. J. Papworth, A. Burrows, C. J. Kiely, G. J. Hutchings, *Phys. Chem. Chem. Phys.*, **2003**, 5, 1917.

144. J. K. Edwards, B. E. Solsona, P. Landon, A. F. Carley, A. A. Herzing, C. J. Kiely, G. J. Hutchings, *J. Catal.*, **2005**, 236, 69.

145. B. E. Solsona, J. K. Edwards, P. Landon, A. F. Carley, A. A. Herzing, C. J. Kiely, G. J. Hutchings, *Chem. Mater.*, **2006**, 18, 2689.

146. J. K. Edwards, B. Solsona, P. Landon, A. F. Carley, A. Herzing, M. Watanabe, C. J. Kiely, G. J. Hutchings, *J. Mater. Chem.*, **2005**, 15, 4595.

147. J. K. Edwards, A. F. Carley, A. A. Herzing, C. J. Kiely, G. J. Hutchings, *Faraday Discuss.*, **2008**, 138, 225.

148. A. A. Herzing, M. Watanabe, J. K. Edwards, M. Conte, Z. R. Tang, G. J. Hutchings, C. J. Kiely, *Faraday Discuss.*, **2008**, 138, 337.

149. J. K. Edwards, B. Solsona, E. Ntainjua N, A. F. Carley, A. A. Herzing, C. J. Kiely, G. J. Hutchings, *Science*, **2009**, 323, 1037.

150. J. C. Zhou, H. C. Guo, X. S. Wang, M. X. Guo, J. L. Zhao, L. X. Chen, W. M. Gong, *Chem. Comm.*, **2005**, 1631.

151. I. Yamanaka, T. Hashimoto, K. Otsuka, *Chem. Lett.*, **2002**, 852.

152. I. Yamanaka, T. Hashimoto, R. Ichihashi, K. Otsuka, *Electrochimica Acta*, **2008**, 53, 4824.

153 I. Yamanaka, *Catalysis Surveys from Asia*, **2008**, 12, 78.

154. I. Yamanaka, T. Murayama, *Angew. Chem. Int. Ed.*, **2008**, 47, 1900.

155. S. Abate, G. Centi, S. Melada, S. Perathoner, F. Pinna, G. Strukul, *Catalysis Today*, **2005**, 104, 323.

156. S. Abate, S. Melada, G. Centi, S. Perathoner, F. Pinna, G. Strukul, *Catalysis Today*, **2006**, 117, 193.

157. S. Abate, G. Centi, S. Perathoner, S. Melada, F. Pinna, G. Strukul, *Top. Catal.*, **2006**, 38, 181.

158. S. Melada, F. Pinna, G. Strukul, S. Perathoner, G. Centi, *J. Catal.*, **2005**, 235, 241.

159. S. Melada, F. Pinna, G. Strukul, S. Perathoner, G. Centi, *J. Catal.*, **2006**, 237, 213.

160. L. Wang, S. G. Bao, J. H. Yi, F. He, Z. T. Mi, *App. Catal. B. Env.*, **2008**, 79, 157.

161. S. Maehara, M. Taneda, K. Kusakabe, *Chem. Eng. Res. Design*, **2008**, 86, 410.

162. Y. Voloshin, R. Halder, A. Lawal, *Catalysis Today*, **2007**, 125, 40.

163. Q. L. Chen, E. J. Beckman, *Green Chem.*, **2007**, 9, 802.

164. G. Blanco-Brieva, M. C. Capel-Sanchez, M. P. de Frutos, A. Padilla-Polo, J. M. Campos-Martin, J. L. G. Fierro, *Ind. Eng. Chem. Res.*, **2008**, 47, 8011.

165. A. M. Joshi, W. N. Delgass, K. T. Thomson, *J. Phys. Chem. C.*, **2007**, 111, 7384.

166. F. Wang, D. J. Zhang, H. Sun, Y, Ding, *J. Phys. Chem. C.*, **2007**, 111, 11590.

167. J. Li, T. Ishihara, K. Yoshizawa, *J. Phys. Chem. C.*, **2011**, 115, 25359.

168. H. C. Ham, G. S. Hwang, J. Ham, S. W. Nam, T. H. Lim, *J. Phys. Chem. Lett. C.*, **2009**, 113, 12945.

169. H. C. Ham, J. Adam Stephens, G. S. Hwang, J. Han, S. W. Nam, Tae Hoon Lim, *Catalysis Today*, **2011**, 165, 138.

170. C. Mingshu, D. W. Goodman, Chin. *J. Catal*., **2008**, 29, 117.

171. C. W. Li, K. Luo, T. Wei, D. W. Goodman, *J. Phys. Chem. B.*, **2005**, 109, 18535.

172. A. M. Venezia, V. La Parola, G. Deganello, B. Pawalec, J. L. G. Fierro, *J. Catal.*, **2003**, 215, 317.

173. A. Sarkany, O. Geszti, G. Safran, *Appl. Catal. A.*, **2008**, 350, 157.

174. J. A. Rodriguez, *Surf. Sci. Rep.*, **1996**, 24, 223.

175. P. Liu, J. K. Norskov, *Phys. Chem. Chem. Phys.*, **2001**, 3, 3814.

176. D. W. Yuan, X. G. Gong, R. Q. Wu, *J. Phys. Chem. C.*, **2008**, 112, 1539.

177. A. F. Lee, C. J. Baddeley, C. Hardacre, R. M. Ormerod, R. M. Lambert, G. Schmid, H. West, *J. Phys. Chem.*, **1995**, 99, 6096.

Chapter 2

2.1 Outline

A range of mono-, bi- and tri-metallic Au, Pd, Pt catalyst compositions supported on TiO_2, Carbon, SiO_2, CeO_2, micro- and meso-porous materials were synthesised, characterised and evaluated for the direct synthesis of hydrogen peroxide. In this chapter, catalyst precursors, preparations, reactor setup and characterisation techniques are discussed.

2.1.1 Catalyst Precursors (Provided by Johnson Matthey)

Compound	Chemical Formula	Purity
Palladium Bromide	$PdBr_2$	99.99% (trace metals basis)
Palladium Chloride	$PdCl_2$	99.99% (trace metals basis)
Palladium Nitrate	$Pd(NO_3)_2$	99.99% (trace metals basis)
Sodium Tetrachloropalladate	Na_2PdCl_4	Pd Assay = 12.04 wt%
Hydrogen Hexachloroplatinic Acid	H_2PtCl_6	99.99% (trace metals basis)
Gold Bromide	$AuBr_3$	99.99% (trace metals basis)
Hydrogen Tetrachloroauric Acid	$HAuCl_4.3H_2O$	Au Assay = 41.21 wt%

Table 2.1 Summary of catalyst precursors.

2.1.2 Supports

Support	Type	Manufacturer
TiO_2	P25	Degussa
	Nano-grade	Aldrich
Carbon	G60	Darco
	Vulcan XC-72	CABOT
	Nuclear-grade (90 and 300 μm particles)	BNFL
SiO_2	<80 μm particles	Johnson Matthey
	200-500 μm particles, 60A^o pore size	Acros Organics
	35-75 μm particles, 90A^o pore size	
	Co-Polyimide, CPI	Solvay
CeO_2	<5 μm particles	Aldrich
	Nano-grade	
Silicalit	Si:Al atom ratio - 85:2	Solvay
Silicalite-1	Si-atoms only	Provided by Dr. C. Hammond, Cardiff University[1]
Zeolite ZSM-5	SiO_2:Al_2O_3 atom ratios - 23, 30, 50, 80, 280	Zeolyst International

Table 2.2 Summary of catalyst supports.

2.1.3 Reagents (Supplied by Aldrich)

Methanol (HPLC), Water (HPLC Chromasolve),

Sodium Chloride, NaCl (99.99%), Sodium Bromide, NaBr (99.99%),

Cerium Sulphate, $Ce(SO_4)_2$ (99.99%),

Polyvinyl Alcohol (MW = 10,000, 80% hydrolysed).

Phosphoric acid (5-10 ppm trace level) stabilised 50 wt% H_2O_2 in water and 1000 ppm metal atomic absorption standards were obtained from Sigma-Aldrich.

2.1.4 Gases

All gases were obtained from BOC Gases or Air Products Ltd. Purity of gases listed below as:

Pure O_2 (99.99%), 25% O_2/CO_2 (99.99%), 5% H_2/CO_2 (99.99%), 5% H_2/Ar (99.95%), 10% H_2/Ar (99.95%), He (99.99%), Ar (99.95%), N_2 (99.95%) and 2% H_2/Air (99.99%).

2.2 Catalyst Preparation

2.2.1 Standard wet impregnation method

Supported 5 wt% Au, 5 wt% Pd, 2.5 wt% Au-2.5 wt% Pd catalysts were synthesized by the standard wet impregnation methodology[2]. Catalysts comprising 2.5 wt% Au-2.5 wt% Pd were prepared using the following standard method with all quantities listed per gram of catalyst. $PdCl_2$ (0.042 g) was dissolved in a solution of $HAuCl_4.3H_2O$ (2.05 ml, 12.25 g Au in 1000 mL, [Au] = 62 mM) while stirring at 80 ^oC until the Pd dissolved completely. The appropriate support (0.95 g, supports described in section 2.1.3) was then added to the solution and stirred at 80 ^oC to form a thick paste or gel (depending on the support used). The material was dried (110 ^oC, 16 h) and subsequently calcined in static air (400 ^oC, 3 h). Monometallic Au and Pd were synthesized using the same protocol, using a predetermined amount of HCl to completely dissolve $PdCl_2$. For the synthesis of supported 5 wt% Au-Pd-Pt catalysts as discussed in chapter 7, a solution of H_2PtCl_2 (1.0g Pt in 25 ml) was introduced *via* wet impregnation in addition to Au/Pd compounds, with the amount added depending on the mono/bi/trimetallic catalyst composition.

Important Note: 2.5 wt%-2.5 wt% Pd represents the bimetallic catalyst composition that has been found to be the most active for direct H_2O_2 synthesis. If not specified otherwise or it the abbreviation "Au-Pd" supported catalysts is used in this thesis, it can therefore be assumed that the standard 2.5 wt% Au- 2.5 wt% Pd composition has been used.

2.2.1.1 Preparation of highly active Au-Pd/TiO_2 catalysts

The influence of water addition during preparation of catalysts *via* wet impregnation was found to be critical for TiO_2-supported catalysts. Although the synthesis methods remains practically identical, an excess of water (2-30 mL) is added during the mixing of Au and Pd precursors with P25 TiO_2 to form a 'slurry' while stirring at 80 ^oC. The slurry was dried (110 ^oC, 16 or 48 h) and subsequently calcined in static air (400 ^oC, 3 h). TiO_2-supported catalysts prepared following this methodology are described in Figure 2.1 and discussed in chapter 3.

2.2.2 Acid pre-treatment of catalyst supports

A series of Au, Pd and Au-Pd catalysts supported on activated carbon were prepared using wet impregnation, the activated carbon was also subjected to acid pre-treatment prior to impregnation of the metals onto the support. This pre-treatment step consists of suspending activated carbon in aqueous 2 v/v% nitric acid, HNO_3 for 3 h, followed by thorough washing (1000 mL H_2O) and drying (110 ^oC, 58 h).

2.2.3 Catalyst synthesis by the deposition precipitation method

Catalysts comprising a 2.5 wt% Au-2.5 wt% Pd maximum theoretical loading were prepared using the following standard method with all quantities listed per gram of catalyst. $PdCl_2$ (0.0416 g) was dissolved in a solution of $HAuCl_4.3H_2O$ (2.05 ml, 12.25 g Au/L) stirring at 80 ^oC prior to adding distilled water (50 mL) followed by P25 Titania (0.95 g). Sodium Hydroxide, NaOH (0.1 M) was slowly added in a drop wise manner until the pH of the slurry reached a value of 10, which was subsequently maintained for 1 h, stirring at 60 ^oC. The material was then washed on a vacuum filter with warm distilled water (>1000 mL) to remove residual chloride. The material was subsequently dried for 16 h prior to optional, mild pre-reduction in 5% H_2/Ar (100 ^oC, 3 h) and calcination in static air (400 ^oC, 3 h).

2.2.4 Catalyst synthesis by the sol-immobilization method

For the preparation of support Au-Pd colloidal materials an aqueous solution of $PdCl_2$ and $HAuCl_4.3H_2O$ compounds of the desired concentration were prepared. Polyvinyl alcohol (PVA) (1 wt % aqueous solution, Aldrich, MW = 10000, 80% hydrolyzed) and an aqueous solution of $NaBH_4$ (0.1 M) were also prepared. For example, a catalyst comprised of Au-Pd nanoparticles with 1 wt% total metal loading on a carbon support (Aldrich G60) was prepared as follows: To an aqueous $PdCl_2$ and $HAuCl_4$ solution of the desired concentration, the required amount of a PVA solution (1 wt %) was added (PVA/(Au+Pd) (wt/wt) = 1.2), a freshly prepared solution of $NaBH_4$ (0.1 M, $NaBH_4$/(Au+Pd) (mol/mol) = 5) was then added to form a dark-brown sol. After 30 min of sol generation, the colloid was immobilized by adding activated carbon (acidified at pH 1 by sulfuric acid) under vigorous stirring conditions. The amount of support material required was calculated so as to have a total final metal loading of 1% wt and the molar ratio of Au:Pd was varied by adjusting the relative concentrations of the metals in solution. After 2 h the slurry was filtered, the catalyst washed thoroughly with distilled water (neutral mother liquors) and dried at 110 °C for 16 h.

Three distinct Au-Pd sols were prepared which differed primarily in the sequence of metal salt addition and reduction. Aqueous solutions of $PdCl_2$ (Johnson Matthey) and $HAuCl_4.3H_2O$ (Johnson Matthey) of the desired concentration were first prepared. Fresh aqueous solutions of poly vinyl alcohol (PVA) (1 wt% aqueous solution, Aldrich, MW=10000, 80% hydrolyzed) and of 0.1 M $NaBH_4$ were also prepared.

2.2.4.1 Au+Pd sol

The $PdCl_2$ and $HAuCl_4$ stock solutions were mixed in the desired ratio and the required amount of a PVA solution (1 wt%) was added (PVA/(Au + Pd) (wt/wt) = 1.2), the freshly prepared solution of $NaBH_4$ ($NaBH_4$/(Au + Pd) (mol/mol) = 5) was then added to the solution to form a dark-brown sol (Figure 2.1). The solution was stirred for a further 30 minutes.

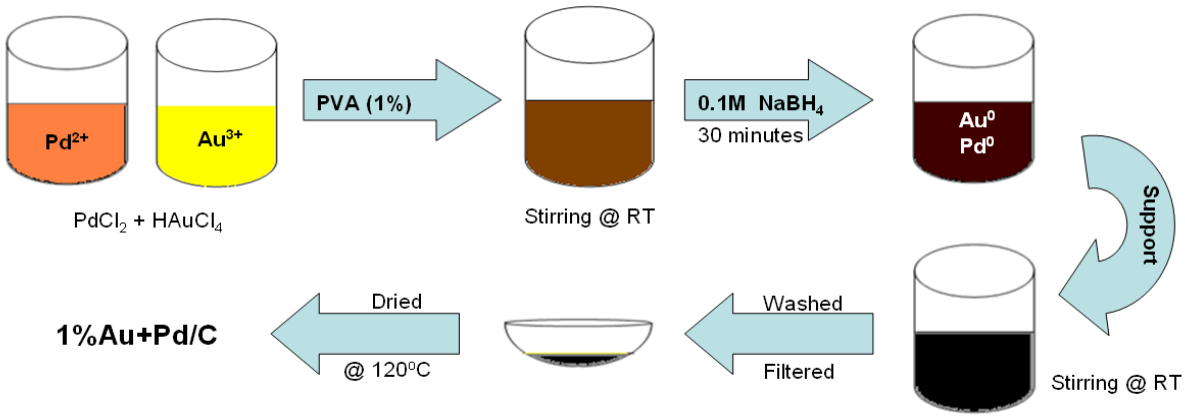

Figure 2.1 Preparation of Au+Pd/C following the sol-immobilization method.

2.2.4.2 Pd{Au} sol

Firstly, the required amount of a PVA solution (1 wt%) was added (PVA/(Au + Pd) (wt/wt) = 1.2) to an aqueous $HAuCl_4$ solution of the desired concentration, a freshly prepared solution of $NaBH_4$ (0.1 M, $NaBH_4$/Au (mol/mol) = 5) was then added to form a red sol. The solution was then stirred for 30 minutes to allow the complete reduction of all the Au^{3+} present in the solution. Then, the required amount of the stock aqueous $PdCl_2$ solution was added, followed by the desired amount of $NaBH_4$ ($NaBH_4$/Pd (mol/mol) = 5), to produce a dark brown sol (Figure 2.2). The solution was stirred for a further 30 minutes.

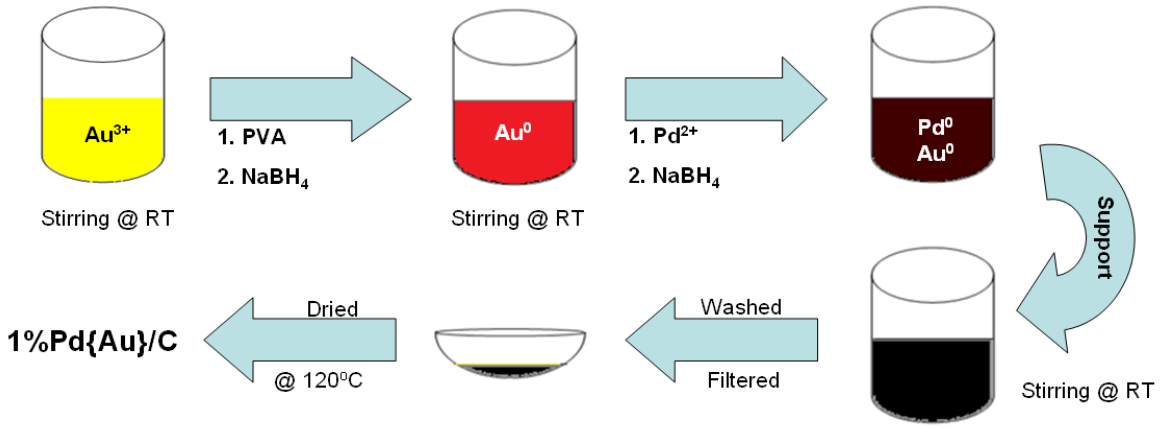

Figure 2.2 Preparation of Pd{Au}/C following the sol-immobilization method.

2.2.4.3 Au{Pd} sol

Firstly, the required amount of a PVA solution (1 wt%) was added (PVA/(Au + Pd) (wt/wt) = 1.2) to an aqueous $PdCl_2$ solution of the desired concentration, a freshly prepared solution of $NaBH_4$ (0.1 M $NaBH_4$/Pd (mol/mol) = 5) was then added to form a brown sol. The solution was stirred for 30 minutes to allow the complete reduction of all the Pd^{2+} present in the solution. Then, the desired amount of the stock $HAuCl_4$ aqueous solution was added, followed by the desired amount of $NaBH_4$ ($NaBH_4$/Au (mol/mol) = 5), until a dark brown sol was obtained (Figure 2.3). The solution was stirred for a further 30 minutes.

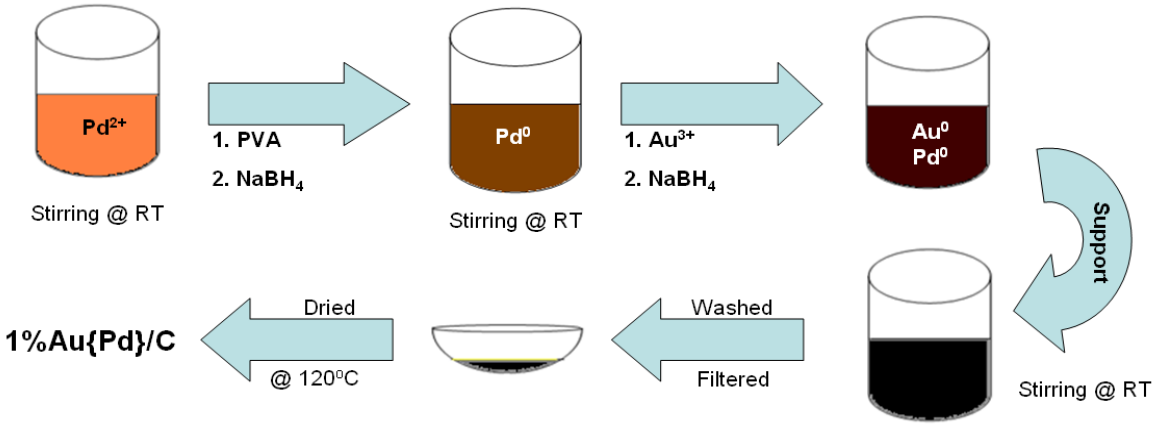

Figure 2.3 Preparation of Au{Pd}/C using sol-immobilization procedure.

2.2.5 Reflux method

Typically, 1.0 g of catalyst was placed in a round bottom flask and the desired volume of solvent (distilled water) was added into the flask. The round bottom flask was connected to a reflux condenser and placed in an oil bath, which was heated at 90 °C. Under vigorous stirring (1200 rpm), the solution was left to reflux for 2 h. The slurry was then filtered and washed thoroughly with distilled water (2 L), followed by overnight drying (110 °C, 16 h).

2.3 Catalyst Testing

In this section, standard reaction protocols are described. These conditions are the outcome of a previous catalyst optimisation study at Cardiff University[2] and are adhered to throughout the course of this thesis. The primary objective is catalyst development and therefore reaction conditions are maintained without addition of acid and/or halide additives, which are described elsewhere in two sister publications.

2.3.1 Hydrogen peroxide synthesis

Catalyst testing was performed using a stainless steel autoclave (Parr Instruments) with a nominal volume of 50 ml and a maximum working pressure of 14 MPa. The autoclave was equipped with an overhead stirrer (0 - 2000 rpm) and had provision for measurement of temperature and pressure. For the standard reaction conditions we have employed previously, the autoclave was charged with the catalyst (0.01 g), solvent (5.6 g MeOH and 2.9 g H_2O), purged three times with 5% H_2/CO_2 (3 MPa) and then filled with 5% H_2/CO_2 and 25% O_2/CO_2 to give a H_2:O_2 ratio of 1:2 at a total pressure of 3.7 MPa. Stirring (1200 rpm) was commenced on reaching the desired temperature (2 ^oC), and experiments were carried out for 30 min. Conversion of H_2 was calculated by gas analysis before and after reaction. H_2O_2 yield was determined by titration of aliquots of the final filtered solution with acidified $Ce(SO_4)_2$ (7 x 10^{-3} mol/l). $Ce(SO_4)_2$ solutions were standardised against $(NH_4)_2Fe(SO_4)_2.6H_2O$ using ferroin as indicator.

Important Note: The amount of hydrogen peroxide formed is represented in this thesis in terms of both rate (productivity / rate of H_2O_2 synthesis / synthesis activity ($mol_{H2O2}kg_{cat}^{-1}h^{-1}$)) and yield (wt% H_2O_2) respectively.

2.3.1.1 Catalyst re-usability experiments

The autoclave was charged with the catalyst (0.05-0.10 g), solvent (5.6 g MeOH and 2.9 g H_2O), purged three times with 5% H_2/CO_2 (100 psi) and then filled with 5% H_2/CO_2 (420 psi) and 25% O_2/CO_2 (160 psi) to give a hydrogen to oxygen ratio of 1:2 at a total pressure of 580 psi. Stirring (1200 rpm) was commenced on reaching the desired temperature (2 ^oC) and experiments were performed for 30 min. After filtration, the catalyst was then dried the oven at 100 ^oC for 2 h. Subsequently, a portion of this catalyst (0.01 g) was re-used as described previously (section 2.3.1).

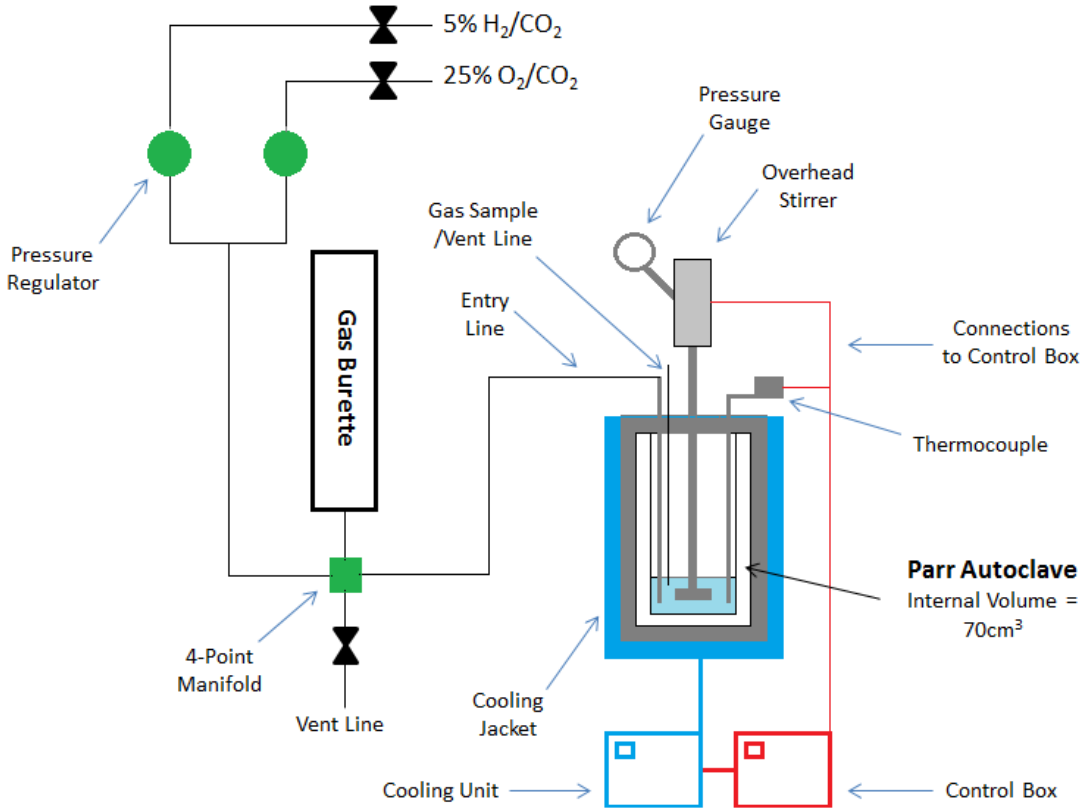

Figure 2.4 Schematic of Parr stainless steel autoclave used for catalytic reaction studies.

2.3.2 Hydrogen peroxide hydrogenation

Hydrogen peroxide hydrogenation was evaluated using a Parr Instruments stainless steel autoclave with a nominal volume of 100 ml and a maximum working pressure of 14 MPa. To test each catalyst for H_2O_2 hydrogenation, the autoclave was charged with catalyst (0.01 g) and a solution containing 4 wt% H_2O_2 (5.6 g MeOH, 2.22 g H_2O and 0.68 g H_2O_2 (50 wt%)). The charged autoclave was then purged three times with 5% H_2/CO_2 (0.7 MPa) before filling with 5% H_2/CO_2 to a pressure of 2.9 MPa at 20 ^oC. The temperature was allowed to decrease to 2 ^oC followed by stirring at 1200 rpm for 30 min. The H_2O_2 remaining after reaction was determined by titration following the procedure described in section 2.2.1.

Important Note: The amount of hydrogen peroxide hydrogenated is represented in this thesis in terms of both rate (rate of H_2O_2 hydrogenated / hydrogenation activity ($mol_{H2O2}kg_{cat}^{-1}h^{-1}$) and consumption (percentage H_2O_2 hydrogenated) terms respectively. For hydrogen peroxide reactions performed at 30 minutes, the relationship between activity and hydrogen peroxide concentration is shown in Table 2.1.

Example	**Activity / $mol_{H2O2}kg_{cat}^{-1}h^{-1}$**	**wt% H_2O_2**
1	50	0.1
2	150	0.3
3	2000	4.0

Table 2.3 Conversion of H_2O_2 synthesis/hydrogenation activities into wt% H_2O_2 values for standard reactions performed at 30 minutes.

In chapter 3, H_2O_2 decomposition experiments were additionally undertaken using the conditions described in section 2.3.2, but instead filling the autoclave with 25% O_2/CO_2 to a pressure of 2.9 MPa. Thermodynamically, the contribution of the H_2O_2 decomposition pathway under standard reaction conditions is minimal and based on a high partial pressure of oxygen, pO_2 (for standard H_2O_2 synthesis reactions - H_2:O_2 = 1:2 molar).

2.4 Characterisation

2.4.1 UV-Visible Spectroscopy (UV-Vis)

Spectroscopy is a fundamental technique that allows quantification of the amount of radiation adsorbed or emitted by a sample, based on the interaction of light with matter. In particular, UV-Vis spectroscopy concerns the absorption of emission of electromagnetic radiation in the ultraviolet or visible spectral region, ranging from 200 to 800 nm. Within this region, molecules typically undergo electronic transitions upon excitation by electromagnetic radiation, and for transition metal centre(s), electronic transitions including d-d transitions and ligand-metal and metal-ligand charge transfer processes can be studied. When light passes through an absorbing species, some energy will be absorbed. This causes the species to move from a lower energy state to one of higher energy. According to the Beer-Lambert law[3], the electromagnetic radiation absorbed by the species is proportional to its concentration:

$$\mathbf{A = \varepsilon.[c].l} \qquad \textbf{(Equation 2.1)}$$

where **A** is the absorbance (no units), **ε** is the molar extinction co-efficient (mol^{-1} L cm^{-1}), **[c]** is the concentration (mol L^{-1}), and **l** is the path length (cm) of the sample cell.

Single-beam spectrophotometers can operate using either a fixed wavelength light source or a continuous source. The simplest instruments use a single-wavelength light source, such as a light-emitting diode (LED), a sample container, and a detector/photomultiplier. Instruments with a continuous source have a dispersing element and aperture to select a single wavelength before the light passes through the sample cell (Figure 2.6).

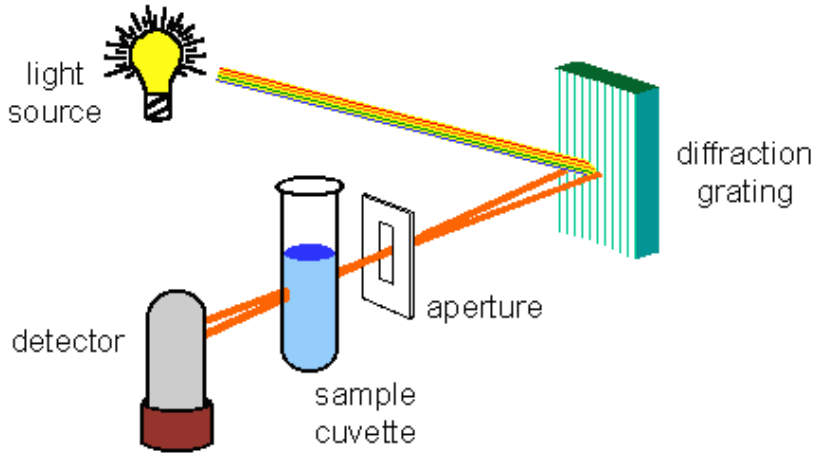

Figure 2.5 Schematic of a wavelength-selectable, single-beam UV-Vis spectrophotometer.

UV-Visible spectroscopy of the colloidal sols was used to monitor the intensity and position of the plasmon resonance band of gold. In addition, the uptake of Au and Pd catalyst precursors on TiO_2 and carbon supports during wet impregnation preparation was monitored by UV-Vis spectroscopy (using a JASCO UV-Vis/NIR V-570 spectrophotometer) between 200 and 800 nm, using distilled water in a quartz cuvette as the reference value. Samples (0.5 ml) were collected during the impregnation step at timed intervals after the support (C or TiO_2) was stirred with Au and Pd metal compounds in solution. Each sample was passed through glass filter paper (Whatman, 55 micron grade) to carefully separate the solution from the support. Concentrated (2 ml water) and dilute (28.5 ml water) metal solutions were studied to assess the effect of concentration on the rate of metal uptake.

2.4.2 Powder X-ray Diffraction (XRD)

Powder XRD is a useful tool allowing characterisation of crystallographic structure and the preferred orientation in powdered solid samples. This is achieved by observing the scattering intensities of an X-ray beam as a function of incident and scattered angle (degrees 2-Theta). X-rays generated from a source are passed through a monochromator to give one specific wavelength of X-ray that is focussed into a beam and directed at the powdered catalyst packed flat in the sample plate giving rise to diffraction[4]. The sample and detector (which is Geiger Muller tube) are moved with the sample at θ and the detector at 2θ.

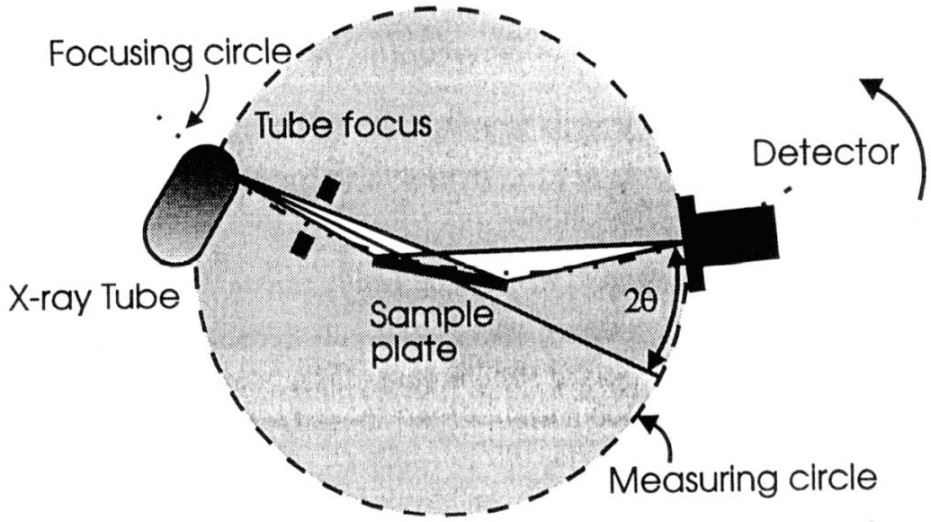

Figure 2.6 Diagram of a typical powder diffractometer setup.

The diffracted X-rays are collected using a moving detector around the circumference of the circle. The resulting pattern shows the relationship between the intensity and degrees 2θ, with the number of X-rays proportional to the intensity. Powder diffraction data is presented as a diffractogram - a plot of the diffracted intensity, I as a function of the scattering angle, 2θ. The interplanar spacing(s), d within the crystalline sample can be calculated using the Bragg equation:

$$\mathbf{n\lambda = 2dsin\theta} \qquad \textbf{(Equation 2.2)}$$

where **n** is the order of the X-ray beam, **λ** = wavelength**, d** is the interplanar spacing, and **θ** is the diffraction angle.

The characteristic sets of d-spacing's generated in a typical X-ray diffractograms can be used as a fingerprint of the same, since each crystalline material has a unique X-ray diffraction pattern, which can be referenced against the JCPDS database allowing for identification for a specific material/phases that constitute a novel material. Catalysts were characterised by powder X-ray diffraction (XRD) using an X'PERT PANalytical diffractometer with a monochromatic Cu-Kα1 source operated at 40 keV and 30 mA. Phases were identified by matching experimental patterns with the JCPDS powder diffraction file.

2.4.3 Thermo-Gravimetric Analysis (TGA)

Thermo-gravimetric analysis (TGA) can be used to track the mass variation for a given sample as a function of increasing temperature, or isothermally as a function of time, in an atmosphere of nitrogen, helium, air or under a vacuum. Thermo-gravimetric analysis was performed on a Seteram TG-DTA. The sample (approximately 30-40 mg) was placed in an aluminium crucible and heated to 350 ^{o}C at a ramp rate of 5 ^{o}C/minute under either air or nitrogen atmosphere. Mass variation, temperature and heat flow were measured to a high degree of accuracy by a microbalance within the machine.

2.4.4 Temperature Programmed Desorption (TPD)

Temperature programmed desorption (TPD) is a method of observing the desorption of molecules from a surface as the surface temperature is increased. In TPD studies, a sample previously equilibrated with an adsorbate is subjected to a programmed temperature increase. When the thermal energy exceeds the adsorption energy of a previously adsorbed species, this gives rise to desorption in order of increasing adsorption energy. As molecules desorb from the surface they are swept by a carrier gas, such as helium, argon or nitrogen, to a thermal conductivity detector where they are quantified. The variation in the thermal conductivity of the gas mixture is measured, to give a plot of the thermal conductivity as a function of sample temperature, allowing quantification and identification of adsorbed species.

Temperature programmed desorption (TPD) can be used to investigate the surface oxygen group(s) on activated carbon supports though desorption of CO_2 and CO gases derived from the decomposition of characteristic organic functionalities, *i.e.* carboxylic acids, phenols and ethers. TPD can be used to track CO_2 and CO desorption upward to 1000 ^{o}C, which can vary based on the activation method (*e.g.* steam, HCl, CO_2) applied to the carbon natural source (*e.g.* date pits, pine trees). Differences in CO_2 and CO desorption are associated with surface chemistry, in general on-set of CO_2 desorption is expected at lower temperatures compared to CO, and is related to the decomposition of functional groups where the carbon atom is bonded to two oxygen atoms as oppose to one oxygen (CO), and therefore correlating with increasing bond strength.

Temperature programmed desorption was performed using a Thermo TPDRO 1100 instrument. All samples (0.10 g) were pre-treated in argon (120 ^{o}C, 3 h), prior to flowing a helium/carrier gas over the sample (flow rate = 20 ml min^{-1}) and applying a heating ramp of 5 ^{o}C min^{-1} until reaching a maximum temperature of 1000 ^{o}C. The desorbed products were monitored by an on-line thermal conductivity detector.

2.4.5 BET Surface Area and Porosimetry Measurements

Nitrogen gas is physically adsorbed through weak Van der Waals bonds at the catalyst surface and desorbed at the same temperature by a decrease in pressure (thus achieving equilibrium). By admitting stepwise known amounts of nitrogen gas into the sample tube an adsorption isotherm was determined. The volume of nitrogen gas adsorbed is equal to the difference in gas admitted and the amount of gas filling the free space in the sample tube. By plotting the volume of adsorbed nitrogen gas against P/P_o (P = equilibrium pressure of adsorbate, P_o = the saturation pressure of adsorbate) a type II adsorption isotherm results.

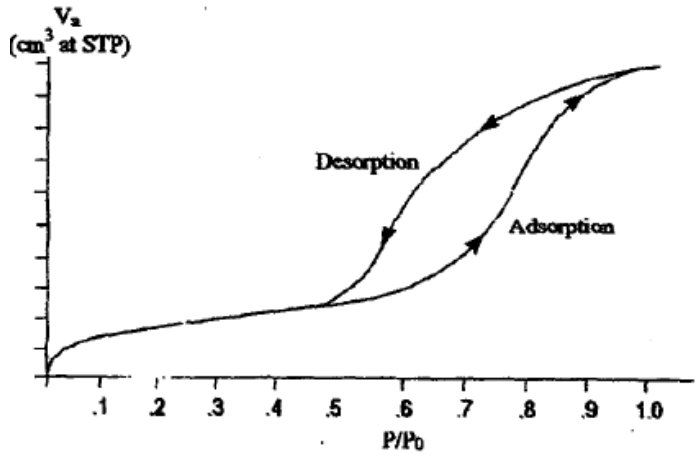

Figure 2.7 Sketch of a type II adsorption isotherm.

The linear region (0.05 – 0.35 P/P_o) represents the development and completion of the monolayer and so was used to determine the surface area. As the molecular cross sectional area for nitrogen is known (a_m = 16.2A^{o2}), then the specific surface area was calculated using BET theory[5]. This determined the amount of nitrogen gas required to cover the external pore surfaces of a solid sample with a complete monolayer of nitrogen. The BET isotherm is an extension of the Langmuir isotherm, and can be used to calculate surface areas based on a model of adsorption employing certain assumptions. The BET equation is described below:

$$\frac{P}{v(P_0 - P)} = \frac{c-1}{v_m c} \cdot \frac{P}{P_0} + \frac{1}{v_m c} \qquad \textbf{(Equation 2.3)}$$

where **P** is the equilibrium pressure, $\mathbf{P_0}$ is the saturation pressure**,** **v** is the quantity of adsorbed gas, $\mathbf{v_m}$ is the volume of monolayer gas adsorbed, and **c** is the BET constant.

Pore-size distributions were calculated using the Barrett, Joyner and Halenda (BJH) method[6]. As the relative pressure of the isotherm increases beyond 0.2, a rapid rise in N_2 adsorption is observed as the mesopores saturate by capillary condensation. The pressure required for saturation depends on the pore diameter and the radius of the curvature of the resulting meniscus formed by condensation of nitrogen gas. The Kelvin equation[7] is then applied to the data:

$$\ln \frac{P}{P_0} = \frac{-2.\gamma.v_m}{RTr_m} \qquad \textbf{(Equation 2.4)}$$

where $\mathbf{P/P_0}$ is the relative pressure of vapour in equilibrium with the meniscus of the condensed gas of radius $\mathbf{r_m}$, $\boldsymbol{\gamma}$ is the surface tension, $\mathbf{v_m}$ is the molar volume, **R** is the universal gas constant, and **T** is the temperature.

Nitrogen Porosimetry was undertaken using a Quantachrome Nova 1200 Porosimeter and NovaWin v2.2 analysis software. Samples were degassed at 120 ^{o}C for 2 h prior to N_2 adsorption. Adsorption/desorption isotherms were recorded at 77K. BET surface areas were calculated over the relative pressure range 0.05-0.2 where a linear relationship was observed. Microporosity was assessed using the t-plot method over the relative pressure range 0.2-0.5, which displayed a linear correlation. Mesopore diameters were calculated by applying the BJH method to the desorption branch.

2.4.6 Fourier Transform Infra-Red Attenuated Total Reflectance (FT-IR ATR) Corrected Spectroscopy

Fourier transform infra-red spectroscopy (FT-IR) represents a special measurement technique for collection of infra-red spectra (IR). Instead of recording the amount of energy absorbed when the frequency of the infra-red light is varied, the IR light is guided through an interferometer. After passing through the sample, the measured signal is the interferogram. Given FT-IR is a type of IR spectroscopy, the principles behind FT-IR spectroscopy are also the same.

Infra-red spectroscopy (IR) measures the absorption of different IR frequencies by a sample placed in the path of an IR beam. Infra-red spectroscopy works because the chemical bonds in molecules within a sample have specific frequencies at which they vibrate, and consequently the molecular vibrations in a sample can be probed. IR spectroscopy can be used to identify different functional groups present in a sample, since different functional groups absorb characteristic radiation at frequencies corresponding to molecular vibrations.

Further to IR spectroscopy, Attenuated Total Reflectance (ATR) is used to study solid materials[3]. Referring to Figure 2.9, IR radiation directed onto a transparent block will strike the flat surfaces at less than the critical angle, giving rise to total internal reflection **(a)**. Subsequently, radiation of a slightly diminished intensity emerges at the far end of the block, although it must be appreciated that while the internal reflection is referred to as ‘total’, radiation actually penetrates beyond the surface of the block during each reflection **(b)**. If the sample material is pressed closely to the outside of the block **(c)** the beam will travel a

small distance through the sample at each reflection and consequently, on emerging at the far end of the block, it will possess the absorption spectrum of the sample. The internal reflection is attenuated by sample absorption, and is highly dependent on the wavelength of radiation used, the angle of incidence and the path length, which must be short to limit the number of total internal reflections through the sample. The 'block' described in Figure 2.9 must be an infra-red transparent material (a germanium single crystal) of refractive index higher than the sample being studied, in order to give rise to total internal reflection.

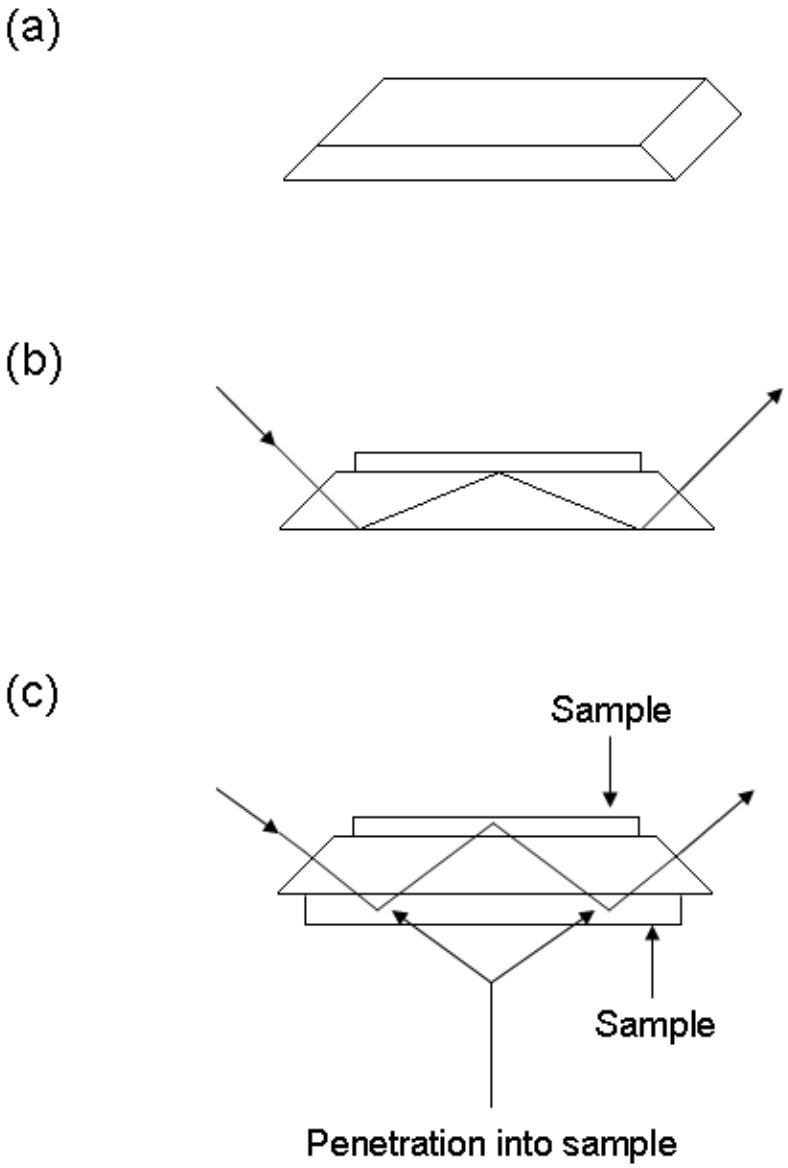

Figure 2.8 Schematic representation of Attenuated Total Reflectance (ATR), describing: (a) the transport block, (b) the internal reflection in the block, and (c) penetration into the sample pressed against the block[3].

FT-IR ATR corrected spectra were measured using a Varian Excalibur 400 FT-IR spectrometer with an UMA 600 microscope. The images were recorded in reflection mode. A small portion of sample was pressed onto a single Germanium crystal/microscope base and irradiated by an Infra-Red source. The sample is exposed to the atmosphere during analysis and so a background spectrum was processed beforehand to allow subtraction of carbon dioxide peaks situated at: 1300-2000 cm^{-1} (broad), 2300-2400 cm^{-1} (sharp), 2840-3000 cm^{-1} (weak) and 3500-4000 cm^{-1} (broad).

2.4.7 Atomic Absorption Spectroscopy (AAS)

Atomic Absorption Spectroscopy (AAS) is used to determine the concentration of a particular metal element in a sample. Specifically, metals are able to absorb UV radiation when excited by heat, with each metal absorbing radiation at a characteristic wavelength, thereby allowing elemental identification. AAS scans for a particular metal by focussing a beam of UV light at a specific wavelength through a flame and onto a detector. The sample is aspirated into the flame and if the metal is present, it will absorb some of the light, leading to a reduction in intensity. The AAS instrument measures the change in intensity, which the data processor converts into an absorbance measurement (which is proportional to metal concentration).

The concentration measurement is determined from a calibration curve after calibrating the instrument using standards of known concentration (0-1000 ppm region). As a result, the concentration of a particular element can be determined with reference to the calibration curve. A typical AAS instrument is shown in Figure 2.9, comprising of a light source, sample cell, monochromator and detector. For successful AAS analysis, the correct flame composition (air/ acetylene/nitrous oxide), careful optical alignment of the lamp with the monochromator, and careful alignment of the burner with the light path in addition to careful preparation of samples and standards are required.

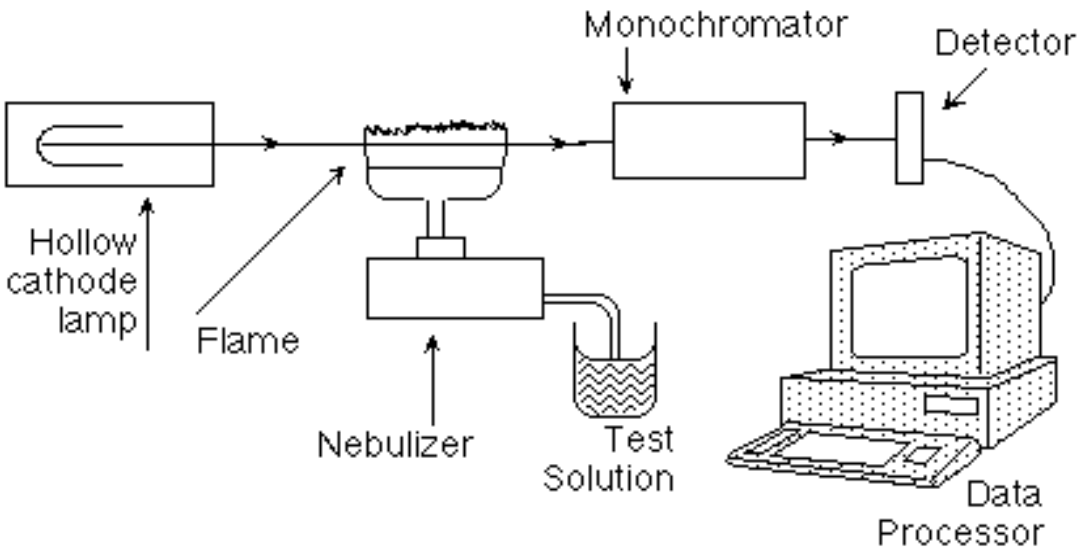

Figure 2.9 Schematic of an atomic absorption spectrophotometer.

AAS measurements were performed using a Perkin–Elmer 2100 Atomic Absorption spectrometer using an air–acetylene flame. Gold/Palladium samples were run at wavelengths of 242.8 nm (Au) and 247.6 nm (Pd). Samples for analysis were prepared by dissolving 0.10 g of the dried catalyst in an aqua regia solution, followed by the addition of 250 mL deionised water to dilute the sample. AAS was used to determine the wt% of the metal incorporated into the support after impregnation, as well as the concentration (ppm) of Au or Pd that had leached out into solution during reaction, by determining the Au and Pd content of the used catalyst and comparing with to the fresh catalyst.

2.4.8 Scanning Transmission Electron Microscopy (STEM)

Scanning Transmission Electron Microscopy (STEM) is a type of Transmission Electron Microscopy (TEM) and an imaging technique in which a highly accelerated beam of electrons are passed through a thin sample, specifically by focusing the electron beam into a narrow spot which is scanned over the sample in a two dimensional raster. A primary beam of electrons are directed at the surface of the sample and undergo inelastic scattering events on collision with atoms in the sample, resulting in the effective spreading of the primary to fill a tear-drop shaped volume, known as the interaction volume, extending from less than 100 nm to around 5 µm into the surface. The rastering of the electron beam across the sample allows for simultaneous operation of elemental analysis techniques, including mapping by X-ray Energy Dispersive Spectroscopy (XEDS) and High Angle Annular Dark Field (HAADF) imaging.

The emission of characteristic X-rays is achieved by focussing a high energy beam of electrons onto a sample, resulting in the possible excitation of an electron in the ground state, leading to ejection from the atom and formation of an electron hole. In order for the excited atom to return to its ground state, an electron from an outer atomic shell falls to the inner shell where an electron was ejected with loss of a specific amount of energy in the form of X-rays.

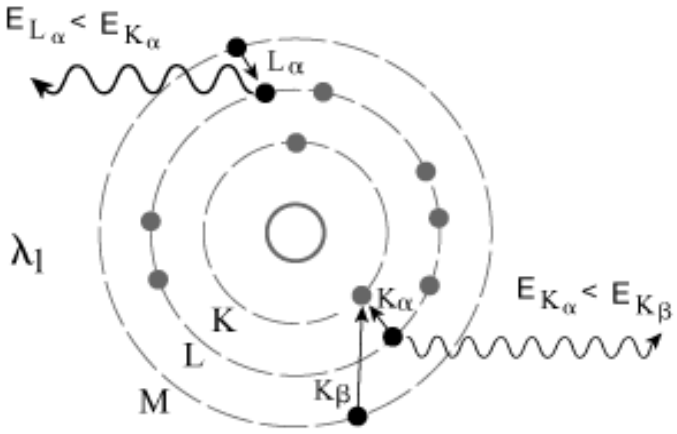

Figure 2.10 Diagram illustrating the principles of XEDS.

X-ray Energy Dispersive Spectroscopy (XEDS) allows elemental analysis since this energy difference is element specific. A detector (a semi-conductor material) measures the energy values of the characteristic X-rays generated within the microscope before an X-ray

microanalysis system converts X-ray energy into an electron count. A spectrum based on the chemical analysis of the sample can be formed using this electron count data, indicating which elements are present from a given k_α value.

Referring to Figure 2.11, a Bright Field (BF) image is formed when unscattered electrons from the incident beam combine with scattered electrons as modified by passage through the entrance aperture. Dark areas in the image arise from the specimen regions which scatter electrons widely and into the entrance aperture. If unscattered electrons are removed, a dark field image formed only from scattered electrons results. The reason why the image is referred to as 'dark field' is because the viewing screen is dark unless a specimen sample is present to scatter electrons. Consequently, dark-field images give rise to a higher level of contrast than produced in bright field mode although longer exposure time to the incident beam is required, based on the reduced intensity of images produced in dark field mode.

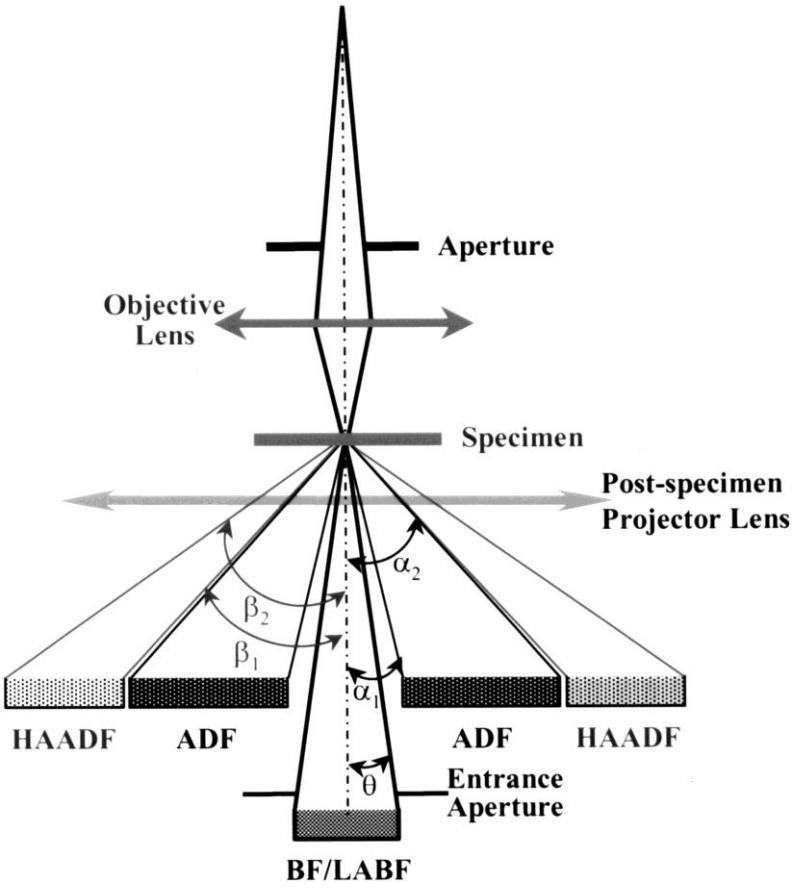

Figure 2.11 Schematic of a Scanning Transmission Electron Microscope[8].

The contrast of HAADF images is highly dependent on the average atomic number of atoms that give rise to high angle scattered electrons *via* inelastic scattering events, as a result it is possible to form atomic resolution images where the contrast is directly related to the atomic number (Z-contrast image), compared to conventional electron microscopy techniques (TEM) which use phase-contrast, producing results which need interpretation by simulation.

MSA is a group of processing techniques[9] that can be used to identify specific features within large sets of data sets such as X-ray spectrum images and to reduce random noise in the data sets in a statistical manner. This technique is useful for the analysis of X-ray maps taken from nanoparticles[10] through performing a data smoothing calculation by portioning the XEDS data by using a probability density function.

Samples for TEM and STEM analysis were prepared by dispersing the dry catalyst powder onto a holey carbon film supported by a 300 mesh copper TEM grid. Samples were first subjected to bright field (BF) diffraction contrast imaging and X-ray energy-dispersive spectrometry (XEDS) in a JEOL 2000FX TEM operating at 200 kV. Then they were further characterized using high angle annular dark field (HAADF) imaging in order to detect any highly dispersed metallic species in a JEOL 2200 FS TEM instrument operating ant 200 kV and equipped with a CEOS probe corrector. A sub-set of samples were examined in an aberration corrected JEOL 2200FS TEM operated in STEM-HAADF imaging and STEM-XEDS modes at 200kV in order to study the structural and compositional details of individual metal nanoparticles. All samples were analysed by Dr. Qian He and Dr. Ramchandra Tiruvalam at Lehigh University, Pennsylvania, USA.

2.4.9 Scanning Electron Microscopy (SEM)

SEM is used to study the surface or near surface structure of bulk specimens. By focussing a high energy beam of electrons, formed by thermionic emission from a tungsten electrode, onto the surface of a sample and detecting signals from the interaction of incident electrons with the sample surface, high resolution images of samples can be obtained in the backscatter and secondary electron modes respectively. SEM relies upon the intrinsic properties of the electron. By aiming an electron beam at the sample, one of two things may happen, the electron may be taken up by the system, which then immediately ejects an electron from itself, which is called a secondary electron. The second situation that can happen in that the incident electron can be back scattered from the sample itself. Specifically the secondary electron signals detected are excited from the top surface layer with energies 0-50 eV.

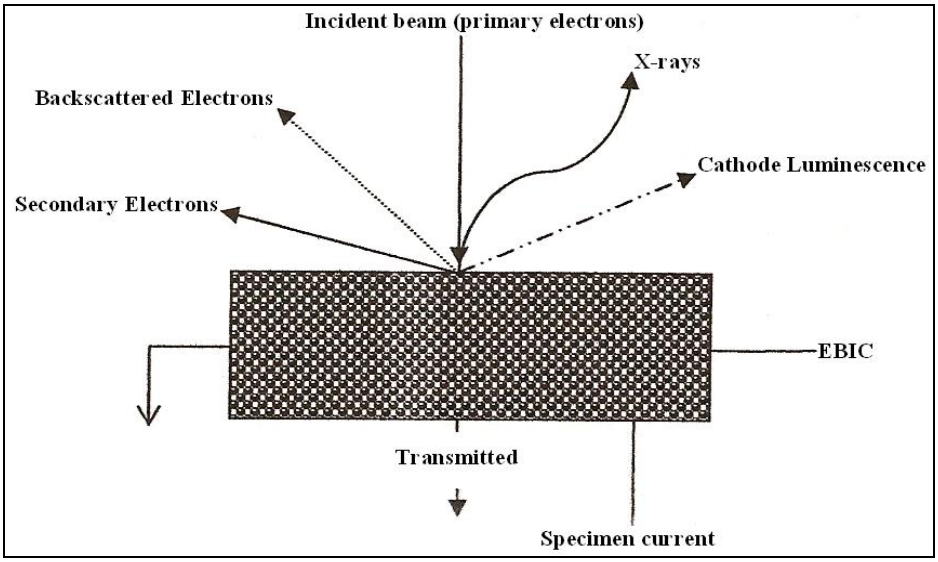

Figure 2.12 The types of signals that are used by SEM.

Specimens for scanning electron microscopy (SEM) analysis were prepared by dry dispersing the powder onto conductive carbon tape attached to an Al stub. The SEM instrument used in this study was a Hitachi 4300SE/N equipped with a Schottky field emission gun. The backscattered electron (BSE) imaging mode was used in the SEM to highlight the heavier metal containing components (Au, Pd) relative to the support material (SiO_2, TiO_2).

2.4.10 X-ray Photoelectron Spectroscopy (XPS)

X-ray XPS is a technique used to probe the atomic energy levels within a sample, and is based on the principles of Einstein's photoelectric effect. Each electron is held in place by the nucleus with a characteristic binding energy and in photoelectron spectroscopy, an electron from any orbital can be removed, depending on the energy of the incident monochromatic radiation. Specifically, an incident X-ray photon collides with an electron, transferring its energy to that electron. If the photon energy is greater than the binding energy, the electron will be ejected from the atom with a specific kinetic energy and velocity, which is defined using the equation:

$$\textbf{Binding Energy} = h\nu - \textbf{Kinetic Energy} \qquad \textbf{(Equation 2.5)}$$

By knowing the energy of the monochromatic exciting radiation, the binding energies of the electrons in the sample can be identified, based on the kinetic energies with which they are ejected. Electrons can be ejected from either the core or valence levels of an atom depending on the energy of the incident radiation. For XPS analysis, electrons from core and inner shells of the atom are ejected and this requires excitation radiation of sufficiently high energy. The X-Ray beam is produced by electron bombardment of a clean, aluminium metal target, resulting in the emission of monochromatic radiation of energy 1486.6 eV.

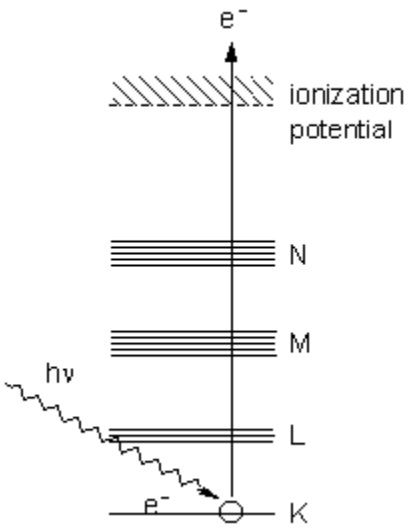

Figure 2.13 Energy level diagram describing XPS[11].

Measurement of the binding energies of electrons ejected from different energy levels in an atom can provide information relation to the top layers of a sample surface (1-12 nm depth), including, chemical composition, oxidation state and differences in the molecular environment and lattice state(s) such as alloying between different elements. Measurement of binding energies is in many ways akin to the chemical shifts in NMR spectroscopy, and reference to various databases (NIST) can be used to identify the chemical environment the atom is in from which the ejected electron originated.

During XPS analysis, the X-ray-induced reduction (photoreduction) of transition metal elements (including Pd, Au and Cu) present in oxides is possible. Feibelman and Knotek[12, 13] and Cazaul[14] have suggested that the XPS photoreduction of metals in oxides appears to be induced by a mechanism referred to as 'Coulombic explosion' due to interatomic (metal–oxygen) Auger decays. Specifically, under a soft X-ray beam, the ejection of photoelectrons from the metal core levels initiates interatomic Auger cascades, which leads to the formation of 2p holes in the oxygen valence orbitals. If such a process leads to the removal of three electrons from the oxygen atom, a temporary formal positive charge is imparted, leading to the formation of O^+ ions and resulting in the desorption of oxygen from the surface due to electrostatic repulsion with the nearest neighbour cations[12-14]. If hydroxide groups are present, these may also undergo thermal dehydration from the X-ray exposure, followed by reduction of the oxide[15-16].

X-ray photoelectron spectra were recorded on a Kratos Axis Ultra DLD spectrometer employing a monochromatic AlK_α X-ray source (75-150 W) and analyser pass energies of 160 eV (for survey scans) or 40 eV (for detailed scans). Samples were mounted using double-sided adhesive tape and binding energies referenced to the C(1s) binding energy of adventitious carbon contamination which was taken to be 284.7 eV.

Important Note: Analysis of Pd(3d) spectra is complicated by the severe overlap between the Pd(3d) doublet and the $Au(4d_{5/2})$ component. However, when the experimental surface Pd:Au molar ratios are calculated based on the $Pd(3d_{5/2})$+ $Pd(3d_{3/2})$ + $Au(4d_{5/2})$ combined integrated intensities and the Au(4f) intensity together with known relative sensitivity factors, we are able to correct the molar ratio by simply subtracting 0.5 from the raw experimental values. It is a simple matter to correct for this overlap problem.

2.4.11 Inelastic Neutron Scattering

Inelastic neutron scattering (INS) is a form of vibrational spectroscopy that is analogous to Raman spectroscopy, the key difference being that the entity scattered is a neutron rather than a photon. The interaction is between the atomic nucleus and the neutron, with the scattered intensity being proportional to the incoherent scattering cross-section (which is element and isotope specific) and the amplitude of bond vibration. For ^{1}H, this cross-section is ~20 times larger than for any other element (or isotope) and since hydrogen is the lightest element, the amplitude of bond vibration is also large[17,18]. While there are no selection rules (since these derive from the photon-electron interaction), these two factors combined create the result that vibrational and bending modes involving hydrogen motion are preferentially observed.

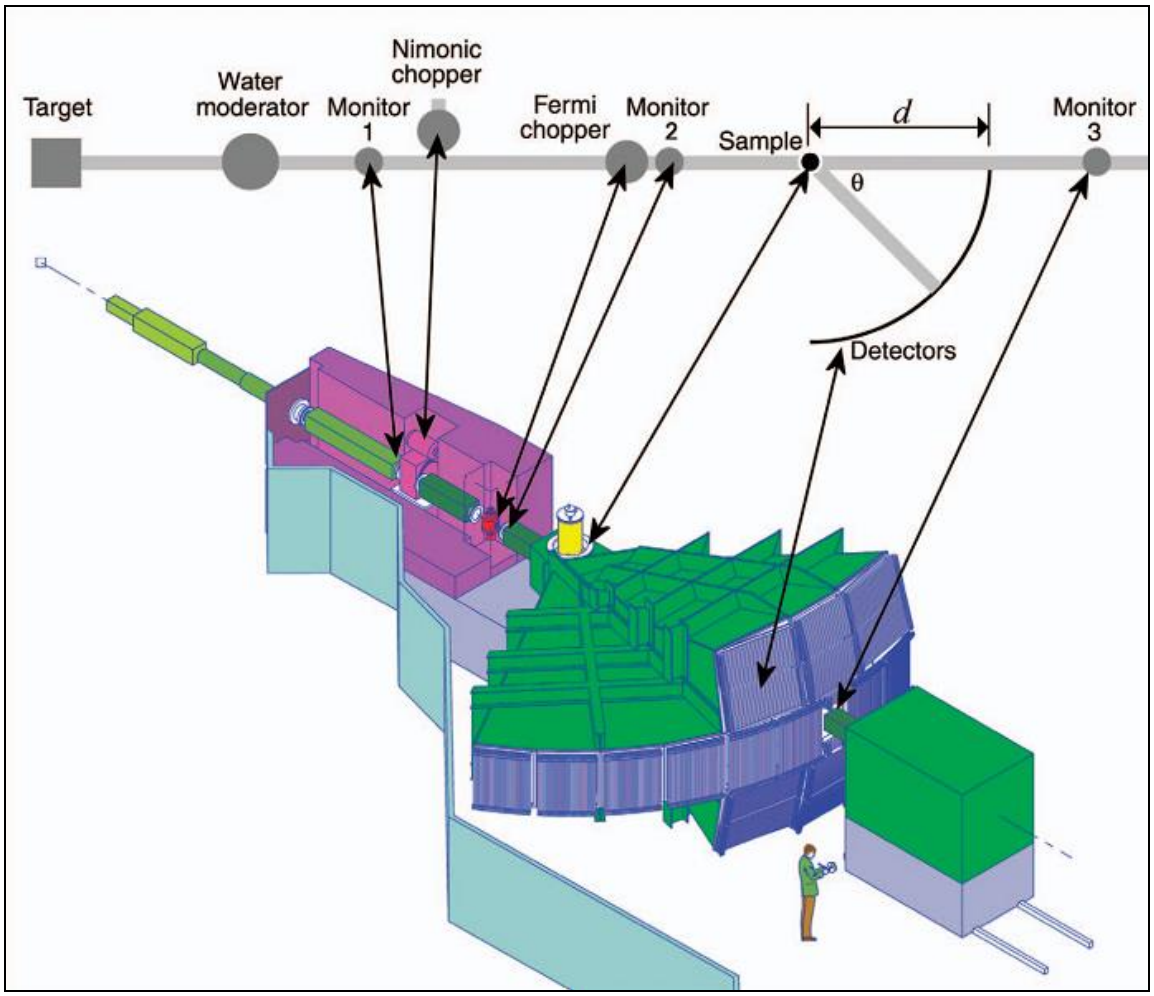

Figure 2.14 Description of MAPS, the instrument used to acquire INS data for this thesis, taking advantage of the pulsed spallation neutron source at Target Station 1, ISIS, Oxford[19].

The INS spectra were recorded with the MAPS spectrometer[20] at ISIS (Chilton, UK), the operating principle of the instrument is described in detail elsewhere. The samples, ~9 g, were loaded into thin-walled, indium sealed aluminium cans. Spectra were measured for ~8 h each at 5 K with 4840 cm^{-1} (600 meV) and 2017 cm^{-1} (250 meV) incident energy (E_i) and selected using Nimonic and Fermi choppers (Figure 2.14). For the MAPS instrumental, the resolution is optimal for energy transfers approaching the incident energy and degrades with smaller energy transfer. The two energies used allow the O–H stretch region (600 meV) and the water bend and librational region and hydroxyl bend regions (250 meV) to be measured with reasonable resolution.

2.5 References

1. C. Hammond, Selective Oxidation of Methane using Zeolites, PhD Thesis, *Cardiff University*, **2011**.
2. J. K. Edwards, B. E. Solsona, P. Landon, A. F. Carley, A. Herzing, C. J. Kiely, G. J. Hutchings, *Journal of Catalysis*, **2005**, 236, 69.
3. C. N. Banwell, E. M. McCash, Fundamentals of Molecular Spectroscopy, Fourth Edition, *McGRAW-Hill Book Company Europe*, **1994**.
4. M. M. Woolfson, An Introduction to X-Ray Crystallography, Second Edition, *Cambridge University Press*, **1997**.
5. S. Brauner, P. H. Emmett, E. J. Teller, *J. Am. Chem. Soc.*, **1938**, 60, 9.
6. S. Lowell, An Introduction to Powder Surface Area, Wiley-Interscience, *John Wiley & Sons Ltd.*, **1979**.
7. E. M. McCash, Surface Chemistry, *Oxford University Press, Oxford*, **2001**.
8. M. Watanabe, D. W. Ackland, C. J. Kiely, D. B. Williams, M. Kanno, R. Hynes, H. Sawada, *JEOL News*, **2006**, 41, 2.
9. N. Bonnet, *Journal of Microscopy*, *Oxford*, **1998**, 190, 2.
10. M. Wanatabe, *Microscopy Microanalysis*, **2004**, 468, 6735.
11. G. Attard, C. Barnes, Surfaces, *Oxford University Press*, *Oxford*, **1998**.
12. P. J. Feibelman, M. L. Knotek, *Phys. Rev. B.*, **1978**, 18, 6531.
13. M. L. Knotek, P. J. Feibelman, *Surf. Sci.*, **1979**, 90, 78.
14. J. Cazaux, *Appl. Surf. Sci.*, **1985**, 20, 457.
15. N. S. McIntyre, S. Sunder, D. W. Shoesmith, F. W. Stanchell, *J. Vac. Sci. Tech.*, **1981**, 18, 714.
16. W. M. Skinner, C. A. Prestidge, R. S. C. Smart, *Surf. Interface Anal.*, **1996**, 24, 620.
17. J. M. Chalmers, P. R. Griffiths, Handbook of Vibrational Spectroscopy, Volume 1: Theory and Instrumentation, *John Wiley & Sons Ltd*, *Chichester*, **2002**.
18. S. F. Parker. A. J. Ramirez-Cuesta, J. Tomkinson, *World Scientific, Singapore*, **2005**.
19. S. F. Parker, D. Lennon, P. W. Albers, *App. Spectroscopy*, **2011**, 65, 1340.
20. C. D. Frost, T. G. Perring, *Int. Coll. Adv. Neutron Sources*, **2000**, 1, 405.

Chapter 3

3.1 Introduction

Bimetallic Au-Pd nanoparticles supported on TiO_2 are active for a range of reactions including benzyl alcohol oxidation[1, 2], 1,2 propane-diol oxidation[3] and the direct synthesis of hydrogen peroxide[4]. Catalysts active for direct H_2O_2 synthesis are typically prepared by simple techniques, *i.e.* wet impregnation, generating a bimodal distribution of Au and Pd nanoparticles in which Au-Pd composition is strongly influenced by calcination and reducing conditions. Transmission electron microscopy of Au-Pd/TiO_2 after calcination at 400 ^oC in air detected small Au-Pd alloy particles (1-8 nm) comprising mainly Pd with a detectable Au component, and larger particles (20-200 nm) which displayed an $Au_{core}Pd_{shell}$ morphology alongside occasional Au-only particles[5]. The core-shell structure to date has been recognised for Al_2O_3 and TiO_2-supported catalysts, while the more active Au-Pd/C catalyst comprises of homogenous Au-Pd alloys only, implying that core-shell formation is not a limiting factor in achieving optimum activity in comparison to particle size effects[6].

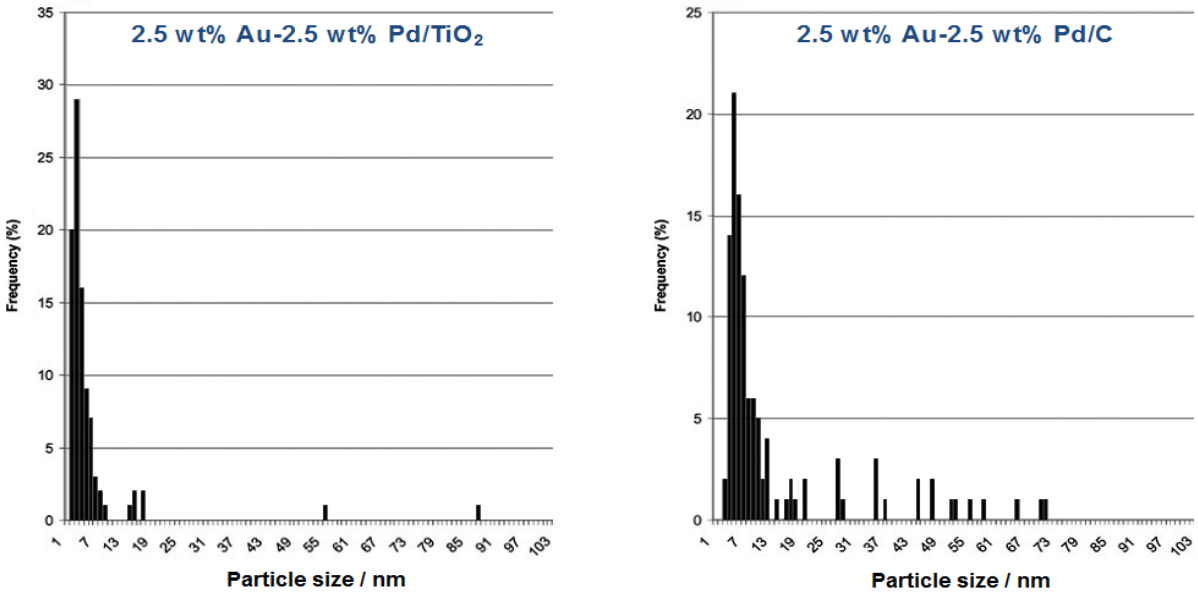

Figure 3.1 Particle size distributions for Au-Pd/C and Au-Pd/TiO_2 catalysts prepared by standard wet impregnation, air dried (110 ^oC, 16 h) and calcined in static air (400 ^oC, 3 h)[6].

Figure 3.1 shows both carbon and TiO_2-supported catalysts comprised mainly of small Au-Pd alloyed particles and a fractional number of larger Au-only particles, present to greater extent in Au-Pd/C. Previous studies concluded that small Au-Pd alloy nanoparticles constituted the synergistic effect observed in the hydrogen peroxide production relative to monometallic Au and Pd catalysts[4, 7, 8]. The composition of alloyed particles is observed to be systematically dependant on particle size and in some instances 2 molar% Au content is sufficient to induce synergy[9].

The wet impregnation technique is different to incipient wetness/dry impregnation, wherein a metal solution is added to a catalyst support containing exactly the same pore volume as the volume of solution added, the maximum loading being limited by solubility of the metal precursor. Exceeding the support pore volume in the case of wet impregnation causes the mode of solution transport to change from capillary to diffusive, influencing mass transfer conditions within pores, concurrent with stirring and heating to slowly evolve excess solution forming a thick, viscous gel[10]. The choice of support is important given P25 Titania has relatively low porosity[11] compared to activated carbon supports, which can be highly porous depending on the activation process.

Ishihara *et al.* studied a 1.7 wt% Au-Pd/TiO_2 (rutile) catalyst for direct H_2O_2 synthesis and suggested the crystal structure of P25 TiO_2 could influence morphology and surface composition of bimetallic nanoparticles due to anatase and rutile lattice mismatch/ surface area[12]. Rutile TiO_2 was proposed to minimise these effects and expose Au-Pd [102] and [010] surface planes considered responsible for 99% H_2 selectivity using 0.5 wt% Au-1.2 wt% Pd/TiO_2 (average particle size 18 nm) in ambient conditions and using trace acid and halide promoters.

Although stable and highly active catalysts can be achieved *via* wet impregnation, improved control of particle size and composition is desired, which has been demonstrated to a greater extent for catalysts synthesized by deposition precipitation (DP)[13] and sol-immobilization methods (S_{Im})[14]. For realistic industrial scale up purposes and since only wet impregnation to date having produced a catalyst that does not hydrogenate H_2O_2, much interest in optimizing parameters within the impregnation method exists, with an emphasis on reducing the ratio of spectator metal to active metal content. Flytzani-Stephanopoulos has demonstrated by means of cyanide leaching that a large proportion of Au can be removed from Au/CeO_2 catalysts without significantly affecting the result activity for the water gas shift reaction, characterisation concluded only Au^{3+} species were preserved on ceria defects[15-20]

It is important to continuously identify improvements in the preparation method leading to the synthesis of stable catalysts with high activity[18] and therefore in this chapter the precise procedure by which Au and Pd metals are co-impregnated onto P25 TiO_2, specifically the amount of water and/or the concentration of precursors used in the preparation, along with drying parameters and their influence on activity for the direct synthesis of hydrogen peroxide, are investigated. Characterisation of catalysts and comparison with an activated carbon support (Darco G60) is undertaken in an effort to understand how catalyst structure and stability are affected. Several terminologies are used throughout chapter 3 and therefore to avoid confusion: addition of water, water treatment, dilution of Au-Pd precursors, and catalyst slurry formation **all represent the volume of H_2O present in the catalyst prior to drying.**

3.2 Effect of wet impregnation parameters on the H_2O_2 synthesis and hydrogenation activity of bimetallic TiO_2-supported catalysts

In previous studies at Cardiff University involving 2.5 wt% Au-2.5 wt% Pd/TiO_2, wet impregnation was used to add a concentrated solution of $HAuCl_4.3H_2O$ and $PdCl_2$ precursors to TiO_2 while stirring and heating to form a thick, viscous gel[4]. This material was air dried (110 ^oC, 16 h) and calcined in static air (400 ^oC, 3 h) and formed a stable catalyst that when tested under standard reaction conditions gave a H_2O_2 synthesis activity of 64 $mol_{H2O2}kg_{cat}^{-1}h^{-1}$ after 30 minutes. The effect of Au and Pd precursor concentrations and the H_2O content of catalyst slurries prior to drying are investigated for 0.5 and 1.0 g scale preparations respectively.

H_2O /ml	**Productivity / $mol_{H2O2}kg_{cat}^{-1}h^{-1}$**	
	0.5 g	**1.0 g**
2 [a]	64	64
2	95	120
5	94	120
7	94	119
10	93	120
15	92	121
20	92	120
25	91	120

Table 3.1 The effect of water addition during the impregnation step on the H_2O_2 synthesis activities of 2.5 wt% Au-2.5 wt% Pd/TiO_2 catalysts prepared on 0.5 and 1.0 g scale. Samples were dried (110 ^oC, 16 h) and calcined in static air (400 ^oC, 3 h). [a] Catalyst formed into a gel by stirring at 80 ^oC to remove 75% of the 2 ml water present in the impregnation step.

Results obtained for 0.5 and 1.0 g preparations are shown in Table 3.1 and indicate both catalyst mass and Au-Pd concentration affect the H_2O_2 productivity measured at 30 minute reaction time. The activity of Au-Pd/TiO_2 catalysts prepared on 1.0 g scale showed a 25-30% enhancement in hydrogen peroxide synthesis activity compared to catalysts prepared on 0.5 g

scale. The Au and Pd concentrations are listed in Table 3.2, taking into account the volume of chloroauric acid solution (1.025 ml for 0.5 g preparation) prior to water addition, forming a partially hydrolysed $[Au(OH)_x(Cl)_{4-x}]^-$ precursor (where $x > 1$) in solution[21]. Further to this, the oven drying time at 110 ^oC drying period was extended from 16 to 48 h in order to assess the contribution of mild heat treatment in the preparation of supported Au-Pd nanoparticles. Results of this variation are presented alongside Au and Pd concentration in Table 3.2.

Added H_2O /ml [a]	**[Au] /mol dm^{-3}**	**[Pd] /mol dm^{-3}**	**Productivity / $mol_{H2O2}kg_{cat}^{-1}h^{-1}$**
2 **[a]**	0.0619	0.115	64
2	0.0211	0.0391	89
5	0.0105	0.0195	87
7	0.0079	0.0146	85
10	0.0058	0.0106	78
15	0.0042	0.0073	76
25	0.0024	0.0045	73
28.5	**0.0021**	**0.0040**	**65**
30	0.0020	0.0038	58

Table 3.2 Summary of the Au and Pd concentrations and H_2O_2 synthesis activities of 2.5 wt% Au-2.5 wt% Pd/TiO_2 catalysts (0.5 g scale). Samples were dried (110 ^oC, 48 h) and calcined in static air (400 ^oC, 3 h). **[a]** Catalyst formed into a gel by stirring at 80 ^oC to remove 75% of the 2 ml water present in the impregnation step.

The calcination step is required to produce a stable, reusable material and in the case of TiO_2-supported catalysts, the calcination promotes the oxidatively driven formation of intermediate sized $Au_{core}Pd_{shell}$ nanoparticles[4, 6]. However, the contribution of preceding drying step(s) on the final activity of the catalysts has not been considered until now.

Extending drying time from 16 to 48 h decreased the H_2O_2 productivity of Au-Pd catalysts as a function of increasing water content, which after addition of 28.5 ml H_2O gave a synthesis activity comparable to when forming a thick, viscous gel (*ca.* 64 $mol_{H2O2}kg_{cat}^{-1}h^{-1}$). It is likely that a reduction in H_2O_2 productivity with Au and Pd concentration after 48 h is because 16 h drying (Table 3.1) is inadequate for very dilute preparations. This is because excess water is slowly evaporated over several hours in a drying oven, and therefore constant H_2O_2 synthesis activity of either ~95 or 120 $mol_{H2O2}kg_{cat}^{-1}h^{-1}$, depending on preparation scale is due to different extents of drying. STEM imaging of non-acid and acid treated Au-Pd/C catalysts in chapter 4 confirmed 16 h drying (no added H_2O) is sufficient to achieve a high dispersion of small and sub-nm sized metal particles, hence the purpose of extended drying is to compensate for initial evaporation of water and compare actual concentration effect(s).

Added H_2O /ml	**Productivity / $mol_{H2O2}kg_{cat}^{-1}h^{-1}$**	**Hydrogenation / $mol_{H2O2}kg_{cat}^{-1}h^{-1}$**	**Decomposition / $mol_{H2O2}kg_{cat}^{-1}h^{-1}$**
2 [a]	64	188	103
2	89	289	172
5	87	292	
7	85	284	
10	78	276	157
15	76	269	
25	73	250	
28.5	**65**	**187**	**104**
30	58	175	

Table 3.3 The effect of water addition during the impregnation step on H_2O_2 synthesis and hydrogenation/decomposition activities of 2.5 wt% Au-2.5 wt% Pd/TiO_2 catalysts (0.5 g scale). Samples were dried (110 ^oC, 48 h) and calcined in static air (400 ^oC, 3 h). [a] Catalyst formed into a gel by stirring at 80 ^oC to remove 75% of the 2 ml water present in the impregnation step.

The effect of the dilution of Au and Pd compounds during the impregnation step was investigated for the consecutive H_2O_2 hydrogenation and decomposition pathways (Table 3.3). In these experiments an initial solution of 4 wt% H_2O_2 was reacted in the presence of H_2 but in the absence of O_2 so that the hydrogenation activity of the catalyst could be determined (and vice-versa for decomposition activity with four results presented, representing part of the hydrogenation measurement which accounts for total H_2O_2 consumption). Both reaction pathways follow a trend similar to that observed for H_2O_2 synthesis, as the amount of water added during the impregnation step is increased, the H_2O_2 hydrogenation and decomposition activities decrease relative to each other. This confirms that the main effect by which the rate of H_2O_2 synthesis is enhanced by using more concentrated Au and Pd salts during the impregnation step originates from an enhanced hydrogenation activity of the catalyst towards both H_2O_2 synthesis and its subsequent hydrogenation.

Added H_2O /ml	**[Au] /mol dm^{-3}**	**[Pd] /mol dm^{-3}**	**Productivity / mol$_{H2O2}$kg$_{cat}^{-1}$h^{-1}**
2	0.0619	0.115	117
5	0.0180	0.0333	117
7	0.0140	0.0260	115
10	0.0106	0.0195	115
15	0.0075	0.0138	112

Table 3.4 The effect of water addition during the impregnation step on the H_2O_2 synthesis activity of 2.5 wt% Au-2.5 wt% Pd/TiO_2 catalysts (1.0 g scale). Samples were dried (110 ^{o}C, 48 h) and calcined in static air (400 ^{o}C, 3 h).

Increasing the drying time from 16 to 48 h was also investigated for Au-Pd catalysts prepared on 1.0 g scale and showed a minimal difference in the H_2O_2 productivity on adding excess water (Table 3.4), supporting the finding that changes in Au and Pd concentration are indeed responsible for the eventual activity. It is apparent that by optimising the preparation conditions that the activity of TiO_2-supported catalysts can be enhanced approximately 2 fold, with the rate of H_2O_2 synthesis increasing from 64 to 110-120 mol$_{H2O2}$kg$_{cat}^{-1}$h^{-1}.

Changing the TiO_2 support from Degussa P25 to Aldrich-sourced material imparted no effect, catalysts could be prepared with activities of 110-120 $mol_{H2O2}kg_{cat}^{-1}h^{-1}$ with both supports using the method described above. Extending the drying time from 16 to 70 h caused a further decrease in activity to *ca.* 80-90 mol H_2O_2 $kg_{cat}^{-1}h^{-1}$, indicating the importance of the duration of the drying step on eventual catalyst performance. In addition, re-wetting of the above materials in water followed by re-drying (110 ^oC, 48 h) prior to calcination does not impart any significant effect on activity and therefore it is concluded that all heat treatment steps used in the preparation of supported Au-Pd nanoparticles are critical.

3.3 Effect of wet impregnation parameters on the H_2O_2 synthesis and hydrogenation activity of monometallic TiO_2-supported catalysts

Modifying the preparation variable for monometallic 5 wt% Pd/TiO_2 catalysts also resulted in comparable high activity (100-105 $mol_{H2O2}kg_{cat}^{-1}h^{-1}$) when dissolving $PdCl_2$ in 2 ml H_2O followed by stirring with TiO_2 *without* evaporating the slurry to form a viscous gel prior to drying (Table 3.5), indicating that Au does not induce a large synergistic effect.

Catalyst Scale / g	**Added H_2O /ml**	**Productivity / $mol_{H2O2}kg_{cat}^{-1}h^{-1}$**	**Hydrogenation / $mol_{H2O2}kg_{cat}^{-1}h^{-1}$**
1.0	2 [a]	31	288
0.5	2	105	
1.0	2	100	329
1.0	5	79	239
1.0	10	68	234
1.0	28.5	23	178

Table 3.5 The effect of water addition during the impregnation step on the H_2O_2 synthesis activity of 5 wt% Pd/TiO_2 catalysts. Samples were dried (110 ^oC, 16 h) and calcined in static air (400 ^oC, 3 h). [a] Catalyst formed into a gel by stirring at 80 ^oC to remove 75% of the 2 ml water present in the impregnation step. [b] H_2O_2 productivity determined on 2nd use.

When preparing 5 wt% Pd/TiO_2 a predetermined amount of HCl was incorporated into the 2 ml volume to dissolve $PdCl_2$ (itself sparingly soluble in water) to form $PdCl_4^{2-}$ ions in solution. As stated Au does not induce a marked synergistic effect on the synthesis activity (increasing from 105 to 120 $mol_{H2O2}kg_{cat}^{-1}h^{-1}$) of the Pd catalyst when using concentrated compounds during the impregnation step and without evaporating the water to form a viscous gel prior to drying. This is in stark contrast to the standard method used in previous studies of Au-Pd/TiO_2 catalysts that were prepared by wet impregnation ensuring the removal of 75% of the initial water present to form a gel, resulting in a marked synergistic effect on activity (increasing from 31 to 64 $mol_{H2O2}kg_{cat}^{-1}h^{-1}$) when Au is added to Pd. The role of Au in enhancing H_2O_2 formation is related to its ability to limit the subsequent hydrogenation and decomposition of H_2O_2 formed, reflected in the higher activities obtained for all reaction pathways when using more concentrated Au-Pd compounds (Table 3.3).

3.4 Effect of wet impregnation parameters on the H_2O_2 synthesis and hydrogenation activity of bimetallic carbon-supported catalysts

The effect of the dilution of Au and Pd precursors and drying time on the activity of 2.5 wt% Au-2.5 wt% Pd/C (Darco G60) was investigated and interestingly no difference in activity was observed, indicating significant differences based on support choice, in particular variation in texture, isoelectric point and the existence of strong metal support interactions[22].

H_2O /ml	**Drying time / h**	**[Au] /mol dm^{-3}**	**[Pd] /mol dm^{-3}**	**Productivity $mol_{H2O2}kg_{cat}^{-1}h^{-1}$**
2	16	0.0619	0.115	120
2	48	0.0619	0.115	120
28.5	48	0.0041	0.0077	124

Table 3.6 The effect of water addition during the impregnation step of catalyst preparation on the H_2O_2 synthesis activity of 2.5 wt% Au-2.5 wt% Pd/C catalysts (1.0 g preparation). Samples were dried (110 ^oC, *X* h) and calcined in static air (400 ^oC, 3 h).

On adding the TiO_2 support to a solution of Au-Pd compounds a cream coloured slurry is formed compared to the carbon support where rapid separation from the added solution is observed (Figure 3.2) when stirring stops. Adsorption of Au and Pd compounds onto carbon occurred immediately and it is proposed that this effect limits the degree with which concentration, volume and drying parameters can influence the outcome of the preparative procedure with the carbon support. This is not the case for TiO_2-supported catalysts where little to no adsorption of Au and Pd is observed (which will be discussed in section 3.5.1).

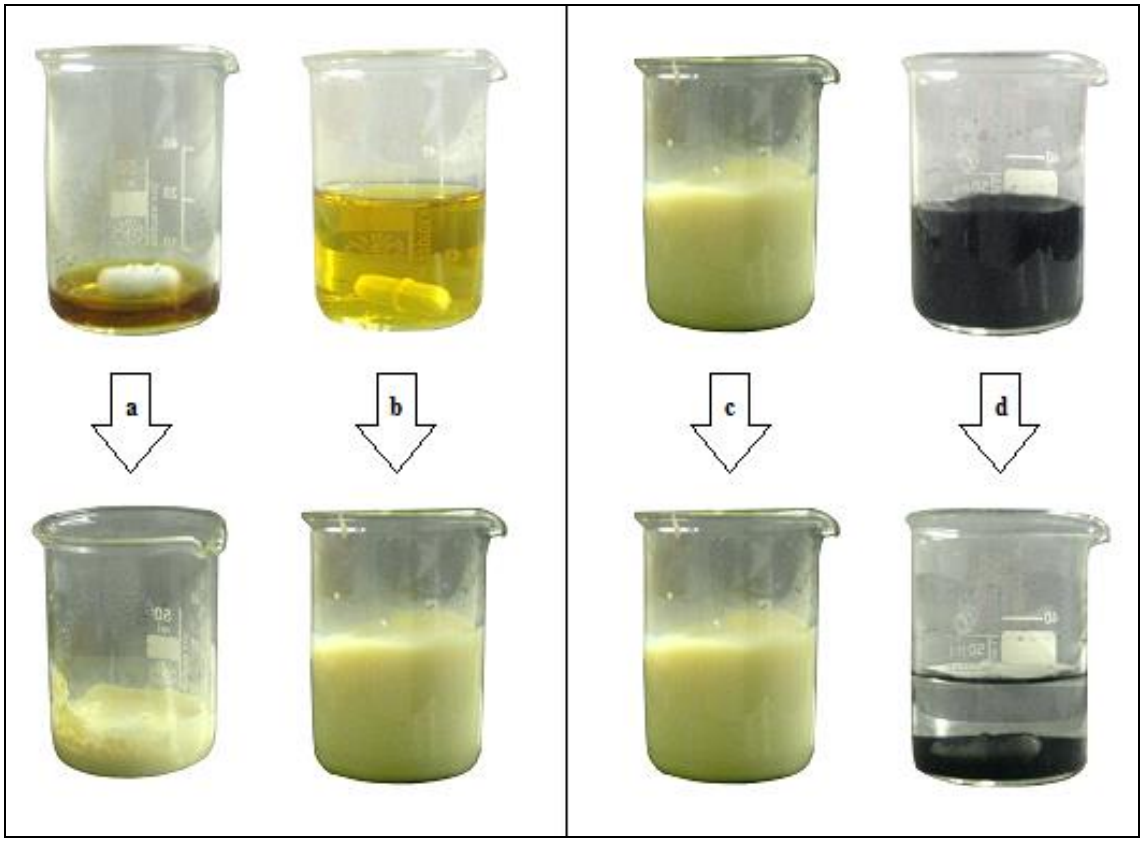

Figure 3.2 Images to show the Au-Pd solution at several points of the impregnation procedure with TiO_2 **(a, b, c)** and carbon **(d)** supports. **(a)** Au-Pd solution (H_2O = 2 ml) before and after TiO_2 addition. Catalyst slurry reduced to a viscous gel under heating. **(b)** Au-Pd solution (H_2O = 28.5 ml) before and after TiO_2 adsorption. **(c)** Au-Pd and TiO_2 slurry stirring on the hotplate / after 30 seconds resting. **(d)** Au-Pd and carbon slurry stirring on the hotplate / after 30 seconds resting. The image shows a near-instant uptake of metal onto carbon exclusively.

3.5 Catalyst Characterisation

The influence of water in the impregnation step and drying on surface composition, alloying, oxidation state and particle size distribution of Au-Pd/TiO_2 and C catalysts has been probed using X-ray photoelectron spectroscopy (XPS) and transmission electron microscopy (TEM), which will be discussed in sections 3.5.2 and 3.5.3 respectively. With reference to catalyst images showing, respectively, gel and slurry consistencies in Figure 3.2, UV-Visible spectroscopy was used to assess the uptake of Au and Pd compounds on TiO_2 and carbon as a function of concentration and stirring time.

3.5.1 Measurement of the uptake of Au and Pd compounds during impregnation using UV-Visible spectroscopy

With the aid of a distilled water reference the rate of metal uptake onto carbon was found to be unaffected by Au-Pd concentration (Figure 3.3). UV-Vis spectra recorded at intervals, 2, 5 and 10 minutes after stirring carbon with the Au-Pd precursor are identical to the water reference, indicating that Au and Pd have been rapidly adsorbed onto the support and supported visually by the rapid separation of water and carbon after stirring (Figure 3.3). In contrast spectra recorded for Au-Pd/TiO_2 slurries showed a characteristic Au plasmon[23] absorbance band in the UV region centred at 218 nm corresponding to a partially hydrolysed $[Au(OH)_x(Cl)_{4-x}]^-$ gold precursor (where $x > 1$) in solution and representing a blue shift from a value of 313 nm recorded for $HAuCl_4$ stabilised in concentrated HCl.

The detection of an absorbance band was anticipated given a brown-gold coloured solution was collected through the glass filter paper beforehand, inferring uptake of Au/Pd onto TiO_2 proceeded significantly slower than observed for carbon. A UV-Vis spectrum was recorded for the starting Au-Pd precursor which was identical to spectra recorded at intervals after TiO_2 addition, showing the 218 nm absorption band remained unchanged. Even after 25 minutes stirring, Au and Pd precursors were detected in solution (28.5 ml H_2O) and it is probable that removal of water to generate a gel is required to facilitate a capillary uptake of metal. In addition the absorbance profiles for Au-Pd/TiO_2 catalysts appeared unaffected by Au-Pd concentration.

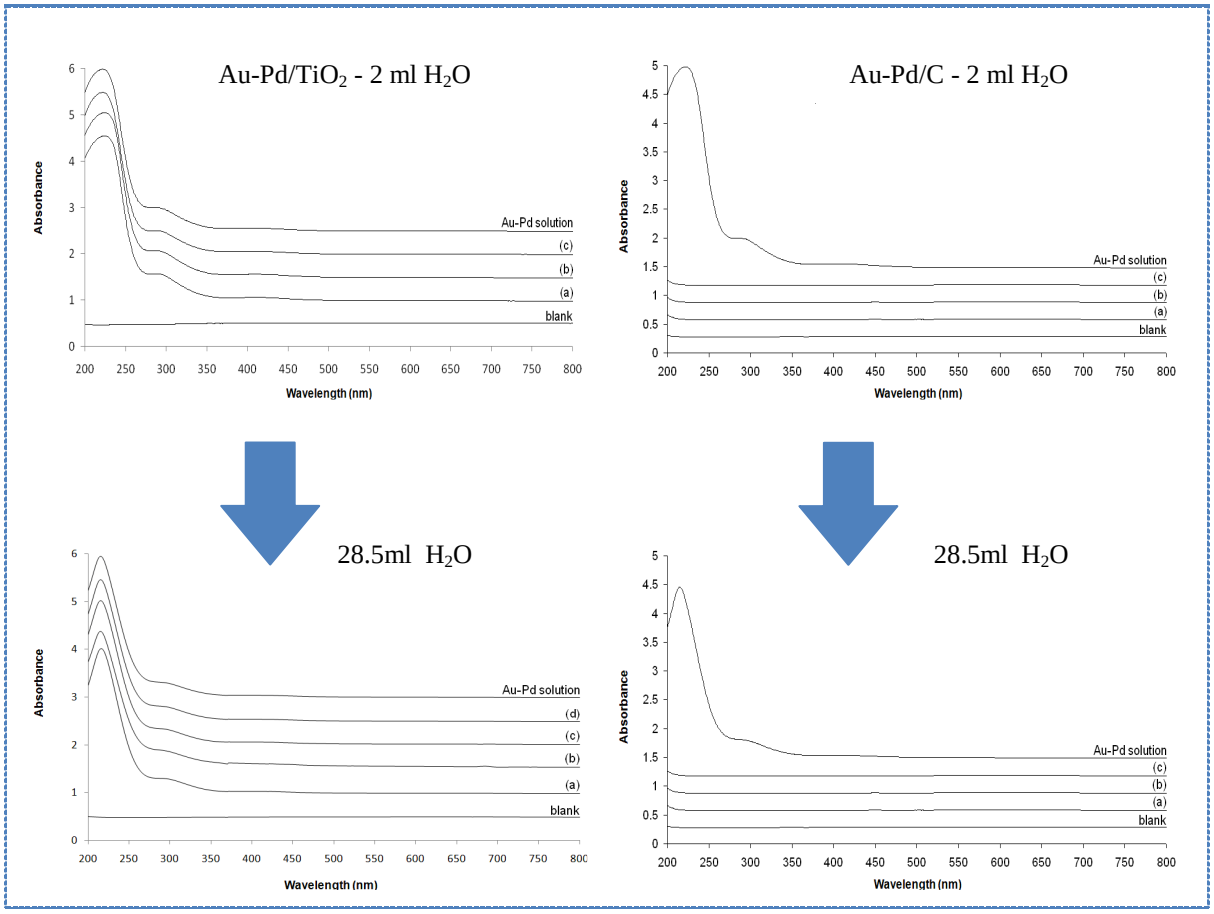

Figure 3.3 UV-Vis spectra recorded for 2.5 wt% Au-2.5 wt% Pd/TiO_2 and 2.5 wt% Au-2.5 wt% Pd/C catalyst solutions. Sample extractions (0.5 ml) were undertaken at intervals: **(a)** 2 min, **(b)** 5 min, **(c)** 10 min, **(d)** 15min, and **(e)** 25 min after stirring the support with the Au-Pd precursor and referenced against the starting Au-Pd solution and distilled water (blank) respectively.

There is a large difference in surface area between C (Aldrich G60 = ~800 m^2/g) and TiO_2 (Degussa P25 = 48 m^2/g) materials and therefore an additional experiment was performed to establish the influence of surface area on Au-Pd uptake. This involved increasing the mass of TiO_2 used from 0.475 to 7.92 g to give an exposed surface area equivalent to carbon, adding additional water to allow effective stirring. The subsequent UV-Vis spectrum (Figure 3.4) showed only minor uptake of Au-Pd onto TiO_2 despite increasing the mass of support, confirming that the rapid uptake of metal onto carbon is not merely a surface area effect and it is implied that the isoelectric point[21,22] of each support (IEP C = pH 3.2, IEP TiO_2 = 6.4) could be critical in understanding this observed behaviour.

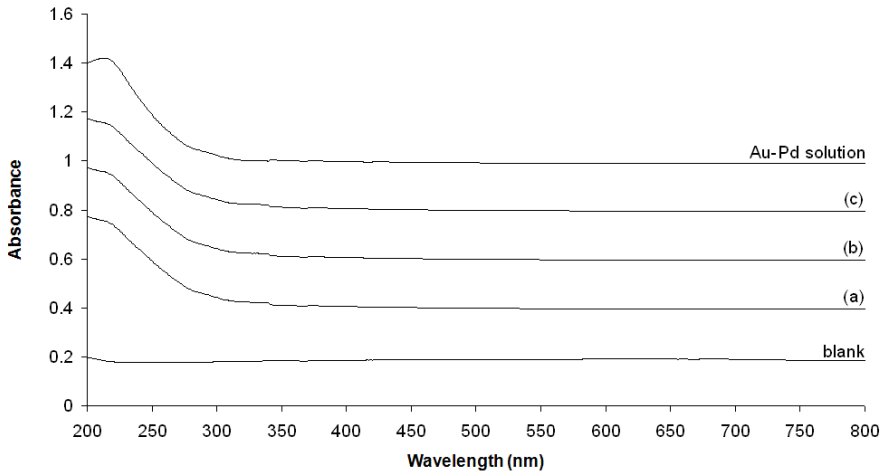

Figure 3.4 Plot of absorbance against wavelength for Au-Pd/TiO_2 catalyst solution (H_2O added = 100 ml). On mixing the Au-Pd precursors with carbon, sample extractions (0.5 ml) were made at intervals: **(a)** 2 min, **(b)** 5 min, **(c)** 10 min and referenced against the starting Au-Pd solution and distilled water (blank). The mass of TiO_2 was increased from 0.475 to 7.92 g to give an exposed surface area approximately equivalent to activated carbon.

3.5.2 X-ray Photoelectron Spectroscopy

Changes in surface composition as a function of water content in the preparation step were investigated by X-ray photoelectron spectroscopy (XPS). Quantified XPS data is summarised in Table 3.6 for a series of Au-Pd/TiO_2 catalysts treated during the impregnation procedure with additional volumes of water in the range 0 - 28.5 ml (and comparing 16 h and 48 h drying times). The addition of water caused a significant decrease in surface chloride concentration with approximately 80% reduction after addition of 28.5 ml H_2O and 48 h drying, and a simultaneous decrease in Pd surface concentration. The latter effect could possibly be related to leaching of Pd from the catalyst surface, while the alternative explanation of the sintering of Pd nanoparticles is not supported by TEM micrographs shown in Figure 3.6.

Inspection of Pd(3d) spectra for all samples analysed showed the presence of both Pd^{2+} and Pd^{0} species, the Pd^{2+} signal being of higher intensity, and curve fitting analysis of these spectra enabled quantification of the Pd^{2+}/Pd^{0} ratio, which is plotted as a function of the amount of water added (Figure 3.5). Treatment with additional water also resulted in a relative increase in the metallic Pd content, which could reflect the preferential leaching of Pd^{2+} species or that smaller Pd particles comprise a higher Pd^{0} concentration.

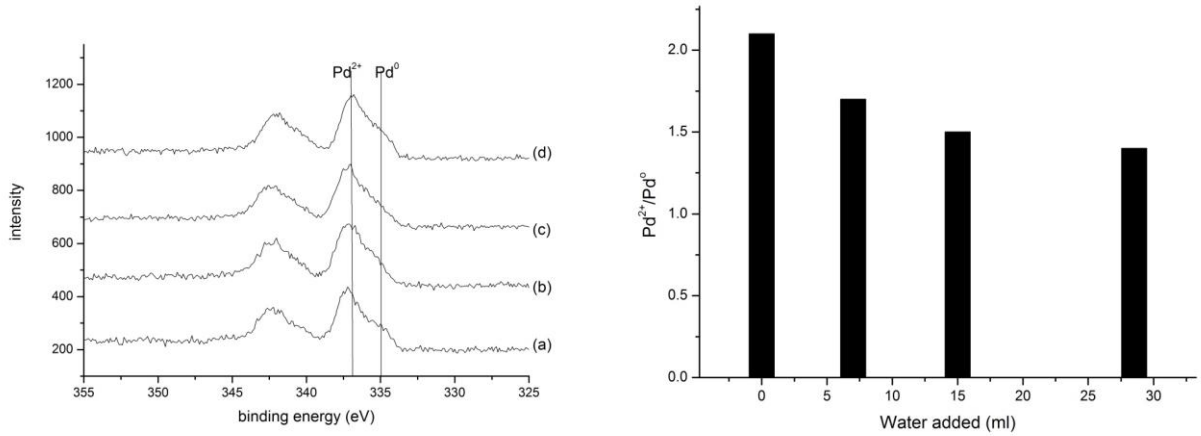

Figure 3.5 Pd(3d) XP spectra for the 2.5 wt% Au-2.5 wt% Pd/TiO_2 catalysts after (a) 0 ml, (b) 7ml, (c) 15 ml, (d) 28.5 ml addition of water during the impregnation step, showing the presence of both oxidised and metallic Pd species **(left)**, and variation of the Pd^{2+}/Pd^{o} ratio for $Au\text{-}Pd/TiO_2$ catalysts with the volume of water added during the impregnation step **(right)**.

3.5.3 Transmission Electron Microscopy

Bright field TEM micrographs of water treated Au-Pd/TiO_2 samples are presented in Figure 3.6, highlighting a bimodal distribution of metal nanoparticles such as seen in image **(a)**. X-ray energy dispersive spectroscopy (XEDS) point analysis showed that the larger particles (20-80 nm) consisted of Au-only in comparison to the smaller particles in the 2-10 nm size range were found to be Pd. The detection limit of the XEDS probe used is very high (~1 atom%) and shows no conclusive evidence of Au-Pd alloying in either small or large particle size distributions. Representative higher magnification views of the smaller 2-10 nm particles are included for the 2 ml **(b)**, 10 ml **(c)** and 28.5 ml **(d)** H_2O treated samples respectively, where the counting of hundreds of individual Pd particles showed a definite shift to a smaller median particle size on increasing water content (Figure 3.7), whereas the population of larger Au particles showed negligible differences in their size distribution.

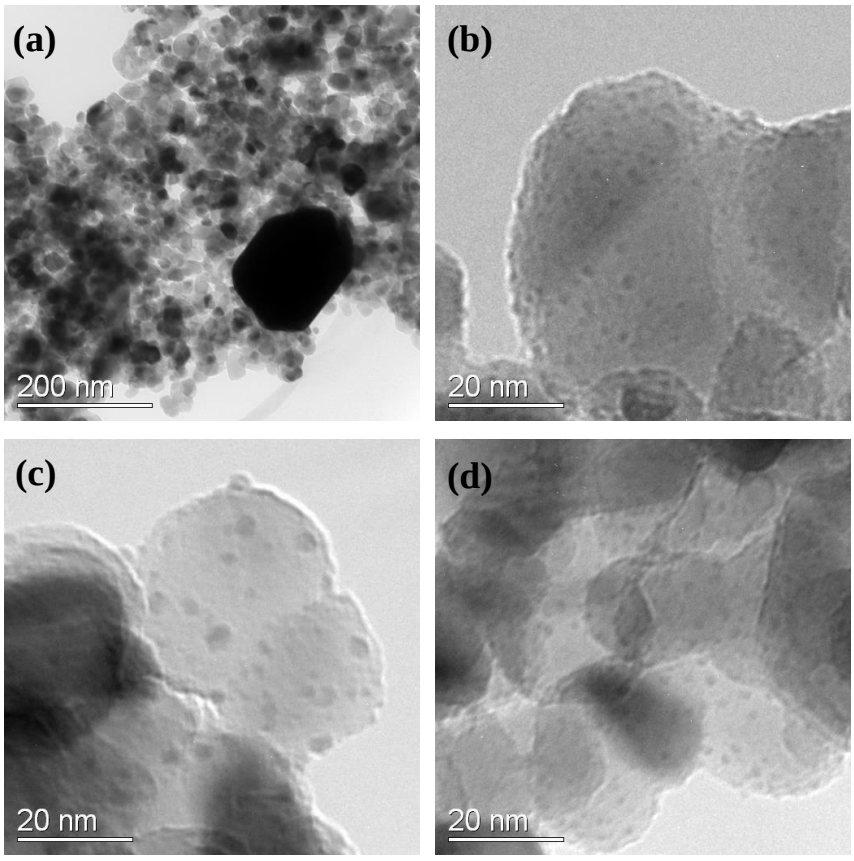

Figure 3.6 Bright field TEM images of 2.5 wt% Au-2.5 wt% Pd/TiO_2 catalysts treated with **(a, b)** 2 ml, **(c)** 10 ml and **(d)** 28.5 ml of water, dried (110 ^{o}C, 48 h) and calcined (400 ^{o}C, 3 h).

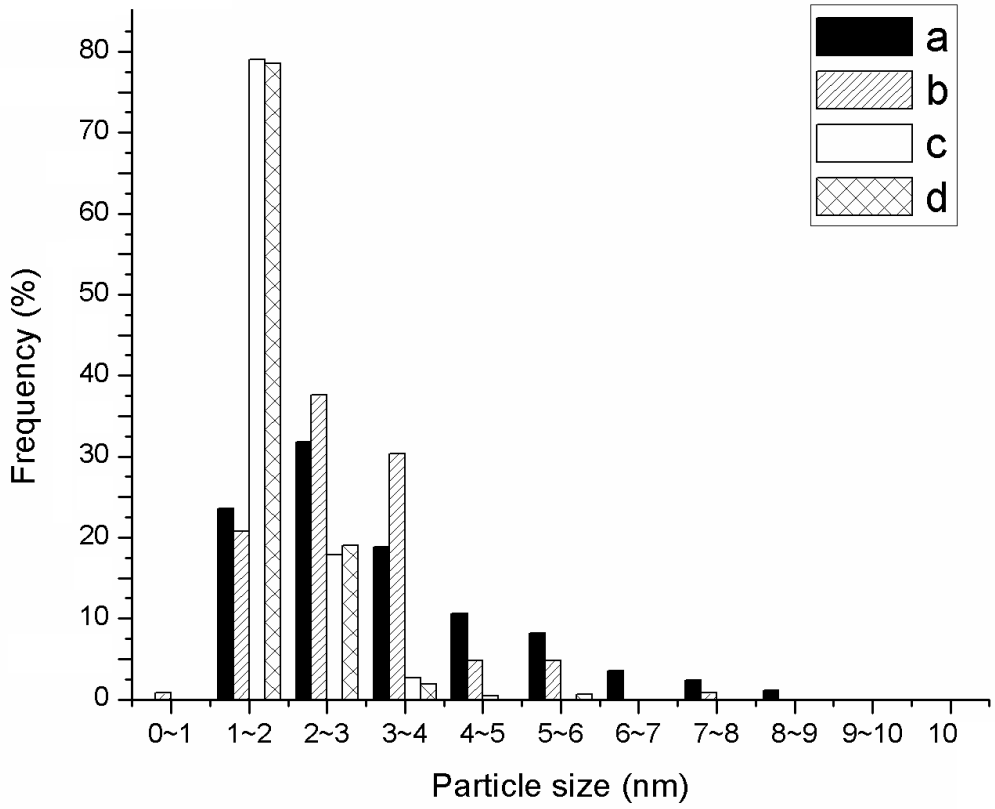

Figure 3.7 Comparison of particle size distributions for the smaller Pd-particles detected in water treated 2.5 wt% Au-2.5 wt% Pd/TiO_2, dried (110 ^oC, 48 h) and calcined (400 ^oC, 3 h). **(a)** Solid Black - 2 ml H_2O added (75% of initial H_2O removed to form a gel), **(b)** Single Line - 2 ml H_2O, **(c)** Solid White - 10 ml H_2O, **(d)** Cross Hatch - 28.5 ml H_2O.

The solid black distribution shown in the above histogram is representative of prior characterisation work for 2.5 wt% Au-2.5 wt% Pd/TiO_2 prepared by wet impregnation and removing 75% of the initial H_2O to form a gel. [4,6] Here a bi-modal size distribution consisting of small Pd-rich particles (1-8 nm) and large Au-rich particles (20-200 nm) was reported, showing Au and Pd alloying to a varying systematic extent in all particles. XEDS analysis provided evidence of $Au_{core}Pd_{shell}$ formation in larger nanoparticles also identified in Au-Pd/Al_2O_3 counterparts[7]. The distribution of smaller particles in the standard 'gel' catalyst **(solid black)** compared to the water treated Au-Pd/TiO_2 samples, contained detectable and significantly higher Au content (~2 atom%), resulting in synergy and explaining the lower rate of H_2O_2 hydrogenation over this catalyst.

Representative electron micrographs of 2.5 wt% Au-2.5 wt% Pd/C catalysts exhibited a bimodal particle size distribution apparently unaffected by water treatment (Figure 3.8). Although the largest particles are not shown entirely below, they ranged from 20-100 nm in size and contained Au-only. The presence of Pd in these particles if at all lies below the XEDS detection limit, however for smaller particles (3-10 nm) only the characteristic Pd XEDS signal was detected. There was no significant difference in the particle size distribution of either the small or large particles found in catalysts treated with 2 and 28.5 ml H_2O, in agreement with the preserved catalytic activity (120-124 $mol_{H2O2}kg_{cat}^{-1}h^{-1}$) for these two samples.

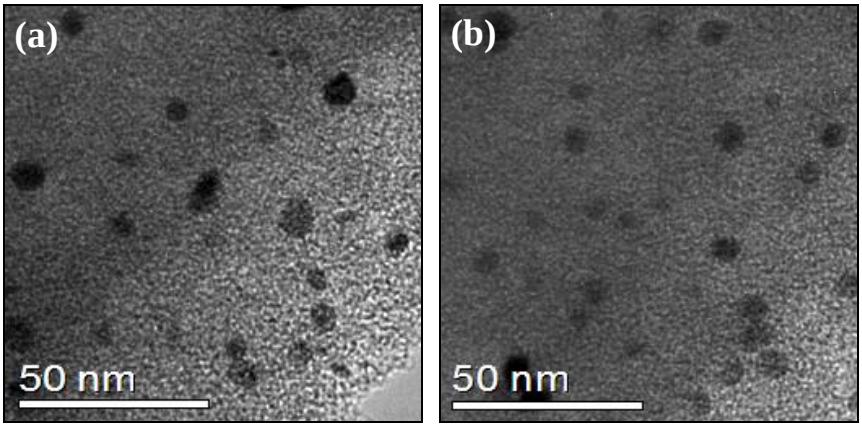

Figure 3.8 Representative bright field TEM images of 2.5 wt% Au-2.5 wt% Pd/C catalysts treated with **(a)** 2 ml, and **(b)** 28.5 ml of water, dried (110 ^oC, 48 h) and calcined (400 ^oC, 3h).

3.6 Evaluation of catalyst reusability

The reusability of water treated Au-Pd/TiO_2 catalysts for hydrogen peroxide synthesis was investigated and compared against carbon-supported counterparts. Au-Pd/C catalysts were stable and could be reused irrespective of the volume of H_2O added in the impregnation step, however the improved, high activity of TiO_2-supported catalysts could not be maintained on subsequent use despite calcination at 400 ^oC (Table 3.8). A significant decrease in H_2O_2 productivity by approximately 3 fold was observed after adding 2 ml H_2O (and 16 h drying) although stability did improve on adding 28.5 ml H_2O and extended drying, leading to a steady decline in activity on second and third use. In addition the productivity of 5 wt% Pd/TiO_2 decreased from 100 to 67 $mol_{H2O2}kg_{cat}^{-1}h^{-1}$ on second use, indicating that stability is not linked to alloying of Au and Pd.

Added H_2O /ml	Productivity / $mol_{H2O2}kg_{cat}^{-1}h^{-1}$		
	1st use	**2nd use**	**3rd use**
2 [a]	64	62	62
2	95	30	21
28.5 [b]	64	54	44

Table 3.8 H_2O_2 reusability experiments for 2.5 wt% Au-2.5 wt% Pd/TiO_2 catalysts prepared using different amounts of water. [a] Catalyst formed into a gel by stirring at 80 ^oC to remove 75% of the 2 ml water present in impregnation step. Samples were dried (110 ^oC, 16 h except [b] 48 h) and calcined in static air (400 ^oC, 3 h).

Stable activity could be achieved for TiO_2-supported catalysts providing no additional water is added in the impregnation step, slowly evaporating 75% of the water present in the chloroauric acid (62 mM, 2 ml), at 80 ^oC forming a gel prior to drying. This is considered as related to the fundamentally different manner in which Au and Pd compounds are adsorbed onto the support during impregnation. For the carbon support this process is facile whereas for TiO_2 lower amounts are adsorbed and variations in the preparation parameters can have a marked effect on the stability and activity of the catalyst. Similarly on an industrial scale, the oxidative efficacy of carbon is exploited in the extraction and reduction of Au^{3+}, which may explain why homogeneous as oppose to core shell Au-Pd alloys are favoured on this support.

3.7 Discussion

Bimetallic Au-Pd/TiO_2 catalysts prepared by wet impregnation in which the catalyst is reduced to a viscous gel prior to drying, show a bimodal distribution of Au and Pd nanoparticles (small particles 1-8 nm and larger particles 20-200 nm) with the larger particles having a core-shell morphology comprising a Au-rich core and Pd-rich surface. The smaller particles were all Au-Pd alloys, with a very high Pd fraction, but still detectable Au content. The presence of these small Au-Pd alloy nanoparticles on the catalytic surface gives rise to the observed synergistic effect and consequently reduction of H_2O_2 hydrogenation activity.

In comparison Au-Pd/TiO_2 catalysts (where 2-28.5 ml of H_2O is present in the catalyst prior to drying) show a bimodal distribution of Au and Pd nanoparticles with larger particles (20-80 nm) containing Au and small particles (1-10 nm) containing Pd, no detectable Au-Pd alloy formation was found in either the smaller or larger particles. The larger Au-only particles are ineffective in limiting H_2O_2 hydrogenation and as a result a reduced synergistic effect of Au is observed, and therefore the higher H_2O_2 synthesis and hydrogenation activities of Pd-only and Au-Pd catalysts prepared using this modified methodology are related to the enhanced Pd dispersion. As a consequence the remaining impregnation catalysts discussed in chapter 3 and all other result chapters have been prepared by standard wet impregnation.

Catalyst	**Pd Precursor**	**Productivity / $mol_{H2O2}kg_{cat}^{-1}h^{-1}$**	**Hydrogenation / $mol_{H2O2}kg_{cat}^{-1}h^{-1}$**
5% Pd / TiO_2	$PdCl_2$	31	288
	$Pd(NO_3)_2$	24	101
2.5% Au-2.5% Pd / TiO_2	$PdCl_2$	64	235
	$Pd(NO_3)_2$	64	162

Table 3.9 Comparison of chloride and nitrate precursors used to prepare 5 wt% Pd and 2.5 wt% Au-2.5 wt% Pd/TiO_2 catalysts for the direct synthesis of hydrogen peroxide.

Interestingly the XPS analysis revealed a decrease in the concentration of surface chloride with water treatment and extended drying. The synthesis of a halide-free catalyst represents a major industrial target[24], however the resulting material must be stable and fully reusable. Table 3.9 shows that changing the Pd precursor from chloride to nitrate-based can produce comparable H_2O_2 formation rates and reduce hydrogenation activity, suggesting that minimising the chloride content could affect particle sintering and composition during the impregnation and calcination steps. For this thesis we are restricted to using the $HAuCl_4.3H_2O$ precursor and therefore cannot synthesise a halide-free catalyst from reagents alone, therefore a brief overview of combined and consecutive preparation techniques aimed at reducing chloride content and improving activity are presented in section 3.8.

3.8 The role of chloride in bimetallic Au-Pd/TiO_2 catalysts

The interaction of chloride anions with Au nanoparticles is generally understood as having a negative effect on the activity of catalytic reactions including CO oxidation and the epoxidation of propylene to propylene oxide.[25-29] Numerous studies have commented on a correlation between the decrease in catalytic activity and the presence of chloride ions in Au/TiO_2 catalysts for CO oxidation, a reaction where catalysts are typically prepared using co-precipitation and deposition precipitation techniques that largely remove chloride and preventing sintering and poisoning. For this reaction Bowker *et al.* developed a method harnessing the benefits of incipient wetness (IW) impregnation and deposition precipitation (DP)[24]. Here the IW technique is used to fill the TiO_2 pores with gold chloride, followed by in-situ reduction with sodium carbonate to precipitate $Au(OH)_3$, resulting in enhanced activity with effective removal of Cl^- ions through washing.

Strukul *et al.* have reported the preparation of Au-Pd/ZrO_2 using consecutive DP and IW techniques to deposit Au and Pd respectively resulted in moderate rates of H_2O_2 synthesis at 10 bar (59% H_2 selectivity) and without halide additives[30]. The same group characterised a stable Au-PdO phase with metallic Pd residing predominantly on edge sites and proposed the oxide phase is responsible for O_2 activation while metallic palladium sites dissociate H_2. Miedziak compared the activity of three Au-Pd catalysts preparation methods for oxidation of benzyl alcohol, determining activity in the order, sol-immobilisation > deposition precipitation > impregnation[31, 32]. The impregnation catalyst formed a significant amount of toluene possibly related to residual chloride increasing the surface acidity of the catalyst, while deposition precipitation was found to improve Au dispersion and Au-Pd alloying.

For this investigation, Pd{Au} and Au{Pd}TiO_2 catalysts were prepared using a consecutive impregnation route, calcining in static air (400 ^oC, 3 h) after impregnating each metal (1st metal denoted in {}). Comparison with standard, 2.5 wt% Au-2.5 wt% Pd/TiO_2 showed that impregnation of Au followed by Pd dramatically increased H_2O_2 synthesis and hydrogenation activity while the reverse addition, Au{Pd} also improved H_2O_2 productivity but importantly decreased the subsequent hydrogenation activity by approximately 3 fold (Table 3.10). Improved rates of H_2O_2 synthesis were not observed for Pd{Au} and Au{Pd}/C catalysts and this was likened to disruption of the spontaneous formation of homogeneous Au-Pd alloys on carbon.

Support	**Sequence**	**Productivity / $mol_{H2O2}kg_{cat}^{-1}h^{-1}$**	**Hydrogenation / $mol_{H2O2}kg_{cat}^{-1}h^{-1}$**
TiO_2	Au-Pd	64	235
	Pd{Au}	164	307
	Au{Pd}	112	86
Carbon	Au-Pd	110	117
	Pd{Au}	85	n.d
	Au{Pd}	73	n.d

Table 3.10 Summary of H_2O_2 synthesis and hydrogenation activities for standard Au-Pd/TiO_2, Pd{Au} and Au{Pd}/TiO_2 catalysts (all 2.5 wt% Au - 2.5 wt% Pd) prepared by consecutive impregnation and 2 x calcination in static air (400 ^oC, 3h), with comparison to activity data obtained for carbon-supported catalysts. n.d = not determined for this investigation.

Power XRD profiles of Au{Pd} and Pd{Au}/TiO_2 catalysts exhibited a characteristic metallic Au [111] reflection at 38.2 degrees 2θ (JCPDS Code: 000-02-1095), indicating alloying of Au and Pd alloying and the existence of amorphous PdO/Pd in both catalysts due to stress-strain effects (PdO [101] reflection not observed at 34 degrees 2θ). By using the Scherrer equation, Au crystallite sizes of 17-18 nm and 21-22 nm were calculated for Pd{Au} and Au{Pd}/TiO_2 respectively.

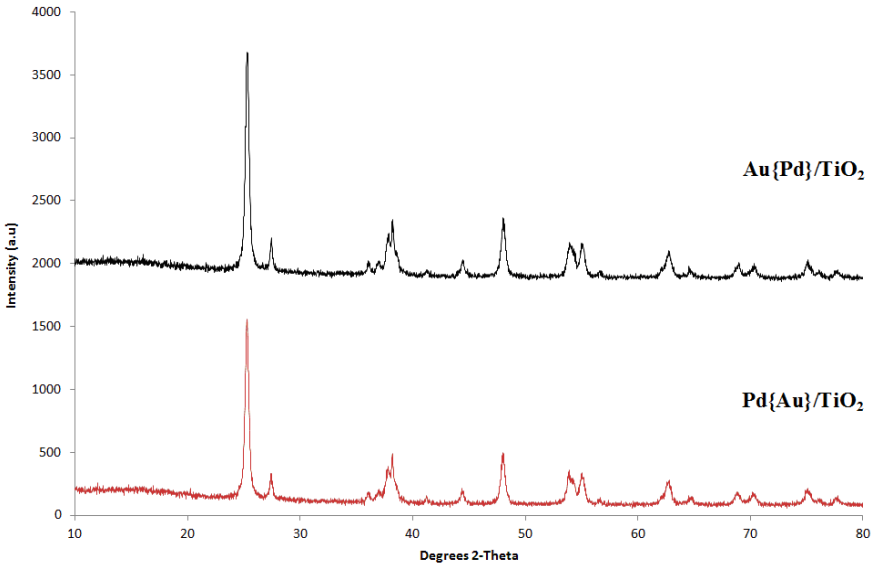

Figure 3.9 Powder XRD profiles of 2.5 wt%-2.5 wt% Au{Pd} and Pd{Au}/TiO_2 catalysts prepared by consecutive impregnation with calcination in static air (400 ^{o}C, 3 h) after each step.

Support	Sequence	Composition atom%			Ratio
		Au	Pd	Cl	Pd/Au [a]
TiO_2	Pd{Au}	0.031	2.15	1.97	68.8
	Au{Pd}	0.086	2.22	1.73	25.3
Carbon	Pd{Au}	0.08	0.70	0.36	8.2
	Au{Pd}	0.23	0.80	0.38	2.9

Table 3.11 Summary XPS derived surface concentrations for TiO_2- and carbon-supported Pd{Au} and Au{Pd} catalysts. [a] Ratio corrected for the overlap of the Pd(3d) doublet and the Au($4d_{5/2}$) component.

Surface concentrations listed in Table 3.11 for consecutive impregnation conclude the development of $Au_{core}Pd_{shell}$ morphologies irrespective of Au and Pd order, with very high Pd/Au ratio observed for Pd{Au}/TiO_2. Both catalysts show Pd surface enrichment relative to co-impregnation of Au and Pd onto TiO_2 (Pd/Au ratio ~12-16) and demonstrating the strong driving force involved in the development of surface Palladium-Oxygen bonds. The Pd/Au ratio for carbon-supported catalysts is also increased albeit to a lesser extent (Pd/Au = 1.8 for co-impregnated Au-Pd/C)[33] but does not improve H_2O_2 yield. The surface concentration of Pd is not markedly different for Pd{Au} and Au{Pd} supported on either TiO_2 or carbon relative to Au exposure which is reduced, leading to higher Pd/Au ratios. The chloride content is approximately 5 fold lower for carbon-supported catalysts and suggesting that use of a second identical calcination has aided in reducing concentration to <0.40 atom%.

Analysis of fresh and used Au-Pd/TiO_2 and C catalysts prepared by standard impregnation confirms that a higher amount of chloride is present on the TiO_2-supported catalyst initially, the majority of which is lost after a single H_2O_2 synthesis reaction and is therefore considered unrelated to the activity, maintained at 64 $mol_{H2O2}kg_{cat}^{-1}h^{-1}$ (Figure 3.10). Performing the heat treatment in a static furnace could possibly explain the presence of residual, chemically unbound chloride originating from the decomposition of Au-Pd compounds. In comparison, low chloride content is detected for Au-Pd/C (and possibly different Cl-species, which will be discussed further in chapter 4) that is largely retained after several reactions. However, insufficient information is available to fully understand the role of halide content on activity as neither the H_2O_2 productivity (110 $mol_{H2O2}kg_{cat}^{-1}h^{-1}$) nor the surface chloride concentration change after reaction.

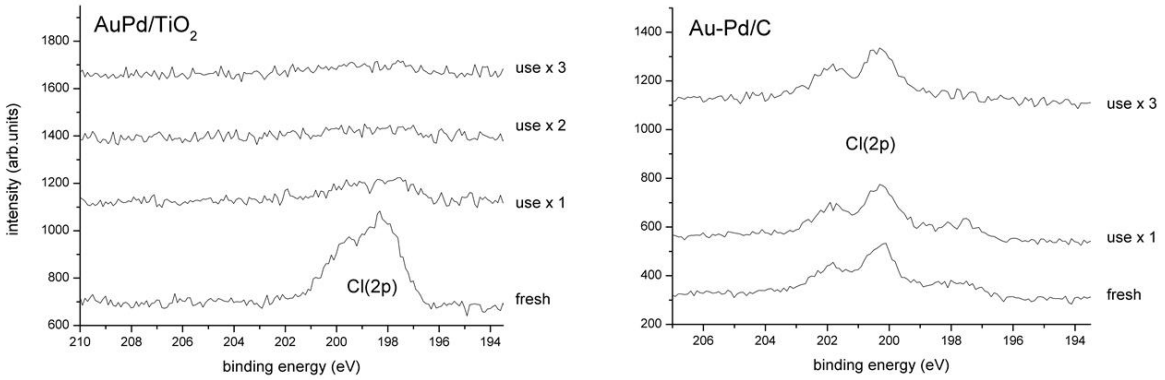

Figure 3.10 Cl(2p) XP spectra for 2.5 wt% Au-2.5 wt% Pd/TiO_2 and C comparing chloride content in fresh and used catalysts for the direct synthesis of hydrogen peroxide.

There is evidence of an inverse correlation between catalyst active for CO oxidation and H_2 activation steps depending on preparation method and presence of residual chloride. Thomas *et al.* [34] reported that combined addition of acid and halide additives is detrimental to the activity of supported Au-Pd catalysts although improvements resulted from their individual use. Addition of acid to the reaction medium decreased sequential H_2O_2 hydrogenation/decomposition activity by different extents depending on factors such as isoelectric point and catalyst morphology (core-shell vs. homogeneous alloy), while addition of bromide at low concentration improved H_2O_2 synthesis through the selective poisoning of hydrogenation and decomposition sites[35]. However, use of higher bromide concentrations also decreased the synthesis activity with the onset of non-selective site poisoning.

Studies have also addressed using excess chloride ions in Au catalyst preparation, which in some cases was unsuccessful due to competitive halide adsorption onto the support[36]. However, 1 wt% Au-Pd/TiO_2 catalysts synthesised by a modified impregnation[37] route were 4 times more active for hydrogen peroxide synthesis compared to using standard impregnation (99 vs. 23 molH_2O_2kg$_{cat}^{-1}$h^{-1}). The activity enhancement was related to formation of a narrow distribution of homogenous Au-Pd alloys (2-6 nm) initiated by excess chloride separating Au and Pd compounds during the impregnation step, limiting agglomeration.

Heat Treatment	**Productivity / mol$_{H2O2}$kg$_{cat}^{-1}$h^{-1}**	**Hydrogenation / mol$_{H2O2}$kg$_{cat}^{-1}$h^{-1}**
Static Air	64	235
99.9% N_2	89	385
5% H_2/Ar	96	597

Table 3.12 The effect of heat treatment atmosphere (400 ^{o}C, 3 h) on H_2O_2 synthesis and hydrogenation activities of 2.5 wt% Au-2.5 wt% Pd/TiO_2 prepared by standard impregnation.

Although Au-Pd/TiO_2 catalysts prepared by modified impregnation were superior for several oxidation reactions, a reduction step (400 ^{o}C, 4 h) was applied to remove chloride ions. This produced a high concentration of metallic Pd in the final catalyst, considered to facilitate sequential H_2O_2 hydrogenation. Comparison with results for 2.5 wt% Au-2.5 wt% Pd/TiO_2 catalysts treated in different atmospheres indicated that inert and reducing conditions improved both rates of H_2O_2 synthesis and hydrogenation over catalysts (Table 3.12).

A recent investigation[33] has highlighted that use of Oxidation-Reduction-Oxidation (ORO) cycles can induce high activity and deactivate the H_2O_2 hydrogenation pathway. However, both high temperature and prolonged heat treatment stages must be oxidising in order to achieve appropriate particle composition and catalyst stability (established for Au-Pd/C). In this chapter, the application of mild, short duration reductive treatments has been investigated to assess whether a chloride free catalyst of low H_2O_2 hydrogenation activity can be prepared by existing techniques.

The deposition precipitation (DP) of Au onto oxide supports, an intimate metal-support preparation technique, has been extensively studied during the past three-decades by Haruta, Bond and Thompson[38-40]. Several mechanisms describing surface processes and active site(s) involved in the oxidation of carbon monoxide on Au/TiO_2 have been proposed, one of the most well-known being the Bond-Thompson model, in which oxidation is described as proceeding at the metal-support interface, comprising both Au^0/Au^{3+} states[41]. The deposition precipitation route is used to precipitate Au-hydroxide specie(s) onto a support and achieved by hydrolysis of $HAuCl_4$, proceeding through a series of complex equilibria on slow addition of base, and typically leads to the formation of 2-4 nm Au particles (Figure 3.11).

$$[AuCl_4]^- + H_2O \rightleftharpoons [AuCl_3(H_2O)] + Cl^-$$
$$[AuCl_3(H_2O)] \rightleftharpoons [AuCl_3(OH)]^- + H^+$$
$$[AuCl_3(OH)]^- + H_2O \rightleftharpoons [AuCl_2(H_2O)(OH)] + H^+ + Cl^-$$
$$[AuCl_2(H_2O)(OH)] \rightleftharpoons [AuCl_2(OH)_2]^- + H^+$$
$$[AuCl_2(OH)_2]^- + H_2O \rightleftharpoons [AuCl(OH)_3]^- + H^+ + Cl^-$$
$$[AuCl(OH)_3]^- + H_2O \rightleftharpoons [Au(OH)_4]^- + H^+ + Cl^-$$

Figure 3.11 Scheme representing the hydrolysis of $[AuCl_4]^-$ on increasing pH value[42].

Particle size and chloride content is highly dependent on the final pH and it has been demonstrated by Moreau[43] that Au/TiO_2 catalysts containing minimal to no chloride could be synthesized on exceeding pH 8. For preparation of bimetallic $Au\text{-}Pd/TiO_2$ catalysts using the DP method a higher pH (10 or above) must be reached in order to effectively hydrolyse the $PdCl_2$ precursor. Changing the pH and therefore the extent of interaction between positively charged TiO_2 surfaces and anionic Au in solution from a rapid to controlled process on moving to higher pH values results in loss of non-deposited metal during filtration and washing stages.

The interaction of Au species with TiO_2 is not fully understood and the subject of on-going debate in the literature. Louis and Zanella[44-46] proposed the reaction of $[AuCl_3(OH)]^-$ at pH 8 with hydroxyl groups of the TiO_2 surface at pH 8, forming a grafted hydroxy-gold species when using NaOH as the base, compared to formation of an amorphous, gold(III) precipitate when using urea as the base. The end catalyst acitvity is highly sensitive to prearation parameters, including the selection of base, temperature, volume, heat treatment and exposure to light.

Here, a methodology developed by Bond and Moreau[47] has been adapted in order to co-deposit Au and Pd onto P25 TiO_2 and for comparison, carbon supports respectively. For TiO_2 deposition the support is present in solution while slowly adding NaOH (0.1 M) to increase the pH to a value of 10 and maintained for one hour, in comparison to carbon deposition where the support is added post-hydrolysis for 5 minutes before filtration and washing. This is due to differences in the iso-electric points of each support and to prevent the uptake of Au and Pd chloride species and basic modification of carbon functional groups (Figure 3.12).

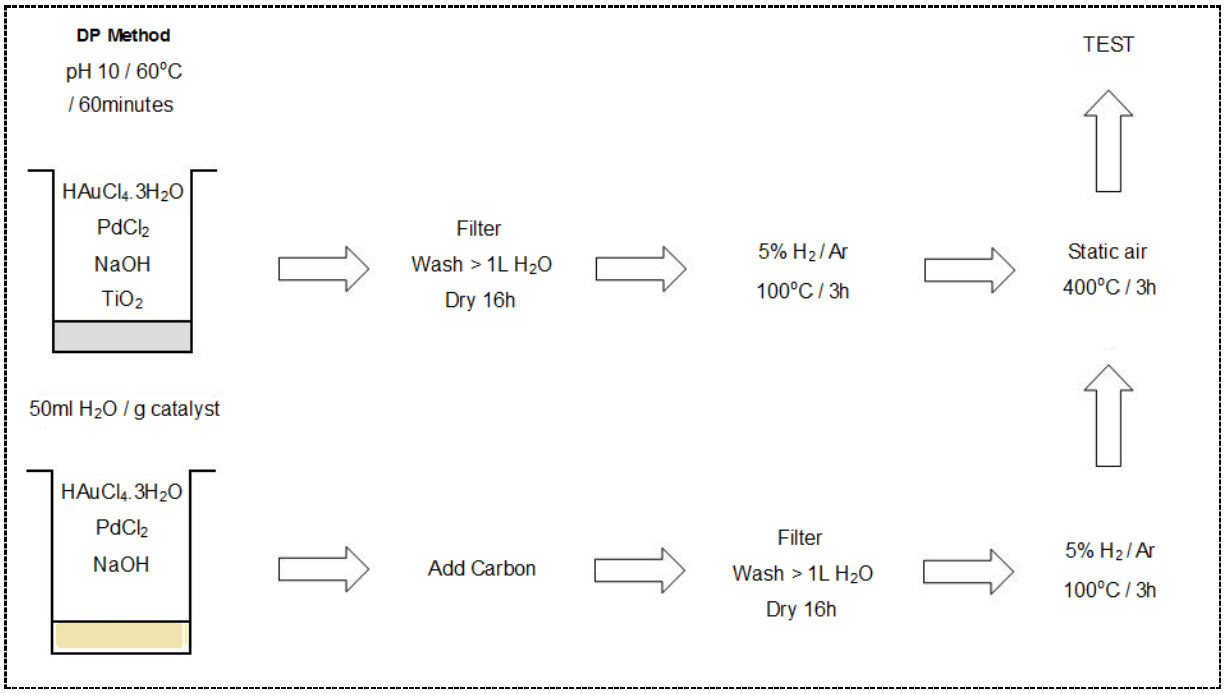

Figure 3.12 Diagram of deposition precipitation techniques to prepare Au-Pd/TiO_2 and C.

For DP preparations the surface chloride concentration has been determined with and without use of the reductive pre-treatment shown in Figure 3.12. Future microscopic analysis is planned as part of a continuing optimisation study and therefore for preliminary experiments, focus is aimed at establishing if a halide-free catalyst can be prepared. Referring to Table 3.13 it is apparent that different Au and Pd loadings, determined by SEM-EDX and activities are achieved depending on the support. The Au/Pd ratio is dramatically changed for Au-Pd/TiO_2 with ~4.5 times more Pd deposited compared to Au, giving a 2.77 wt% Au + Pd loading.

Catalyst	**Cl (atom %)**	**Productivity / $mol_{H2O2}kg_{cat}^{-1}h^{-1}$**	**Hydrogenation / $mol_{H2O2}kg_{cat}^{-1}h^{-1}$**
0.50% Au - 2.27% Pd/TiO_2			
Calcined	**0.14**	62	313
Reduced + Calcined	**0.11**	58	461
1.18% Au - 1.31% Pd/C			
Calcined	**0.06**	21	69
Reduced + Calcined	**0.02**	19	33

Table 3.13 The effect of co-deposition precipitation of Au and Pd metals onto TiO_2 and carbon supports on the direct synthesis of hydrogen peroxide, comparing chloride content and reductive treatment on H_2O_2 synthesis and hydrogenation activities.

Similar metal loading is achieved for Au-Pd/C (2.49 wt% Au + Pd), however Au/Pd weight ratio on carbon is close to unity and both the H_2O_2 hydrogenation activity and chloride are significantly reduced (Table 3.13). Inclusion of a mild pre-reduction decreased the surface chloride content to 0.02 atom% indicating that even before optimisation of the deposition procedure the halide contribution can virtually be eliminated. The H_2O_2 productivities over Au-Pd/TiO_2 catalysts are approximately 3 times higher than observed for carbon-supported catalysts (19-21 $mol_{H2O2}kg_{cat}^{-1}h^{-1}$) but are accompanied by high H_2O_2 hydrogenation rates. Differences in the pH equilibria and rates of $HAuCl_4$ and $PdCl_2$ hydrolysis limit simultaneous control of metal loading and Au/Pd ratio in a single step, necessitating further optimisation including possibility of using combined preparations, *i.e.* for example DP-Impregnation as shown in Table 3.14.

Catalyst	Cl (atom %)	Productivity / $mol_{H2O2}kg_{cat}^{-1}h^{-1}$	Hydrogenation / $mol_{H2O2}kg_{cat}^{-1}h^{-1}$
0.72% Pd {0.72% Au}/TiO_2	**0.20**	46	227
1.37% Pd {1.37% Au}/C	**0.07**	44	70

Table 3.14 The effect of deposition precipitation of Au followed by impregnation of Pd onto TiO_2 and carbon supports on the direct synthesis of hydrogen peroxide, comparing chloride content and reductive treatment on H_2O_2 synthesis and hydrogenation activities.

The deposition precipitation method outlined in Figure 3.12 was used to deposit $[Au_x(OH)_{4-x}]^-$ species onto TiO_2 and carbon supports (100% Au uptake equating to a 2.5 wt% loading) and it can be seen in Table 3.14 that a higher proportion of Au was deposited onto carbon (1.37 wt% determined by SEM-EDX) at pH 10. After mild reduction of the Au-only catalyst, $Pd(NO_3)$ was introduced by impregnation and calcined in air (400 ^oC, 3 h) to give a calculated 1:1 by weight Pd[Au] loading, however, the final chloride content of both catalysts was not reduced to the extent achieved by co-deposition of Au-Pd (Tale 3.13). The rate of H_2O_2 production for Pd{Au}/C was improved relative to the co-deposited counterparts (44 compared to ~20 $mol_{H2O2}kg_{cat}^{-1}h^{-1}$), whereas Pd{Au}/$TiO_2$ was significantly less active than its co-deposited counterpart owing to lower Pd loading *via* deposition-impregnation.

Further improvements in H_2 selectivity are required so that catalysts can be used at higher temperatures and afford H_2 selectivity exceeding the current 70-80% achieved using standard batch operation at 2 ^oC. Pre-treatment of carbon in dilute acid[9] can increase the H_2 selectivity to >98%, however this effect to date is recognised only for Au-Pd/C catalysts (to be discussed in chapter 4). As a result continual interest exists in alternatives leading to improved selectivity and removal of residual chloride, especially for the development of in-situ/continuous processes utilising hydrogen peroxide as the oxidant including the selective epoxidation of propene to propene oxide.

3.9 Conclusion

In chapter 3, it was shown that for 5 wt% Au-Pd/TiO_2 catalysts prepared *via* wet impregnation, the addition of minimal amounts of water to form a catalyst slurry, which subsequently was not heated to form a thick, viscous gel (*i.e.* still contained 2 ml of H_2O) prior to drying and calcination steps, resulted in highly active H_2O_2 synthesis catalysts (*ca.* 120 $mol_{H2O2}kg_{cat}^{-1}h^{-1}$) of comparable activity to 5 wt% Au-Pd/C catalysts. The addition of more water (2-30 ml) during the wet impregnation step prior to drying dramatically altered the particle size distribution, with a modified bimodal distribution of Au and Pd nanoparticles comprising large Au-only particles (20-80 nm) and small Pd-only particles (1-10 nm) now observed for Au-Pd/TiO_2 catalysts. The larger, Au-only particles are ineffective in limiting H_2O_2 hydrogenation and consequently a reduced synergistic effect of Au is observed. And therefore the higher H_2O_2 synthesis and hydrogenation activities observed over Pd-only and Au-Pd catalysts prepared using this modified methodology are related to an enhanced Pd dispersion. Furthermore, TiO_2-supported catalysts prepared in this manner are neither stable nor fully reusable. However, catalysts prepared by wet-impregnation ensuring the removal of *ca.* 75% of the initial water present to form a viscous, gel consistency prior to drying, were both stable and fully reusable (and comprised intermediate, $Au_{core}Pd_{shell}$ alloyed nanoparticles).

Contrarily, for Au-Pd/C catalysts, addition of water during the catalyst impregnation step (*ca.* 2-30 ml) did not affect either structure or activity and these catalysts could be re-used without loss of catalyst performance. A major difference was established in the rate of Au and Pd uptake onto TiO_2 and carbon supports, with instant adsorption of Au and Pd precursors onto carbon irrespective of water addition/concentration, compared to negligible uptake onto TiO_2, which was determined as being influenced by surface iso-electric point. Additional experiments presented toward the close of chapter 3 confirm that reduced halide content/halide free catalysts can be synthesized using deposition precipitation routes and mild reduction treatments, leading to moderately active H_2O_2 synthesis and hydrogenation catalysts. A possible drawback with using deposition precipitation methodology to co-deposit $Au(OH)_3$ and $Pd(OH)_2$ species onto TiO_2 and carbon supports is that control over the fraction of each metal deposited onto a given support is limited, since $AuCl_4$ and $PdCl_2$ precursors are hydrolysed at different pH values and may deposit at different rates onto the support, with higher Pd content detected in the final catalysts.

3.10 References

1. D. I. Enache, J. K. Edwards, P. Landon, B. E. Solsona, A. F. Carley, A. A. Herzing, M. Watanabe, C. J. Kiely, D. W. Knight, G. J. Hutchings, *Science*, **2006**, 311, 362.
2. S. Meenakshisundaram, E. Nowicka, P. J. Miedziak, G. L. Brett, R. L. Jenkins, N. Dimitratos, S. H. Taylor, D. W. Knight, D. Bethell, G. J. Hutchings, *Faraday Discuss.*, **2010**, 145, 341.
3. G. L. Brett, P. J. Miedziak, N. Dimitratos, J. A. Lopez-Sanchez, N. F. Dummer, R. Tiruvalam, C. J. Kiely, D. W. Knight, S. H. Taylor, D. J. Morgan, A. F. Carley, G. J. Hutchings, *Catal. Sci. Tech.*, **2012**, 2, 97.
4. J. K. Edwards, G. J. Hutchings, *Angew. Chem. Int. Ed.*, **2008**, 47, 9192.
5. J. K. Edwards, B. E. Solsona, P. Landon, A. F. Carley, A. Herzing, C. J. Kiely, G. J. Hutchings, *J. Catal.*, **2005**, 236, 69.
6. J. K. Edwards, A. F. Carley, A. A. Herzing, C. J. Kiely, G. J. Hutchings, *Faraday Discuss.*, **2008**, 138, 225.
7. B. E. Solsona, J. K. Edwards, P. Landon, A. F. Carley, A. A. Herzing, C. J. Kiely, G. J. Hutchings, *Chem. Mater.*, **2006**, 18, 2689.
8. J. K. Edwards, B. Solsona, P. Landon, A. F. Carley, A. Herzing, M. Watanabe, C. J. Kiely, G. J. Hutchings, *J. Mater. Chem.*, **2005**, 15, 4595.
9. J. K. Edwards, B. Solsona, E. Ntainjua N, A. F. Carley, A. A. Herzing, C. J. Kiely and G. J. Hutchings, *Science*, **2009**, 323, 1037.
10. S. S. Kulkarni, G. R. Mauze, J. A. Schwarz, *J. Catal.*, **1981**, 69, 445.
11. K. J. A. Raj, B. Wiswanathan, *Indian. J. Chem.*, **2009**, 48, 1378.
12. T. Ishihara, Y. Hata, Y. Nomura, K. Kaneko, H. Matsumoto, *Chem. Lett.*, **2007**, 36, 7.
13. J. A. Lopez-Sanchez, N. Dimitratos, N. Glanville, L. Kesavan, C. Hammond, J. K. Edwards, A. F. Carley, C. J. Kiely, G. J. Hutchings, *App. Catal. A. Gen.*, **2011**, 391, 400.
14. L. Kesavan, R. Tiruvalam, M. H. Ab-Rahim, M. I. bin Saimon, D. I. Enache, R. L. Jenkins, N. Dimitratos, J. A. Lopez-Sanchez, D. W. Knight, S. H. Taylor, C. J. Kiely, G. J. Hutchings, *Science*, **2011**, 331, 195.
15. Q. Fu, W. Deng, H. Saltsburg, M. Flytzani-Stephanopoulos, *App. Catal. B. Env.*, **2005**, 56, 57.
16. W. Deng, J. de Jesus, H. Saltsburg, M. Flytzani-Stephanopoulos, *App. Catal. A. Gen.*, **2005**, 291, 126.

17. M. Manzoli, F. Boccuzzi, A. Chiorino, F. Vindigni, W. Deng, M. Flytzani-Stephanopoulos, *J. Catal.*, **2007**, 245, 308.
18. W. Deng, C. Carpenter, N. Yi, M. Flytzani-Stephanopoulos, *Top. Catal.*, **2007**, 44, 200.
19. W. Deng, A. I. Frenkel, R. Si, M. Flytzani-Stephanopoulos, *J. Phys. Chem. C.*, **2008**, 112, 12834.
20. Y. Guan, E. J. M. Hensen, *Phys. Chem. Chem. Phys.*, **2009**, 11, 9578.
21. M. C. Kung, R. J. Davis, H. H. Kung, *J. Phys. Chem. C.*, **2007**, 11, 11767.
22. J. A. Lopez-Sanchez, N. Dimitratos, P. J. Miedziak, E. Ntainjua N, J. K. Edwards, D. J. Morgan, A. F. Carley, R. C. Tiruvalam, C. J. Kiely and G. J. Hutchings, *Phys. Chem. Chem. Phys.*, **2008**, 10, 1921.
23. H. H. Kung, M. C. Kung, C. K. Costello, *J. Catal.*, **2003**, 216, 425.
24. M. Bowker, A. Nuhu, J. Soares, *Catalysis Today*, **2007**, 122, 245.
25. M. Haruta, *Catalysis Today*, **1997**, 36, 153.
26. M. Okumura, Y. Kitagawa, M. Haruta, K. Yamaguchi, *Chem. Phys. Lett.*, **2001**, 346, 163.
27. M. Haruta, M. Date, *App. Catal. A. Gen.*, **2011**, 222, 427.
28. K. Okazaki, S. Ichikawa, Y. Maeda, M. Haruta, M. Kohyama, *App. Catal. A. Gen.*, **2005**, 291, 45.
29. J. Yan. X. Zhang, T. Akita, M. Haruta, Q. Xu, *J. Am. Chem. Soc.*, **2010**, 132, 5326.
30. F. Menegazzo, M. Signoretto, M. Manzoli, F. Boccuzzi, G. Cruciani, F. Pinna, G. Strukul, *J. Catal.*, **2009**, 268, 122.
31. P. J. Miedziak, Q. He, J. K. Edwards, S. H. Talyor, D. W. Knight, B. Tarbit, C. J. Kiely, G. J. Hutchings, *Catalysis Today*, **2011**, 163, 47.
32. P. J. Miedziak, M. Sankar, N. Dimitratos, J. A. Lopez-Sanchez, A. F. Carley, D. W. Knight, S. H. Taylor, C. J. Kiely, G. J. Hutchings, *Catalysis Today*, **2011**, 164, 315.
33. J. K. Edwards, J. C. Pritchard, M. Piccinini, G. Shaw, Q. He, A. F. Carley, G. J. Hutchings, *J. Catal.*, **2012**, 292, 227.
34. J. K. Edwards, A. Thomas, A. F. Carley, A. A. Herzing, C. J. Kiely, G. J. Hutchings, *Green. Chem.*, **2008**, 10, 388.
35. E. Ntainjua. N, M. Piccinini, J. C. Pritchard, Q. He, J. K. Edwards, A. F. Carley, J. A. Moulijn, C. J. Kiely, G. J. Hutchings, *ChemCatChem*, **2009**, 1, 1.
36. C. Baatz, N. Decker, U. Pruze, *J. Catal.*, **2008**, 258, 165.

37. S. Meenakshisundaram, Q. He, M. Morad, J. C. Pritchard, S. J. Freakley, J. K. Edwards, S. H. Taylor, D. J. Morgan, A. F. Carley, D. W. Knight, *ACS Nano*, **2012**, 6, 6600.
38. M. Haruta, N. Yamada, T. Kobayashi, S. Iijima, *J. Catal.*, **1989**, 115, 301.
39. M. Haruta, T. Kobayashi, H. Sano, N. Yamada, *Chem. Lett.*, **1987**, 16, 408.
40. G. C. Bond, M. A. Keane, H. Kral, J. A. Lercher, *Catal. Rev. Sci. Eng.*, **2000**, 42, 323.
41. G. C Bond, D. T. Thompson, *Catal. Rev. Sci. Eng.*, **1999**, 41, 319.
42. A. S. K. Hashmi, G. J. Hutchings, *Angew. Int. Chem. Ed.*, **2006**, 45, 7896.
43. F. Moreau, G. C. Bond, *Catal. Comm.*, **2007**, 8, 1403.
44. R. Zanella, C. Louis, *Catalysis Today*, **2005**, 107, 768.
45. R. Zanella, L. Delannoy, C. Louis, *App. Catal. A. Gen.*, **2005**, 291, 62.
46. R. Zanella, C. Louis, S. Giorgio, R. Touroude, *J. Catal*., **2004**, 223, 328.
47. F. Moreau, G. C. Bond, *Catalysis Today*, **2007**, 8, 1403.

Chapter 4

4.1 Introduction

Treatment of an activated carbon support in dilute nitric acid prior to the impregnation of Au and Pd metals and calcination in static air are necessary steps leading to the formation of a stable and highly active, supported Au-Pd catalyst in which the non-selective hydrogenation of H_2O_2 to H_2O is switched-off[1]. Application of this method to TiO_2 and SiO_2 supports[2, 3] also improved the rate of H_2O_2 synthesis over supported Au-Pd catalysts and considerably reduced the rate of hydrogenation, but did not switch-off the hydrogenation pathway as observed for 2.5 wt% Au-2.5 wt% Pd/C. This effect is solely observed for bimetallic Au-Pd catalysts. Monometallic Au catalysts are poorly active for the direct synthesis reaction irrespective of acid pre-treatment, while minimal to no differences are recognised for monometallic Pd catalysts for either H_2O_2 synthesis or hydrogenation pathways, as illustrated in Table 4.1.

Catalyst	**Productivity / $mol_{H2O2}kg_{cat}^{-1}h^{-1}$**	**Hydrogenation / $mol_{H2O2}kg_{cat}^{-1}h^{-1}$**
5 wt% Au/C		
Non-acid treated	1	0
Acid treated	1	0
5 wt% Pd/C		
Non-acid treated	55	135
Acid treated	60	126

Table 4.1 H_2O_2 synthesis and hydrogenation activities for 5 wt% Au and Pd catalysts supported on non-acid treated and 2 vol% nitric acid treated carbons. All Catalysts were calcined in static air at 400 ^oC (3 h).

In order to preserve catalytic activity over repeated H_2O_2 synthesis reactions using supported Au-Pd catalysts, a calcination step performed in static air at 400 ^oC is required to stabilise active sites dispersed across the support material[4]. The rates of hydrogen peroxide production and hydrogenation over dried-only materials and of those calcined at temperatures below 400 ^oC are typically very high, falling sharply with increasing calcination temperature, and are unstable due to deactivation and leaching of active metal into solution. As already discussed in chapter 3, variation in the wet impregnation method can impart a dramatic effect on both catalyst activity and stability and therefore careful control at every stage of the catalyst preparation procedure must be followed[5].

The aim of chapter 4 is to improve the understanding of the role of the heat treatment in the preparation of non-acid treated and acid treated 2.5 wt% Au-2.5 wt% Pd/C catalysts and to identity possible differences in catalyst structure that may constitute deactivation of the H_2O_2 hydrogenation pathway. Characterisation of carbon supports prior to the impregnation of Au and Pd metals, and for 2.5 wt% Au-2.5 wt% Pd/C catalysts calcined in static air at 200, 300 and 400 ^oC has been undertaken using a range of characterisation techniques to probe change(s) in the bulk and surface structure initiated by acid pre-treatment (Figure 4.1). Experiments comparing the effect of different heat treatment conditions on the structure and activity of catalysts are presented and discussed with a proposed mechanism.

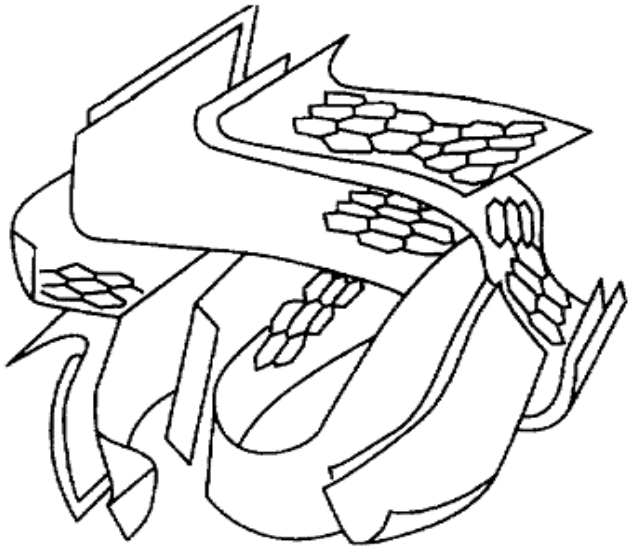

Figure 4.1 Schematic of the structure of activated carbon showing planes of graphitic structures overlapping and in-between plane space corresponding to micro porous features[6].

4.1.1 Experimental Conditions

The reaction conditions adopted in Chapter 4, unless stated otherwise are:

(a) Hydrogen Peroxide Synthesis catalyst (10 mg), 5% H_2/CO_2 (420 psi), 25% O_2/CO_2 (160 psi), 5.6 g MeOH and 2.9 g H_2O as solvent, 2 ^oC, 30 minutes.

(b) Hydrogen Peroxide Hydrogenation catalyst (10 mg), 5% H_2/CO_2 (420 psi), 5.6 g MeOH, 2.22 g H_2O and 0.68 g 50 wt% H_2O_2 as solvent, 2 ^oC, 30 minutes.

Important Note: In this chapter we have primarily investigated the effect of pre-treating a carbon support (G60 activated carbon supplied by Darco) in dilute, 2 vol% nitric acid, prior to impregnation of Au and Pd precursors and calcination in static to air. Bimetallic 2.5 wt% Au-2.5 wt% Pd catalysts supported on non-acid treated/acid treated G60 carbon are referrred to throughout this chapter as: **non-acid treated Au-Pd/C**, while catalysts supported on 2 vol% nitric acid treated carbon are referred to throughout this chapter as: **acid treated Au-Pd/C.**

Experiments comparing other other acid pre-treatments are presented in this chapter, for examaple acetic acid, and this is mentioned in the main text where necessary, i.e. **acetic acid treated Au-Pd/C**, to prevent confusion with terminology for nitric acid pre-treated samples. Characterisation of carbon supports (before Au-Pd impregnation) and 2.5 wt% Au-2.5 wt% Pd/C catalysts are presented separately in sections 4.2 and 4.4 respectively, while catalyst testing data is presenting in section 4.3.

4.2 Characterisation of the carbon support

In an effort to determine the origin of the different activities observed for Au-Pd/C catalysts based on pre-treatment of the carbon support in 2 vol% nitric acid, both non-acid treated and acid treated carbon supports were studied by XPS. The C(1s) and O(1s) spectra recorded before and after Thermo-gravimetric analysis (TGA) in nitrogen (in order to remove any physisorbed species retained after washing and drying of support, *e.g.* water) are presented in Figure 4.2, and interestingly show no major differences between non-acid treated and acid treated carbons, implying that acid pre-treatment of carbon has not modified support structure through the development of new functional groups. Comparison of TGA profiles recorded for non-acid treated and acid treated carbons (Appendix A4.1) showed despite extended oven drying (110 ^{o}C, 58 h) that approximately 3% by mass was evolved from both carbon supports on heating to 350 ^{o}C, which was likened to the removal of physisorbed water molecules from pores of activated carbon.

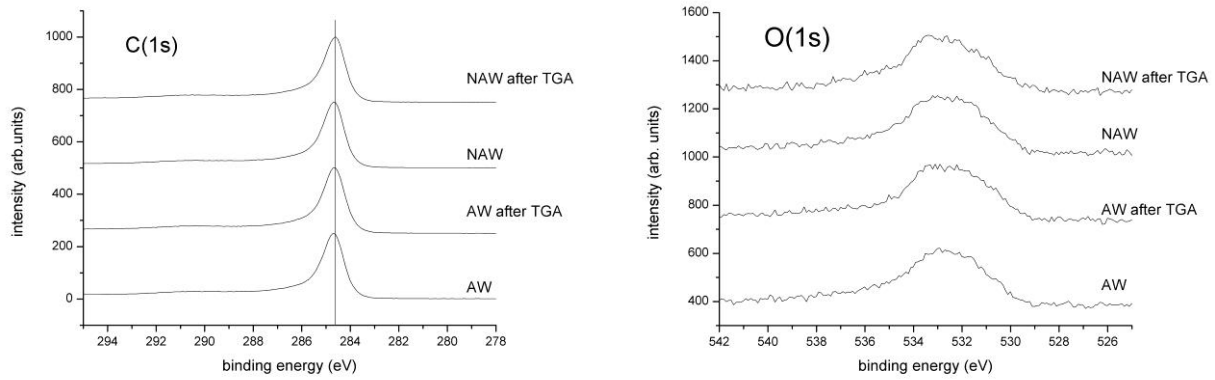

Figure 4.2 C(1s) and O(1s) XP spectra observed for non-acid treated/washed (NAW) and acid treated/washed (AW) carbon supports before and after thermo-gravimetric analysis under nitrogen atmosphere.

FTIR-ATR corrected spectra recorded for carbon materials before and after treatment with 2 vol% nitric and acetic acids respectively are presented in Figure 4.3. Comparison of the non-acid treated and nitric acid treated carbons showed a small increase in the carbonyl absorption region that is attributed to the carbonyl group in CH_3COOH and identified also on acetic acid treated carbon. Edwards *et al.* showed that changing the concentration of nitric acid pre-treatment (from 0.5 to 70 vol%) did not affect the rate of H_2O_2 hydrogenation over 2.5 wt% Au-2.5 wt% Pd/C catalysts (i.e. the hydrogenation was always completely suppressed),

implying that quantification of specific functional group content does not serve as the absolute indicator as to why acid pre-treatment is effective[1, 3]. A possible reason for this is that only a minor modification of the activated carbon structure is required after which concentration, time and temperature are ineffective. This point will be discussed further in sections 4.4 and 4.6 with respect to XPS and STEM-HAADF characterisation of catalysts.

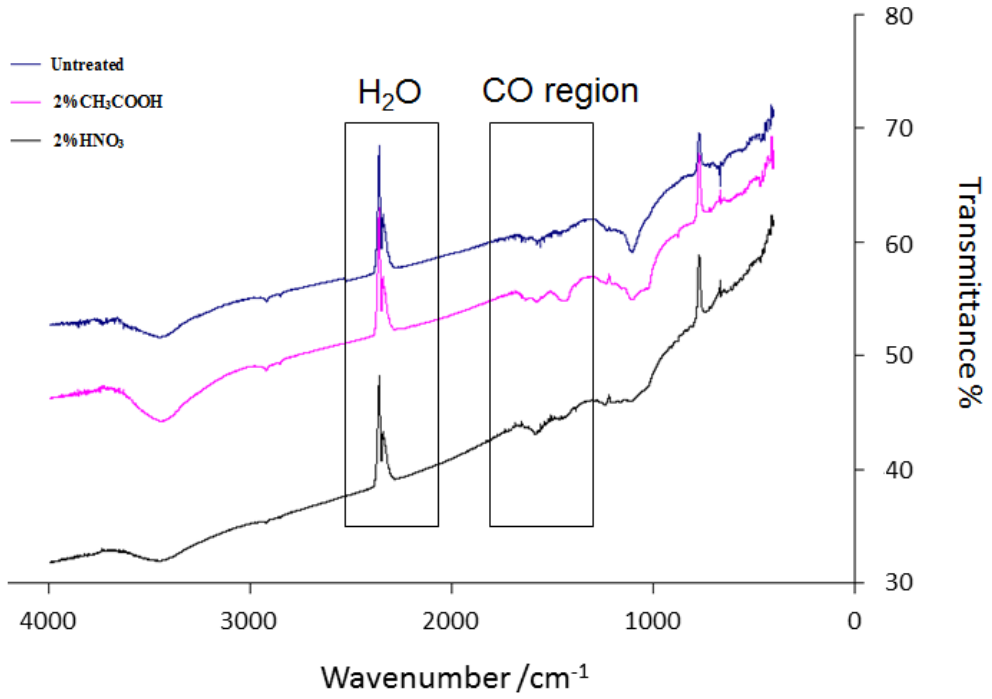

Figure 4.3 FTIR-ATR corrected spectra for carbon supports, non-acid treated (blue), 2% HNO_3 pre-treated (black) and 2% CH_3COOH treated (pink) respectively.

TPD profiles of non-acid treated and 2% HNO_3 treated carbons show differences in surface oxygen content related to CO_2 desorption (Figure 4.4). A 40 mV increase in the TCD signal at ~180 ^oC for 2% HNO_3 pre-treated carbon (blue) indicates an increase in the number of carboxylic acid groups[7-10] attached to the carbon, while a broad signal from 240-350 ^oC implies a further increase in the number of carboxylic functional groups[10]. A smaller response signal is detected in the same region for non-acid treated carbon (black), showing that a baseline number of functional groups are present on carbon, present due to the activation step employed by the manufacturer[11].

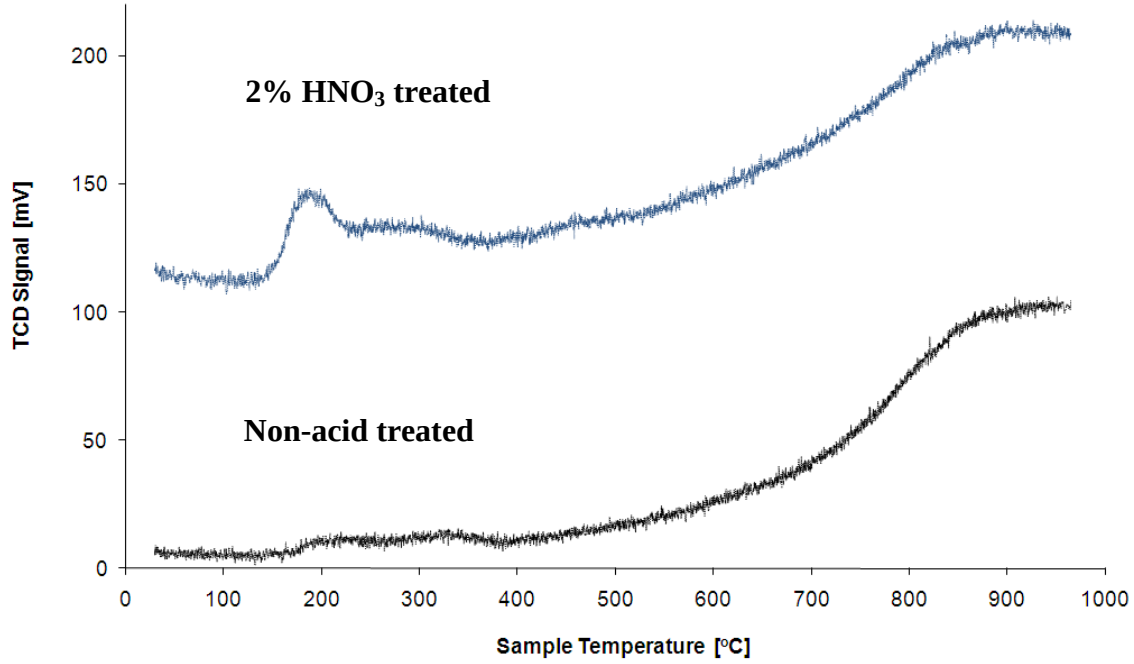

Figure 4.4 Temperature programmed desorption profiles for 2% HNO_3 treated (blue line) and non-acid treated (black line) carbon supports only.

In both profiles shown in Figure 4.4, the TPD signal increases from 400 to 700 ^{o}C and is consistent with high temperature functionalities on carbon derived from decomposition of carboxylic anhydrides, lactones and ether groups, all of which are known to decompose at elevated temperatures[7-10]. Differences in the signal gradient between supports are observed, with non-acid treated carbon (blue) showing a steeper signal variation from 700-850 ^{o}C.

Decomposition of carboxylic anhydrides and their subsequent interpretation can become convoluted as the temperature range attributed to on-set of CO desorption may overlap with the desorption of CO_2 derived from decomposition of carbonyl/carboxylic units, and therefore any increase(s) in the TCD signal at higher temperature could represent a CO/CO_2 composite. Overall, the TCD signals recorded from 400 to 950 ^{o}C for non-acid treated and acid treated carbons increased by 80 and 91 mV respectively, the difference of which is attributed to a small increase in functional group content on the acid treated carbon.

Nitrogen adsorption/desorption isotherms for non-acid treated and acid treated carbons were recorded and subsequently compared. Both the adsorption isotherms and BET surfaces areas of each support were found to be identical within experimental error (approximately 1000 m^2/g quoted to an accuracy of ± 10%). The BJH pore size distribution measurements shown in Figure 4.5 for non-acid treated and acid treated carbons in addition were determined as near identical and confirmed a mesoporous structure.

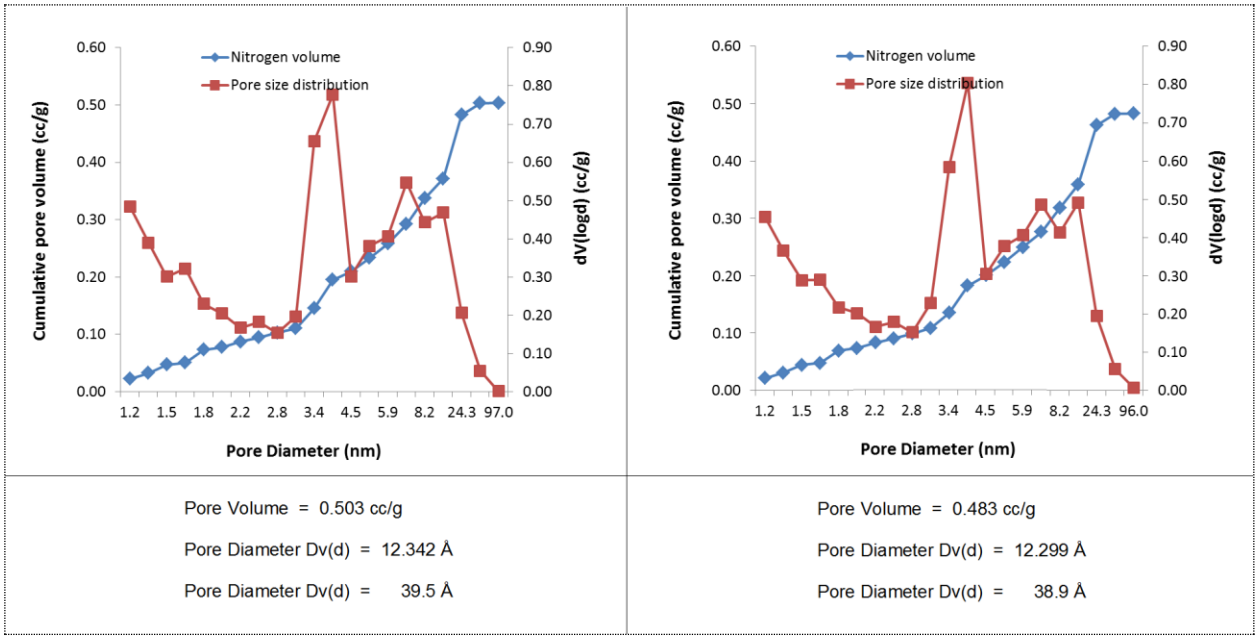

Figure 4.5 BJH Distrubtion Plots for non-acid treated (left) and acid treated (right) carbon supports with pore volume and diameter measurements summarised underneath. BET surface areas for carbon were determined as 1011 m^2/g (non-acid treated) and 955 m^2/g (acid treated).

From the techniques used in section 4.2 to characterise possible differences between non-acid and acid treated carbons, it is apparent that no specific chemical differences result from pre-treatment of carbon in 2 vol% nitric acid, as noted in C(1s) and O(1s) spectra respectively. In contrast, an enhancement in the concentration of functional groups initially present on non-acid treated carbon, specifically carboxylic acid groups (originating from the activation process employed by Darco) is implied in FT-IR ATR corrected spectra and TPD profiles respectively. Changes in surface area and pore size distribution is also considered, however, due to the high surface areas associated with activated carbons and similarities in pore size distributions between samples, both of which are mesoporous, it is difficult to conclude whether actual changes have occurred.

4.3 Effect of acid pre-treatment on the direct synthesis of H_2O_2

The variation in the rate of H_2O_2 production with calcination temperature for acid treated 2.5 wt% Au-2.5 wt% Pd/C catalysts followed a trend similar to that reported for TiO_2-supported counterparts[5], with the dried-only sample exhibiting the highest H_2O_2 productivity (212 $mol_{H2O2}kg_{cat}^{-1}h^{-1}$), which subsequently decreased on second use by over 50% to 101 $mol_{H2O2}kg_{cat}^{-1}h^{-1}$, and was attributed to insufficient catalyst stability in the absence of adequate heat treatment (Table 4.2). While H_2O_2 productivity declined further on increasing the calcination temperature, catalysts retained more than 50% of their initial activity on their second use, suggesting an improvement in the degree of stability until calcination at 400 ^oC formed a stable, highly active material (160 $mol_{H2O2}kg_{cat}^{-1}h^{-1}$ – an activity that is maintained beyond 10 x H_2O_2 synthesis reactions).

Heat Treatment	**Productivity / $mol_{H2O2}kg_{cat}^{-1}h^{-1}$**		**Hydrogenation / $mol_{H2O2}kg_{cat}^{-1}h^{-1}$**
	1st Use	**2nd Use**	
Dried 120 °C	212	101	736
Calcined 200 °C	180	106	617
Calcined 300 °C	174	124	546
Calcined 400 °C	160	160	0

Table 4.2 H_2O_2 synthesis and hydrogenation activities over 2.5 wt% Au-2.5 wt% Pd/C catalysts (2% HNO_3 pre-treated). Catalysts dried in air 110 ^oC and calcined for 3 h in static air as indicated.

The H_2O_2 hydrogenation rate over the catalysts was also found to be affected by the calcination temperature, with the dried-only material exhibiting the highest rate of H_2O_2 hydrogenation (736 $mol_{H2O2}kg_{cat}^{-1}h^{-1}$), corresponding to a 36% consumption of the initial 4 wt% H_2O_2 present in solution. Increasing the calcination temperature decreased the rate of hydrogenation so that by 400 ^oC, hydrogenation activity over the catalyst was switched-off. This implies that different sites on the Au-Pd/C catalyst surface are responsible for the synthesis and hydrogenation of hydrogen peroxide reactions, and secondly that these sites are affected to different extents by calcination temperature, *i.e.* the rate of H_2O_2 hydrogenation

remains elevated until 300 ^{o}C before decreasing dramatically thereafter. In response, a portion of the dried-only material was calcined at 350 ^{o}C, and was still found to hydrogenate a considerable fraction of H_2O_2 (279 $mol_{H2O2}kg_{cat}^{-1}h^{-1}$). It is known that the melting point of Au decreases as particle size gets progressively smaller and therefore this could aid in the understanding as to why the activity of the H_2O_2 hydrogenation pathway is switched-off over a narrow temperature range (>350-400 ^{o}C).

Heat Treatment	**Productivity / $mol_{H2O2}kg_{cat}^{-1}h^{-1}$**		**Hydrogenation / $mol_{H2O2}kg_{cat}^{-1}h^{-1}$**
	1st Use	**2nd Use**	
Dried 120 °C	120	79	729
Calcined 200 °C	120	105	707
Calcined 300 °C	130	108	499
Calcined 400 °C	110	110	120

Table 4.3 H_2O_2 synthesis and hydrogenation activities over 2.5 wt% Au-2.5 wt% Pd/C catalysts (non-acid treated). Catalysts dried in air 110 ^{o}C and then calcined for 3 h in static air as indicated.

The same calcination series was investigated for 2.5 wt% Au-2.5 wt% Pd supported on non-acid treated carbon, and H_2O_2 production and hydrogenation rates are shown in Table 4.3. It is clear that the non-acid treated 2.5 wt% Au-2.5 wt% Pd/C catalyst does hydrogenate hydrogen peroxide after calcination at 400 ^{o}C and gives a H_2O_2 productivity (110 $mol_{H2O2}kg_{cat}^{-1}h^{-1}$) that is approximately 35% less than its acid treated counterpart. However, in the absence of pre-treatment, the catalyst does not appear as sensitive toward calcination temperature. The productivity of the dried-only catalyst is 120 $mol_{H2O2}kg_{cat}^{-1}h^{-1}$, and thus only marginally higher than the productivity of the 400 ^{o}C calcined catalyst. The dried-only and calcined 200 and 300 ^{o}C catalysts were shown to retain a higher proportion of their original activity on second use, while initial rate measurements at 2 min concluded that the dried-only Au-Pd/C catalyst was the most active material, followed in descending order by catalysts calcined at 200, 300 and 400 ^{o}C (Figure 4.6).

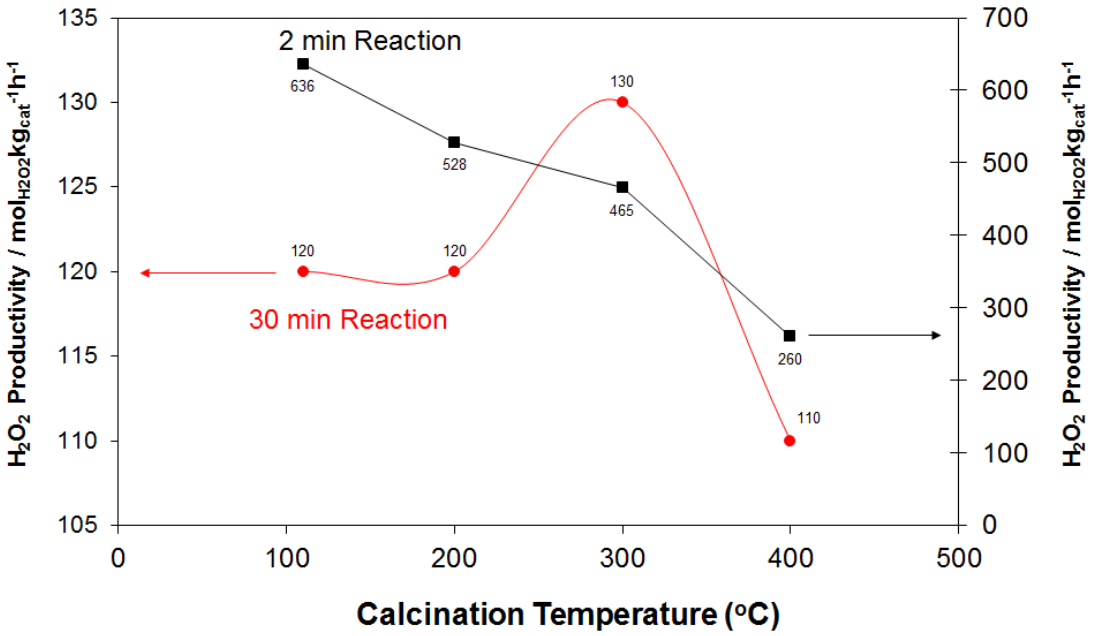

Figure 4.6 Effect of reaction time on the H_2O_2 synthesis and hydrogenation activities over 2.5 wt% Au-2.5 wt% Pd/C catalysts (non-acid treated). Catalysts dried in air 110 ^{o}C and calcined for 3 h in static air as indicated (except the dried-only Au-Pd/C catalyst, which for the purpose of the graph is plotted on the horizontal axis as calcined 110 ^{o}C)

Since three out of four of the Au-Pd/C catalysts (dried-only, calcined 200 and 300 ^{o}C) are unstable and that initial rates were measured after 2 minutes, the leaching of Au and Pd precursors could initiate the homogenous catalysed production of H_2O_2, explaining why the dried-only/uncalcined catalyst is the most active material in addition to electronic and particle size effects. Once again, calcination at 400 ^{o}C is required to form a stable and reusable catalyst. While rates of H_2O_2 hydrogenation over non-acid treated Au-Pd/C catalysts are comparable to those observed over acid treated Au-Pd/C up to calcination temperatures of 300 ^{o}C, the key difference is that H_2O_2 hydrogenation over non-acid treated Au-Pd/C calcined at 400 ^{o}C is moderate (120 $mol_{H2O2}kg_{cat}^{-1}h^{-1}$) as oppose to being switched-off. In section 4.4, the influence of acid pre-treatment and calcination temperature on alloying, oxidation state and particle size distribution for Au-Pd/C catalysts has been investigated using X-ray photoelectron spectroscopy and detailed microscopy (STEM-HAADF, XEDS).

4.4 Characterisation of the carbon-supported Au-Pd catalysts

4.4.1 Electron Microscopy characterisation

The structure of Au and Pd on activated carbon as a function of calcination temperature for fresh, unused catalysts was probed using detailed scanning transmission electron microscopy techniques. Bright field TEM micrographs of acid treated Au-Pd/C catalysts both dried at 120 ^{o}C and calcined at 400 ^{o}C samples are presented in Figure 4.7 (calcined 200 and 300 °C are shown in Appendix A4.2) and show occasional metallic particles exist in the 30-100 nm range on the support irrespective of calcination temperature. X-ray dispersive energy spectra (XEDS) concluded that larger metallic particles consisted predominantly of Au, while areas without any 'large' particles comprised solely of Pd, implying the presence of highly dispersed species on activated carbon that cannot be observed via conventional BF-TEM imaging.

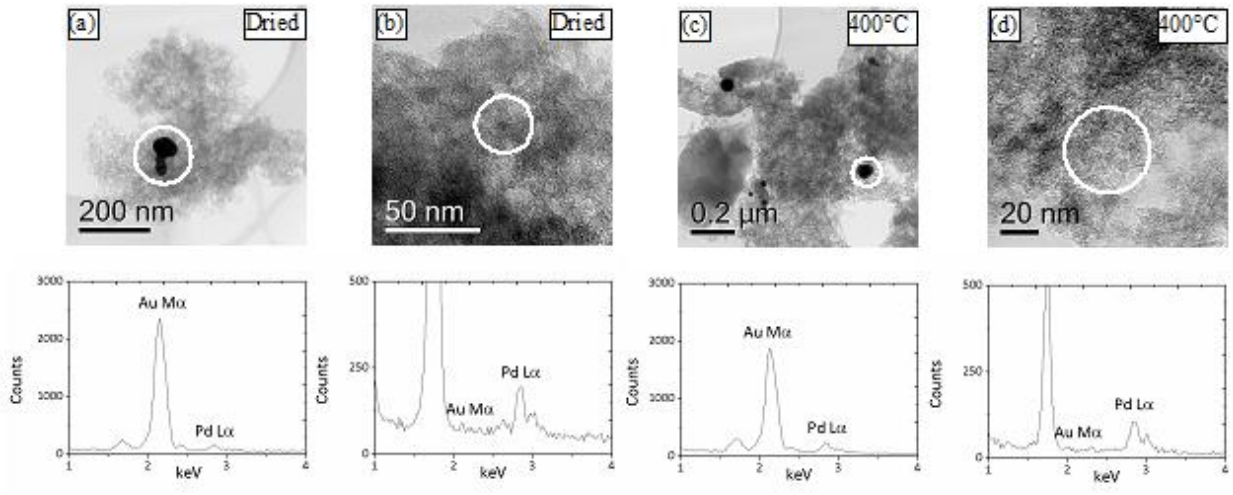

Figure 4.7 XEDS spectra of acid treated 2.5 wt% Au-2.5 wt% Pd/C catalysts, **(a, b)** dried 120 ^{o}C, and **(c, d)** calcined at 400 °C. Data acquired inside the regions marked by white circles.

The catalyst nanostructure was further investigated using STEM-HAADF imaging. Figure 4.8 indeed shows highly dispersed Pd metal species exist for acid treated Au-Pd/C, with sub-nm clusters and single atoms present on the carbon surface in all samples, the population of sub-nm clusters of which progressively decreases at higher calcinations temperatures, suggesting the calcination process is assisting in dispersing the sub-nm clusters into atomically dispersed species, although differences between the morphology of samples with different calcination temperatures are subtle and do not exceed the instrument detection limit.

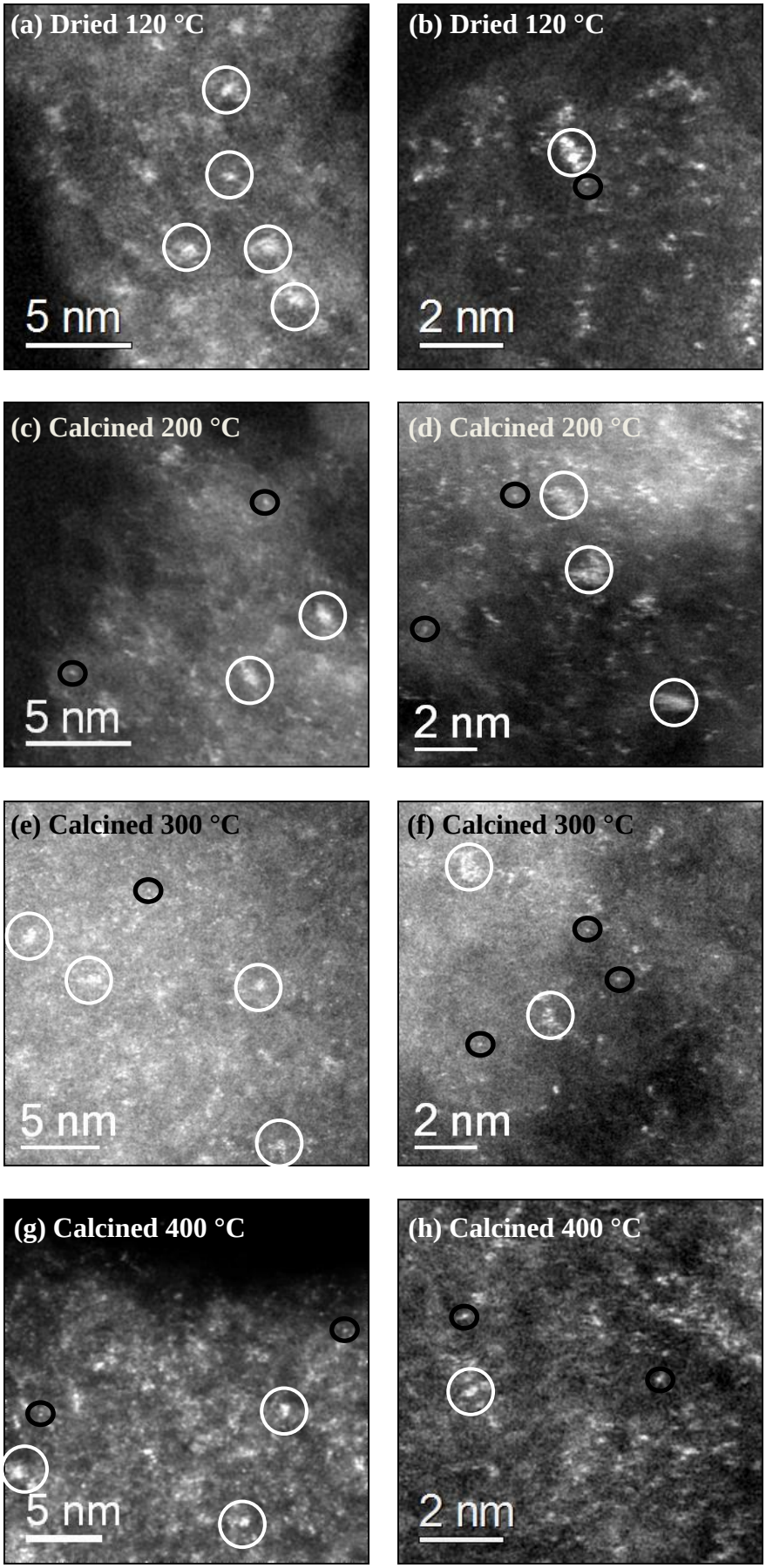

Figure 4.8 Representative STEM-HAADF images of acid treated Au-Pd/C catalysts calcined at different temperatures.

(a, b) Dried 120 °C
(c, d) Calcined 200 °C
(e, f) Calcined 300 °C
(g, h) Calcined 400 ^{o}C

There are two types of highly dispersed metal species, namely sub-nm clusters (circled in white) and isolated atoms (circled in black); of which the number of sub-nm clusters appears to decrease on increasing the calcination temperature.

Representative STEM-HAADF images for the non-acid treated Au-Pd/C catalyst series in Figure 4.9 are structurally similar to their acid treated counterparts (Figure 4.8) in addition to the population density of sub-nm species again showing an inverse dependency with calcination temperature, indicating that catalyst morphology and metal dispersion are not substantially influenced, if at all, through acid treating the carbon support.

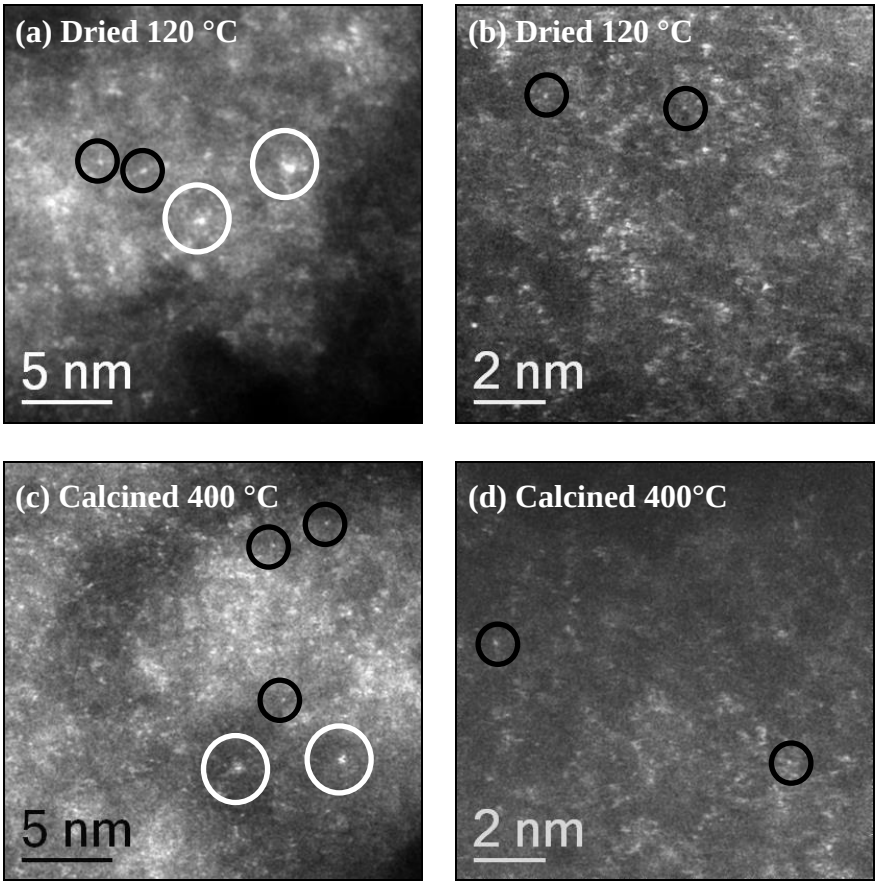

Figure 4.9 STEM-HAADF images of non-acid treated Au-Pd/C catalysts calcined at different temperatures, **(a, b)** dried 120 °C, and **(c, d)** calcined 400 °C. Sub-nm clusters (circled in white) and isolated atoms (circled in black) are shown in both samples. The morphologies are very similar to their acid treated Au-Pd/C counterparts.

In Figures 4.10 and 4.11, STEM-HAADF images of monometallic Au/C and Pd/C catalysts (all calcined at 400 °C) respectively are presented, serving as a baseline comparison to the aberration corrected microscopy investigation into highly dispersed species already detected for the Au-Pd/C samples. Firstly for the Pd/C sample, in addition to occasional nanoparticles observed in the bright field region, sub-nm clusters and isolated Pd atoms were detected in both non-acid treated and acid treated samples and of similar density to species found in their respective bimetallic counterparts.

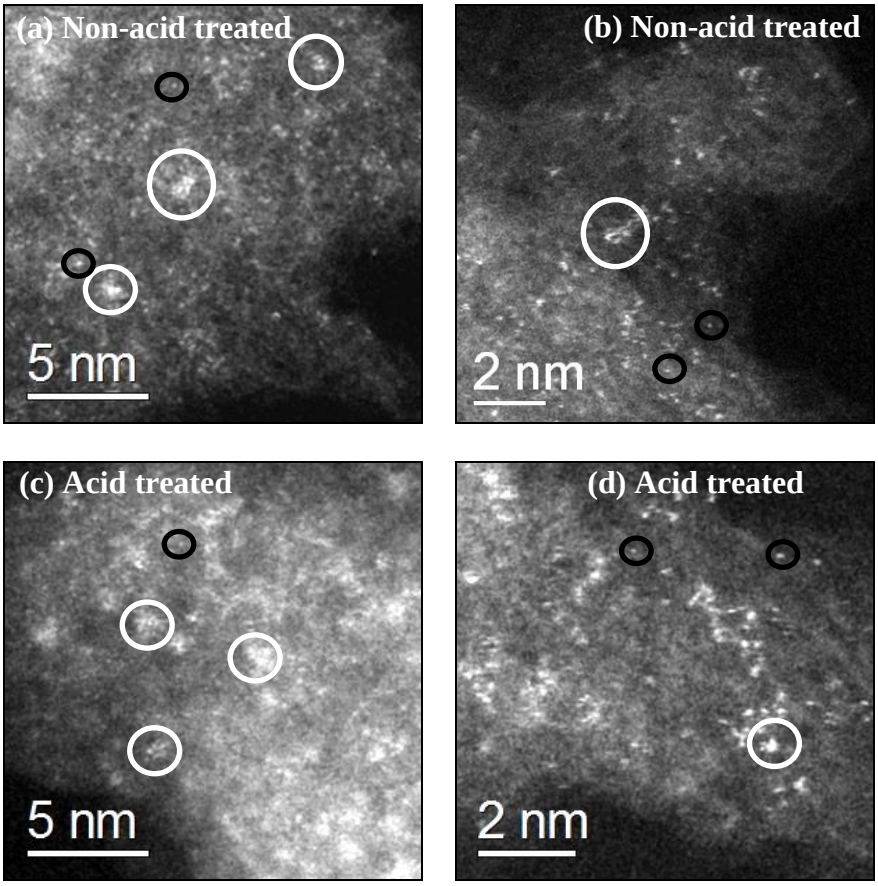

Figure 4.10 STEM-HAADF images of monometallic Pd/C catalysts calcined at 400 °C, both non-acid treated **(a, b),** and acid treated **(c, d)**. Sub-nm Pd clusters (circled in white) and isolated Pd atoms (circled in black) were identified, and their population densities are similar to those noted for their bimetallic Au-Pd/C counterparts.

On inspecting the Au/C sample, nanoparticles and a small fraction of isolated Au atoms (of lower number density than observed in Au-Pd samples) were found, unfortunately the chemical identity of the sub-nm species and isolated atoms in bimetallic Au-Pd/C catalysts cannot be directly determined using atomic level Z-contrast measurements due to the rough nature of the support, resulting in complicating height variations between neighbouring metallic species. Examination of the monometallic samples can however give some insight as to what is probably happening in the bimetallic Au-Pd/C system, microscopy shows that Pd tends to be more highly dispersed when preparing catalysts using the impregnation methodology, but that there is most likely a very dilute concentration of atomically dispersed Au atoms intermixed within the atomically dispersed Pd species in the bimetallic system.

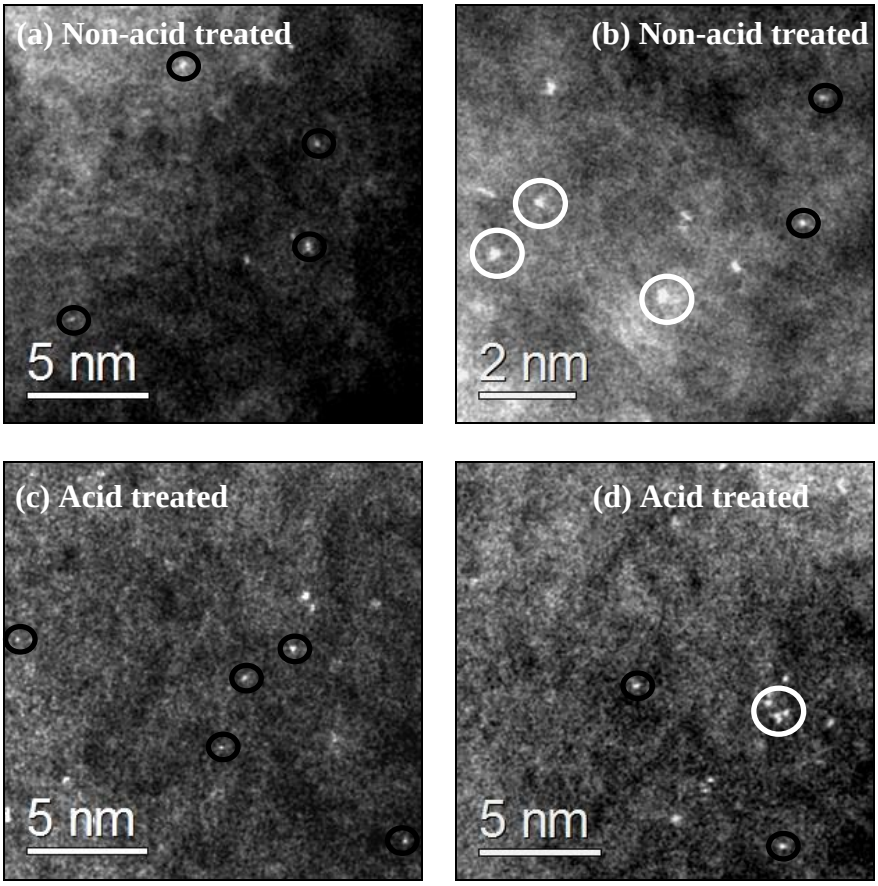

Figure 4.11 STEM-HAADF images of monometallic Au/C catalysts calcined at 400 °C, both non-acid treated **(e, f)** and acid treated **(g, h)**. For these Au/C samples, only a low density of high intensity isolated Au atoms were found in addition to the much larger gold nanoparticles.

Aberration corrected electron microscopy in summary shows that both non-acid treated and acid-treated Au-Pd/C samples calcined at 400 °C consist of Au-rich nanoparticles and a highly dispersed coverage of atomic and cluster-like Pd species, intermixed with a small amount of atomically dispersed Au. The heat treatment appears to improve the overall metal dispersion, although acid pre-treatment of the support does not seem to affect the catalyst morphology or the dispersion of metallic species, suggesting the improvement in activity for acid treated Au-Pd/C samples could instead be induced by changes in metal oxidation state and residual species (*i.e.* chloride) and therefore catalysts have been studied using X-ray photoelectron spectroscopy in section 4.4.2.

4.4.2 X-Ray Photoelectron Spectroscopy

Au-Pd catalysts supported on non-acid treated and acid treated carbon were analysed by XPS to assess the impact of calcination temperature on surface structure and state. Pd(3d) spectra for both supports are presented in Figure 4.12.

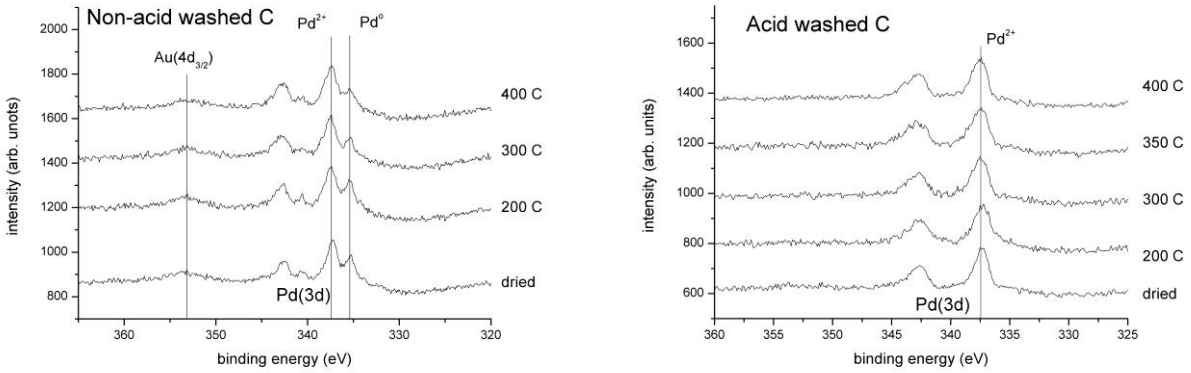

Figure 4.12 Pd(3d) spectra observed for the 2.5 wt% Au-2.5 wt% Pd catalysts supported on non-acid treated carbon and calcined at the temperatures indicated.

Both Pd^{2+} and Pd^{o} species are present for catalysts prepared on the non-acid treated support, for which the ratio changes little on increasing calcination temperature (Table 4.4). Interestingly, catalysts prepared on the acid treated support predominantly consisted of Pd^{2+} species in excess of 90% at each calcination temperature. However, reference to catalytic data for Au-Pd catalysts calcined at temperatures below 400 ^{o}C shows a decrease in H_2O_2 synthesis activity on second use - corresponding XPS data (Table 4.5) reveals a transformation of Pd^{2+}

into metallic Pd that is more pronounced for the dried-only material. The intensity of Pd(3d) signal is markedly decreased too indicated leaching of metal from the carbon surface.

Molar ratios	**Pd/Au**	**(Pd+Au)/C (x100)**	**Cl/C (x100)**	**Pd^{2+}(%)**
Non-acid treated				
Dried 120 ^{o}C	1.0	0.70	0.61	60
200 ^{o}C	1.1	0.66	0.51	57
300 ^{o}C	1.3	0.61	0.50	69
400 ^{o}C	1.4	0.63	0.44	68
Acid treated				
Dried 120 ^{o}C	2.7	0.44	0.71	>90
200 ^{o}C	3.8	0.45	0.61	>90
300 ^{o}C	4.3	0.46	0.51	>90
350 ^{o}C	4.1	0.41	0.44	>90
400 ^{o}C	4.2	0.50	0.42	>90

Table 4.4 Quantified XP data for the 2.5 wt% Au-2.5 wt% Pd/C catalysts, data are included for the both the non-acid treated and acid-treated supports.

Pd^{2+}(%)	**Calcination Temperature**			
	Dried 120 ^{o}C	**200 ^{o}C**	**300 ^{o}C**	**400 ^{o}C**
Fresh	>90	>90	>90	>90
Used x 1	16	35	43	>90

Table 4.5 Quantified XP data for acid treated 2.5 wt% Au-2.5 wt% Pd/C catalysts comparing the surface Pd^{2+} concentration in fresh and used catalysts (1 x H_2O_2 synthesis reaction).

Referring to quantified XPS data in Table 4.4, a clear difference in Pd/Au ratio can be observed between carbon supports. Catalysts prepared on the non-acid treated carbon support exhibit a low Pd/Au ratio that is relatively constant as a function of calcination temperature, having a value in the range 1.0-1.4. The molar ratio for a nominal 2.5 wt% Au-2.5 wt% Pd loading is 1:1.85 proving that Au-Pd nanoparticles are homogeneous alloys in nature. Contrarily a significant increase in the Pd/Au ratio with calcination temperature is apparent for catalysts prepared on the acid treated carbon that could reflect the formation of core-shell type particles. The variation in Pd^{2+}/Pd^{0} ratio and suggested core-shell formation does not affect the Au oxidation state in bimetallic samples, which is metallic for all samples (Figure 4.13).

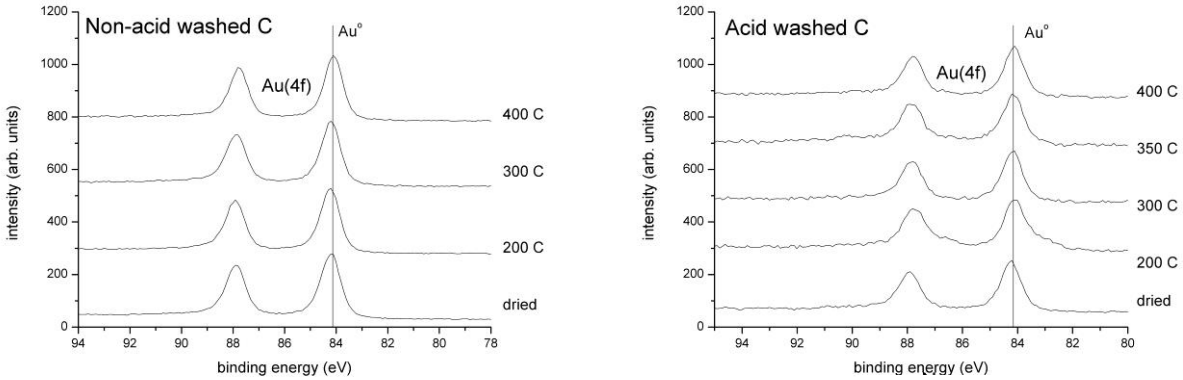

Figure 4.13 Au(4f) spectra observed for the 2.5 wt% Au-2.5 wt% Pd catalysts supported on non-acid treated carbon and calcined at the temperatures indicated.

Comparison of Cl(2p) spectra for non-acid and acid treated supports show several doublets are present, Cl(2p) spectra from non-acid treated samples consist of two (spin-orbit) 2p doublets, the relative intensities changing with calcination temperature while three (spin-orbit) 2p doublets are recognised in the spectra for acid treated samples, implying the presence of different species and concentrations of surface chloride[10]. For both supports, calcination at 400 ^{o}C leads to the doublet at higher binding energies dominating, which is attributed to a highly ionic and negatively charged chloride species. On the following page, quantified curve-fitted data is presented in Table 4.6, corresponding to the Cl(2p) XP spectra of both non-acid treated and acid treated Au-Pd/C catalysts shown in Figure 4.14.

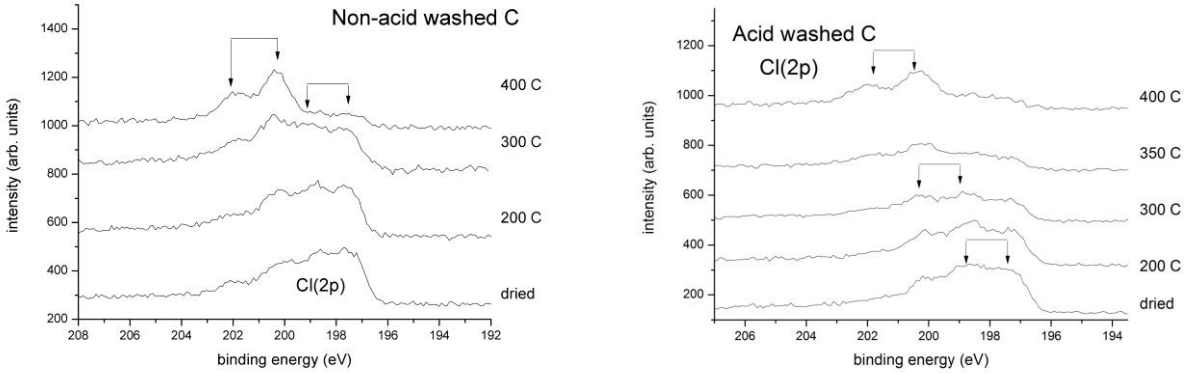

Figure 4.14 Cl(2p) spectra observed for the 2.5 wt% Au-2.5 wt% Pd catalysts supported on non-acid treated carbon and calcined at the temperatures indicated.

Treatment	Binding energy (eV)		% Concentration	
	#1	#2	#1	#2
Dried 120 ^{o}C	197.7	200.4	73	27
200 ^{o}C	197.8	200.4	74	26
300 ^{o}C	198.1	200.5	65	35
400 ^{o}C	197.7	200.4	26	74

Table 4.6 Quantified curve-fitted data for the Cl(2p) spectra recorded for the catalysts prepared on the non-acid treated C support (ref Figure 4.7).

In summary, XPS analysis in section 4.4 highlights the most important distinguishing feature between non-acid treated and acid treated Au-Pd/C catalysts as being the concentration of cationic Pd species **associated with O^{2-} and/ or Cl^{-} electronic modification**, with >90% Pd^{2+} present in acid treated catalysts. Regarding the different chloride species noted between catalysts in Figure 4.14, a possible modification relating to the interaction between chloride species and activated carbon was reported by Simonov *et al.*, who studied H_2PdCl_4 adsorption onto graphite-like carbon, identifying two competitive adsorption pathways[12-15].

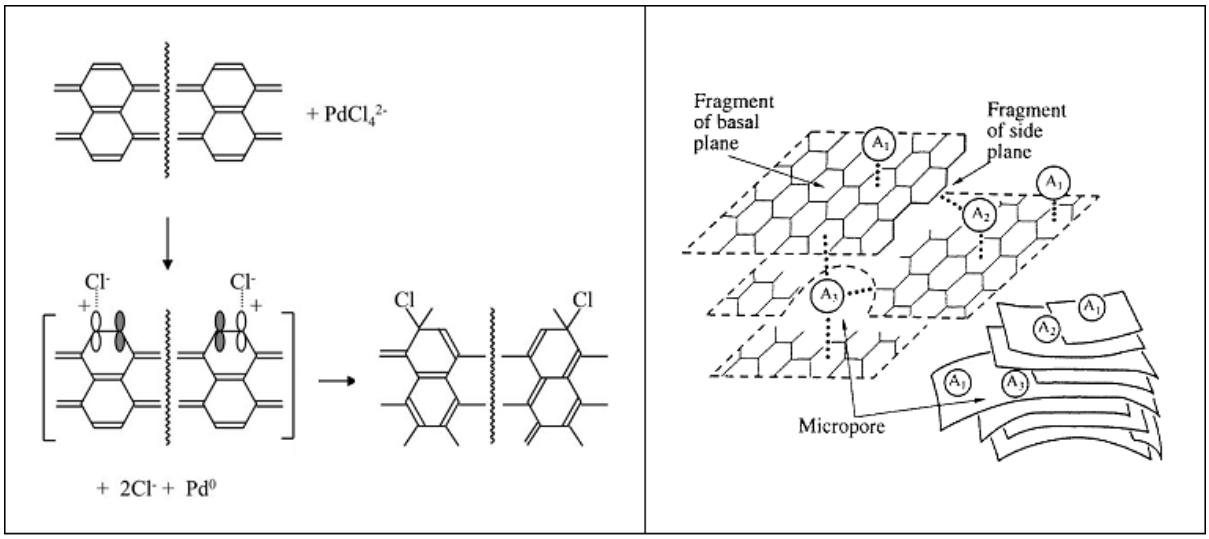

Figure 4.15 Schematics showing the adsorption of chloride ions on C^{+} sites (left) and the probable positions in which adsorption of H_2PdCl_4 could proceed on carbon surface (right)[13, 14].

The first involved reduction of Pd (based on the high reducing power of carbon) close to the exterior of carbon particles, forming electropositive C holes that are charge compensated by the adsorption of chloride ions[13, 14]. The second involved $PdCl_2$ forming π-complexes with C=C fragments of different bond strength along the surface, with strong strong/irreversible bonds representing micropores. As a result, cationic Pd^{2+} species migrate along the surface during the drying step to form clusters centred on step sites where the adsorption probability is high[12-15] (Figure 4.15), and could assist in explaining the high concentration of small Pd^{2+} clusters detected in acid treated Au-Pd/C catalysts at all calcination temperatures (Figures 4.8 and 4.10). In the following section, a study of different calcination atmospheres is undertaken in an effort to ascertain the extent that calcination in static air is linked to switching off the H_2O_2 hydrogenation pathway for acid treated Au-Pd/C catalysts, with investigation into different reduction/oxidation cycles on activity and Pd^0/Pd^{2+} concentration.

4.5 Effect of calcination atmosphere on H_2O_2 synthesis and hydrogenation

Catalysts until now have been calcined in static air, which aids in maintaining the >90% Pd^{2+} concentration present in the dried-only, acid treated Au-Pd/C catalyst and imparts long term catalyst stability/reusability for direct H_2O_2 synthesis. As anticipated, the reduction of acid treated Au-Pd/C in 5% H_2/Ar (Table 4.7) forms a highly active H_2O_2 hydrogenation catalyst *via* reduction of surface Pd^{2+} to Pd^0, while He calcination formed a catalyst with a H_2O_2 productivity comparable to static air calcination (150 $mol_{H2O2}kg_{cat}^{-1}h^{-1}$). However, heat treatment in either reducing or inert atmosphere did not form a stable catalyst.

Heat Treatment	**Productivity / $mol_{H2O2}kg_{cat}^{-1}h^{-1}$**		**Hydrogenation / $mol_{H2O2}kg_{cat}^{-1}h^{-1}$**
	1st Use	**2nd Use**	
Non-acid treated			
Static Air	110	110	117
Helium	116	86	117
Acid treated			
Static Air	160	160	0
Helium	150	140	0
Oxygen	252	n.d	46
5% H_2/Ar	98	62	630

Table 4.7 Effect of heat treatment atmosphere (all 400 ^oC, 3 h) on the rates of H_2O_2 synthesis, hydrogenation and reusability over 2.5 wt% Au-2.5 wt% Pd/C catalysts.

The presence of oxygen is linked to the formation of surface PdO/Pd^{2+} and although acid treated Au-Pd/C contains >90% Pd^{2+} before calcination, a high proportion of the Pd^{2+} present will be associated with the $PdCl_2$ precursor. The relative intensities of chloride species identified by XPS change on increasing calcination temperature, correlating to a given extent with decomposition of $PdCl_2$ to metallic/oxidised Pd species (including PdO), and depends on the nature of the metal-support interaction[6].

The interaction of Au and Pd with the activated carbon defects is not fully understood, but is known to an extent as depending on the carbon type and activation process used by the manufacturer (Darco G60 is activated in HCl/steam flow[11]). Specifically, these materials can contain any number of functional groups/oxygen termination points through which interactions with Au/Pd species are possible (Figure 4.16). TPD experiments showed that nitric acid pre-treatment increased the amount of carboxylic acid groups on the support and therefore it is feasible that a reduction treatment is detrimental to catalyst stability by reductive elimination of functional groups/oxidic defects.

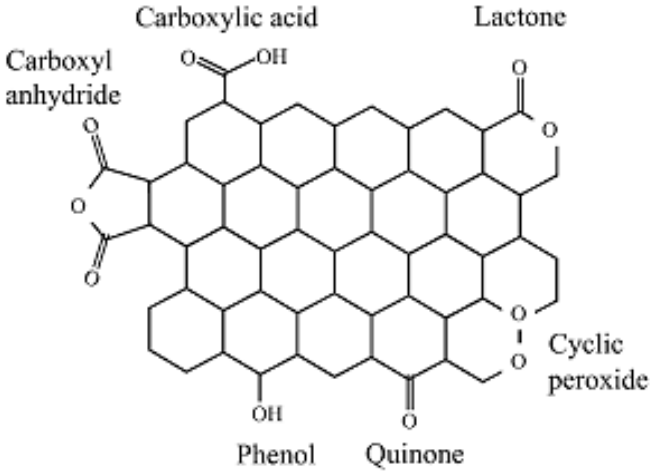

Figure 4.16 Schematic diagram showing the different types of oxygen containing functional groups that can be incorporated into graphic planes of activated carbon supports[16].

Results in Table 4.7 indicated that calcination in either static air or helium at 400 ^{o}C gave H_2O_2 productivities exceeding 150 $mol_{H2O2}kg_{cat}^{-1}h^{-1}$ (corresponding to a 0.40 wt% H_2O_2 solution) and switched-off the hydrogenation pathway. Figure 4.17 shows that acid treated Au-Pd/C catalysts calcined in helium (b) and static air (c) comprised predominantly of Pd^{2+} with minimal evidence of metallic Pd. The reason Pd^{2+} concentration is quoted as >90% as opposed to >99% is because of the difficulties in applying curve-fitting to metallic features situated at 334-336 eV (335.2 eV corresponds to bulk metallic Pd) at such low levels, and therefore the possibility of there being a low percentage of metallic Pd^0 species present alongside the cationic Pd^{2+} excess cannot be excluded.

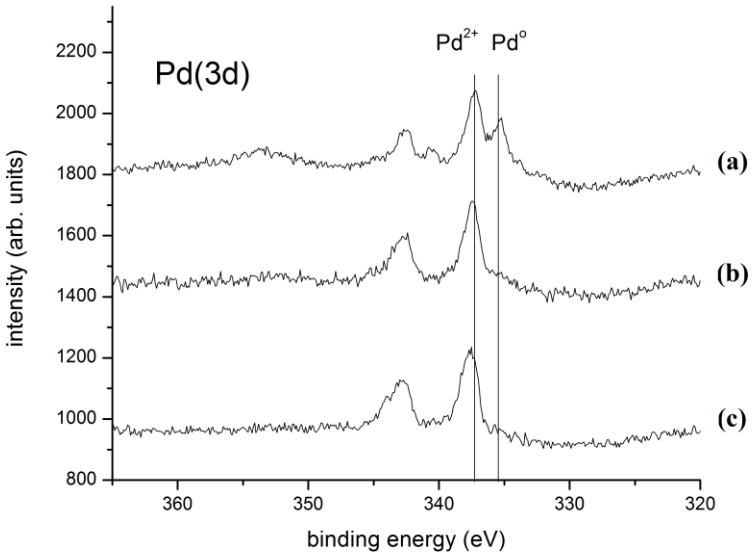

Figure 4.17 XPS comparison of support pre-treatment and heat treatment on the Pd^{2+}/Pd^{0} spectral features of 2.5 wt% Au-2.5 wt% Pd/C catalysts prepared / calcined on: (a) non-acid treated C / Air, 400 ^{o}C, (b) acid treated C / He, 400 ^{o}C, and (c) acid treated C / Air, 400 ^{o}C.

Detection of Pd^{0} in non-acid treated Au-Pd/C (a) is straightforward (~60:40 atom% Pd^{2+}/Pd^{0}) while to the best ability only cationic Pd^{2+} could be detected in acid treated Au-Pd/C catalysts. Already it is understood that TPD analysis of acid treated carbon shows a broad CO_2 signal from 200 to 400 ^{o}C corresponding to decomposition of carboxylic acid groups. Decomposition of the same groups during calcination in helium could therefore compromise catalyst stability (*via* anchorage of Au-Pd species to the surface of activated carbon) by the possible internal supply of oxygen derived from decomposition of functional groups to produce CO and CO_2.

Consequently, the high surface Pd^{2+} concentration found in the dried-only, acid treated Au-Pd/C catalysts is maintained after calcination in helium (400 ^{o}C, 3 h), but the resulting catalyst lacks the same degree of metal-support interactions critical to the development of a stable, reusable catalyst, and found in static air calcined counterparts. In section 4.5.1, the effect of pre-heating activated carbon in helium prior to impregnation of Au and Pd on the resulting direct H_2O_2 synthesis activity of the catalyst is also considered, and in addition the standard calcination step is modified to determine if it is indeed possible to switch-off the H_2O_2 hydrogenation pathway of a non-acid treated Au-Pd/C catalyst.

4.5.1 Effect of heat treatment on activated carbon

Table 4.8 demonstrates the effect of pre-heating activated carbon, using conditions akin to TPD experiments, before impregnation of Au and Pd. Results show a significant loss in both H_2O_2 synthesis and hydrogenation activity after heating the carbon support at 950 ^oC (which as shown in TPD experiments due to the decomposition of a higher percentage of functional groups on carbon) and the importance of using an activated carbon support in catalyst preparation. Reference to H_2O_2 synthesis and hydrogenation activities for Au-Pd supported on non-functionalised, nuclear grade carbon sourced from BNFL (Appendix Table A4.2) showed a similar low set of activities and corroborated the role of surface functional groups which are barely if at all enhanced by nitric acid pre-treatment - the respective TPD profiles are both featureless (Appendix Fig A4.3).

Treatment	**Productivity / $mol_{H2O2}kg_{cat}^{-1}h^{-1}$**	**Hydrogenation / $mol_{H2O2}kg_{cat}^{-1}h^{-1}$**
None	110	117
He / 450 ^oC / 12 h	37	98
He / 950 ^oC / 12 h	17	5

Table 4.8 Effect of pre-heating activated carbon (1.0 g batches) on the H_2O_2 synthesis and hydrogenation activities of non-acid treated 2.5 wt% Au-2.5 wt% Pd/C catalysts.

Referring to Table 4.7, it is observed that calcination of acid treated Au-Pd/C in pure oxygen at 400 ^{o}C formed a highly active catalyst (252 $mol_{H2O2}kg_{cat}^{-1}h^{-1}$) accompanied by H_2O_2 hydrogenation activity. However, approximately 25-30% of the catalyst mass was lost during the calcination step due to burn-off of the carbon support in excess oxygen, and consequently the resulting high H_2O_2 synthesis activity is related to a higher metal loading and particle sintering. TGA of dried-only, acid treated Au-Pd/C showed a mass variation that is attributed to loss of physisorbed H_2O, decomposition of Au-Pd precursors and burn-off of the carbon support at temperatures >400 ^{o}C. This represents the highest temperature that can be used for static air calcinations without causing significant damage to the catalyst structure.

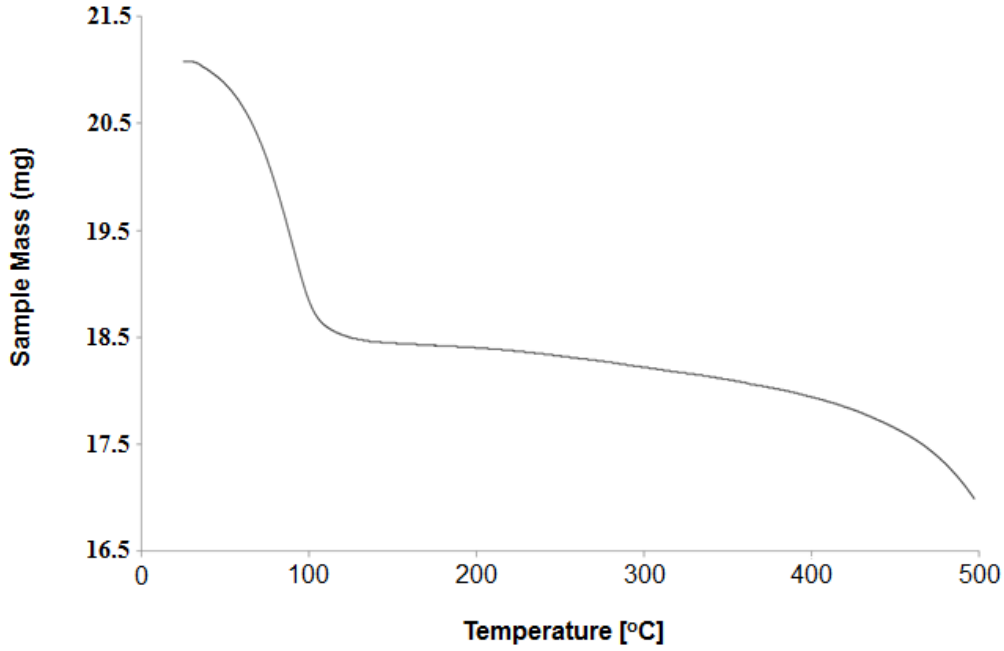

Figure 4.18 TGA profile recorded for acid treated 2.5 wt% Au-2.5 wt% Pd/C (dried-only).

In section 4.3, H_2O_2 hydrogenation activity over non-acid treated Au-Pd/C catalysts (Table 4.3) was reduced on increasing the calcination temperature to 400 ^{o}C but was not switched-off. Based on this finding, a modified, two-step calcination where non-acid treated Au-Pd/C was first calcined in static air at 400 ^{o}C (3 h) before a second calcination in helium at 500 ^{o}C (3 h) to suppress carbon burn-off was performed to establish whether the H_2O_2 hydrogenation activity of a *non-acid treated catalyst* could be switched-off using calcination temperatures above 400 ^{o}C, avoiding substantial burn-off of activated carbon.

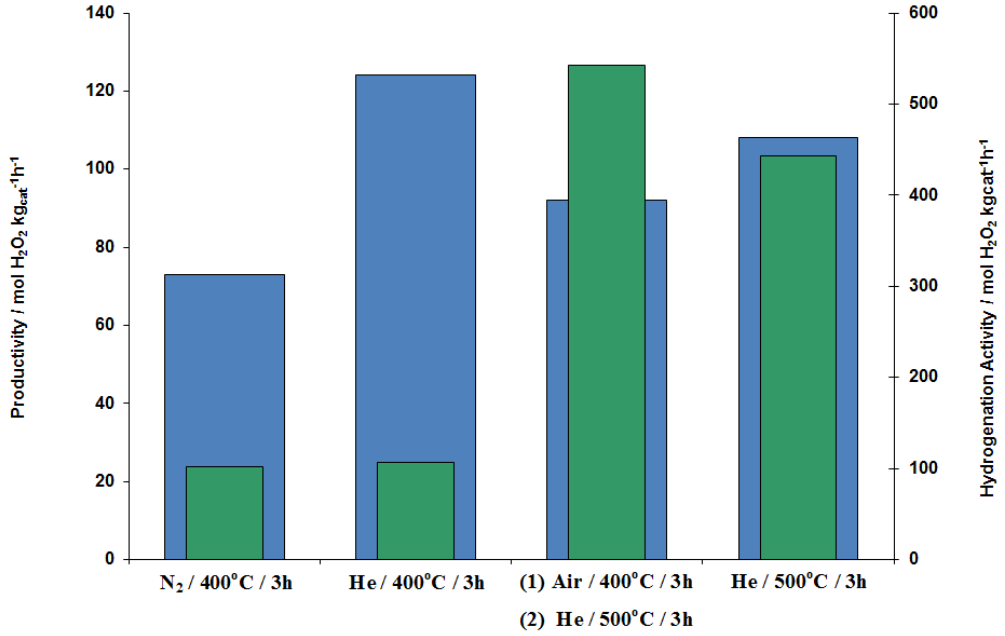

Figure 4.19 Comparison of calcination conditions and effect of a double calcination on the H_2O_2 synthesis (blue bars) and hydrogenation (green bars) activities of non-acid treated 2.5 wt% Au-2.5 wt% Pd/C.

Although the use of a two-step calcination resulted in a high H_2O_2 productivity of 92 $mol_{H2O2}kg_{cat}^{-1}h^{-1}$, the subsequent hydrogenation activity over the catalyst actually increased substantially to 543 $mol_{H2O2}kg_{cat}^{-1}h^{-1}$ (Figure 4.19). This was attributed to longer exposure to high temperatures, which was necessary as the first calcination in static air was required for catalyst stability (refer to Table 4.7), alongside with further loss of surface chloride species from the catalyst, which are understood to aid in dispersing Au and Pd species during the calcination step and minimise the sequential H_2O_2 hydrogenation/decomposition activity of supported Au-Pd catalysts (in the absence of acid promoters).

It can be concluded that application of calcination atmospheres alternative to static air in the preparation of 2.5 wt% Au-2.5 wt% Pd/C do not form stable, reusable catalysts and in some cases may negatively affect the structure of activated carbon, which participates in the switching off of H_2O_2 hydrogenation activity. The final experiments in section 4.5.2 review the effect of oxidation/reduction cycles and are intended to highlight the significance of reversibly modifying the surface Pd oxidation state of acid-treated Au-Pd/C catalysts after calcination. This will lead into a discussion and conclusion of the aims outlined for chapter 4.

4.5.2 Effect of oxidation and reduction cycles of Pd^{2+}/Pd^{0} ratio

Although the identity of the precise feature responsible for switching off H_2O_2 hydrogenation was not established, key experiments show that Pd oxidation state is an important factor. The significance of acid treated Au-Pd catalysts containing a high surface Pd^{2+} concentration is demonstrated in an initial series of Oxidation-Reduction-Oxidation (ORO) experiments. With reference to Table 4.9, acid treated 2.5 wt% Au-2.5 wt% Pd/C, the preparation of which was adjusted to give a partial H_2O_2 hydrogenation catalyst, was first oxidised in static air **(1)** prior to reduction in dilute hydrogen **(2)**, performed at 100 ^{o}C to initiate Pd^{0} formation and limit particle sintering/variation in morphology. Consequently, the rate of H_2O_2 hydrogenation increased as did the intensity of Pd^{0} signal in corresponding XPS analyses (Figure 4.20). A second oxidation step **(3)** then reduced the rate of H_2O_2 hydrogenation, switching-off this pathway when following step **iii**.

ORO Sequence	**Productivity / $mol_{H2O2}kg_{cat}^{-1}h^{-1}$**	**Hydrogenation / $mol_{H2O2}kg_{cat}^{-1}h^{-1}$**	**Spectrum on Pd(3d) figure**
(1) Static Air, 400 ^{o}C / 3 h [a]	150	19	(a)
(2) 5%H_2/Ar, 100 ^{o}C / 1 h	76	161	(b)
(3) + 1 Step from i-iii.			
i. Static Air, 300 ^{o}C / 3 h	94	127	(c)
ii. O_2, 100 ^{o}C / 1 h	48	100	(d)
iii. O_2, 200 ^{o}C / 3 h	34	0	(e)

Table 4.9 Summary of Oxidation-Reduction-Oxidation study applied to an acid treated Au-Pd/C catalyst that hydrogenates 1% H_2O_2 after calcination at 400 ^{o}C **(1)**, before a reduction step **(2)**, and one of oxidation steps **i-iii (3)**.

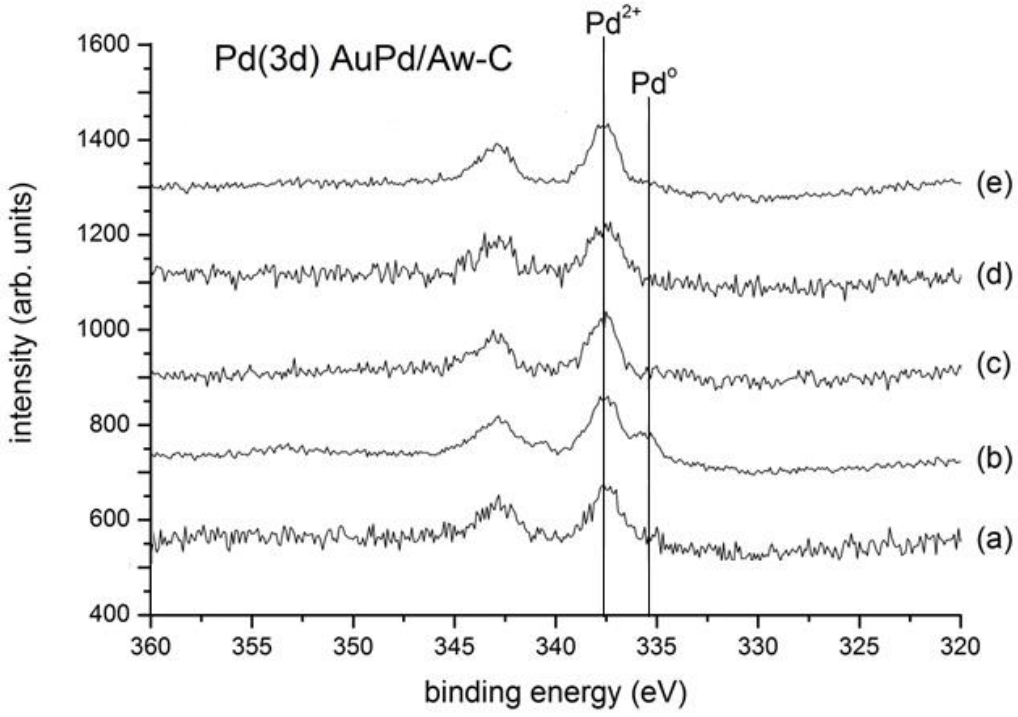

Figure 4.20 XPS comparison of Oxidation-Reduction-Oxidation cycles listed in Table 4.8.

On reviewing XP spectra presented in Figure 4.20, corresponding to the ORO sequences discussed on the previous page (Table 4.19), the intensity of the Pd^0 signal was shown to decrease on moving from spectrum **(b)** to spectra **(c)** and **(d),** with metallic Pd^0 content remaining just above signal to noise level. On switching off the H_2O_2 hydrogenation activity the Pd^0 signal disappeared in spectrum **(e)**, although it must be appreciated that H_2O_2 synthesis activity was also reduced in this experiment, and therefore this result serves only as proof of concept and a basis for further investigation. Shaw *et al.* reported that careful tuning of the **ORO** conditions applied to Au-Pd/C catalysts enabled H_2O_2 hydrogenation to follow the sequence: residual hydrogenation > moderate hydrogenation > no hydrogenation, and restored the H_2O_2 synthesis activity to its original value without compromising Au-Pd particle size[17].

4.6 Discussion

In this chapter a systematic study into the effect of pre-treating an activated carbon support in aqueous 2 vol% nitric acid was undertaken, using a range of characterisation techniques to probe changes in the structure of both carbon supports and the resulting bimetallic Au-Pd/C catalysts prepared by wet impregnation and calcined in static air across a range of temperatures. The H_2O_2 synthesis and hydrogenation activities over non-acid and acid treated Au-Pd/C catalysts were compared and contrasted as a function of calcination temperature. A minimum temperature of 400 ^oC was required to form both a highly active, stable and fully reusable catalyst, and simultaneously decreasing the H_2O_2 hydrogenation activity to the extent that for acid treated Au-Pd/C it was switched-off.

Various underlying differences in the characterisation of carbon-supported bimetallic Au-Pd catalysts may provide an explanation as to the precise manner with which the H_2O_2 hydrogenation pathway is switched-off. Characterisation of non-acid and acid treated carbons by FT-IR ATR spectroscopy and in particular TPD showed an increase specifically in the amount of carboxylic acid groups, while XPS analysis of the supports showed that no new/different carbon and oxygen species were introduced by nitric acid pre-treatment. Aside from confirming mesoporous structure and high surface area (>900 m^2g^{-1}), no real differences between the two supports could be ascertained from BET surface area and BJH pore-size distribution measurements. Based on these observation, is concluded that acid pre-treatment has increased the number of pre-existing carboxylic acid groups on G60 activated carbon.

Base treatment of activated carbon is reported as being detrimental for the direct synthesis reaction since it facilitates base-catalysed decomposition of hydrogen peroxide and additionally several acids have also been recognised as unsuitable, including HCl, H_3PO_4 and H_2SO_4, with the nature of the counter-ion, *e.g.* Cl^-, PO_4^{3-}, SO_4^{2-}, considered as playing a contributing role[1]. To date, the H_2O_2 hydrogenation activity has only been switched-off by nitric acid and is found to be irrespective of concentration, with hydrogenation switched-off using 0.5, 2, 10 and 70 vol% HNO_3 solutions[2, 3]. This implies a minor modification in structure is required to switch-off H_2O_2 hydrogenation after which further acid imparts no effect. NH_3-TPD experiments are planned to quantify surface acidity, with focus on dilute acid

pre-treatments using concentrations below 0.5 vol% in order to determine the exact point at which the sequential hydrogenation activity for resulting Au-Pd/C catalysts is switched-off.

Characterisation of non-acid and acid treated Au-Pd/C gave an informative picture as to how the resulting catalyst nanostructure is affected. Because the beneficial effect of acid pre-treatment with respect to direct H_2O_2 synthesis is a recent development, the available literature has not commented on the effect of catalyst preparation in switching-off H_2O_2 hydrogenation. In this study, all catalysts were synthesized by wet impregnation, a relatively straightforward method that can be conveniently scaled up to meet industrial requirements. Using batch conditions at Cardiff University, concentrations >0.40 wt% H_2O_2 can already be produced by impregnated, acid treated Au-Pd/C catalysts, prompting further characterization and optimization studies into wet impregnation prior to other preparation methods (DP, Sol-Immobilization) known to afford better control over particle composition/size distribution[18, 19].

The surface composition and structure of non-acid and acid treated Au-Pd/C catalysts was studied using XPS and STEM-HAADF imaging techniques. Aberration corrected electron microscopy showed that both non-acid treated and acid-treated Au-Pd/C samples calcined at 400 °C consisted of Au-rich nanoparticles and a highly dispersed coverage of atomic and cluster-like Pd species, intermixed with a small amount of atomically dispersed Au. Calcination appears to improve the overall metal dispersion, although acid pre-treatment of the support does not seem to affect the catalyst morphology or the dispersion of metallic species, suggesting the enhancement in observed activity for acid treated Au-Pd/C samples could be related to changes in metal oxidation state and residual surface species.

Indeed XPS analysis showed the most important distinguishing feature between non-acid treated and acid treated Au-Pd/C catalysts as being the concentration of surface Pd^{2+} species associated with O^{2-} and/or Cl^- electronic modification, with >90% Pd^{2+} present in all acid treated catalysts. The stability of surface Pd^{2+} species was however found to be dependent on calcination temperature. For all catalysts calcined in static air at temperatures below 400 ^oC, reduction to metallic Pd during hydrogen peroxide synthesis occurred (alongside possible leaching of Au and Pd from the catalyst), corresponding with a loss of H_2O_2 synthesis activity on second use.

A subtle variation in dispersion of Au and Pd species cannot be excluded as a reason for improved catalytic activity and surface Pd^{2+} concentration after acid pre-treating carbon, given the inability to directly determine the chemical identity of sub-nm species and isolated atoms in bimetallic Au-Pd/C catalysts using atomic level Z-contrast measurements due to the rough nature of the support. Microscopy for monometallic Au and Pd samples implies that a small concentration of atomically dispersed Au atoms is intermixed within atomically dispersed Pd species in bimetallic alloys, and XPS analysis reported higher than anticipated Pd/Au ratios on acid treated Au-Pd/C catalysts. The mechanism proposed below in Figure 4.21 links the increased number of carboxylic acid groups on activated carbon with an improved anatomic dispersion of Au atoms, and for simplicity does not show the functional groups present on activated carbon prior to acid pre-treatment.

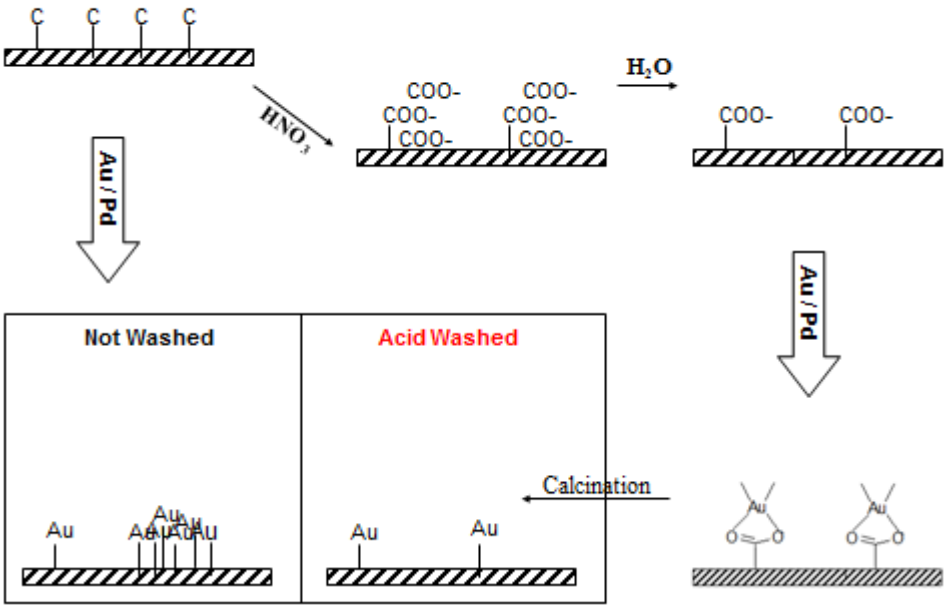

Figure 4.21 Proposed mechanism contrasting the atom dispersion of Au species on carbon.

Firstly, Au and Pd metals are electrostatically anchored to carbon during impregnation by COO^- charged defects to form sub-nm clusters. Subsequent calcination in static air helps disperse these sub-nm clusters into smaller, isolated systems (around 10-20 atoms in size) comprising predominantly Pd intermixed with several gold atoms dispersed to a higher extent due to the additional carboxylic groups on acid treated carbon.

The surface free energy favoured development of PdO results in an $Au_{core}Pd_{shell}$ structure on sub-nm scale, reflected in the improved Pd/Au ratios detected by XPS. Because HAADF imaging does not reveal any significant morphological differences after acid pre-treatment, further investigation is required using a microscope capable of performing XEDS analysis of individual atoms, instruments that are now beginning to enter the scientific domain[20, 21].

Finally, regarding the choice of calcination conditions applied in the preparation of acid treated Au-Pd/C catalysts, calcination in static air at 400 ^{o}C is mandatory to form a stable catalyst that can be reused for the direct synthesis reaction. This is not afforded via heat treatment in reducing, inert or oxygen rich atmospheres and is likely due to the sensitivity of the activated carbon material toward these environments. The critical role of surface Pd^{2+} species with respect to H_2O_2 yield was further demonstration by redox cycle experiments, showing that post-treatment in mild reducing/oxidising condition could reversibly modify the surface Pd oxidation state of acid-treated Au-Pd/C and switch on/off corresponding H_2O_2 hydrogenation.

4.7 Conclusion

In chapter 4, the H_2O_2 synthesis and hydrogenation activities over non-acid and acid treated Au-Pd/C catalysts were compared and contrasted as a function of calcination temperature. A minimum and also optimum temperature of 400 ^{o}C was required to form a highly active and fully reusable catalyst, simultaneously decreasing the H_2O_2 hydrogenation activity to the extent that for acid treated Au-Pd/C it was switched-off. Characterisation of non-acid and acid treated carbons by FT-IR ATR spectroscopy and TPD showed an increase in carboxylic acid functional group content, due to the strong oxidising ability of nitric acid. Aberration corrected electron microscopy showed the overall metal dispersion on G60 carbon is improved by the calcination step. However, acid pre-treatment of the support did not appear to affect either the catalyst morphology or the dispersion of metallic species, suggesting that the enhancement in observed activity for acid treated Au-Pd/C samples could be related to changes in metal oxidation state and residual surface species. This was confirmed by XPS analysis, which showed that the most important distinguishing feature between non-acid treated and acid treated Au-Pd/C catalysts as being the concentration of surface Pd^{2+} species, with >90% Pd^{2+} present in all acid treated catalysts.

4.8 References

1. J. K. Edwards, B. E. Solsona, E. Ntainjua N, A. F. Carley, A. A. Herzing, C. J. Kiely, G. J. Hutchings, *Science*, **2009**, 323, 1037.
2. J. K. Edwards, E. Ntainjua N, A. F. Carley, A. A. Herzing, C. J. Kiely, G. J. Hutchings, *Angew. Chem. Int. Ed.*, **2009**, 48, 8512.
3. J. K. Edwards, The Direct Synthesis of Hydrogen Peroxide using Gold Based Catalysts, PhD Thesis, *Cardiff University*, **2006**.
4. J. K. Edwards, B. E. Solsona, P. Landon, A. F. Carley, A. Herzing, C. J. Kiely, G. J. Hutchings, *Journal of Catalysis*, **2005**, 236, 69.
5. J. C. Pritchard, Q. He, E. Ntainjua N, M. Piccinini, J. K. Edwards, A. A. Herzing, A. F. Carley, J. A. Moulijn, C. J. Kiely, G. J. Hutchings, *Green Chem.*, **2010**, 12, 915.
6. M. L. Toebes, J. A. van Dillen, K. P. de Jong, *J. Mol. Cat. A. Chem.*, **2001**, 173, 75.
7. M. Belhachemi, R. Rios, F. Addoun, J. Silvestre-Albero, A. Sepulveda-Escribano, F. Rodriguez-Reinoso, *J. Anal. App. Pyrolysis*, **2009**, 86, 168.
8. F. Maia, R. Silva, B. Jarrais, A. R. Silva, C. Freire, M. F. R. Pereira, J. L. Figueiredo, *J. Colloid Interface Sci*., **2008**, 328, 314.
9. E. Castillejos-Lopez, D. M. Nevskaia, V. Munoz, A. Guerrero-Ruiz, *Carbon*, **2008**, 46, 870.
10. J. Y. Li, L. Ma, X. N. Li, C. S. Lu, H. Z. Liu, *Ind. Eng. Chem. Res*., **2005**, 44, 5478.
11. C. C. Leng, N. G. Pinto, *Carbon*, **1997**, 35, 1375.
12. Y. A. Ryndin, O. S. Alekseev, P. A. Simonov, V. A. Likholobov, *J. Mol. Catal.*, **1989**, 55, 109.
13. P. A. Simonov, A. V. Romanenko, I. P. Prosvirin, E. M. Moroz, A. I. Boronin, A. L. Chuvilin, V. A. Likholobov, *Carbon*, **1997**, 35, 73.
14. P. A. Simonov, S. Y. Troitskii, V. A. Likholobov, *Kinetic Catalysis*, **2001**, 41, 255.
15. E. M. Moroz, P. A. Simonov, S. V. Bogdanov, A. L. Chuvilin, *Mater. Sci. Forum*, **2000**, 1074, 321.
16. G. Ertl, H. Knozinger, J. Weitkamp, Preparation of Solid Catalysts, Chapters 3 and 4, *Wiley, Weinheim*, **1999**.
17. J. K. Edwards, J. C. Pritchard, M. Piccinini, G. Shaw, Q. He, A. F. Carley, G. J. Hutchings, *J. Catal.*, **2012**, 292, 227.

18. J. A. Lopez-Sanchez, N. Dimitratos, N. Glanville, L. Kesavan, C. Hammond, J. K. Edwards, A. F. Carley, C. J. Kiely, G. J. Hutchings, *App. Catal. A. Gen.*, **2011**, 391, 400.
19. L. Kesavan, R. Tiruvalam, M. H. Ab-Rahim, M. I. bin Saimon, D. I. Enache, R. L. Jenkins, N. Dimitratos, J. A. Lopez-Sanchez, D. W. Knight, S. H. Taylor, C. J. Kiely, G. J. Hutchings, *Science*, **2011**, 331, 195.
20. J. Wen, J. Mabon, C. Lei, S. Burdin, E. Sammann, I. Petrov, A. B. Shah, V. Chobpattana, J. Zhang, K. Ran, J-M. Zuo, S. Mishina, T. Aoki, *Microsc. Microanal.*, **2010**, 16, 183.
21. Q. He, Study of Heterogeneous Gold and Gold Alloy Catalysts *via* Analytical Electron Microscopy, PhD Thesis, *Lehigh University*, *Pennsylvania*, USA, **2012**.

Chapter 5

5.1 Introduction

In Chapter 3, the catalyst preparation method was investigated and identified several factors as critical to achieving high catalytic activity. Despite the impregnation method being convenient for industrial scale-up, limited control of particle size distribution and chemical composition of Au-Pd nanoparticles is afforded. Sol-immobilization (S_{Im}) is one alternative method for preparing Au-Pd nanoparticles and involves reduction of Au and Pd precursors in solution by sodium borohydride, generating alloyed Au-Pd nanoparticles in the presence of a stabilising ligand such as polyvinyl alcohol (PVA)[1].

The classic method used to prepare Au nanoparticles involved citrate ion reduction, forming Au sols >10 nm, which are too large to be catalytically active[2]. In the times since, the preparation method has been developed to form Au sols of smaller particle size *via* the inclusion of stabilising ligands. In particular, Prati and co-workers[3-9] have demonstrated that Au sols, stabilised using PVA ligands and subsequently immobilized onto carbon and oxide supports are highly active and selective catalysts for the liquid phase oxidation of alcohols.

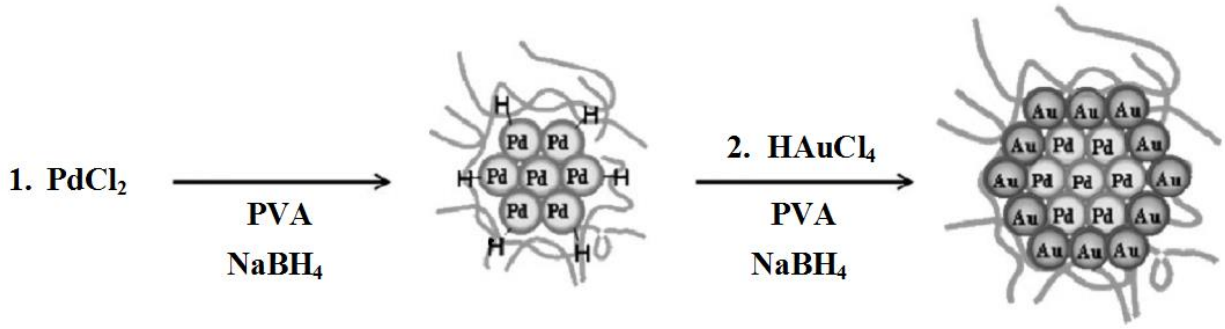

Figure 5.1 Diagram of the step-wise formation of bimetallic colloidal nanoparticles 'sols' - grey lines represent polyvinyl alcohol, PVA ligands.

Polymerized ligands impart control over nanoparticle growth and agglomeration prior to immobilization of colloids onto carbon and TiO_2 supports. Homogeneous and core-shell morphology colloidal nanoparticles can be formed depending on the order of Au^{3+} and Pd^{2+} reduction in solution by $NaBH_4$ prior to immobilization onto a support, *e.g.* carbon and TiO_2. In principle three different types of Au-Pd nanoparticles can be prepared, including: (i) homogeneous alloys - Au+Pd, (ii) Pd_{shell}-Au_{core} - Pd{Au}, and (iii) Au_{shell}-Pd_{core} - Au{Pd} respectively. An example of Au{Pd} colloidal sol/nanoparticle formation is shown in Figure 5.1.

The development of Au-Pd core-shell morphology particles was first reported[10] by Turkevich and Kim in 1970. This was followed by articles detailing the preparation of a range of different possible morphologies such as bi- and tri-layered structures[11-24] and use of other protecting ligands such as polyvinyl pyrrolidine (PVP) and ethylene glycol. Careful control of multiple variables during preparation of sol-immobilized catalysts must be followed to yield desired particle morphologies and in specific cases prevent phase separation and clustering effects[25], demonstrating the complexity of colloidal preparation. In addition, differences between rates of metal ion reduction and the stabilities of resultant Au-Pd nanoparticle phases in the colloidal sol can impart a dramatic effect on the potential for phase separation, agglomeration and consequent catalytic activity.

Hutchings and co-workers[26] reported that homogeneous alloy, Au+Pd sol immobilized catalysts dried at 110 °C were more active for the oxidation of benzyl alcohol to benzaldehyde than their impregnation counterparts on both carbon and TiO_2 supports and stable over consecutive uses[25]. While the presence of PVA ligands on the catalyst were not believed to hinder activity (i.e. blocking of active sites, reaction with solvents) in the liquid phase, temperatures in excess of 300 ^{o}C are required to completely remove the ligand from alloy nanoparticles, at which point the catalytic activity is significantly reduced.

Considerable interest exists in using Au+Pd core-shell nanoparticles in catalysis in addition to their monometallic counterparts and reasons why a difference in catalyst activity might be expected using core-shell structures are related to the compatibility of lattice interactions between the core and shell metals[27] (strain effect) and probability of different size and thicknesses respectively, and consequently the influence of alloying on surface structure and oxidation state[28] (ligand effect).

Relatively small particles may be associated with the reactivity[29] for the direct synthesis of hydrogen peroxide when supported on carbon and TiO_2. However, only low number densities of ultra-small alloy particles are formed *via* wet-impregnation methodology, which generates small Au-Pd alloy particles (1-8 nm) comprising mainly of Pd with a detectable Au component, and larger particles (20-200 nm) exhibiting an $Au_{core}Pd_{shell}$ morphology in addition to occasional Au-only particles. Some selective and non-selective techniques used to prepare bimetallic catalysts are described in Figure 5.2. Methods **1** and **3** can be used as a general guideline to show immobilisation of Au+Pd and Pd{Au} or Au{Pd} nanoparticles onto a support, representing selective techniques. Method **2** is likened to the impregnation of Au and Pd precursors onto a support, a non-selective technique forming particles of different size and composition respectively.

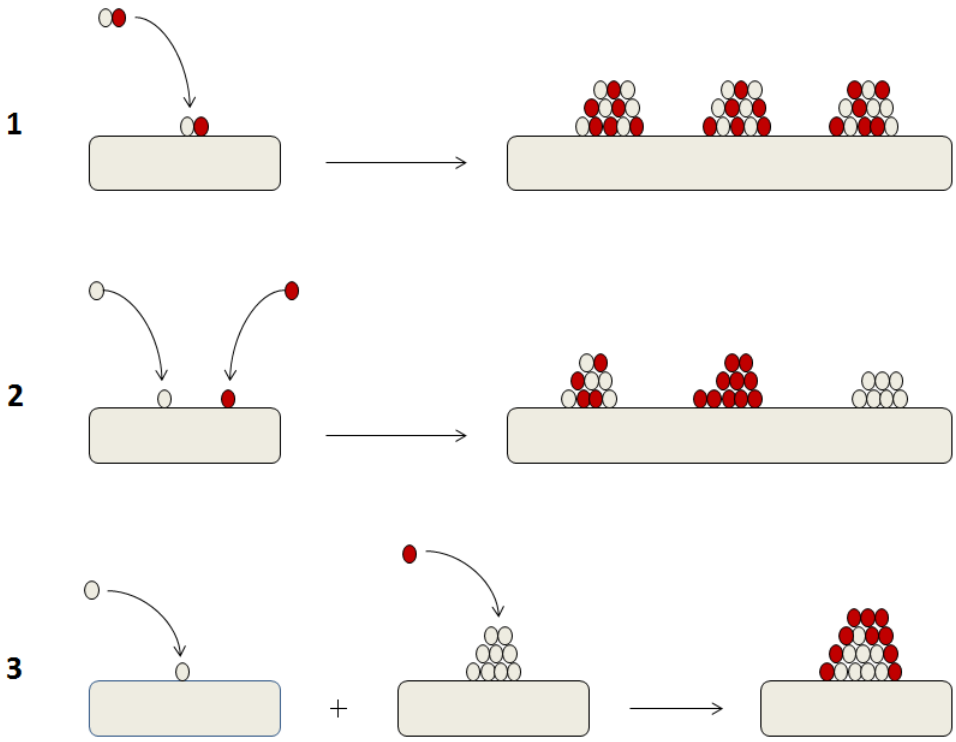

Figure 5.2 Schematic representation of three methods used to prepare bimetallic catalysts: (1) selective / immobilization of Au+Pd, (2) non-selective / impregnation of Au and Pd, and (3) selective / immobilization of Au and Pd, showing the different types of metal-metal interactions expected from each method[30].

As a result, the pre-fabrication of Au-Pd colloidal nanoparticles could overcome the limitations encountered using impregnation methodology providing the size distribution can be retained after nanoparticles are immobilized onto a support. In chapter 5, a series of carbon and TiO_2-supported 1 wt% Au-Pd catalysts (Au:Pd molar = 1:2 - Au:Pd weight = 1:1) were prepared by sol-immobilization (S_{Im}) and evaluated for the direct synthesis of H_2O_2 with the aim of understanding how the structure and activity of Au-Pd catalysts are influenced by the order of Au and Pd reduction during nanoparticle synthesis, *i.e.* Au+Pd, Pd{Au} and Au{Pd}. Prior to their immobilization onto a support, the Au+Pd, Pd{Au} and Au{Pd} colloidal nanoparticles (known as 'starting colloids') were characterised by XPS and advanced aberration corrected electron microscopy. STEM-HAADF imaging and XEDS analysis were used to compare the particle size and composition of colloids before and after immobilization on carbon and TiO_2 and assist in determining the optimum particle morphology and support for the direct synthesis reaction.

Secondly, the effect of calcination temperature on the structure and activity of sol-immobilized Pd{Au}/C and TiO_2 catalysts has been investigated with the aid of advanced characterisation techniques to establish if the rate of H_2O_2 hydrogenation over S_{Im} catalysts be minimised using a suitable heat treatment. Finally, for highly active sol-immobilized Au+Pd/C catalysts, the effect of changing Au:Pd ratio on structure and activity (maintaining a 1 wt% metal loading) has been examined with aim of further improving the high rates of H_2O_2 production and more specifically turnover frequency (TOF) achieved *via* sol-immobilization.

5.2 Electron Microscopy Characterization of Sol-Immobilized Catalysts

5.2.1 Au+Pd, Pd{Au} and Au{Pd} Colloids

STEM microscopy of the Au+Pd, Pd{Au} and Au{Pd} starting colloids highlighted similar mean particle sizes of 2.9 nm, 3.0 nm and 2.6 nm respectively (Table 5.1). The mean particle size of Au+Pd and Au{Pd} colloids increased slightly after immobilization on carbon and TiO_2 and air drying (110 ^{o}C, 16 h), with the largest size difference between supports recognised for Au{Pd} catalysts.

Support	**Morphology**		
	Au+Pd	**Pd{Au}**	**Au{Pd}**
None	2.9	2.6	3.0
C	3.7	4.3	3.1
TiO_2	3.9	4.6	4.6

Table 5.1 Summary of the mean particle sizes for Au+Pd, Au{Pd} and Au{Pd} starting colloids and corresponding sol-immobilized catalysts, dried at 110 °C for 16 h.

A range of different shaped particles were detected using STEM-HAADF to study starting colloids dispersed on a continuous carbon film. Particle morphologies identified in images of Au+Pd colloids were: icosahedral (I_h), decahedral (D_h) and cub-octahedral (co) in nature, ranging 1-5 nm in diameter and exhibiting intensity variations characteristic of random alloying. Both Pd{Au} and Au{Pd} colloids comprised icosahedral (I_h), decahedral (D_h), cub-octahedral (co) in addition to dodecahedral (DD_h) and singly twinned particles (STP) particle morphologies.

Colloid	Size (nm)	
	Core	Shell
Au{Pd}	2-5	0.5-1.0
Pd{Au}	2-4	2-5 AL

Table 5.2 Summary of core size and shell thickness in starting colloids. AL = Atomic Layers.

Advanced *Z*-contrasting and XEDS measurements confirmed that Pd_{core}-Au_{shell} and Au_{core}-Pd_{shell} morphologies were formed, with respective core-shell thickness measurements listed in Table 5.2. It must be noted that off-centre cores, particles with incomplete shell coverage and those simply lacking the core-shell structure were occasionally observed for Pd{Au} and Au{Pd} colloids, with variation and non-uniformity in the Au shell coverage of Pd-core particles most likely the result of insufficient 'shell' material being provided during nanoparticle formation. (Appendix A5.1).

5.2.2 Au+Pd, Pd{Au} and Au{Pd}/C and TiO_2 catalysts

Referring to Table 5.1, the drying process did not promote significant sintering of particles on either carbon or TiO_2 supports. High resolution images of immobilized Au+Pd particles identified a non-wetting interaction between the 'rounded' Au+Pd particles and activated carbon. In comparison, an extended flat interface was formed between the mainly 'faceted' Au+Pd particles and TiO_2, evidence of wetting behavior independent of the order of reduction of Au and Pd salts (Figure 5.3). Such wetting behavior on TiO_2 is attributed to the development of strong metal-support interactions (SMSI), resulting in displacement of PVA ligands from interfacial regions across the catalyst surface.

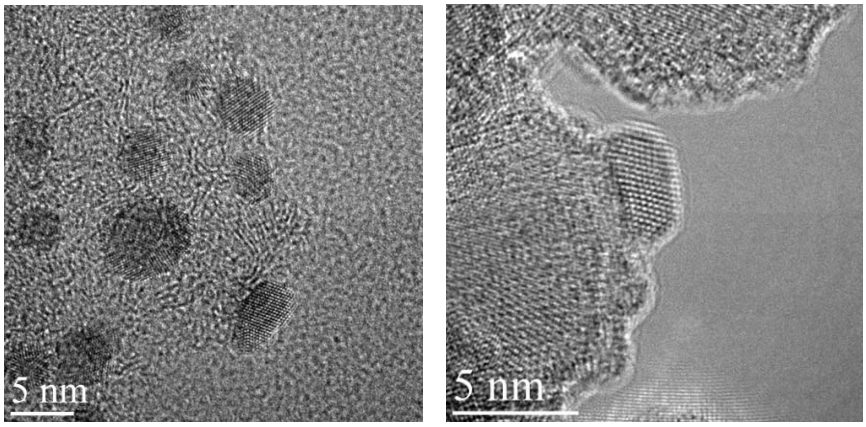

Figure 5.3 High resolution electron microscopy of sol-immobilized Au+Pd/C (left) and Au+Pd/TiO_2 (right) catalysts, dried at 110 °C for 16 h.

Representative STEM-HAADF of sol-immobilized Au+Pd/C and TiO_2 catalysts and use of Z-contrast measurements confirmed random Au+Pd alloy nanoparticles were present on both supports (Figure 5.4). The smallest nanoparticles characteristic of the starting colloid were no longer being present, having undergone sintering into larger particles during the drying step.

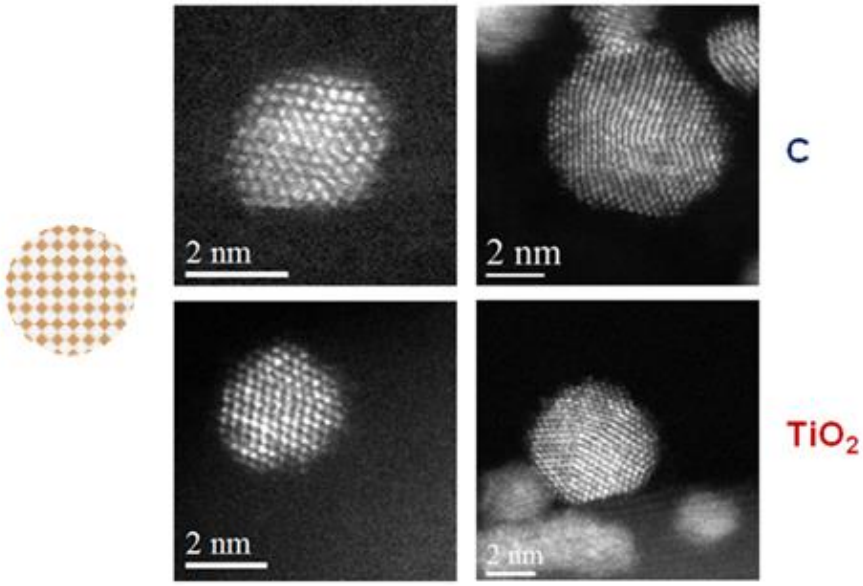

Figure 5.4 STEM-HAADF images of sol-immobilized Au+Pd nanoparticles on carbon (top) and TiO_2 (bottom) supports, dried at 110 °C for 16 h.

Figure 5.5 (left) highlights the existence of Pd_{core}-Au_{shell} morphologies for Au{Pd} particles immobilized on carbon and TiO_2, which were greater than 3 nm in size and comprised Au shells of thickness 1 nm or lower. The Au shell component was difficult to observe on particles smaller than 3 nm and in some cases faceted *monometallic* particles were detected on both supports. Similar to the structure of Au+Pd catalysts as shown in Figure 5.4, the smallest nm-scale alloys have sintered into larger particles during the drying step.

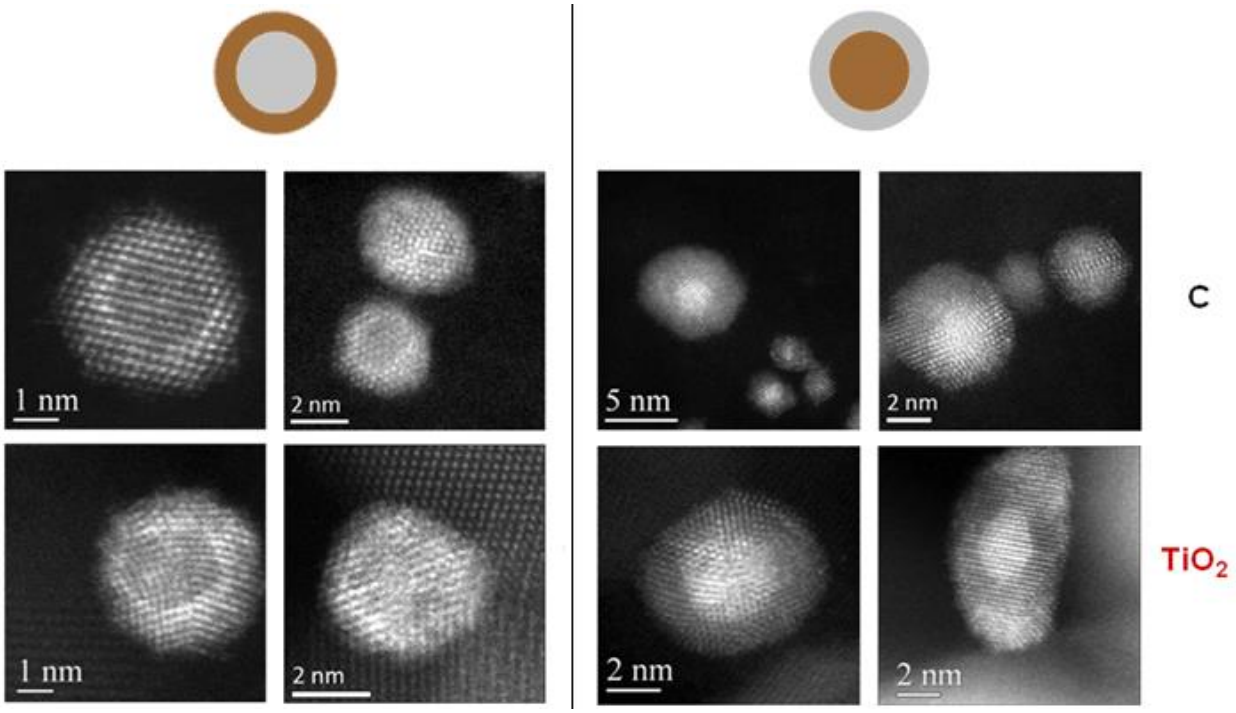

Figure 5.5 STEM-HAADF images of Au{Pd} (left) and Pd{Au} (right) nanoparticles immobilized onto carbon (top) and TiO_2 (bottom) supports, dried at 110 °C for 16 h.

Figure 5.5 (right) indicates the presence of Au_{core}-Pd_{shell} morphologies for Pd{Au} particles immobilized on carbon and TiO_2, which were greater than 5 nm in size and comprised Pd shells of thickness 2 nm or higher. Similar to the Au{Pd} distribution, the Pd shell component was difficult to observe on Pd{Au} particles smaller than 3 nm, and again some particles were identified as *monometallic*, implying that a minority of Au core particles may not have received significant Pd shell coverage during preparation of the starting colloid.

5.2.3 The effect of sol-immobilization on the direct synthesis of H_2O_2

Time on-line H_2O_2 synthesis and hydrogenation activities of sol immobilized 1 wt% Au+Pd, Pd{Au} and Au{Pd}/C and TiO_2 catalysts are summarised in Tables 5.3 and 5.4 respectively. Carbon-supported catalysts were approximately 5 times more active than their TiO_2-supported counterparts for direct hydrogen peroxide synthesis across all reaction times and outperformed wet-impregnated, 5 wt% Au-Pd/C (110 $mol_{H2O2}kg_{cat}^{-1}h^{-1}$) catalysts. This represents a critical result given 5 times less Au and Pd is present in catalysts synthesised *via* sol-immobilization methodology. Exceptionally high initial rates of H_2O_2 production corresponding to the net formation of 0.16-0.19 wt% H_2O_2 after 30 seconds were noted for carbon-supported catalysts. The concentration of hydrogen peroxide produced after just 30 seconds by carbon-supported catalysts exceeded the values achieved by many wet-impregnated[31], 5 wt% Au-Pd counterparts after 30 minutes, indicating enhanced utilisation of active metal with approximately 8-10 fold improvement in turnover frequency (TOF).

Catalyst	**Productivity / $mol_{H2O2}kg_{cat}^{-1}h^{-1}$**		
	30 min	**2 min**	**30 sec**
C			
Au+Pd	158	720	1303
Pd{Au}	143	706	1384
Au{Pd}	142	929	1641
TiO_2			
Au+Pd	31	159	254
Pd{Au}	25	117	231
Au{Pd}	29	117	238

Table 5.3 Summary of time on-line H_2O_2 productivity over sol-immobilized Au+Pd, Pd{Au}, Au{Pd}/C and TiO_2 catalysts (dried at 110 ^oC for 16 h).

Homogeneous alloyed Au+Pd/C and TiO_2 supported catalysts in general demonstrated higher rates of H_2O_2 synthesis that core shell AuPd catalysts, although Au{Pd}/C was more active at some shorter reaction times, possibly due to a higher Au (shell) surface content, consequently lowering the rate of H_2O_2 hydrogenation relative to other catalysts. Time-on-line analysis showed the rate of hydrogen peroxide synthesis falls as the reaction proceeds due to high conversion of reactant gases, which decreases the partial pressure of hydrogen in the autoclave and reduces the H_2 selectivity over the catalyst.

Catalyst	**Hydrogenation / $mol_{H2O2}kg_{cat}^{-1}h^{-1}$**		
	30 min	**2 min**	**30 sec**
C			
Au+Pd	546	4560	17200
Pd{Au}	654	4120	13700
Au{Pd}	370	5640	19700
TiO_2			
Au+Pd	384	6030	19300
Pd{Au}	371	4120	14600
Au{Pd}	331	4660	15600

Table 5.4 Summary of time on-line H_2O_2 hydrogenation over sol-immobilized Au+Pd, Pd{Au}, Au{Pd}/C and TiO_2 catalysts (dried at 110 ^oC for 16 h).

Referring to Table 5.4, it is observed that high rates of H_2O_2 hydrogenation were obtained using Au+Pd, Pd{Au} and Au{Pd}/C and TiO_2 catalysts. Initial rates of H_2O_2 hydrogenation reported in the range 13000-19700 $mol_{H2O2}kg_{cat}^{-1}h^{-1}$ imply that in the direct synthesis reaction, a high fraction of H_2O_2 molecules undergo rapid hydrogenation to H_2O almost immediately after they are formed.

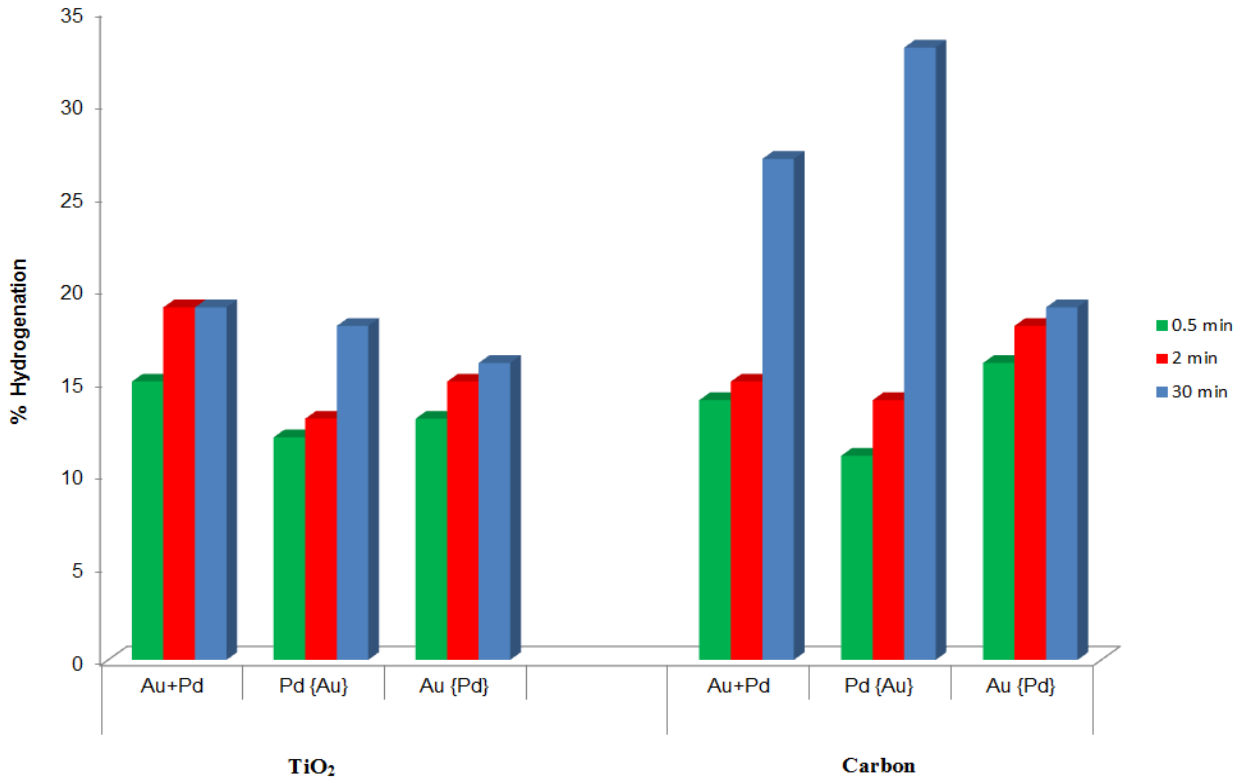

Figure 5.5 Summary of time on-line percentage H_2O_2 hydrogenation over sol-immobilized Au+Pd, Pd{Au}, Au{Pd}/C and TiO_2 catalysts (dried at 110 ^oC for 16 h).

Comparison of H_2O_2 hydrogenation using different catalysts in terms of percentage consumption in Figure 5.5 revealed that a significant portion of total H_2O_2 hydrogenated after 30 minutes (blue) is actually consumed within the first 2 minutes (green and red) of reaction. Although comparable hydrogenation percentages were reported at 30 sec and 2 min for Au+Pd/C and Pd{Au}/C, considerable H_2O_2 hydrogenation continued after this period, which could be connected to catalyst structure (*i.e.* the amount of exposed metallic Pd and particle composition), catalyst deactivation (refer to Figure 5.20) and importantly the complex interplay of simultaneous reaction pathways and dependency on reactant concentration.

The direct synthesis reaction is performed in a sealed autoclave containing a finite amount of hydrogen, oxygen and carbon dioxide (580 psi total). The hydrogen concentration decreases as hydrogen peroxide is produced, which can react further through the hydrogenation and decomposition pathways, of which hydrogenation decreases the hydrogen concentration more. As the concentration of hydrogen peroxide increases with time, consecutive reactions play a more important role and therefore the rate of hydrogen peroxide synthesis is a composite of several reactions.

$H_2 + O_2 \xrightarrow{k_1} H_2O_2$	$\frac{dc_{H_2}}{dt} = -k_1 c_{H_2}^a c_{O_2}^b - k_2 c_{H_2}^c c_{O_2}^d - k_3 c_{H_2O_2} c_{H_2}^e$
$H_2 + \frac{1}{2} O_2 \xrightarrow{k_2} H_2O$	$\frac{dc_{O_2}}{dt} = -k_1 c_{H_2}^a c_{O_2}^b - k_2 c_{H_2}^c c_{O_2}^d$
$H_2O_2 + H_2 \xrightarrow{k_3} 2\,H_2O$	$\frac{dc_{H_2O_2}}{dt} = k_1 c_{H_2}^a c_{O_2}^b - k_3 c_{H_2O_2} c_{H_2}^e$
$H_2O_2 \xrightarrow{k_4} H_2O + \frac{1}{2}\,O_2$	$\frac{dc_{H_2O}}{dt} = k_2 c_{H_2}^c c_{O_2}^d + 2\,k_3 c_{H_2O_2} c_{H_2}^e$

Equations showing the direct synthesis of hydrogen peroxide and parallel and consecutive reactions leading to the non-selective formation of water (left). Changes in the concentration of both H_2 and O_2 gaseous reactants and H_2O_2 and H_2O products are represented using differential equations (right). Rate constants are denoted $\boldsymbol{k_1}$-$\boldsymbol{k_4}$ and the reaction coefficients are denoted ***a*-*e*** respectively[32].

Oxygen is present in excess when using our standard reaction conditions and the decomposition activity is minimal (and even switched-off) for the majority of our catalysts. However decomposition is taken into account when performing hydrogenation experiments as subsequent activities are the sum of all H_2O_2 consumption pathways. Individual reaction pathways are difficult to deconvolute, prompting investigation into the direct synthesis reaction at very short reaction times where changes in hydrogen concentration and effect of sequential reactions are minimised as best as possible. These data present a realistic image of the initial activity of these sol immobilized catalysts and confirm that they are very active for both hydrogen peroxide hydrogenation and decomposition.

5.3 The effect of heat treatment on catalyst structure

In an effort to determine if the high rates of hydrogen peroxide hydrogenation using sol-immobilized Au-Pd catalysts could be reduced by catalyst modification, the effect of static air calcination temperature on Au+Pd, Pd{Au} and Au{Pd} morphologies was investigated. Particular attention is focussed on using immobilized Pd{Au} colloids due to the high surface exposed Pd content characteristic of this deposition method and possibility of forming an alloyed Au-Pd catalyst retaining a narrow particle size distribution and consisting of a high surface Pd^{2+} concentration, the benefits of which were previously reported in a detailed investigation and discussed in chapter 4.

5.3.1 Characterisation of materials calcined at 200 °C

Both Pd{Au}/C and Pd{Au}/TiO_2 catalysts calcined at 200 °C in static air (3 h) were generally found to retain their Au_{core}-Pd_{shell} morphology despite moderate sintering having taken place on activated carbon (Figure 5.6). This was attributed to the weaker particle/support interactions on activated carbon in comparison to the extended flat network formed on TiO_2, leading to improved adhesion and resistance to sintering, although the onset of core-shell destabilization was observed on TiO_2 after calcination at 200 °C.

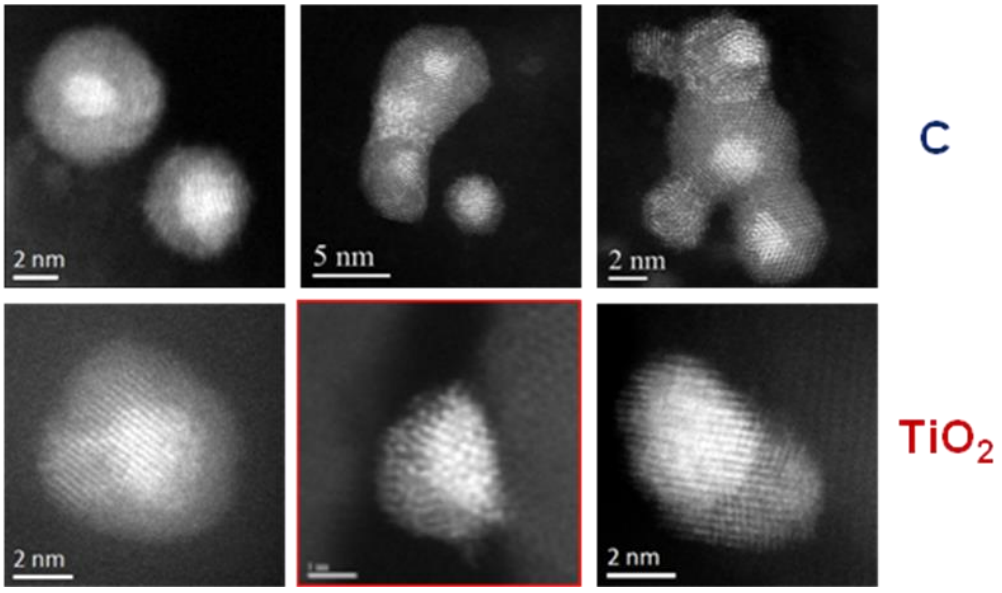

Figure 5.6 STEM-HAADF images of individual nanoparticles on sol-immobilized Pd{Au}/C (top) and Pd{Au}/TiO_2 (bottom) catalysts, calcined in static air at 200 °C for 3 h.

For some nanoparticles present on TiO_2 support, the Au component had diffused inward, becoming preferentially attached to the TiO_2 surface with the Pd component now displaced outward as a result (Figure 5.6).

5.3.2 Characterisation of materials calcined at 400 °C

Calcination of Pd{Au}/C at 400 °C in static air (3 h) initiated burn-off of the carbon support leading to loss of surface area, PVA ligands on exceeding 300 °C and a mean Au+Pd particle size of ~35 nm. The decrease in support mass appears unique to sol immobilization methodology given no significant burn-off is reported when calcining impregnated Au-Pd/C counterparts using the same regime, and implied that Pd enrichment had occurred alongside sintering as the XPS derived surface Pd:Au ratio increased approximately 3 fold (Table 5.4). The sintering behavior identified for Pd{Au}/C was also identified on Au+Pd and Au{Pd}/C catalysts and illustrated by bright field TEM analysis of Au+Pd/C catalysts in Figure 5.7, both before and after calcination at 400 °C.

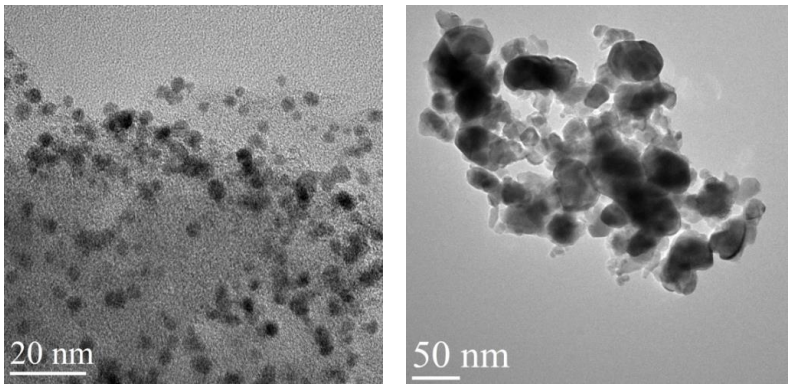

Figure 5.7 Representative bright field TEM micrographs of sol-immobilized Au+Pd/C, before (left) and after (right) after calcination in static air at 400 °C for 3 h.

In comparison, a completely different effect was observed on the surfaces of Au+Pd, Au{Pd} and Pd{Au}/TiO_2 catalysts after 400 °C air calcination with HAADF imaging of Au+Pd/TiO_2 highlighting good preservation of small random alloyed particles due to a strong metal-support wetting interaction restricting nanoparticle sintering irrespective of PVA ligand contribution (Figure 5.8). However both Au{Pd}/TiO_2 and Pd{Au}/TiO_2 catalysts lost their original core-shell morphologies, which destabilized to form bright particles with faint tails (blue arrow), and isolated bright and faint particles (yellow and red arrows) respectively.

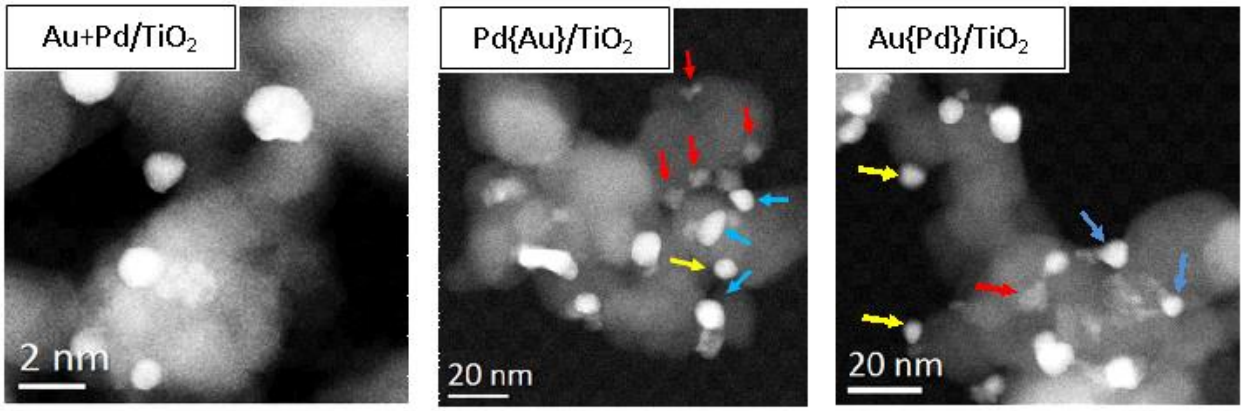

Figure 5.8 STEM-HAADF images of: Au+Pd/TiO_2, Pd{Au}/TiO_2 and Au{Pd}/TiO_2 catalysts after calcination in static air at 400 °C for 3 h.

STEM-XEDS measurements of different particle structures concluded the bright regions were Au-rich and faint regions as being Pd-rich in nature and therefore elongated head-tail particles are indicative of Au and Pd phase separation from the original Pd_{core}-Au_{shell} and Au_{core}-Pd_{shell} nanoparticles with increasing calcination temperature (Figure 5.9).

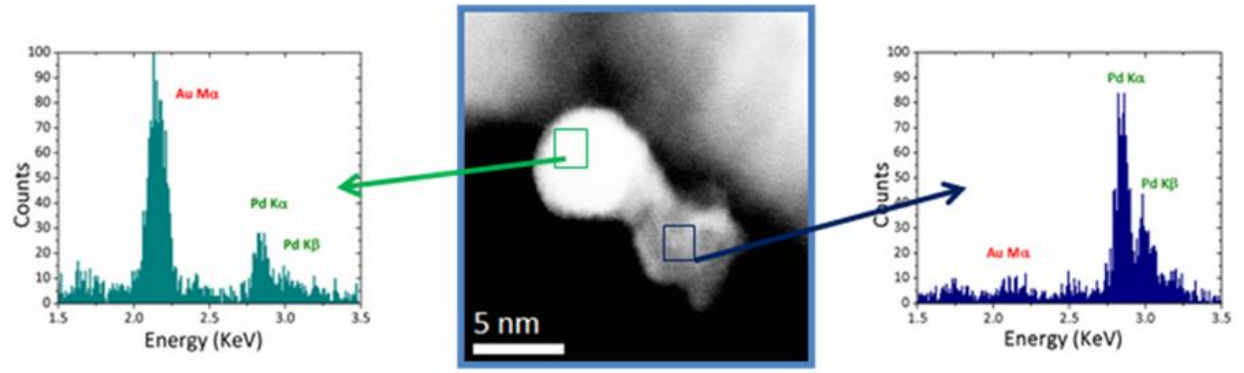

Figure 5.9 STEM-XEDS point spectra of bright and faint regions in elongated 'tailed' particles present on Pd{Au}/C after calcination at 400 °C, and highlighted by blue arrows in Figure 5.8.

XPS analysis presented in Table 5.4 reported a simultaneous oxidation of metallic Pd to Pd^{2+}, which is attributed to the tendency of Pd to form PdO, in this case by diffusing away from Au-Pd alloys and hence forming a 'tail' during the calcination step. Analysis of Pd(3d) and Au(4f) spectral regions showed that heat treatment did not significantly affect the Pd:Au surface molar ratio of Pd{Au}/TiO_2 catalysts. To conclude, the XEDS analysis of 'bright' and 'faint' isolated components again confirmed existence of Au-rich and Pd-rich alloys respectively, which may be derived from insufficiently covered <3 nm Au and Pd "seed" particles in the starting colloids, prior to immobilization onto carbon and TiO_2 (Appendix A5.1).

Catalyst	**Heat Treatment**	**Mean size (nm)**	**Pd:Au molar ratio**	**Pd^{2+}/Pd^{o} valence ratio**
Pd{Au}/C	110 °C	5.6	2.2	0.42
	200 °C	5.3	2.5	0.67
	300 °C	9.4	4.0	2.65
	400 °C	27	5.7	23.4
Pd{Au}/TiO_2	110 °C	4.6	1.6	0.47
	200 °C	4.6	2.2	1.81
	300 °C	5.8	n.d.	n.d.
	400 °C	6.0	1.5	2.40

Table 5.4 Summary of the mean particle size, Pd:Au molar ratio and Pd oxidation states of 1 wt% Pd{Au}/C and TiO_2 catalysts calcined at various temperatures in static air for 3 h.

5.4 The effect of heat treatment on the direct synthesis of hydrogen peroxide

The use of high calcination temperatures were found to be detrimental to the H_2O_2 synthesis activities of supported Pd{Au}/C and TiO_2 catalysts, resulting in near complete deactivation after 400 ^oC calcination in static air. As already observed in Table 5.5, Au-Pd colloids immobilized on carbon are approximately 5-6 times more active than TiO_2-supported counterparts, with H_2O_2 synthesis activities comparable to those for optimized (acid treated), wet-impregnated 5 wt% Au-Pd/C catalysts (160 $mol_{H2O2}kg_{cat}^{-1}h^{-1}$)[29].

Catalyst	**Heat Treatment**	**Productivity / $mol_{H2O2}kg_{cat}^{-1}h^{-1}$**	**Hydrogenation / $mol_{H2O2}kg_{cat}^{-1}h^{-1}$**
Pd{Au}/C	110 ºC	143	654
	200 ºC	155	280
	300 ºC	91	137
	400 ºC	4	252
Pd{Au}/TiO_2	110 °C	25	370
	200 ºC	24	248
	300 ºC	12	236
	400 ºC	4	275

Table 5.5 Effect of calcination temperature on the rates of H_2O_2 synthesis and hydrogenation over 1 wt% Pd{Au}/C and TiO_2 catalysts calcined at various temperatures in static air for 3 h.

Surprising, calcination at 200 °C actually increased the H_2O_2 synthesis activity of Pd{Au}/C from 143 to 155 $mol_{H2O2}kg_{cat}^{-1}h^{-1}$. This was attributed to minor variation in the morphology and size of spherical Pd{Au} nanoparticles on carbon and partial degradation of PVA ligands prior to a significant reduction in synthesis activity on further increasing the calcination temperature due to particle sintering. The same enhancement was not apparent for Pd{Au}/TiO_2 due to the on-set of core-shell destabilisation at 200 ^oC and the existence of strong metal support interactions across an extended flat interface. The preference of faceted

nanoparticles on TiO_2 is also predicted to decrease the population of low co-ordination number corner and edge sites[33] relative to more rounded, spherical particles on carbon.

The H_2O_2 hydrogenation activity of Pd{Au}/C and TiO_2 catalysts simultaneously decreased moving from 110 to 400 ^oC, with the majority of the loss in hydrogenation activity having occurred by 200 ^oC and corresponding to a decrease from 654 to 280 $mol_{H2O2}kg_{cat}^{-1}h^{-1}$. A similar trend was observed for Pd{Au}/TiO_2 and indicated that mild heat treatment of sol-immobilized catalysts can moderately improve H_2O_2 synthesis activity and considerably minimise sequential hydrogenation, while retaining a high degree of their original particle structure. The rapid decline in H_2O_2 hydrogenation with increasing calcination temperature implied the partial removal of PVA as being critical to increasing the amount of active sites available for direct H_2O_2 synthesis. Though H_2O_2 hydrogenation activity continued to decline on exceeding 300 ^oC, catalyst structure by now was seriously compromised resulting in loss of the high synthesis activity demonstrated by Pd{Au}/C before calcination.

Referring to Figure 5.8, phase separation of Au and Pd components did not occur on Au+Pd/TiO_2 after 400 ^oC calcination, implying that lattice interactions in randomly alloyed particles are of sufficient strength to counter Au-Pd phase separation and PdO formation. To conclude further investigation of the heat treatment parameter leading to better control of surface Pd^{2+}/Pd^0 concentration while maintaining original Au-Pd colloid composition is required.

Moving on to section 5.5, the effect of changing Au:Pd ratio on both the structure and activity of catalysts toward the direct synthesis reaction has been investigated with aim of further improving the high rates of H_2O_2 synthesis and simultaneous minimising sequential hydrogenation activity observed for Au+Pd nanoparticles immobilized on carbon. Edwards *et al.* previously reported that for acid pre-treated Au-Pd/C catalysts prepared using wet impregnation[29], the smallest particles detected comprised mainly Pd and that 3-5 nm Au-Pd nanoparticles comprised typically 98% Pd 2% Au. Since the high H_2O_2 synthesis activity of this catalyst (160 $mol_{H2O2}kg_{cat}^{-1}h$) was considered to be associated with these small particles, it was postulated that for optimum activity, development of a method to synthesise a catalyst containing a uniform population of 3-5 nm Au-Pd particles comprising >95% Pd was critical, prompting the following investigation into the effect of Au:Pd molar ratios.

5.5 The effect of Au:Pd ratio on catalyst structure and activity

In addition to preparation of Au+Pd, Pd{Au} and Au{Pd} colloids and evaluation of calcination conditions, the composition of highly active Au+Pd colloids of different Au:Pd molar ratio immobilized on activated carbon was investigated. A series of 10 catalysts of varying molar ratio (Au:Pd = 1:0, 7:1, 3:1, 2:1, 1:1, 1:1.85, 1:2, 1:3, 1:7, 0:1) were prepared, characterized and tested for the direct synthesis of hydrogen peroxide.

5.5.1 UV-Visible spectroscopy of Au:Pd colloids

Prior to catalyst testing, colloidal solutions (extracted after reduction by $NaBH_4$) were analysed using UV-Visible spectroscopy, which observed a plasmon band centred at 505 nm characteristic of monometallic Au nanoparticles[34] below 10 nm in size that is not observed for monometallic Pd. On increasing the Pd content in Au+Pd bimetallic sols a gradual disappearance of the Au plasmon was observed for spectra presented in Figure 5.10. This was attributed to changes in the band structure of Au particles alloyed with Pd to form randomly alloyed Au+Pd nanoparticles.[36-38]

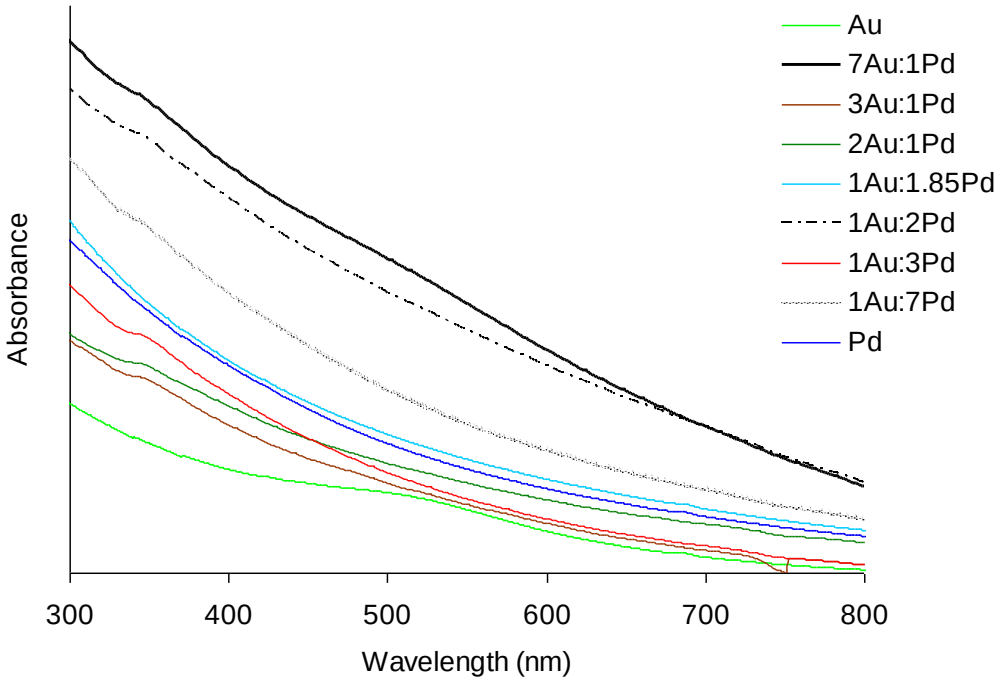

Figure 5.10 UV-Visible spectra of simultaneously reduced Au_xPd_y colloidal solutions.

5.6 Characterisation of Au_xPd_y/C sol-immobilized catalysts

5.6.1 X-ray photoelectron spectroscopy

Analysis of the Au(4f) region confirmed the presence of Au^0 exclusively in Au_xPd_y/C samples and evidence of Au+Pd alloying based on a binding energy downshift moving from Au_1Pd_0 (84.2 eV) to Au_1Pd_1 (84.0 eV) compositions. In comparison analysis of the Au(4d)+Pd(3d) region indicated metallic Pd species for catalysts comprising Pd:Au ratios <1, while Pd^{2+} species were detected alongside metallic Pd for catalysts comprising Pd:Au ratios >1, the relative amount of which increased with Pd molar content (Figure 5.11).

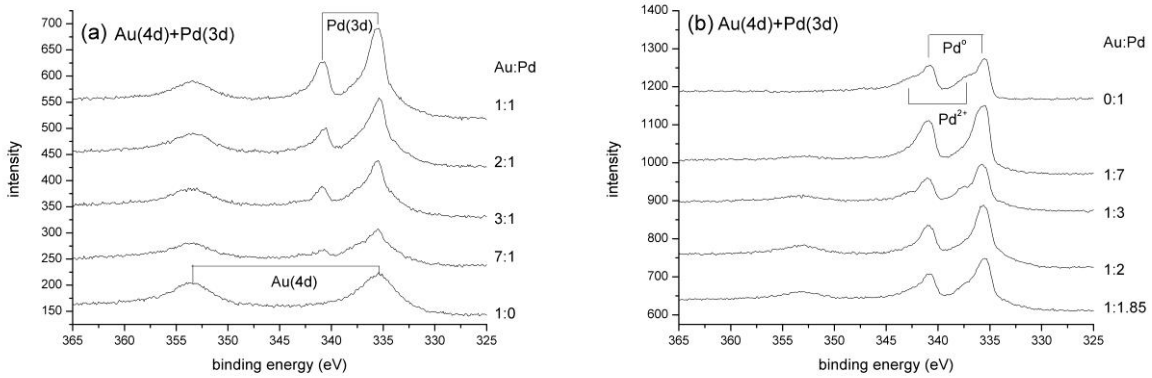

Figure 5.11 Pd(3d) spectra for sol-immobilized Au+Pd/C catalysts of varying molar ratio.

The relationship between the XPS-derived Pd:Au (corrected for Pd($3d_{5/2}$) and Au($4d_{5/2}$) component overlap) and nominal Pd:Au molar ratio moving from 0 to 1 was determined as being directly proportional, after which the XPS-derived surface ratios were a factor of ~2 lower than the nominal Pd:Au ratios used in catalyst preparation (Appendix A5.3). With reference to HAADF images shown in Figure 5.12, differences in Au and Pd particle size and/or compositional variation (larger Pd-rich signals) could give rise to lower signal intensity reflected in the XPS-derived molar ratios.

5.6.2 Electron microscopy characterisation

The mean and median particle sizes of Au-only, Pd-only and Au_xPd_y/C catalysts imaged in bright field TEM mode (Appendix 5.4) did not identify a general systematic variation in particle size with colloid composition, although the median particle sizes of Au_xPd_y/C alloys were all lower than reported for monometallic Pd/C (5.4 nm) and more 'tightly' distributed (Figure 5.13). XEDS analysis of immobilized nanoparticles in the bright field (BF) region detected both Au and Pd signals of intensity correlating with nominal Au:Pd molar ratios respectively, indicating formation of homogeneous Au+Pd alloys.

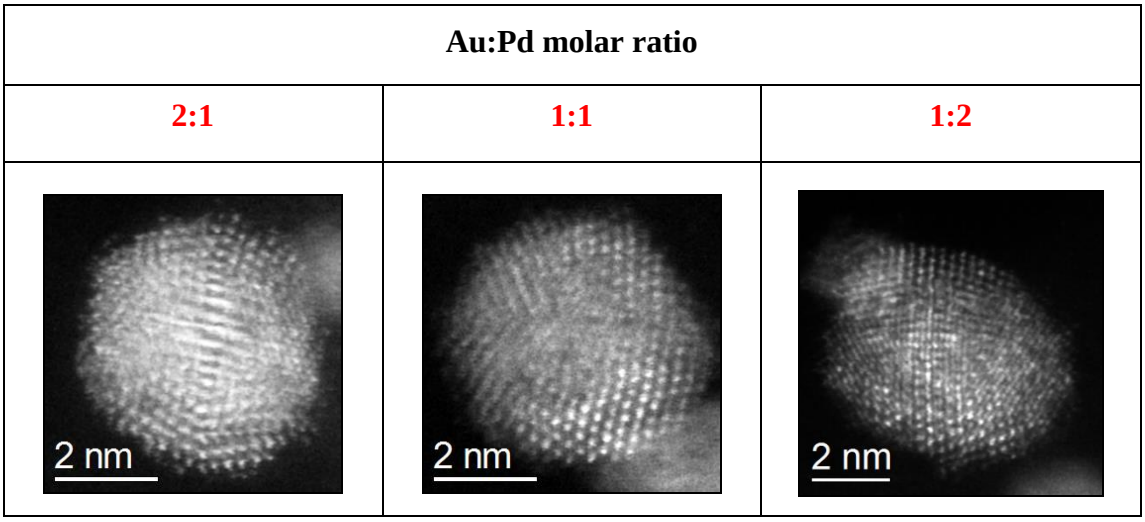

Figure 5.12 Representative STEM-HAADF images of homogeneous Au+Pd nanoparticles of varying Au:Pd molar compostion.

Indeed STEM-HADDF images of alloyed nanoparticles present in Au_2Pd_1, Au_1Pd_1 and Au_1Pd_2 compositions confirmed the existence of spherical, non-wetting homogeneous alloys with a face centred cubic, [f.c.c] structure formed exclusively with no evidence of core-shell/segregated Au-Pd structures by means of Z-contrast measurements (Figure 5.12). Despite the synthesis of random Au+Pd alloys, evidence of systematic composition variation with particle size was established when studying Au+Pd/C (Au:Pd = 1:7) and completely opposite to the composition variation exhibited by impregnation catalysts. The XEDS point analysis of 1-12 nm particles as shown in Figure 5.14 consistently highlighted the existence small Au-rich particles, intermediate Au+Pd particles and large Pd-rich particles across the support.

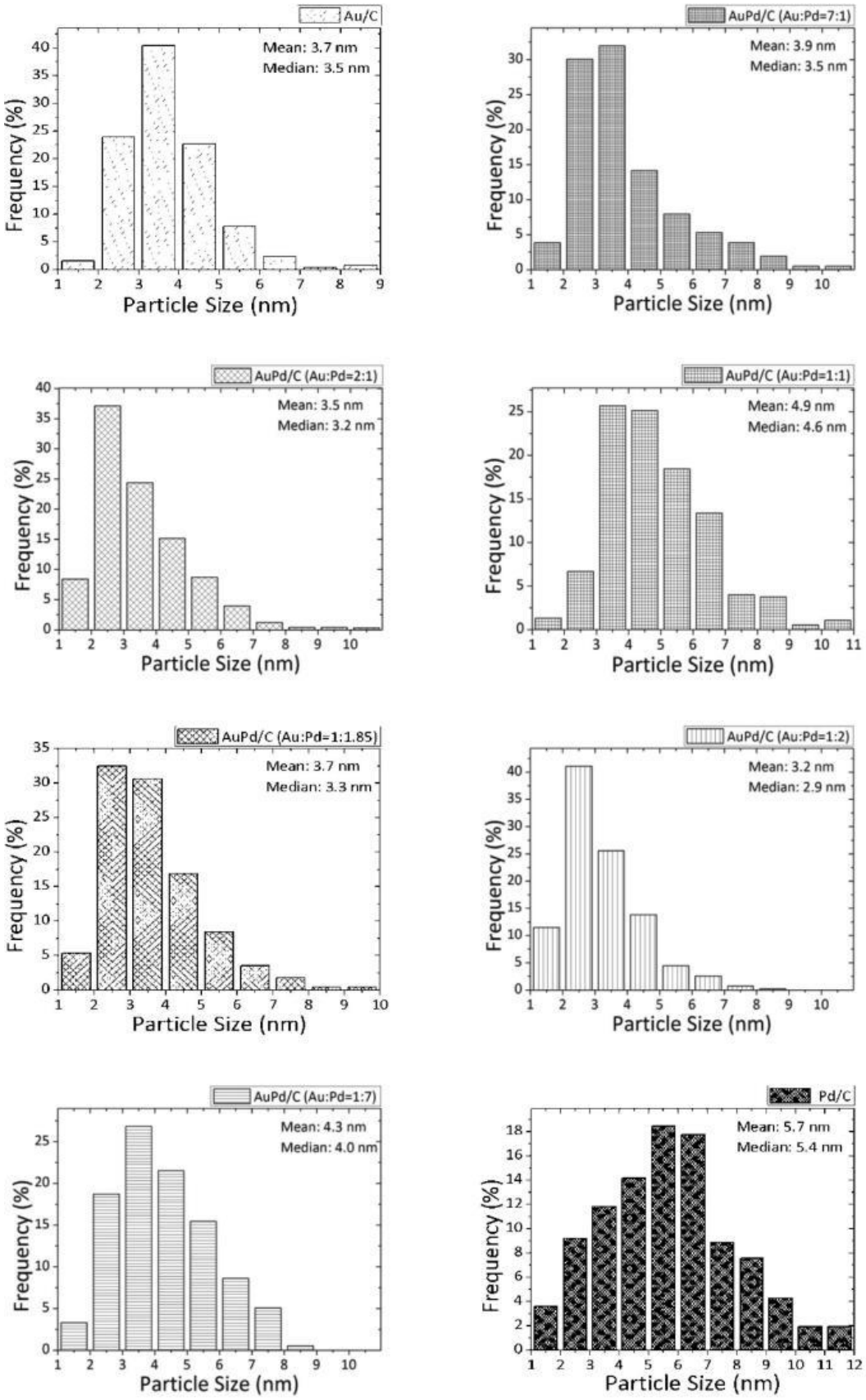

Figure 5.13 Summary of particle size distributions for Au_xPd_y particles immobilized on carbon: (a) Au only, (b) Au:Pd=7:1, (c) Au:Pd=2:1, (d) Au:Pd=1:1, (e) Au:Pd=1:1.85, (f) Au:Pd=1:2, (g) Au:Pd=1:7, and (h) Pd only**.**

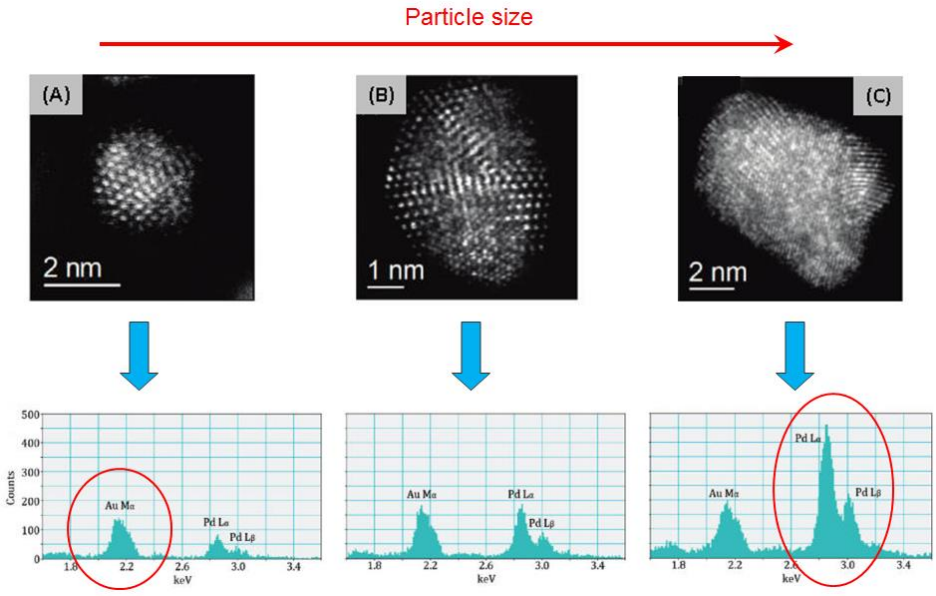

Figure 5.14 XEDS point spectra measurements of HAADF imaged nanoparticles, analysing the low (a), medium (b) and high (c) of the particle size distribution in Au+Pd/C (Au:Pd = 1:7).

The contribution of Ostwald ripening[35-37] and/or support mediated sintering of Au+Pd nanoparticles was discounted after XEDS analysis of the starting colloid (Au:Pd = 1:1.85) detected a similar systematic composition variation within which Pd content increased with particle size (Figure 5.15 (left)). The size distribution upper limit increased by ~2 nm after the Au+Pd colloid was immobilized on carbon and dried at 110 ^{o}C (Figure 5.15, right) with the Pd wt% for the majority of particles in the 2-7 nm range remaining intact. It is probable that differences in the reduction rates of Au^{3+} and Pd^{2+} species during 'co-reduction' could lead to particle agglomeration and subsequently compositional inhomogeneity.

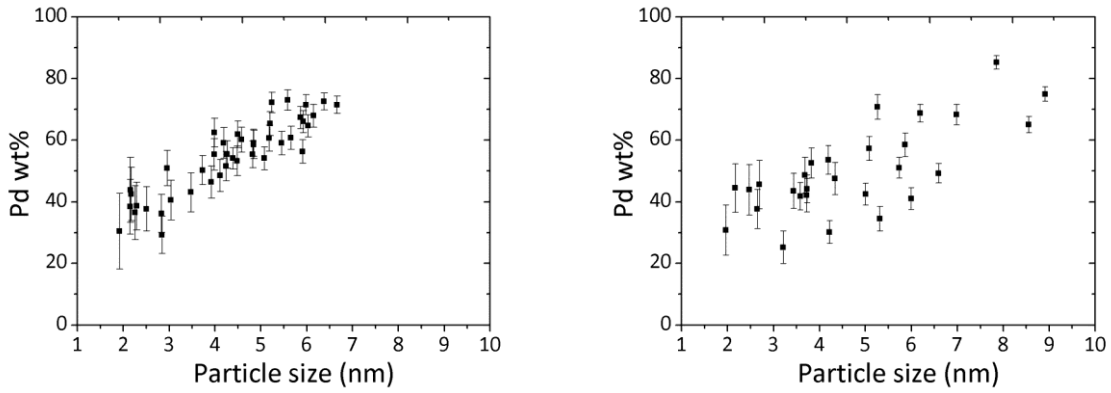

Figure 5.15 Particle size composition scatter diagrams of the Au-Pd colloid (Au:Pd = 1:1.85) before (left) and after immobilization on carbon and drying at 110 ^{o}C for 16 h (right).

5.6.3 Effect of Au:Pd molar ratio on H_2O_2 synthesis and hydrogenation

High H_2O_2 productivities were demonstrated after 2 and 30 minute reactions using sol-immobilized 1 wt% Au_xPd_y/C catalysts. The optimum composition, Au_1Pd_2 exhibited a productivity of 188 $mol_{H2O2}kg_{cat}^{-1}h^{-1}$, forming 0.38 wt% H_2O_2 after 30 minutes and closely followed by the $Au_1Pd_{1.85}$/C composition. After 2 minutes, the latter composition produced 0.10 wt% H_2O_2 - comparable to the yield obtained using a 2.5 wt% Au-2.5 wt% Pd/TiO_2 catalyst prepared by wet impregnation after a 30 minute reaction and indicating improved utilisation of Au and Pd metals via colloidal immobilization.

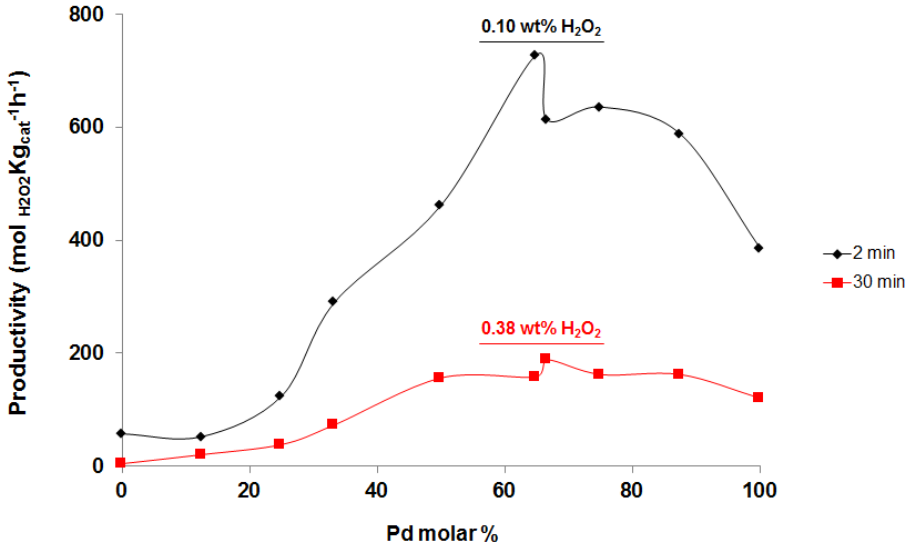

Figure 5.16 The effect of Au:Pd molar ratio on the H_2O_2 productivity of 1 wt% Au_xPd_y/C sol-immobilized catalysts after 2 and 30 minute reaction times – optimum yield (wt%) denoted.

Hydrogen peroxide productivity and Au_xPd_y composition, denoted as Pd molar% in scatter profiles obeyed an asymmetric 'volcano' relationship situated between the low and surprisingly high productivities demonstrated by Au/C and Pd/C (120 $mol_{H2O2}kg_{cat}^{-1}h^{-1}$) catalysts respectively. XPS showed the monometallic Pd catalyst comprised both Pd^{2+}/Pd^0 species, and exhibited the highest Pd^{2+} concentration out of all the compositions investigated. The mean particle size of monometallic Pd/C was only 1-2 nm greater than Au_xPd_y alloys, with a majority of particles remaining 6 nm or less in size, factors that could facilitate the reduced albeit still elevated rate of H_2O_2 hydrogenation that is recognised in Figure 5.17.

Representation of H_2O_2 production in terms of: **(i)** productivity / $mol_{H2O2}kg_{cat}^{-1}h^{-1}$, and **(ii)** turnover frequency / h^{-1}, taking into account total number of Au+Pd moles in each sample both followed an asymmetric 'volcano' relationship as a function of Au_xPd_y composition. Furthermore, particle counting and surface area measurements of spherical Au+Pd particles imaged in bright field TEM analysis of $Au_1Pd_{1.1.85}$/C estimated a high turnover frequency of 31,000 molecules H_2O_2 surface $atom^{-1}$ h^{-1}, compared to a value 2183 mol H_2O_2 mol_{metal}^{-1} h^{-1} calculated from nominal Au:Pd metal loadings.

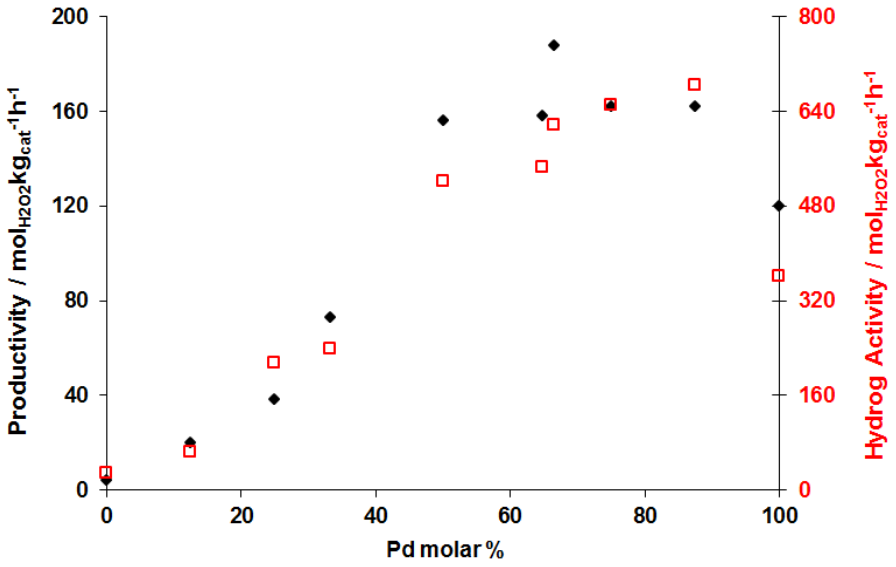

Figure 5.17 The effect of Au:Pd molar ratio on the H_2O_2 productivity *(black diamonds)* and hydrogenation activity *(red squares)* of 1 wt% Au_xPd_y/C sol-immobilized catalysts after 30 minute reaction time.

The most active Au_xPd_y catalysts for H_2O_2 synthesis also gave the highest rates of sequential hydrogenation, correlating with an increase in Pd content with the notable exception of monometallic Pd/C and implying that the addition of Au to Pd actually enhanced the rate of H_2O_2 hydrogenation, with the highest rate achieved by Au_1Pd_7/C (683 $mol_{H2O2}kg_{cat}^{-1}h^{-1}$). Referring to previous XPS analysis of sol-immobilized Au, Pd and Au+Pd/C catalysts by Carley *et al*. and listed in Table 5.6, it is suggested that random alloying of Au and Pd components promotes an increased surface Pd molar concentration coupled with a gradual reduction in Pd^{2+}/Pd^0 ratio, which is highest for the monometallic Pd/C catalyst.

Catalyst	Surface molar %		
	Au	**Pd**	**Pd/Au**
Au/C	0.0251		
Pd/C		0.0141	
AuPd/C	0.0166	0.0219	1.32

Table 5.6 Surface molar concentrations for sol-immobilized 1 wt% Au, Pd and Au_xPd_y/C (Au:Pd = 1:2) catalysts[34].

The fact that addition of Au to Pd improves not only the rate of hydrogen peroxide production but also its sequential hydrogenation to water represents a negative consequence of synergy when attempting to synthesise an intermediate as opposed to a total oxidation product. Despite this conclusion, small immobilized Au-Pd nanoparticles are still superior in terms of productivity and H_2O_2 yield (values in reality are much higher when eliminating the hydrogenation factor). To conclude section 5.6, we intend to continue optimization studies of Au+Pd colloids with the objective of minimising the rates of H_2O_2 hydrogenation over catalyst without significantly compromising particle size and compositional distributions.

5.7 The stability of sol-immobilized Au-Pd catalysts

Sol-immobilized 1 wt% Au+Pd/C and TiO_2 catalysts (Au:Pd = 1:2) were found to be unstable for the direct synthesis reaction on repeat use (Figure 5.18). Over four reactions, the H_2O_2 synthesis activity of Au+Pd/TiO_2 steadily decreased from 31 to 12 $mol_{H2O2}kg_{cat}^{-1}h^{-1}$ while the fraction of the initial activity lost on each successive use of Au+Pd/C increased, and after four reactions was approximately one-third of the initial activity (51 $mol_{H2O2}kg_{cat}^{-1}h^{-1}$) but still exceeded the activity of TiO_2-supported catalysts. Under standard reaction conditions there is a possibility of hydrogen peroxide facilitating the decomposition of the PVA ligands, compromising the structure of colloidal nanoparticles and leading to agglomeration, which is suggested in upcoming microscopy (Figure 5.19).

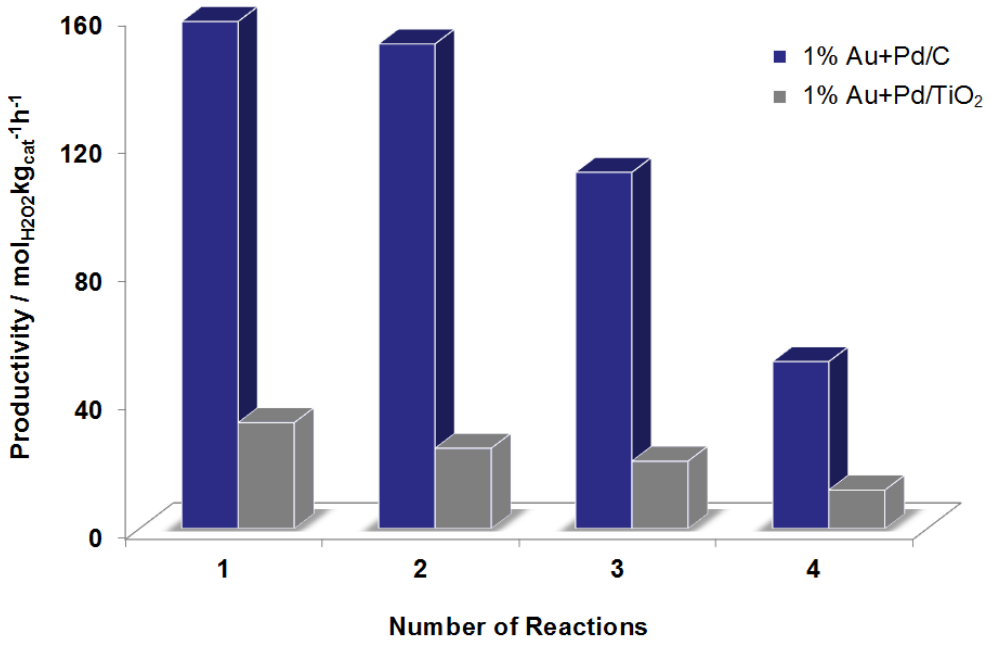

Figure 5.18 Evaluation of the catalyst reusability of sol-immobilized 1 wt% Au+Pd/C and TiO_2 catalysts for the direct synthesis of hydrogen peroxide (dried at 110 ^oC, 16 h).

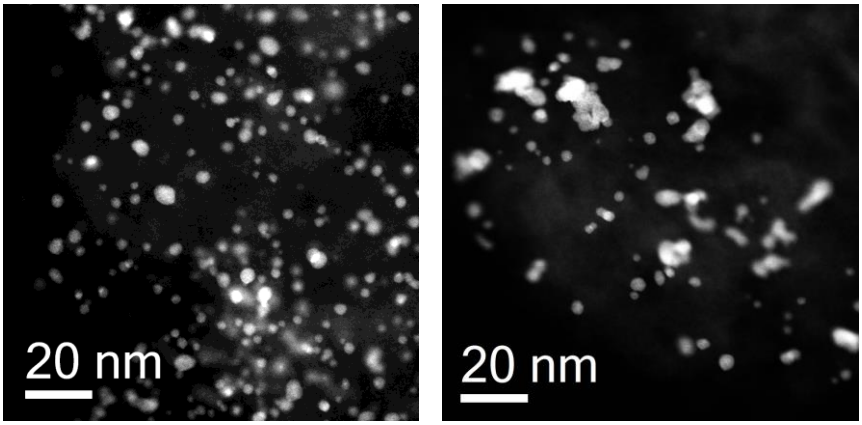

Figure 5.19 STEM-HAADF images of 1 wt% Au+Pd/C before (left) and after (right) 3 x H_2O_2 synthesis reactions (right).

STEM-HAADF imaging of the 1 wt% Au+Pd/C catalyst before and after three consecutive synthesis reactions showed the agglomeration of many <5 nm particles into nanoparticles several times larger in diameter, which are responsible for the residual H_2O_2 productivity on each subsequent use. Elemental mapping was used to study the composition of nanoparticles present on carbon recovered after 3 x H_2O_2 synthesis indicated minimal variation in Au:Pd composition relative to the starting colloid (Au:Pd = 1:1.85) and sintered particles generally maintained their homogeneous composition as oppose to forming phase-separated/core-shell structures (Figure 5.20). Currently, the concentration of PVA ligands on a sol catalyst recovered after reaction(s) cannot be quantified because visualisation of ligands in either the bright field (BF) or high angle annular dark field (HAADF) modes cannot be achieved.

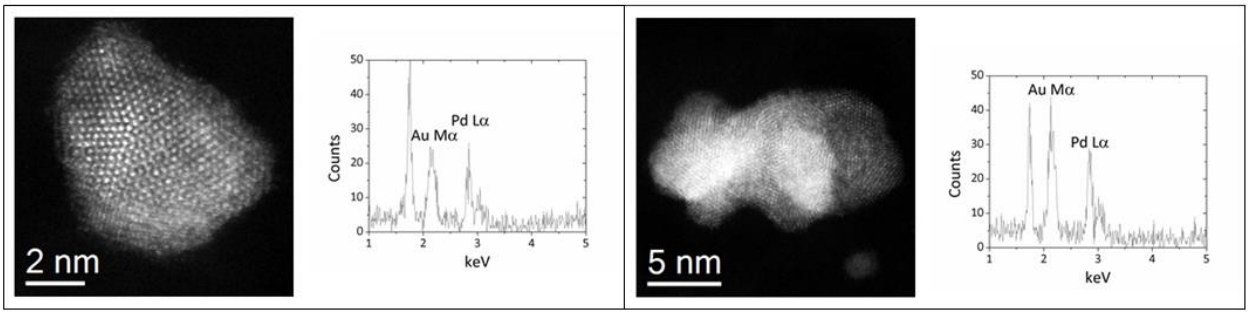

Figure 5.20 STEM-XEDS mapping spectra of 1 wt% Au+Pd/C after 3 x H_2O_2 synthesis reactions showing the composition of sintered nanoparticles: (left) a round-shaped, large particle, and (right) a large particle originating from agglomeration of 2-3 smaller nanoparticles.

XPS analysis of the used samples confirmed retention of a low nominal Pd/Au ratio on both carbon and TiO_2 supported catalysts (Table 5.7) and that Au and Pd surface concentrations were not significantly altered after each successive reaction, implying the agglomeration of nanoparticles sintering as being the primary cause of catalyst deactivation as oppose to metal leaching. SEM-EDX measurements also displayed consistent Au and Pd signals for the used samples in lieu of atomic absorption spectroscopy, given the carbon support cannot be dissolved in aqua-regia to liberate Au and Pd into solution and because any metal leached inside the autoclaves can readily deposit onto stainless components, preventing a true determination of metal leached into solution. Inductively Couple Plasma (ICP) analysis[34] previously used to show 100% immobilization of Au and Pd colloids on supports is planned to examine the used samples in future.

No. Reactions	**Surface atomic %**		**Pd/Au Molar ratio**
	Au	**Pd**	
Au+Pd/C			
1	0.51	1.08	1.62
2	0.49	0.92	1.39
3	0.47	0.92	1.49
Au+Pd/TiO_2			
1	0.09	0.15	1.29
2	0.10	0.19	1.36
3	0.12	0.19	1.13

Table 5.7 Surface atomic compositions of used Au+Pd/C and TiO_2 catalysts determined using X-ray photoelectron spectroscopy.

When planning the investigation to evaluate the use of sol-immobilized Au-Pd nanoparticles as catalysts for the direct synthesis of hydrogen peroxide, it was already understood that these materials were stable and could be reused several times with minimal differences in particle size and morphology for selective glycerol[37], benzyl alcohol[38] and toluene oxidation reactions[39]. It is now apparent that a post-modification step is mandatory in the development of a highly active, stable and reusable catalyst for direct H_2O_2 production.

Catalyst	**Productivity / $mol_{H2O2}kg_{cat}^{-1}h^{-1}$**	
	1st Use	**2nd Use**
Pd{Au}/C	155	115
Pd{Au}/TiO_2	24	18

Table 5.8 The effect of calcination at 200 ^oC in static air (3 h) on the reusability of sol-immobilized 1 wt% Pd{Au}/C and TiO_2 catalysts for the direct synthesis of hydrogen peroxide.

Calcination of sol-immobilized 1 wt% Pd{Au}/C and TiO_2 catalysts using a lower temperature of 200 ^oC (Table 5.8) still resulted in a loss of H_2O_2 productivity on repeat use and although further investigation is required, it appears unlikely based on this observation that a highly active and fully reusable catalyst can be derived using a single heat treatment step performed in static air, which is supported further by results for Au+Pd/TiO_2 listed in Table 5.9.

5.8 Comment on reflux and reduction methods

Refluxing of sol-immobilized catalysts in water to remove PVA ligands and retain particle size and composition were published recently in Nature Chemistry[40], demonstrating an optimum reflux temperature of 90 ^oC increased the activity of several reactions including CO oxidation, benzyl alcohol and glycerol oxidation (Appendix A5.2). Given the solvent composition used for hydrogen peroxide synthesis comprises 66 vol% MeOH: 33 vol% H_2O, the partial removal of PVA ligands during the course of the reaction is anticipated.

Catalyst	**Polymer / Treatment**	**Productivity / $mol_{H2O2}kg_{cat}^{-1}h^{-1}$**	**Hydrogenation / $mol_{H2O2}kg_{cat}^{-1}h^{-1}$**
Au+Pd/C	PVA	158	546
	PVA + Refluxed 90 ^{o}C	129	829
	PVA + Reduced 400 ^{o}C	40	525
Au+Pd/TiO_2	PVA	31	384
	PVA + Refluxed 90 ^{o}C	32	390
	PVA + Reduced 400 ^{o}C	51 [a]	320

Table 5.9 Summary of the H_2O_2 synthesis and hydrogenation activities for sol-immobilized 1 wt% Au+Pd/C and TiO_2 (Au:Pd = 1:1.85) catalysts prepared with additional reflux (water) or reduction steps. [a] denotes that catalyst can be reused without loss of activity.

A final set of experiments comparing the effect of water reflux and heat treatment in 5% H_2/Ar highlight two advantages of using TiO_2 as the support. Though rates of H_2O_2 synthesis are approximately 5-6 times lower over TiO_2-supported catalysts, refluxing the catalyst in water is not deleterious to activity and importantly reduction forms a more active and stable catalyst, neither of which are achieved using carbon as the support (Table 5.9).

The rate of H_2O_2 hydrogenation after reduction remains elevated due to the presence of high surface Pd^0 content and in future it may be possible to design more active catalysts with minimised hydrogenation activity *via* oxidation-reduction-oxidation (ORO) conditions instead of a single heat treatment step, which we concluded as being insufficient in forming a highly active and fully reusable catalyst, with minimal to no sequential H_2O_2 hydrogenation. Both characterisation of the reduced 1 wt% Au+Pd/TiO_2 catalyst and further investigation into the role of heat treatment on catalyst structure and activity will be undertaken in a follow-on study.

5.9 Discussion

It can be concluded from investigation into the preparation of Au+Pd, Au{Pd} and Pd{Au} colloidal nanoparticles that the order of Au and Pd metal reduction during colloid synthesis and prior to immobilization on carbon and TiO_2 supports can affect the resulting activity of catalysts active toward both the synthesis and hydrogenation of hydrogen peroxide as summarised for the carbon-supported series in Figure 5.21. Initial rates of H_2O_2 synthesis over sol-immobilized catalysts are exceptionally high and in some instances as much as 0.19 wt% H_2O_2 can be produced after 2 minutes, which is higher than many of the yields reported for 5 wt% catalysts prepared by wet-impregnation after 30 minutes. This also represents a 7-8 fold improvement in terms of turnover frequency given sol-immobilisation catalysts are prepared using 5 times less Au and Pd metal relative to impregnation.

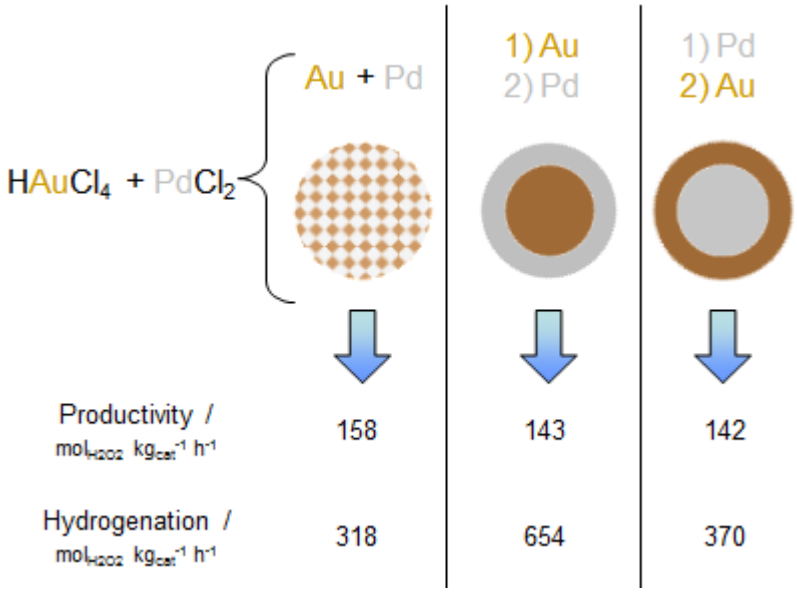

Figure 5.21 Summary of the H_2O_2 synthesis and hydrogenation activities by Au+Pd, Pd{Au} and Au{Pd} nanoparticles immobilized on carbon.

The H_2O_2 synthesis activities of sol-immobilized Au+Pd, Pd{Au} and Au{Pd}/C catalysts are approximately 5-6 times higher than their TiO_2-supported counterparts and characterisation of catalysts by advanced aberration corrected electron microscopy concludes a dramatically different particle structure and metal-support interaction manifests depending on the choice of support. Specifically, high resolution images of immobilized Au+Pd particles identified a non-wetting interaction between 'rounded' Au+Pd particles and activated carbon, compared to formation of an extended flat interface was between mainly 'faceted' Au+Pd

particles and TiO_2. The latter observation is evidence of surface wetting behavior and is independent of the order Au and Pd reduction during nanoparticle synthesis and is attributed to the development of strong metal-support interactions and consequently the displacement of PVA ligands in close proximity to metal-support interfaces.

Although the preparation of Au-Pd nanoparticles by sol-immobilisation was undertaken in order to generate catalysts of improved particle size and composition, microscopic analysis of nanoparticles before and after immobilisation onto carbon and TiO_2 did detect some off-centre cores, particles with incomplete shell coverage and those simply lacking the core-shell structure with respect to Pd{Au} and Au{Pd} colloids. The variation and non-uniformity in the Au-shell coverage of Pd-core particles is likely the result of insufficient 'shell' material being provided during nanoparticle formation. Estimates of the total weight fraction of the shell element theoretically required to obtain complete coverage of the core element with an integer number of shell layers has been considered for Au{Pd} and Pd{Au} nanoparticles using the Mackay icosahedral model and calcinations are summarised extensively elsewhere.

Briefly, one calculation performed for a 4.3 nm Au core (comprising 1415 Au atoms) showed that only 20 wt% of Pd was required to form a complete monolayer shell, compared to 45 wt% Au being required to form a complete monolayer shell around a 4.1 nm Pd core (again comprising Pd 1415 atoms). Given the wt% of Au present was fixed at 50 wt%, this amount would be insufficient for achieving a complete coverage of sub-3 nm Pd cores (as the size of core-shell particles decreases, the wt% of shell material required for monolayer coverage increases) during the preparation of Au{Pd} nanoparticles, which explains why many smaller Pd particles exhibited partial to no Au-shell coverage.

The study in chapter 5 also illustrates that use of a heat treatment step, specifically calcination in static air can dramatically affect both the morphology and oxidation state of metallic components in bimetallic Au-Pd nanoparticles. Characterisation of catalysts by XPS and STEM-HAADF suggested minimal oxidation of the Pd component during the 110 °C drying step, which was irrespective of Au+Pd, Pd{Au} and Au{Pd} nanoparticle structure or the support. On calcining the catalysts at 400 °C, significant changes were observed in the structure of nanoparticles immobilized on both carbon and TiO_2 supports.

For Au+Pd, Pd{Au} and Au{Pd}/C materials, calcination resulted in 'burn-off' of the carbon support and the sintering of nanoparticles to give an approximately 35 nm average particle size. However, for Au+Pd, Pd{Au} and Au{Pd}/TiO_2 counterparts, immobilized Au+Pd nanoparticles retained a random alloy structure and did not show evidence of phase separation, while interesting for Pd{Au} and Au{Pd} nanoparticle on TiO_2, development of (i) Au-rich particles associated with long PdO tails, (ii) Au-rich particles and (iii) PdO particles was tracked with increasing calcination temperature. The latter two morphologies suggest that monometallic Au and Pd particles are formed alongside core-shell nanoparticles during preparation of Au{Pd} and Pd{Au} nanoparticles.

A key of using a low temperature treatment is to remove the stabilising ligand from the catalyst, in this case PVA, which has been proposed as blocking active sites on the catalyst to an undetermined extent, without compromising the particle morphology and size of the 'starting sol'. It is evident that calcination temperature influenced the activity of Pd{Au} nanoparticles to a greater extent after immobilization onto carbon as oppose TiO_2. This is due to different degrees of particle growth between the supports, in addition to variation in Pd oxidation state (with calcination in air promoting the development of surface Pd^{2+}/PdO species) and the poorer thermal stability of the activated carbon, which appears to exacerbated for catalysts prepared by sol-immobilisation, in part perhaps due to the efficacy of very-small, Au^0-Pd^0 alloyed particles at catalysing the degradation of activated carbon.

Finally, a series of Au+Pd alloy colloidal nanoparticles having a range of Au:Pd ratios were immobilized on carbon and evaluated for hydrogen peroxide synthesis. Structural characterisation of the catalysts by UV-Vis spectroscopy indicated the disappearance of the surface plasmon resonance band associated with Au nanoparticles on developing Au+Pd/C catalysts, indicating the presence of alloying as also confirmed by transmission electron microscopy and XPS analysis. In all cases, the Au-Pd nanoparticles were found to be homogeneous alloys, with the optimum H_2O_2 synthesis activity attained using a catalyst with Au:Pd molar ratio of 1:2. Activity in terms of both H_2O_2 synthesis and hydrogenation obeyed a distorted 'volcano' relationship with increasing Pd molar content. Referring to XPS studies, the hydrogenation activity of Au+Pd/C catalysts was suggested to increase with rising Pd content due to systematic variation in the quantity of surface exposed Pd and Pd^0/Pd^{2+} ratio, which as a result cancels the positive effect of adding Pd to the Au nanoparticles.

Comparison of TOF values for bimetallic Au-Pd catalysts in Table 5.10 shows that approximately 7-8 times more hydrogen peroxide is produced per mole of metal when using sol-immobilized catalysts. At best this representation serves as an estimate because in reality it remains unknown how much and what exact phase of metal is 'active' for the direct synthesis of hydrogen peroxide.

Catalyst	**Productivity / $mol_{H2O2}kg\text{-}cat^{-1}h^{-1}$**	**TOF / $mol_{H2O2}\, mol_{Metal}^{-1}h^{-1}$**
0.5 wt% Au-0.5 wt% Pd/C S_{IM}	158	2183
0.5 wt% Au-0.5 wt% Pd/C C_{IM}	60	832
2.5 wt% Au-2.5 wt% Pd/C C_{IM}	110	303

Table 5.10 Turnover Frequency, TOF comparison for catalysts of different loading prepared by conventional, wet impregnation (C_{IM}) and sol-immobilization (S_{IM}) methods.

5.10 Conclusion

From the investigation into the preparation of Au+Pd, Au{Pd} and Pd{Au} colloidal nanoparticles, it was concluded that the order of Au and Pd metal reduction during colloid synthesis and prior to immobilization on carbon and TiO_2 supports can affect the resulting activity of catalysts active toward both the synthesis and hydrogenation of hydrogen peroxide. The H_2O_2 synthesis activities of sol-immobilized Au+Pd, Pd{Au} and Au{Pd)/C catalysts are approximately 5-6 times higher than their TiO_2-supported counterparts. Characterisation of catalysts by advanced aberration corrected electron microscopy concluded that a different particle structure and metal-support interaction manifests depending on the choice of support. Finally, a series of Au+Pd alloy colloidal nanoparticles having a range of Au:Pd ratios were immobilized on carbon and evaluated. For all catalysts, the Au-Pd nanoparticles were found to be homogeneous alloys, with the optimum H_2O_2 synthesis activity achieved using a catalyst with Au:Pd molar ratio of 1:2. Activity in terms of both H_2O_2 synthesis and hydrogenation obeyed a 'volcano' relationship with increasing Pd molar content, the hydrogenation activity of which was suggested to increasing with rising Pd content due to systematic variation in the quantity of surface exposed Pd.

5.11 References

1. J. C. Pritchard. L. Kesavan, M. Piccinini, Q. He, R. Tiruvalam, N. Dimitratos, J. A. Lopez-Sanchez, A. F Carley, J. K. Edwards, C. J. Kiely, G. J. Hutchings, *Langmuir*, **2010**, 26, 16568.
2. M. Haruta, *Faraday Discuss.*, **2011**, 152, 11.
3. L. Prati, G. Marta, *Gold Bull.*, **1999**, 32, 96.
4. F. Porta, L. Prati, M. Rossi, S. Coluccia, G. Marta, *Catalysis Today*, **2000**, 61, 165.
5. F. Porta, L. Prati, M. Rossi, G. Scari, *J. Catal.*, **2002**, 211, 464.
6. S. Biella, L. Prati, M. Rossi, *Inorg. Chim. Acta.*, **2003**, 349, 253.
7. M. Comotti, C. Della Pina, M. Rossi, A. Siani, *App. Catal. A. Gen.*, **2005**, 291, 204.
8. C. L. Bianchi, P. Canton, N. Dimitratos, F. Porta, L. Prati, *Catalysis Today*, **2005**, 102, 203.
9. N. Dimitratos, F. Porta, L. Prati, *App. Catal. A. Gen.*, **2005**, 291, 210.
10. J. Turkevich, G. Kim, *Science*, **1970**, 169, 873.
11. S. J. Mejia-Rosales, C. Fernandez-Navarro, E. Perez-Tijerina, D. A. Blom, L. F. Allard, M. Jose-Yacaman, *J. Phys. Chem. C.*, **2006**, 111**,** 1256.
12. V. I. Parvulescu, V. Parvulescu, U. Endruschat, G. E. Filoti, F. Wagner, C. Kubel, R. Richards, *Chem. Euro. J.*, **2006**, 12, 2343.
13. D. Wang, A. Villa, F. Porta, L. Prati, D. Su, *J. Phys. Chem. C.*, **2008**, 112, 8617.
14. M. R. Knecht, M. G. Weir, A. I. Frenkel, R. M. Crooks, *Chem. Mater.*, **2007**, 20, 1019.
15. S. Mandal, A. B. Mandale, M. Sastry, *J. Mater. Chem.*, **2004**, 14, 4.
16. M. L. Wu, D. H. Chen, T. C. Huang, *Langmuir*, **2001**, 17, 3877.
17. Y. Mizukoshi, K. Okitsu, Y. Maeda, T. A. Yamamoto, R. Oshima Y. Nagata, *J. Phys. Chem. B.*, **1997**, 101, 7033.
18. J. W. Hu, Y. Zhang, J. F. Li, Z. Liu, B. Ren, S. G. Sun, Z. Q. Tian, T. Lian, *Chem. Phys. Lett.*, **2005**, 408**,** 354.
19. G. Schmid, A. Lehnert, J. O. Malm, J. O. Bovin, *Angew. Chem.*, **1991**, 30, 874.
20. R. Ferrando, J. Jellinek, R. L. Johnston, *Chem. Rev.*, **2008**, 108, 845.
21. C. Kan, *J. Phys. D: App. Phys.*, **2003**, 36, 1609.
22. R. Harpeness, A. Gedanken, *Langmuir*, **2004**, 20, 3431.
23. D. Ferrer, A. Torres-Castro, X. Gao, S. Sepulveda-Guzman, U. Ortiz-Mendez, M. Jose-Yacaman, *Nano Lett.*, **2007**, 7, 1701.

24. D. Ferrer, D. A. Blom, L. F. Allard, S. Mejia, E. Perez-Tijerina, M. Jose-Yacaman, *J. Mater. Chem.*, **2008**, 18, 2442.
25. A. S. Shirinyan, M. Wautelet, *Nanotech.*, **2004**, 15, 1720.
26. N. Dimitratos, J. A. Lopez-Sanchez, D. J. Morgan, A. F. Carley, R. Tiruvalam, C. J. Kiely, D. Bethell, G. J. Hutchings, *Phys. Chem. Chem. Phys.*, **2009**, 11, 5142.
27. J. Zhang, H. M. Jin, C. B. Sullivan, F. Chiang, H. Lim, P. Wu, *Phys. Chem. Chem. Phys.*, **2009**, 11, 1441.
28. L. Guczi, *Catalysis Today*, **2005**, 101, 53.
29. J. K. Edwards, E. Ntainjua N, A. F. Carley, A. A. Herzing, C. J. Kiely, G. J. Hutchings, *Angew. Chem. Int. Ed.*, **2009**, 48, 8512.
30. G. Budroni, Preparation and Characterisation of Catalysts, PhD Thesis, *Cardiff University*, **2004**.
31. C. Samanta, *App. Catal. A. Gen.*, **2008**, 350, 133.
32. J. K. Edwards, B. E. Solsona, P. Landon, A. F. Carley, A. Herzing, C. J. Kiely, G. J. Hutchings, *J. Catal.*, **2005**, 236, 69.
33. C. L. Bianchi, P. Canton, N. Dimitratos, F. Porta, L. Prati, *Catalysis Today*, **2005**, 102, 203.
34. J. A. Lopez-Sanchez, N. Dimitratos, P. Miedziak, E. Ntainjua, J. K. Edwards, D. Morgan, A. F. Carley, R. Tiruvalam, C. J. Kiely and G. J. Hutchings, *Phys. Chem. Chem. Phys.*, **2008**, 10, 1921.
35. D. Alloyeau, G. Prevot, Y. Le Bouar, T. Oikawa, C. Langlois, A. Loiseau, C. Ricolleau, *Phys. Rev. Lett.*, **2010**, 105, 255901.
36. V. M. Burlakov, L. Kantorovich, *J. Chem. Phys.*, **2011**, 134, 024521.
37. G. L. Brett, P. J. Miedziak, N. Dimitratos, J. A. Lopez-Sanchez, N. F. Dummer, R. Tiruvalam, C. J. Kiely, D. W. Knight, S. H. Taylor, D. J. Morgan, A. F. Carley, G. J. Hutchings, *Catal. Sci. Technol.*, **2012**, 2, 97.
38. S. Meenakshisundaram, E. Nowicka, P. J. Miedziak, G. L. Brett, R. L .Jenkins, N. Dimitratos, S. H. Taylor, D. W. Knight, D. Bethell, G. J. Hutchings, *Faraday Discuss.*, **2010**, 145, 341.
39. L. Kesavan, R. Tiruvalam, M. H. Ab-Rahim, M. I. bin Saimon, D. I. Enache, R. L. Jenkins, N. Dimitratos, J. A. Lopez-Sanchez, D. W. Knight, S. H. Taylor, C. J. Kiely, G. J. Hutchings, *Science*, **2011**, 331, 195.

40. J. A. Lopez-Sanchez, N. Dimitratos, C. Hammond, G. L. Brett, L. Kesavan, S. White, P. J. Miedziak, R. Tiruvalam, R. L Jenkins, A. F. Carley, D. W. Knight, C. J. Kiely, G. J. Hutchings, *Nat. Chem.*, **2011**, 3, 551.

Chapter 6

6.1 Introduction

A range of supports have been successfully utilised for Au-Pd catalysts in the direct synthesis of hydrogen peroxide, with the monometallic Pd catalyst showing greater activity for the direct synthesis activity than the pure Au catalysts, the bimetallic Au-Pd catalysts, however, show higher activity than either the Pd or Au monometallic catalysts *i.e.* a synergistic effect is observed, all in the absence of any acid or halide promoters[1]. Interestingly, the morphology of the nanoparticles was shown to be support dependent, with metal oxide materials supporting Au core-Pd shell particles, and carbon supporting homogeneous Au-Pd alloys. Furthermore, acid treatment of TiO_2 and activated carbon prior to metal deposition during the catalysts synthesis results in materials far more active and selective in the direct synthesis reaction that still do not require chemical promoters[2, 3]. The support of choice for Pd catalysts, developed by Lunsford and Choudhary[5-7], is SiO_2, and whilst Au/SiO_2 catalysts were found by Ishihara[7] and Haruta[8] to show some activity for the direct synthesis of H_2O_2, this is small compared to Pd/SiO_2 catalysts.

While it was demonstrated in previous studies that TiO_2 and activated carbon give high activity for Au-Pd catalysts, both of these supports have some disadvantages from an industrial viewpoint. For TiO_2 it is possible that hydroperoxide species could be formed that can pose a hazard with any solvent used in the direct synthesis process, whereas for activated carbon the variability of the support material can pose problems in the manufacture of very large tonnage amounts required for commercial catalyst synthesis. The support of choice for a direct synthesis process is, however, silica. SiO_2 has been extensively used for Pd catalysts and these were initially studied by Lunsford and Choudhary[5-7], who found that SiO_2 can be used to prepare highly active catalysts with Pd nanoparticles as long as halides and acids are included in the reaction medium.

Studies have focussed on improving Pd dispersion on SiO_2 using techniques including the Stober method to form Pd core-silica shell particles, Pd@SiO_2, and have suggested the resultant stabilization of less co-ordinated Pd crystals in a highly dispersed state by core-shell formation is effective in achieving improved rates of H_2O_2 production[9]. Park *et al.* have investigated the effect of functionalizing SiO_2 and TiO_2 supports with SO_3H groups prior to depositing Pd metal on the rates of H_2O_2 synthesis[10-17], which resulted in improved H_2O_2 selectivity and yield realtive to untreated Pd/SiO_2 and Pd/TiO_2 catalysts, concluding that the SO_3H functionalized supports served as an alternative acid source for the direct synthesis reaction, illustrated in Figure 6.1. The same group has studied the effect of incorporationg Pd nanoparticles into $Cs_XH_{3-X}PW_{12}O_{40}$ containging heteropolyacid and MCF silica materials and identified a correlation betwen surface acidity and the activity exhibited by catalysts in the production of H_2O_2.

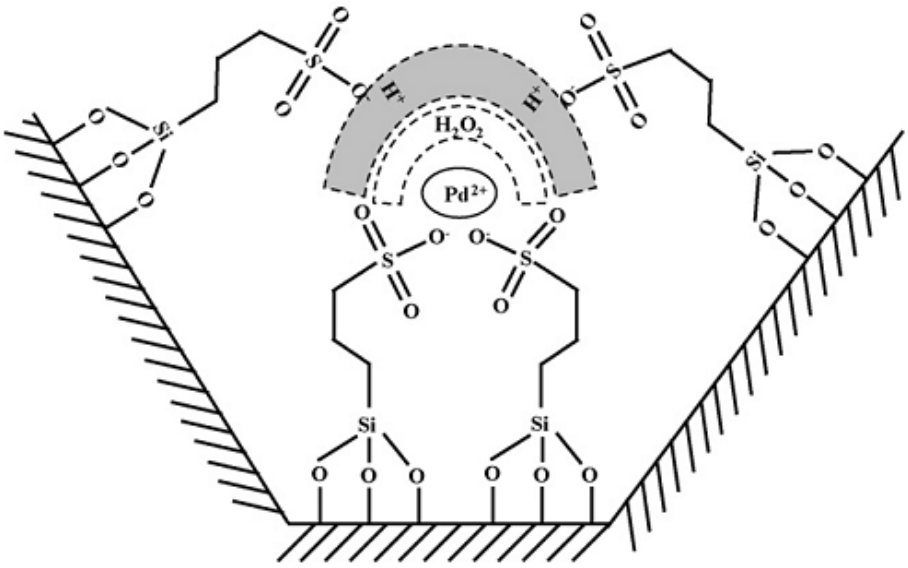

Figure 6.1 Schematic of the possible stabilisation effect[14] imparted by protonated sulfonyl groups on the H_2O_2 molecules produced by anchored Pd^{2+} species on mesoporous SiO_2.

Strukul[18] and Centi[19] have stated that high dispersion Pd can conversely be detrimental for hydrogen peroxide synthesis and leads to deactivation effects depending on the structure of the catalyst support. For example, Mesoporous SBA-15 silica possesses an ordered pore structure and small pores approximately 4 nm in diameter, whereas MCF silica has a characteristic disordered pore structure comprising large pores in the range 8-10 nm. Operation of the direct synthesis reaction under batch or semi-batch conditions and using a Pd/SBA-15 catalyst in CO_2-expaned methanol solvent resulted in catalyst deactivation due to loss of

exposed, active Pd metal through sintering and in-situ reduction by H_2 feed gas dissolved in solution - a more facile process on Pd/SBA-15 in comparison to Pd/SiO_2 counterparts. Specifically, the presence of ordered mesoporosity promoted migration of Pd metal into the SBA-15 channels to form elongated nanoparticles compared to the sintering of smaller Pd nanoparticles into 20-25 nm agglomerates[19, 20].

In a separate study[21], Strukul *et al.* reported 60% H_2 selectivity over a Pd/SiO_2 catalyst for the direct synthesis reaction under mild conditions, superior relative to both untreated and sulphated ZrO_2 and CeO_2 supports. With reference to HRTEM and chemisorption measurements, the selectivity was attributed to the ratio of more energetic, exposed sites on small Pd particles responsible for dissociative chemisorption of hydrogen peroxide and oxygen molecules (O atoms or OH species subsequently reacting with chemisorbed hydrogen to form H_2O), and less energetic, exposed Pd sites that can chemisorb oxygen in a non-dissociative manner (leading to formation of H_2O_2). The dependency of this conclusion as a function of Pd particle size is presented below (Figure 6.2).

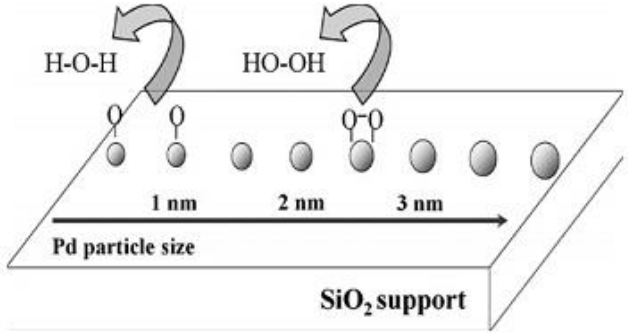

Figure 6.2 Schematic of dissociative behaviour of oxygen molecules chemisorbed on small Pd particles[21] supported on SiO_2.

This has prompted investigation into the use of SiO_2 as a catalyst support for hydrogen peroxide synthesis using supported Au-Pd nanoparticles. In this chapter, it is shown that highly active Au-Pd/SiO_2 catalysts can be indeed prepared and used for the direct synthesis of H_2O_2 without the addition of halide and acid promoters. In contrast to all previously studied oxide supports, acid pre-treatment of SiO_2 is required to observe synergy for the interaction of Au and Pd on this support and herein a detailed characterisation study of these materials is presented, both for bare supports and after wet impregnation of Au and Pd metals.

6.2 Effect of acid pre-treatment on H_2O_2 synthesis and hydrogenation activity

A series of Au, Pd and Au-Pd catalysts supported on SiO_2 (Johnson Matthey) were prepared by standard wet impregnation and calcined in static air. The SiO_2 support was also pre-treated in dilute nitric acid and washed prior to Au and Pd impregnation, following the procedure previously described in chapter 4. Table 6.1 shows that both the untreated and acid treated Au-only catalysts are active for H_2O_2 production and afford a reduced rate of H_2O_2 hydrogenation relative to the bare support. However, no synergy was observed for the bimetallic Au-Pd/SiO_2 catalyst compared to monometallic 2.5 wt% Pd/SiO_2 (53 vs. 51 $mol_{H2O2}kg_{cat}^{-1}h^{-1}$), which increased to 74 $mol_{H2O2}kg_{cat}^{-1}h^{-1}$ on doubling the catalyst loading to 5 wt% Pd.

Catalyst	**Productivity / $mol_{H2O2}kg_{cat}^{-1}h^{-1}$**		**Hydrogenation / $mol_{H2O2}kg_{cat}^{-1}h^{-1}$**	
	Untreated	**Acid Treated**	**Untreated**	**Acid Treated**
SiO_2	0	0	158	134
5% Au	7	7	112	104
2.5% Au-2.5% Pd	53	83	275	127
2.5% Pd	51	69	401	300
5% Pd	74	85	488	359

Table 6.1 Summary of H_2O_2 synthesis and hydrogenation activities over both untreated and acid treated 5 wt% Au, 2.5 and 5 wt% Pd and 2.5 wt% Au-2.5 wt% Pd/SiO_2 catalysts respectively. Samples were dried (110 ^oC, 16 h) and calcined in static air (400 ^oC, 3 h).

Acid pre-treatment of the support dramatically increased the H_2O_2 productivity of the bimetallic Au-Pd catalyst in addition to raising the activity of monometallic 2.5 and 5 wt% Pd catalysts, and considered to arise from an enhanced dispersion initiated by changes in Si-OH concentration, which will be discussed in section 6.4. Most importantly there is evidence of synergy between Au and Pd after acid pre-treatment, the H_2O_2 productivity of the bimetallic catalyst is improved to 83 $mol_{H2O2}kg_{cat}^{-1}h^{-1}$ compared to an activity of 69 $mol_{H2O2}kg_{cat}^{-1}h^{-1}$ obtained for 2.5 wt% Pd/SiO_2.

This increase in the productivity of monometallic Pd catalysts is more pronounced than for TiO_2- and carbon-supported counterparts, where minimal to no differences were reported. Acid pre-treatment of the support also reduced the sequential hydrogenation activity of all the catalysts, including the bare support. The rates of H_2O_2 hydrogenation in descending order were: 5 wt% Pd/SiO_2 > 2.5 wt% Pd/SiO_2 > 2.5 wt% Au-2.5 wt% Pd/SiO_2 > 5 wt% Au/SiO_2. Pre-treating the support in nitric acid significantly decreased the hydrogenation activity of 5 wt% Au/SiO_2 and 2.5 wt% Au-2.5 wt% Pd/SiO_2 catalysts below the rate observed over the bare support (134 $mol_{H2O2}kg_{cat}^{-1}h^{-1}$), in both instances indicating that Au and Pd metals are not introducing the sites responsible for the observed hydrogenation activity.

6.3 Catalyst Reusability

The rates of H_2O_2 production over untreated and acid treated 2.5 wt% Au-2.5 wt% Pd/SiO_2 catalysts decreased on second use irrespective of calcination in static air (Table 6.2). The productivity of the acid treated Au-Pd/SiO_2 catalyst fell from 83 to 53 $mol_{H2O2}kg_{cat}^{-1}h^{-1}$, identical to the activity of the untreated catalyst after first use (Table 6.2). Li and co-workers have stated that the highly negatively charged surface of SiO_2 (IEP = pH ~2-3) limits the effective incorporation of anionic $[Au(OH)_xCl_{4-x}]^-$ complexes derived from hydrolysis of the $HAuCl_4$ precursor, resulting in the formation of large Au particles (>10 nm) and impacting on the extent of Au-Pd alloying[22] (discussed in section 6.4).

Productivity / $mol_{H2O2}kg_{cat}^{-1}h^{-1}$	**Untreated**		**Acid Treated**	
	1st Use	**2nd Use**	**1st Use**	**2nd Use**
Dried 110°C	131	n.d	158	n.d
400°C	53	27	83	53

Table 6.2 H_2O_2 productivities of bimetallic 2.5 wt% Au-2.5 wt% Pd catalysts supported on untreated and acid treated SiO_2, and the effect of calcination temperature on the resulting activity and reusability of catalysts. n.d = not determined for this study.

Atomic absorption experiments summarised in Table 6.3 show that both untreated and acid treated 2.5 wt% Au-2.5 wt% Pd/SiO_2 catalysts (calcined 400 °C, 3 h) leached Au and Pd metal during the H_2O_2 synthesis reaction. The total metal leached did not exceed 20% of the original loading with at least 2 wt% Au and 2 wt% Pd remaining after reaction, implying the calcination in static air has introduced partial stability, given that >90% Au and Pd loss has previously been reported for uncalcined materials. Interestingly, more leaching was detected for acid treated Au-Pd/SiO_2 particularly with respect to Au content and likely representing an artefact of changes in the structure of the SiO_2 support induced by acid pre-treatment.

Au-Pd / SiO_2	**Untreated**		**Acid treated**	
	Fresh	**Used**	**Fresh**	**Used**
wt% Au	2.44	2.28	2.45	2.00
wt% Pd	2.46	2.32	2.59	2.13

Table 6.3 Summary of Atomic Absorption Spectroscopy studies to determine the initial and final metal loadings of bimetallic 2.5 wt% Au-2.5 wt% Pd catalysts prepared using untreated and acid treated SiO_2 supports, dried (110 °C, 16 h) and calcined in static air (400 °C, 3 h).

Despite retention of 80% or more of the original Au-Pd loading, there is considerable loss of activity on second use, indicating that not all of the metal impregnated onto the support is active for the direct synthesis reaction. Edwards *et al.* [23] have reported that the cyanide leaching of 5 wt% Au/SiO_2 catalysts did not result in significant loss of activity when tested for the oxidation of benzyl alcohol, despite almost no Au remaining on the catalyst, while Flytzani-Stephanopoulos[24] has separately demonstrated a similar result for the water gas shift reaction using leached Au/CeO_2 catalysts.

As a consequence of the low isoelectric point of SiO_2, control over particle size, composition and catalyst stability by means of a suitable heat treatment is limited, while the $PdCl_2$ precursor can be decomposed alone using high temperature reduction to form a stable monometallic Pd/SiO_2 comprising high surface Pd^0 concentration (Appendix A6.1). However, the hydrogenation activity of the catalyst is elevated through using reducing conditions and therefore it appears unlikely that manipulating the heat treatment alone will form a stable, fully reusable $Au\text{-}Pd/SiO_2$ catalyst synthesized from chloride precursors.

Comparison of oxidising and reducing heat treatments on the stability and H_2O_2 synthesis rates of bimetallic Au-Pd catalysts confirmed this is the case. Figure 6.3 shows that reducing the catalyst at 400-450 ^oC increased the H_2O_2 productivity from 53 to 138 $mol_{H2O2}kg_{cat}^{-1}h^{-1}$ (black bars) and decreased the loss of activity on repeat use (grey bars). Reduced Au-Pd/SiO_2 catalysts were also more active for H_2O_2 hydrogenation compared to the materials calcined in static air and consequently other methods to address the catalyst stability parameter will be discussed at the conclusion of chapter 6.

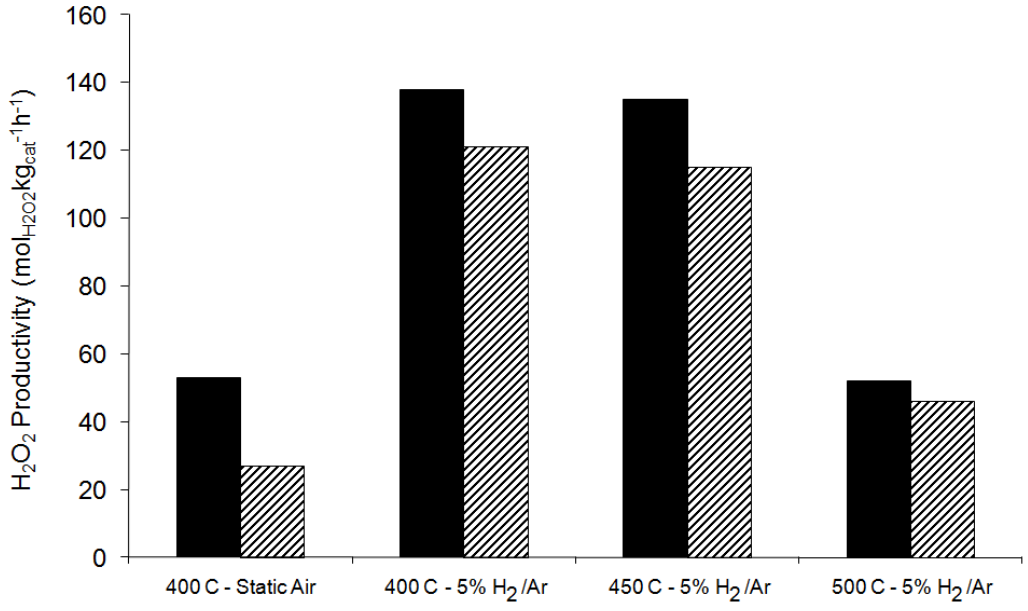

Figure 6.3 Comparison of the H_2O_2 productivities of 2.5 wt% Au-2.5 wt% Pd/SiO_2 catalysts prepared by standard impregnation on untreated SiO_2, dried (110 ^oC, 16 h) and calcined in static air or reduced in 5% H_2/Ar at different temperatures for 3 h total.

In sections 6.4 and 6.5, respectively, characterisation techniques have been applied to understand how acid-pre-treatment of SiO_2 modifies the structure of the bare support and the subsequent 2.5 wt% Au-2.5 wt% Pd/SiO_2 catalysts, where synergy between Au and Pd metals was only apparent after acid pre-treatment of the support.

6.4 Characterisation of the SiO_2 support

6.4.1 FT-IR ATR Spectroscopy

In an effort to determine the origin of the different activities observed for supported Au-Pd/SiO_2 catalysts (Table 6.2), the untreated and acid treated supports were characterised by spectroscopic, microscopic and bulk techniques. The supports were first compared using Fourier transform infra-red attenuated total reflectance (FT-IR ATR) spectroscopy**,** which revealed no discernible differences between the non-acid treated and acid pre-treated SiO_2 (Figure 6.4). In the IR spectrum, characteristic SiO_2 absorbance bands were observed for both supports and these were centred at 804, 977 and 1076 cm^{-1} and are assigned to Si-O-Si bending, and the Si-OH and Si-O-Si stretching modes respectively[25].

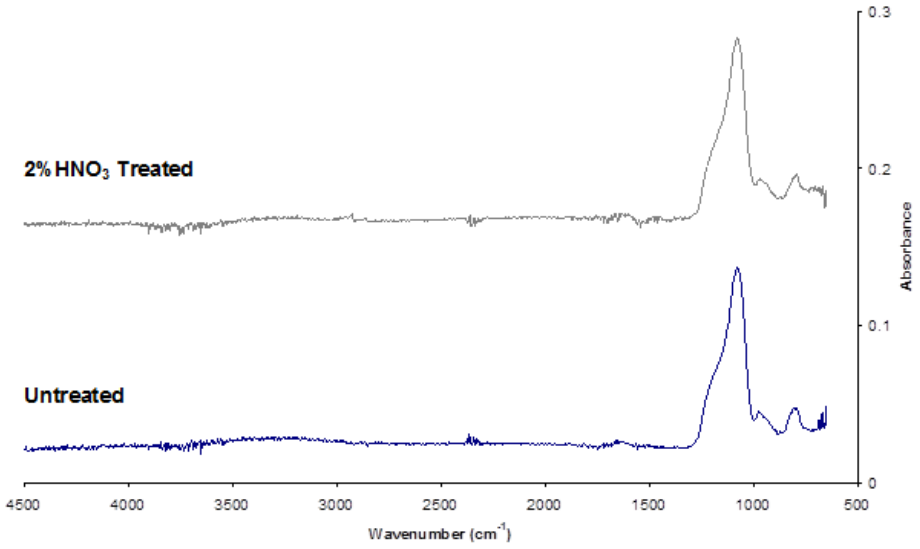

Figure 6.4 FT-IR ATR corrected spectra recorded for untreated (blue line) and 2% HNO_3 pre-treated (black line) SiO_2 supports.

6.4.2 Thermogravimetric Analysis

TGA reported near-identical mass losses (~3.1 wt%) for untreated and acid treated SiO_2 associated with loss of physisorbed water at temperatures up to 150 ^oC (Appendix A6.2), indicating that any water adsorbed during acid-pretreatment was sufficiently removed by the drying step (110 ^oC, 58 h). For both supports minimal mass losses were detected in the range 150-350 ^oC, which in conjunction with TPD experiments concluded that desorption of surface hydroxyl groups proceeds at higher temperature.

6.4.3 Temperature Programmed Desorption

Temperature Programmed Desorption profiles of untreated and the acid pre-treated SiO_2 supports showed a broad signal consistent with loss of physisorbed water from the support below approximately 200 ^oC. However, on increasing temperature a distinct difference was noted between desorption profiles with respect to the temperatures of desorption maxima (Figure 6.5).

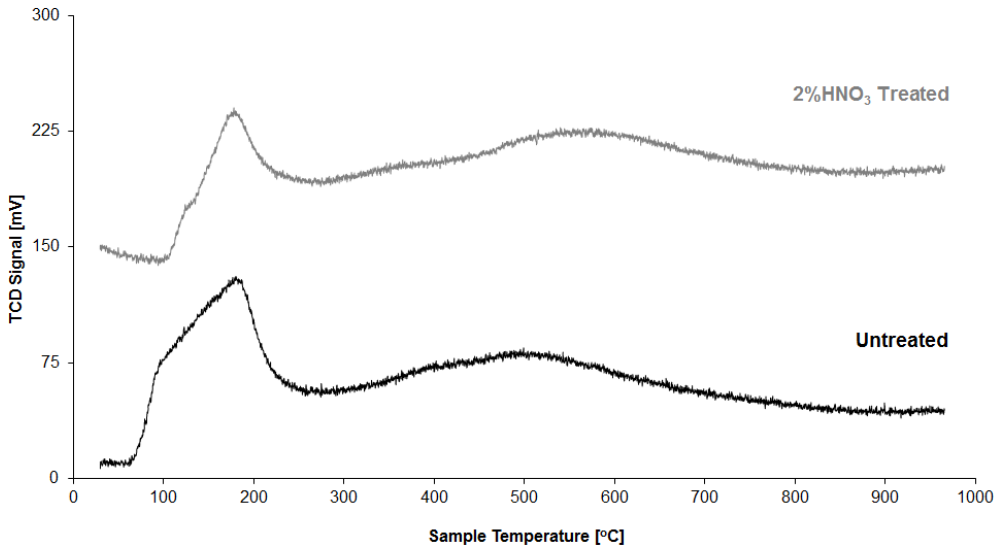

Figure 6.5 TPD profiles recorded for untreated and 2% HNO_3 pre-treated SiO_2 supports. Experiments were performed without the magnesium perchlorate filter to permit the detection of OH and H_2O species.

The signal intensity broadly increased by 20-30 mV upon further increasing temperature, resulting in a peak maximum centred at 500 ^{o}C for as-received SiO_2 and a higher value of 560-570 ^{o}C for the acid pre-treated SiO_2 comparable feature. These desorption features are associated with Si-OH surface hydroxyl functionalities, which are known to decompose and desorb from the silica surface at higher temperatures due to enhanced hydrogen and covalent bonding properties[26].

The observed difference of 60 ^{o}C in the maxima of these features far exceeds experimental error and may, therefore, be interpreted as a true contrast in the nature of the Si-OH groups present on each support in terms of their respective concentration and arrangement on the support surface. Additional comparison was made between pre-treating the support with dilute nitric and acetic acids, the latter of which displayed a further increase in the peak maximum temperature for Si-OH desorption (Figure 6.6), although this change in desorption behaviour does not constitute a further decline in H_2O_2 hydrogenation activity (Table 6.4).

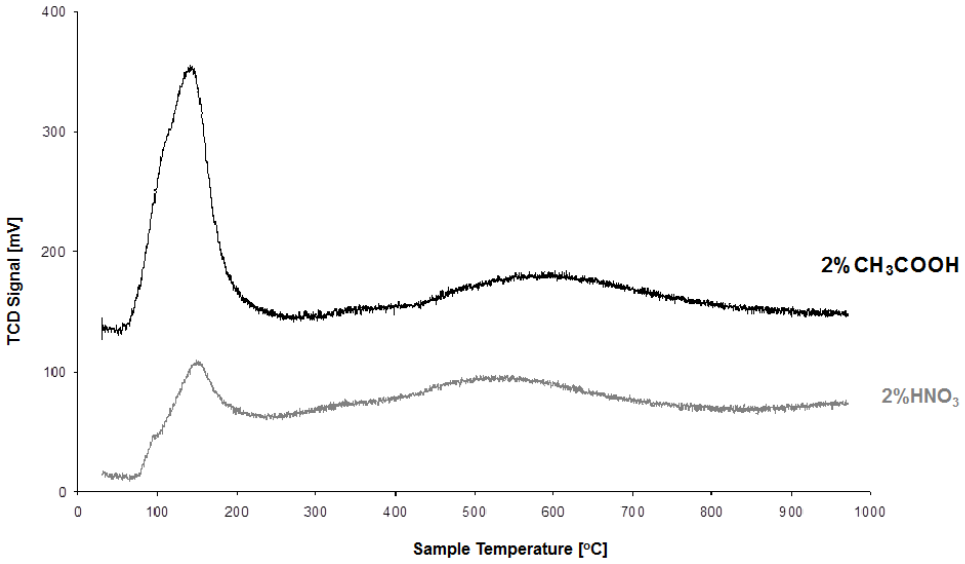

Figure 6.6 TPD profiles recorded for nitric and acetic acid pre-treated SiO_2 supports. Experiments were performed without the magnesium perchlorate filter to permit detection of OH/H_2O species.

Catalyst	**Productivity / $mol_{H2O2}kg_{cat}^{-1}h^{-1}$**	**Hydrogenation / $mol_{H2O2}kg_{cat}^{-1}h^{-1}$**
SiO_2		
Untreated	0	158
2% HNO_3	0	134
2% CH_3COOH	0	4
2.5 wt% Au-2.5 wt% Pd/SiO_2		
Untreated	53	275
2% HNO_3	83	127
2% CH_3COOH	**91**	**237**

Table 6.4 Summary of the H_2O_2 synthesis and hydrogenation activities obtained for untreated, nitric acid and acetic acid pre-treated SiO_2 supports and 2.5 wt% Au-2.5 wt% Pd/SiO_2 catalysts respectively. Samples were dried (110 ^oC, 16 h) and calcined in static air (400 ^oC, 3 h).

6.4.4 Inelastic Neutron Scattering

Figure 6.7 shows the inelastic neutron scattering (INS) spectra of the untreated SiO_2 support (black line), the acid-treated SiO_2 (red line) and the difference (blue line) recorded at 4840 cm^{-1} (600 meV) and 2017 cm^{-1} (250 cm^{-1}) incident energies respectively. The vertical displacement of the acid treated relative to the untreated support is a consequence of the increased hydrogen content of the former.

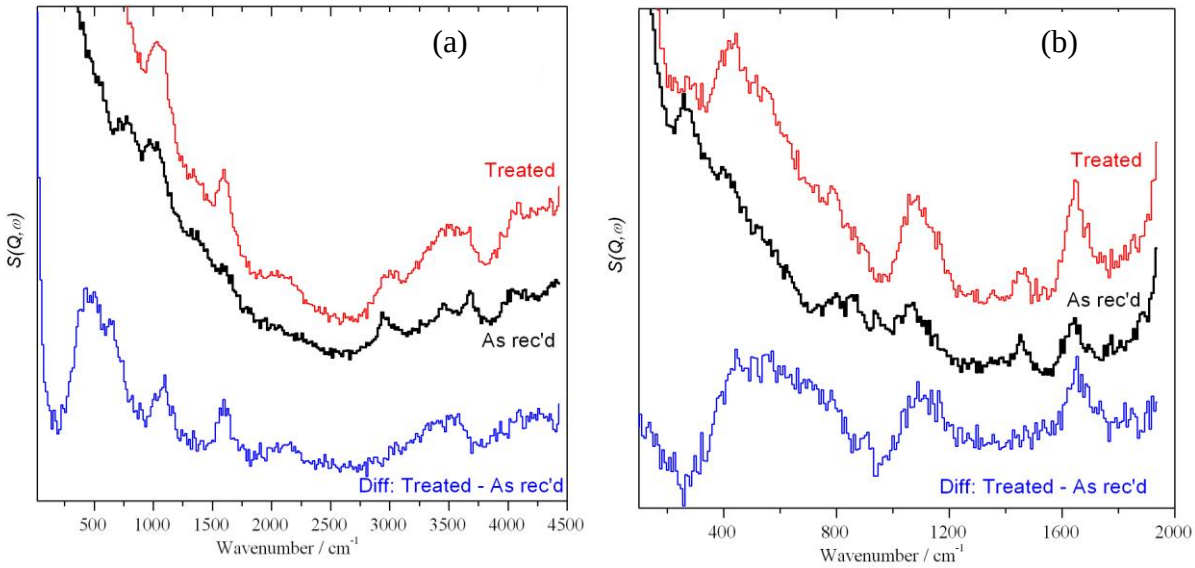

Figure 6.7 INS spectra of untreated (as-received / black line) and acid pre-treated (treated / red line) SiO_2 with 600 (a) and 250 (b) meV incident energies respectively.

There are clear differences between the two samples: in the acid-treated sample the intensity in the O–H stretch region (~3500 cm^{-1}) has increased as have the bands at 1635, 1070 and 430 cm^{-1}. The 1635 and 430 cm^{-1} bands can be assigned to the bend and vibrational modes of H-O-H (water) respectively[27]. The feature at 1070 cm^{-1} that has markedly increased, is assigned to the in-plane Si–O–H bending mode of a hydroxyl group[28, 29]. Since the integrated intensity of an INS transition is directly proportional to the number of scattering centres in the path of the beam, it is estimated that the number of surface hydroxyls has increased by a factor of 2.3 as a result of the acid treatment. The amount of water present has also increased by a similar amount, presumably because there are more sites for hydrogen bonding. The weak peaks at 2940 and 1450 cm^{-1} that do not change probably originate from a small amount of hydrocarbon contamination in the silica.

INS spectra were also recorded for untreated and acid treated TiO_2 (Degussa P25) and carbon (Darco G60) supports respectively. At this time it is not possible to comment on any changes in the concentration of surface hydroxyl groups on carbon because of ice interference present in the spectrometer caused by freezing of trace water present on the support which was not removed despite prolonged drying in advance of experiments. Differences were however found in spectra recorded at the 250 and 600 meV incident energies for untreated and acid treated TiO_2 supports, in agreement with the observations made for SiO_2 (Figure 6.8). INS spectra reported an increase in the intensity in the O–H stretch region (~3500 cm^{-1}) for the acid treated TiO_2 samples and suggest a very small difference in the amount of water present (peak at 1600 cm^{-1}) and the possibility of a weak, broad feature at ~800 cm^{-1} consistent with hydroxyls, although this is right on the limit of detection and may be part of the tail of the water librational modes (onset at ~400 cm^{-1}).

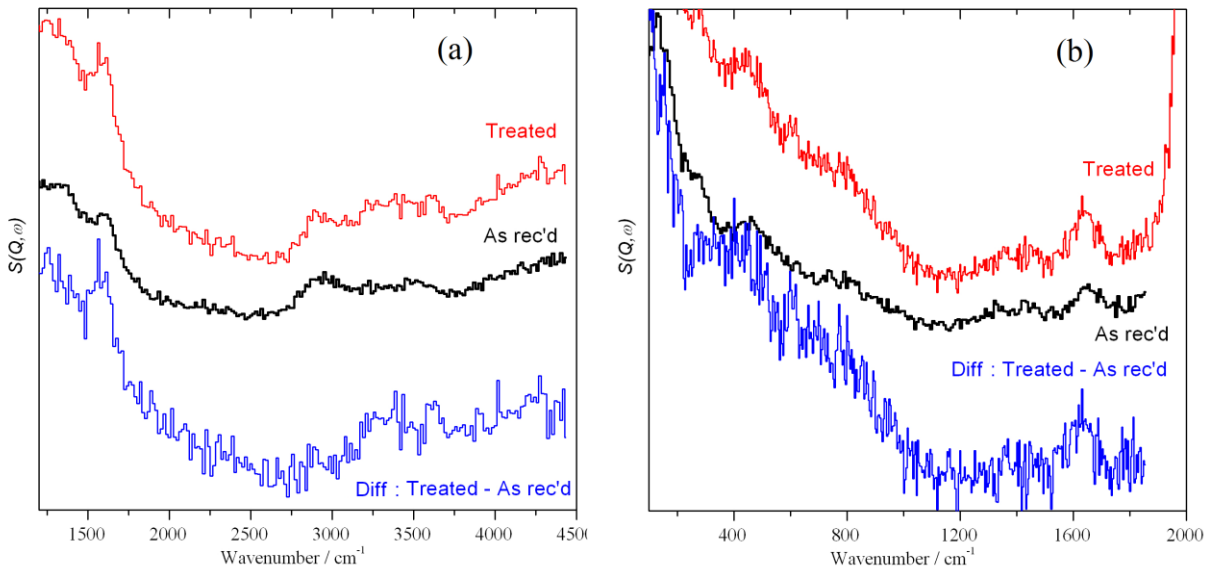

Figure 6.8 INS spectra of untreated (as-received / black line) and acid pre-treated (treated / red line) SiO_2 with 600 (a) and 250 (b) meV incident energies respectively.

6.4.5 X-ray photoelectron spectroscopy

The O(1s) XP spectra for both untreated and acid pre-treated SiO_2 supports might be expected to show features corresponding to increases in hydroxyl and water species, however, the spectrum obtained from SiO_2 has a binding energy overlapping with the expected position of OH(a) and H_2O adsorbed species, and therefore new components could not be observed. There is a small increase in the O/Si molar ratio after acid pre-treatment (from 2.3 to 2.4), but this is inside experimental error. In addition, there were no nitrogen containing species present on the sample within the detection limits of this technique after pre-treatment in nitric acid, functional groups that were incorporated when acid pre-treating the P25 TiO_2 support and implied in corresponding TPD profiles by very broad, low and high temperature decomposition signals (Appendix A6.3). However, these features are very difficult to distinguish in the INS spectra due to overlap with the O-H stretching region (Figure 6.8).

6.5 Characterisation of the Au-Pd/SiO_2 catalysts

6.5.1 Electron microscopy characterisation

The combined application of STEM and SEM techniques was used to characterize the metal dispersion in Au-Pd/SiO_2 catalysts prepared by standard impregnation and to effectively cover the very broad range of particle sizes recognised in these samples. Representative high angle annular dark field (HAADF) STEM images of both untreated and acid-treated 2.5 wt% Au-2.5 wt% Pd/SiO_2 catalysts presented in Figure 6.9 showed a large population of homogeneously dispersed particles in the 2-5 nm size range were found in both samples, with no significant differences observed in the particle size distribution.

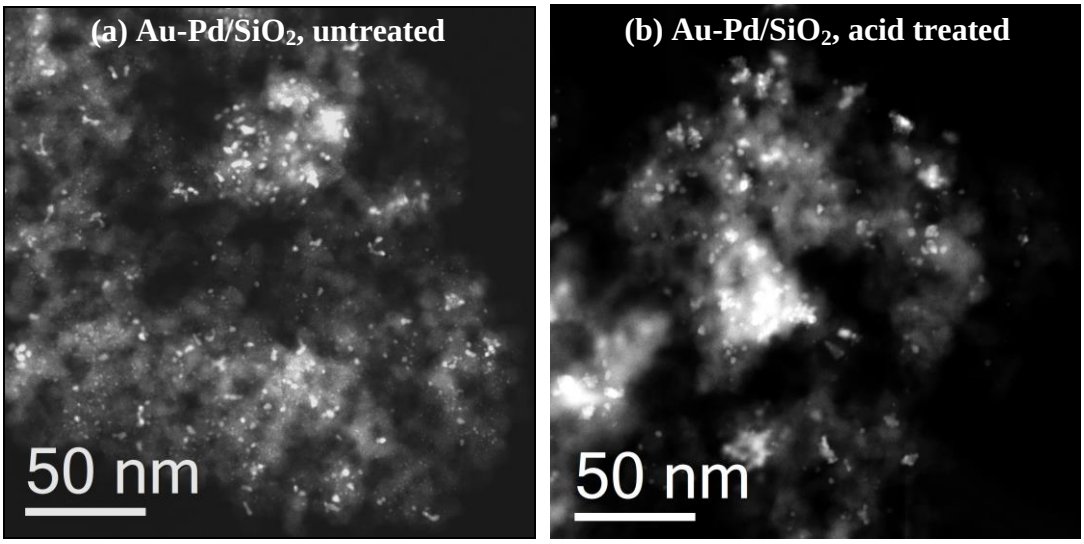

Figure 6.9 STEM-HAADF images of (a) untreated and (b) acid treated 2.5 wt% Au-2.5 wt% Pd/SiO_2 catalysts respectively.

Analysis of bimetallic catalysts by X-ray energy dispersive spectroscopy (XEDS) showed that the 2-5nm particles presented in both samples only exhibited the characteristic Pd-signal with no detectable Au content (Figure 6.10), implying that these particles were either Pd-only or contained occasional Au atoms (present at a level below the XEDS detection limit).

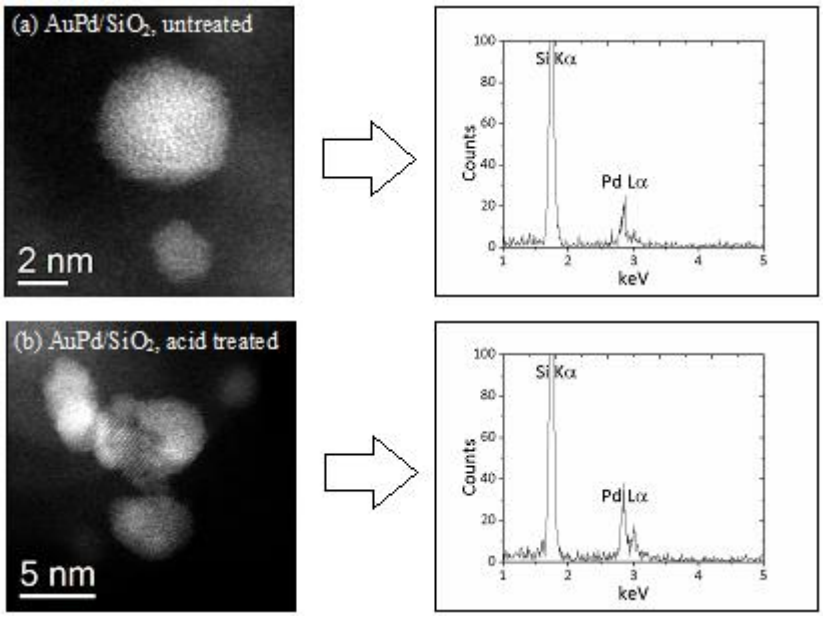

Figure 6.10 STEM-HAADF images and the corresponding XEDS spectra from individual nanoparticles in (a) untreated and (b) acid treated 2.5 wt% Au-2.5 wt% Pd/SiO_2 catalysts respectively.

The absence of the Au component in these samples can be explained by SEM-BSD (back-scatter detection) measurements displayed in Figure 6.11, which show that a significant proportion of the Au-rich particles present in both untreated and acid treated Au-Pd/SiO_2 samples are several hundred nanometres in diameter. XEDS analysis of these large particles did report a weak Pd signal, although it cannot be concluded from spectra whether particles were Au-Pd alloys or merely if the weak Pd signal originated from 2-5 nm Pd particles either adjacent or even underneath the larger Au-particles. Occasional μm scale Pd-rich particles were also detected in both samples with an associated strong Cl XEDS signal, suggesting that they could be residues from the $PdCl_2$ precursor insufficiently dissolved in the impregnation step.

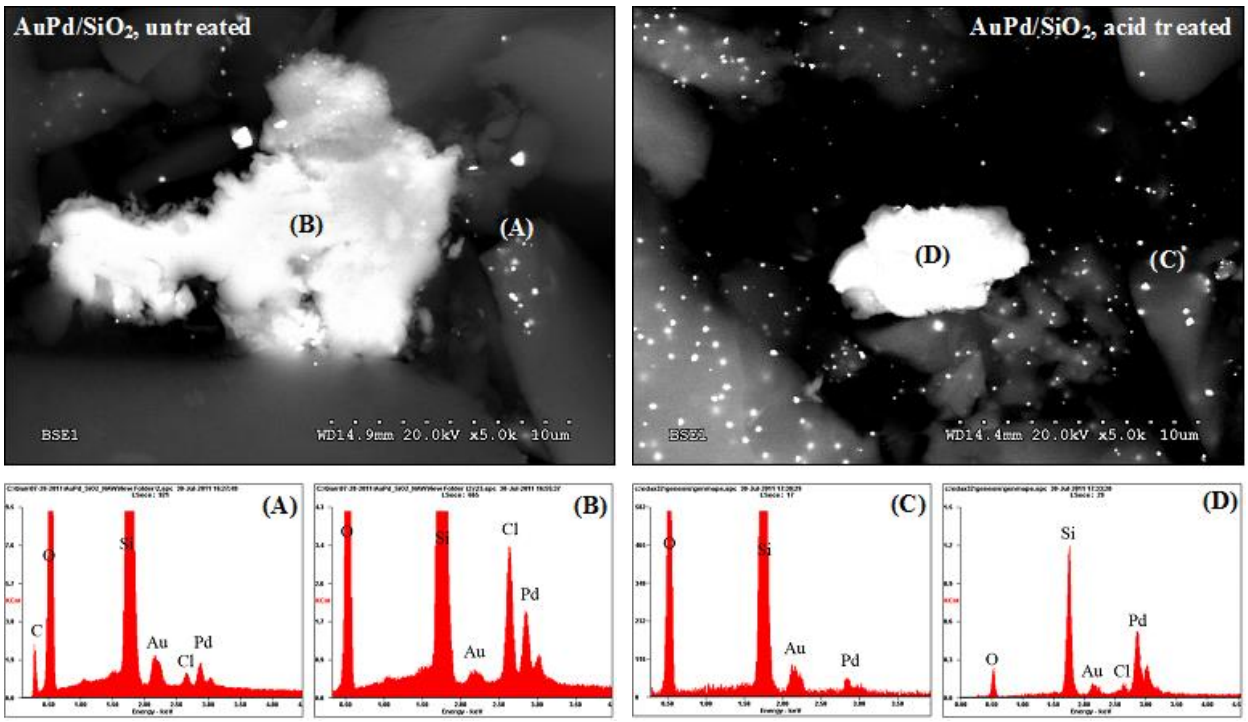

Figure 6.11 SEM-BSD images and XEDS spectra obtained from two areas of the untreated Au-Pd/SiO_2 catalyst (left), showing Au-rich particles that are several hundred nm in size (A), and large Pd-containing particles in excess of 10 μm, possibly originating from $PdCl_2$ (B). Spectra recorded for the acid treated Au-Pd/SiO_2 catalyst (right) also shows Au-rich particles several hundred nm in size (C), and Pd-containing particles around 10 μm in size (D).

Based on the observations made using both electron microscopy techniques, it is concluded that the wet impregnation method can only finely disperse the Pd component on the SiO_2 support, and that negligible structural or morphological differences are observed between the particles impregnated on the untreated and 2% HNO_3 pre-treated SiO_2 supports respectively.

6.5.2 X-ray photoelectron spectroscopy

Characterisation of Au-Pd catalysts supported on untreated and acid treated SiO_2 by X-ray photoelectron spectroscopy determined that in both samples the Pd is present as Pd^{2+} entirely (Figure 6.12). In addition very weak Au signals were detected in both samples, for the untreated support, the Au intensity is below detection limits and for the acid treated support the Pd:Au surface molar ratio is 18:1, a finding not in agreement with the formation of core-shell structures due to the imaging of Au-rich particles several hundred nm in size. Given that Pd particles 2-5 nm in size provides the majority of the exposed surface area in the catalysts, it is consistent that the Pd signal should be the dominant feature in the XPS spectra of both samples. From the XPS data it can be concluded that acid pre-treatment of the SiO_2 support improves the dispersion of Au compared to the untreated support, albeit to a minor extent as it is still evident that standard wet impregnation does not effectively disperse the $HAuCl_4$ precursor and hence Au metal onto the highly negatively charged surface of SiO_2.

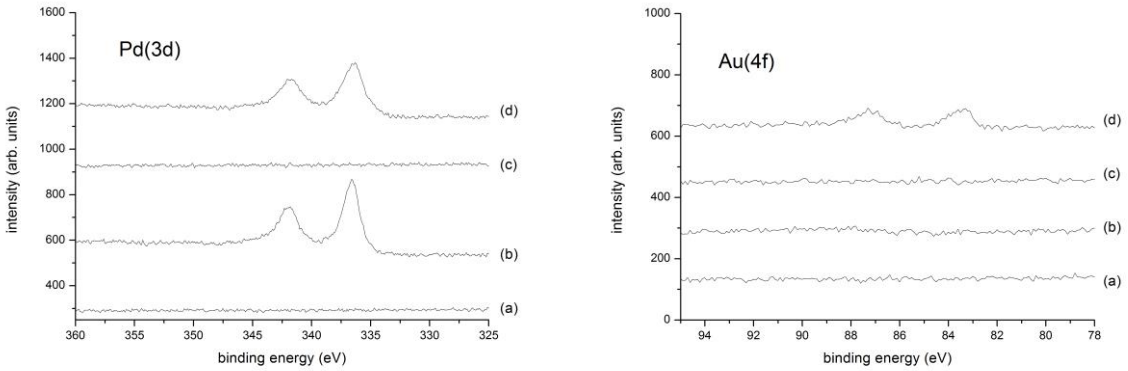

Figure 6.12 Pd(3d) and Au(4f) XP spectra recorded for (a) the bare untreated silica support, (b) 2.5 wt% Au-2.5 wt% Pd/SiO_2 prepared using the untreated support, (c) the bare acid treated silica support, and (d) 2.5 wt% Au-2.5 wt% Pd/SiO_2 prepared using the acid treated support.

6.5.3 Discussion

As stated in the paragraph above, Pd^{2+} species were detected (within the experimental limits of the technique) in both the untreated and acid pre-treated Au-Pd/SiO_2 catalysts, which were active for the hydrogenation of H_2O_2 (275 and 127 $mol_{H2O2}kg_{cat}^{-1}h^{-1}$ respectively). The XPS observation of improved Au dispersion, albeit to a lesser extent after acid pre-treatment is somewhat consistent with findings reported in chapter 3 for carbon-supported Au-Pd catalysts. However, while large Au particles (30-100 nm) were also detected on the carbon support for Au and Au-Pd/C samples, these particles were generally smaller than the several hundred nanometre particle sizes identified for silica-supported Au-Pd catalysts and could be imaged using bright field TEM microscopy as oppose to SEM measurements. The clear difference between supports is that subsequent hydrogenation of H_2O_2 can be switched-off on the carbon support, whereas it can only be moderately reduced for Au-Pd/SiO_2 counterparts, despite both catalysts comprising >90% surface Pd^{2+} concentration.

In addition, results presented in chapter 4 for Au-Pd/C catalysts also illustrate the important role of the Pd^{2+} oxidation state, and proposed alloying of Pd with a minor proportion of Au as contributing to the high observed surface Pd^{2+} concentration and constituting the unique switching-off phenomenon on G60 carbon pre-treated with nitric acid. Based on the differences in Pd/Au molar ratio, the implied development of Au-core Pd-shell nanoparticles and the type of functional groups present on each support (taking into account isoelectric point and possible influence(s) on catalyst stability), it is suggested these critical factors assist in explaining why the sequential hydrogenation of H_2O_2 is not switched-off on SiO_2-supported 2.5 wt% Au-2.5 wt% Pd catalysts in addition TiO_2-supported catalysts, as reported previously.

The lack of synergy induced between Au-Pd metals has prompted a short investigation into the preparation of bimetallic 2.5 wt% Au-2.5 wt% Pd catalysts on different SiO_2 and Si-based supports in section 6.6, including a Silicalite framework and zeolite ZSM-5. The acid pre-treatment of Si-Al containing supports and the consequential effect on leaching and catalyst activity has also been considered and discussed in response to the possible negative effects in SiO_2 pre-treatment and functionalization reported in the literature by Centi and Strukul groups respectively[18-20].

6.6 Comparison of different SiO_2 and Si-supports

6.6.1 Silicalite

The framework structure of Silicalite is identical to that of Titanium-Silicalite (TS-1), a material hydrothermally synthesized using tetrapropyl ammonium hydroxide (TPAOH) as the template, substituting the Ti-atoms with Si-atoms and preserving angstrom level pore-size dimensions[30]. The Silicalite material was prepared under hydrothermal synthesis conditions at Cardiff University and calcined in N_2 (650 ^oC, 2h, 1 ^oC min^{-1} heating ramp) to remove the tetrapropyl ammonium hydroxide, TPAOH template prior to impregnation of Au and Pd salts. It is clear from data shown in Table 6.5 that partial synergy is induced for the 2.5 wt% Au-2.5 wt% Pd composition with respect to the formation of hydrogen peroxide, although the subsequent hydrogenation activity of the catalyst is simultaneously increased relative to the 2.5 wt% Pd catalyst and of comparable activity to 5 wt% Pd/Silicalite (158 $mol_{H2O2}kg_{cat}^{-1}h^{-1}$).

Catalyst	**Productivity / $mol_{H2O2}kg_{cat}^{-1}h^{-1}$**	**Hydrogenation / $mol_{H2O2}kg_{cat}^{-1}h^{-1}$**
5% Au	3	22
2.5% Au-2.5% Pd	74	164
2.5% Pd	62	58
5% Pd	70	158

Table 6.5 Summary of the H_2O_2 synthesis and hydrogenation activities obtained for Silicalite-supported 5 wt% Au, 2.5 and 5 wt% Pd and 2.5 wt% Au-2.5 wt% Pd catalysts prepared by standard wet impregnation, dried (110 ^oC, 16 h) and calcined in static air (400 ^oC, 3 h).

As such these pore-size constraints will limit the extent of interaction and dispersion between the Au and Pd metals added using wet impregnation techniques as oppose to complex and precise preparations such as ion-exchange, used to incorporated metal content far less than the nominal 5 wt% Au-Pd loading and resulting in a vastly different structure and dispersion relative to supported nanoparticles, and comparable to interactions in metal-organic framework (MOF) or porous co-ordination polymer (PCP) materials. Corma *et al.* [31] applied a

post-synthesis method to introduce Au from solution into the cavities of an IRMOF-3-SI type metal organic framework (Figure 6.13), representing the first reported example of a catalytically active Au-MOF containing an isolated gold species. IRMOF-3 was reacted with salicylaldehyde in equimolar amounts to yield a crystalline IRMOF-3-SI structure - reaction with 2,4 DNPH confirmed 3% of NH_2 groups were modified. Thermo-gravimetric analysis showed IRMOF-3-SI-Au was thermally stable and unaltered upward to 300 ^oC, while TPR studies determined the oxidation state of Au as +3 exclusively. IRMOF-3-SI-Au was evaluated for the hydrogenation of 1,3 butadiene and found to be stable on repeat use (defined and controlled sites maintained) and exhibited catalytic activity one order of magnitude better than Au/TiO_2 catalysts of higher loading and prepared by deposition precipitation[31].

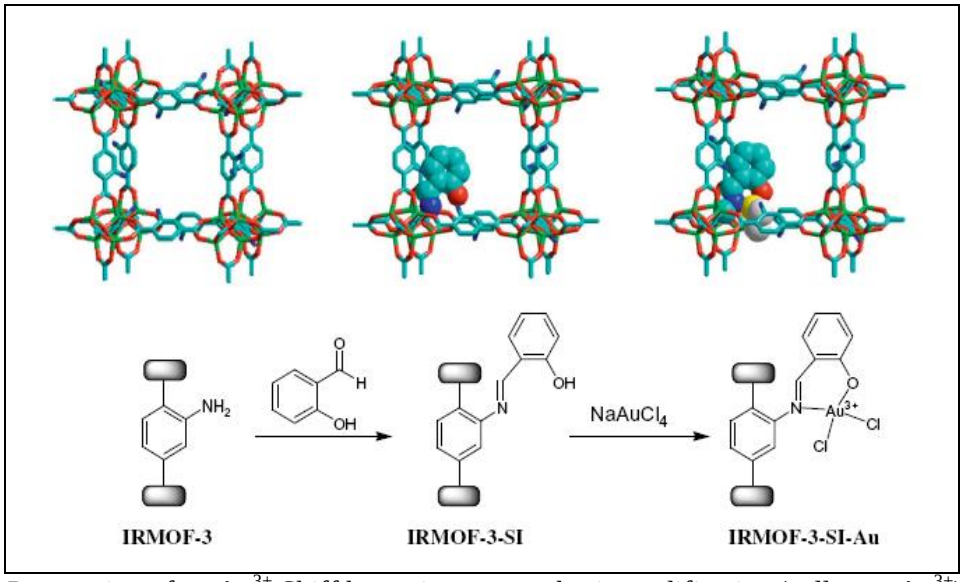

Figure 6.13 Preparation of an Au^{3+} Shiff base via post-synthesis modification (yellow = Au^{3+}) [31].

Similarities exist between MOF and zeolite structures though thermal and chemical stabilities of the latter are considerably greater. The MOF structure is far more flexible in terms of potentially limitless design possibilities and origin of framework stability which can be influenced by hydrogen bonding and ion-pairing interactions, particularly for nitrogen donating groups but are still insufficient compared to zeolites[32]. Carboxylate based MOFs and Zeolite-Imidazolate frameworks developed by Haruta (ZIF-8, 9, 10) are stable in air and decompose in the range 300-400 ^oC, while frameworks assembled using terephthalate groups are highly air sensitive[33]. The hydrothermal stability is a key concern for MOF-5, MOF-177

and all IRMOF structures, which are sensitive to moisture leading to framework damage/phase transformation in water and for MOF-5 an irreversible collapse[34] at 8 vol% H_2O.

The thermal and solvent constraints encountered for a range of MOF structures, many of which entail long synthesis procedures (the crystallisation of these materials can take several days) is not favoured in the development of a direct synthesis reaction to produce aqueous, 3-8 wt% H_2O_2 solutions. The synthesis of metal organic frameworks and porous co-ordination polymers and discovery of their potential environmental application, *i.e.* hydrogen storage (based on very high surface areas) has been made in the last two decades and therefore it is anticipated that the tolerance of these materials in open atmosphere, a wide range of solvents and high temperature heat treatments (>400 ^oC) will be addressed in future publications.

6.6.2 Zeolites

Zeolites ZSM-5 and Y supported Au catalysts prepared by wet impregnation, however, have proven effective for the direct synthesis of H_2O_2, exhibiting productivities comparable to Au/Al_2O_3 catalysts and superior to Au/silica counterparts, best illustrated by Zeolite Y [11]. Reactivity data for supported 5 wt% catalysts interestingly correlated with aluminium content with a dependency on pore structure of Zeolite Y. Appropriate pore channel and cavity dimensions are critical to catalytic activity and are controlled to an extent by the secondary building units. Although synthesis methods are not developed to the extent where dynamically accessible pores can be designed, static porosity in natural and rigid porous materials including zeolites has been made possible. Favourable rates of H_2O_2 production were achieved using 2.5 wt% Au-1.8 wt%/ZSM-5 and Y catalysts (102 and 78 $mol_{H2O2}kg_{cat}^{-1}h^{-1}$ respectively) although the rates of H_2O_2 hydrogenation/decomposition over these supports were in some instances observed as high as 1,000 $mol_{H2O2}kg_{cat}^{-1}h^{-1}$ (50% H_2O_2 loss) after 0.5 h reaction.

In this study the aluminium content of ZSM-5 supports obtained from Zeolyst ® was varied and their viability as a support for 2.5 wt% Au-2.5 wt% Pd catalysts was evaluated for the direct synthesis of hydrogen peroxide, as shown in Figure 6.14, using black and red lines to represent H_2O_2 productivity and hydrogenation activity values respectively.

Decreasing the Al content in ZSM-5 resulted in a three-fold increase in H_2O_2 synthesis activity over supported 2.5 wt% Au-2.5 wt% Pd catalysts ranging from Si/Al = 23 to 80 (atom ratio) and corresponding to a simultaneous decrease in the H_2O_2 hydrogenation activity of the catalyst, which in turn is lowest at Si/Al = 80 (140 $mol_{H2O2}kg_{cat}^{-1}h^{-1}$).

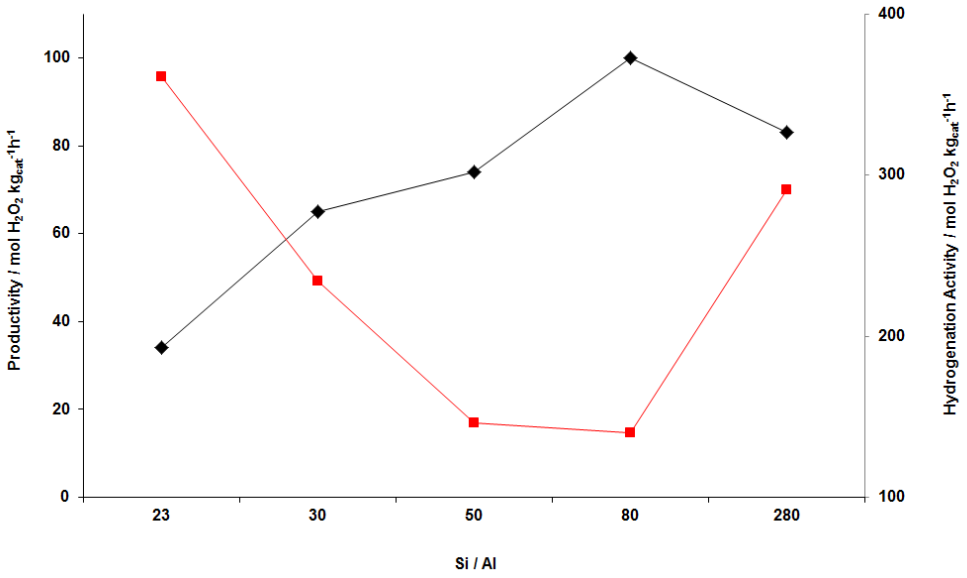

Figure 6.14 Effect of zeolite Si:Al molar ratio on the H_2O_2 synthesis *(black line)* and hydrogenation *(red line)* activities of 2.5 wt% Au-2.5 wt% Pd/ZSM-5 catalysts prepared by standard wet impregnation, dried (110 ^oC, 16 h) and calcined in static air (400 ^oC, 3 h).

Reducing the Al content in zeolite ZSM-5 increases the amount of surface exposed Si-atoms and hence modifies the iso-electric point of the support, and affecting the interaction between the metal and support and the base catalysed hydrogenation of hydrogen peroxide by tetrahedral AlO_4^- units. As a result the hydrogenation of H_2O_2 is elevated over Al_2O_3, Fe_2O_3 and MgO supports and therefore moving to a higher density of exposed, solid acid Si-sites which may also be attributed to the marked decrease in H_2O_2 hydrogenation. Powder XRD analysis of 2.5 wt% Au-2.5 wt% Pd/ZSM-5 (Si/Au = 23, 30, 80 and 280) catalysts in Figure 6.15 also indicated possible differences in the bulk content of PdO and Pd^o phases located at 34 and 40 degrees 2θ respectively (JCPDS code: 00-006-0515), which were found to decrease on moving from ZSM-5 (50) to (280). This was accompanied by a marked decrease in intensity of the major Au^o [111] reflection at 38 degrees 2θ (JCPDS code: 00-002-1095), although caution must be stated in these observations due to the possibility of overlap with reflections characteristic of the ZSM-5 material in the same regions.

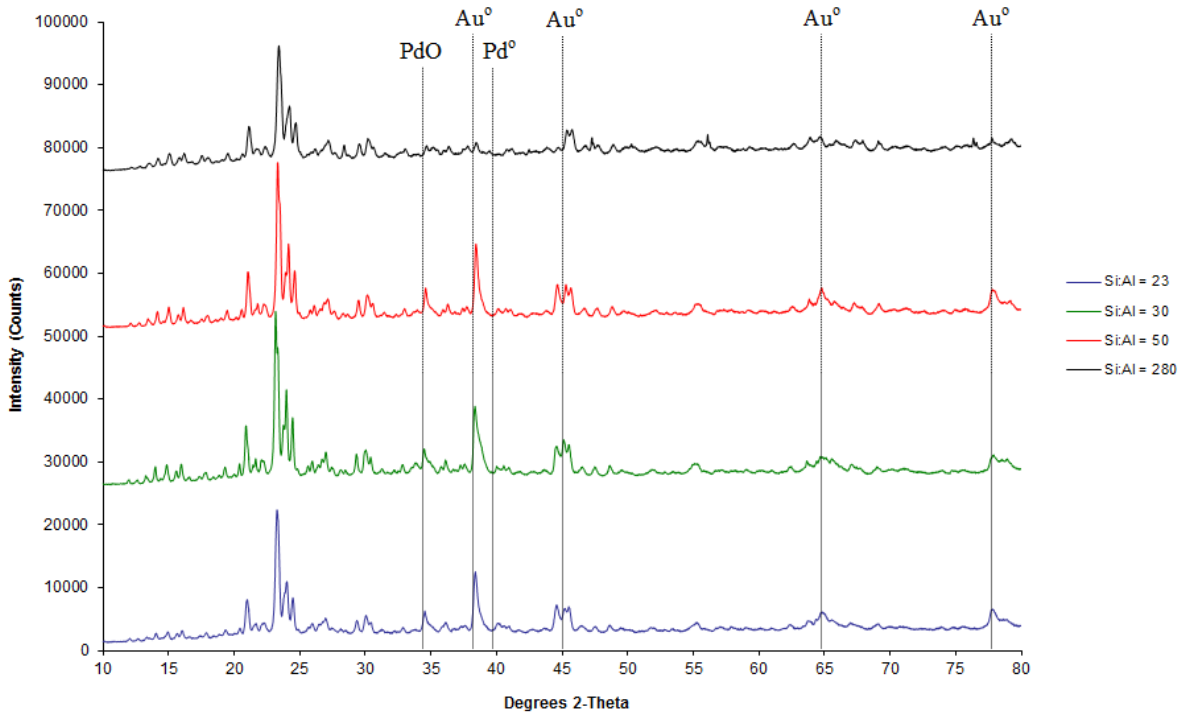

Figure 6.15 Powder XRD profiles of 2.5 wt% Au-2.5 wt% Pd/ZSM-5 (Si/Al = 23, 30, 50 and 280) catalysts respectively.

Further investigation into the application of zeolites as supports for the direct synthesis reaction is intended, although here it is concluded that high rates of H_2O_2 formation are not maintained on repeat use, illustrated for Au-Pd/ZSM-5 (Si/Al: 280) and several other Si-based supported catalysts in Table 6.7. Given this loss in H_2O_2 productivity (a decrease from 83 to 23 $mol_{H2O2}kg_{cat}^{-1}h^{-1}$), leaching of active Au and Pd metal into solution and the possibility of a homogeneous contribution to observed rates of H_2O_2 synthesis and hydrogenation cannot be discounted for ZSM-5-supported catalysts.

The homogeneous activities of solutions of Au and Pd compounds of comparable metal content to supported 5 wt% Au, Pd and Au-Pd catalysts has been determined, showing that use of Pd precursors alone can give rates of H_2O_2 synthesis and hydrogenation as high as 80 and 500 $mol_{H2O2}kg_{cat}^{-1}h^{-1}$ respectiviely (Appendix Table A6.1). Consequently, the impregnation of Au and Pd metals onto complex framework-type structures does not result in a stable, fully reusable catalyst or sufficiently address the target of switching-off sequential hydrogenation of H_2O_2 produced *in-situ*, and therefore alternative incorporation methods are required.

6.6.3 Silicalit (Solvay ®)

In addition to the findings reported for zeolite ZSM-5, the effect of nitric acid pre-treatment on the composition of Silicalit (Si:Al = 85:2) supports sourced from Solvay ® and the rates of H_2O_2 synthesis and hydrogenation of supported Au-Pd catalysts has been investigated. Powder XRD analysis of Silicalit before and after pre-treatment in dilute nitric acid (Figure 6.16) showed a significant loss of Al content, as evidenced by a reduction in the intensity of aluminosilicate reflections and a post Si:Al ratio of approximately 277:1 determined using SEM-EDX analysis.

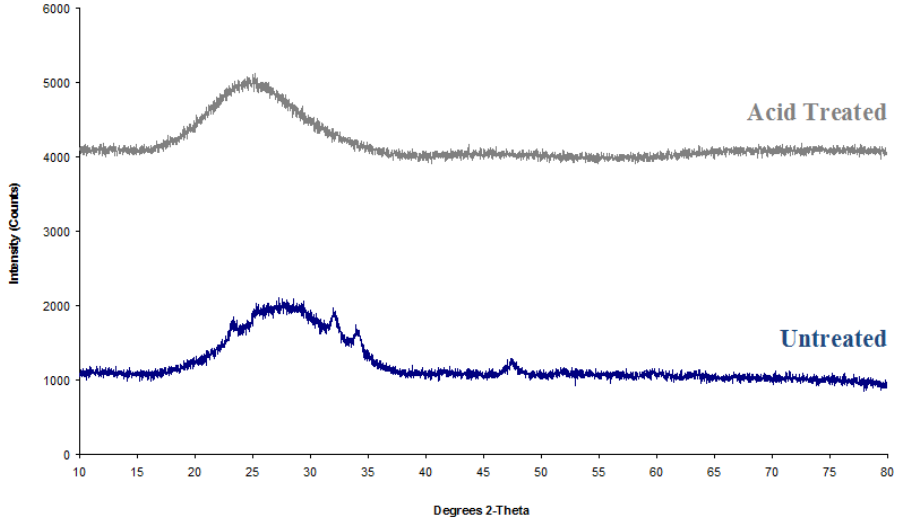

Figure 6.16 Powder XRD profiles of Silicalit support before and after 2% HNO_3 pre-treatment.

Surprisingly, there is virtually no enhancement in either the rates of H_2O_2 synthesis or hydrogenation over bimetallic 2.5 wt% Au-2.5 wt% Pd catalysts after acid pre-treating the Silicalit support, compared to pronounced reduction in the hydrogenation rates over supported 5 wt% Au and 2.5 wt% Pd catalysts and improved synthesis rates over both monometallic Pd catalysts (Table 6.6). These observations were similar to those reported in Table 6.1 for SiO_2-supported catalysts, and this enhancement in H_2O_2 productivity is best illustrated for the 2.5 wt% Pd catalyst and implies that pre-treatment of Silicalit improves the Pd dispersion and coverage of hydrogenation sites characteristic of the Silicalit material, noted in particular for 5 wt% Au/Silicalit (22 $mol_{H2O2}kg_{cat}^{-1}h^{-1}$). Compared to SiO_2-supported catalysts, evidence of synergy is noted with bimetallic Au-Pd catalysts exhibiting higher rates of H_2O_2 synthesis relative to monometallic 2.5 and 5 wt% Pd counterparts irrespective of acid pre-treatment.

Catalyst[1]	Productivity / $mol_{H2O2}kg_{cat}^{-1}h^{-1}$		Hydrogenation / $mol_{H2O2}kg_{cat}^{-1}h^{-1}$	
	Untreated	Acid Treated	Untreated	Acid Treated
5% Au	5	6	106	22
2.5% Au-2.5% Pd	77	81	179	180
2.5% Pd	34	51	240	97
5% Pd	56	65	114	261

Table 6.6 Comparison of the H_2O_2 synthesis and hydrogenation activities for untreated and acid treated 5 wt% Au, 2.5 and 5 wt% Pd and 2.5 wt% Au-2.5 wt% Pd/Silicalit (Si:Al = 85:2) catalysts prepared by standard wet impregnation, dried and calcined in static air (400 ^{o}C, 3 h).

6.6.4 Porous glass and other SiO_2 sources

To conclude the evaluation of different supports, a co-polyimide (CPI), porous glass type silica and SiO_2 supports of different particulate and pore size dimensions (Acros Organics) were provided by Solvay and evaluated for the direct synthesis reaction. Co-polyimide glass structures have been applied as supports for monometallic 0.25-1.0 wt% Pd catalysts used in Heck and Suzuki coupling reactions and the ambient pressure, liquid-phase hydrogenation of C=C, C=N and N=N bonds exclusively in terpenoid substrates, with 90-100% yields reported[35]. For the majority of C-C coupling reactions in the presence of a base, deactivation after one reaction cycle was noted, and while catalysts were easily recovered, a reactivation step prior to repeat use was necessitated due to the partial, *in-situ* reduction of surface Pd^{2+} species.

CPI SiO_2-supported Au-Pd catalysts were found to be moderately active for hydrogen peroxide synthesis with productivity tripling in value from 17 to 49 $mol_{H2O2}kg_{cat}^{-1}h^{-1}$ on decreasing the particulate size of the support from 500 μm to 80 μm (Figure 6.17). This was accompanied by an increase in the rate of hydrogenation over the catalysts, attributed to a possible increase in Pd dispersion, which is implied in scanning electron micrographs (Appendix A6.4, A6.5).

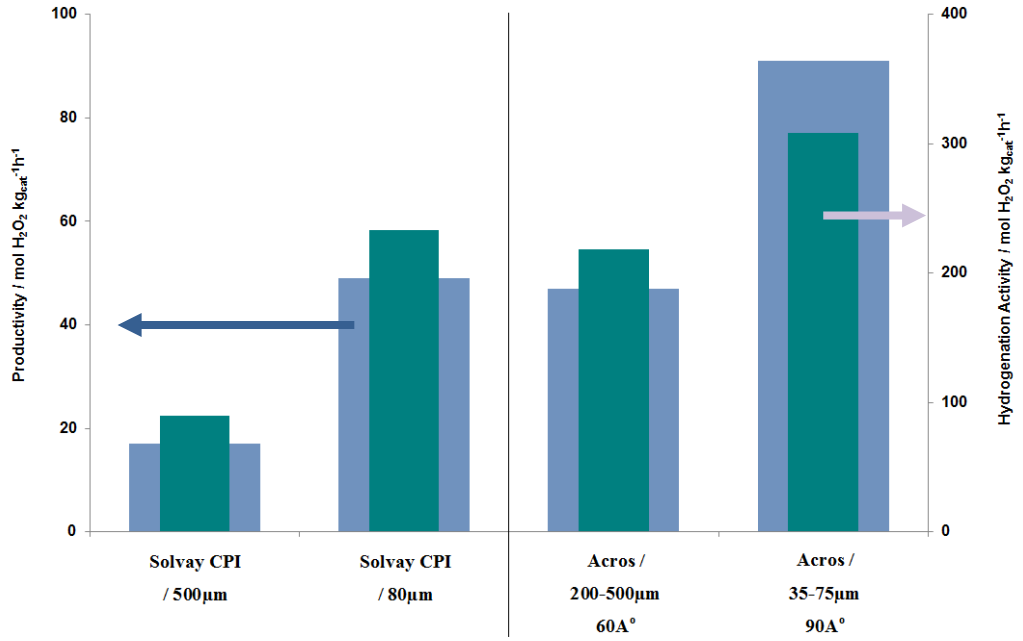

Figure 6.17 Assessment of different SiO_2 supports of different particulate and pore sizes on the H_2O_2 synthesis and hydrogenation activities of 2.5 wt% Au-2.5 wt% Pd/SiO_2 catalysts prepared by standard wet impregnation, dried and calcined in static air (400 °C, 3 h).

SEM-EDX (back-scatter detection) analysis of CPI-SiO_2 catalysts detected µm-sized agglomerates comprising a predominantly Au-signal (Appendix A6.4, A6.5), which is in agreement with limited dispersion of Au shown on other silica supports. Further to this, an increase in the intensity of the PdO [101] reflection at 34 degrees 2θ in corresponding XRD diffractograms may indicate the presence of separate bulk Au and Pd phases on 500 µm SiO_2 particulates (in addition to several low intensity Pd^0 reflections manifested in Figure 6.18 (right).

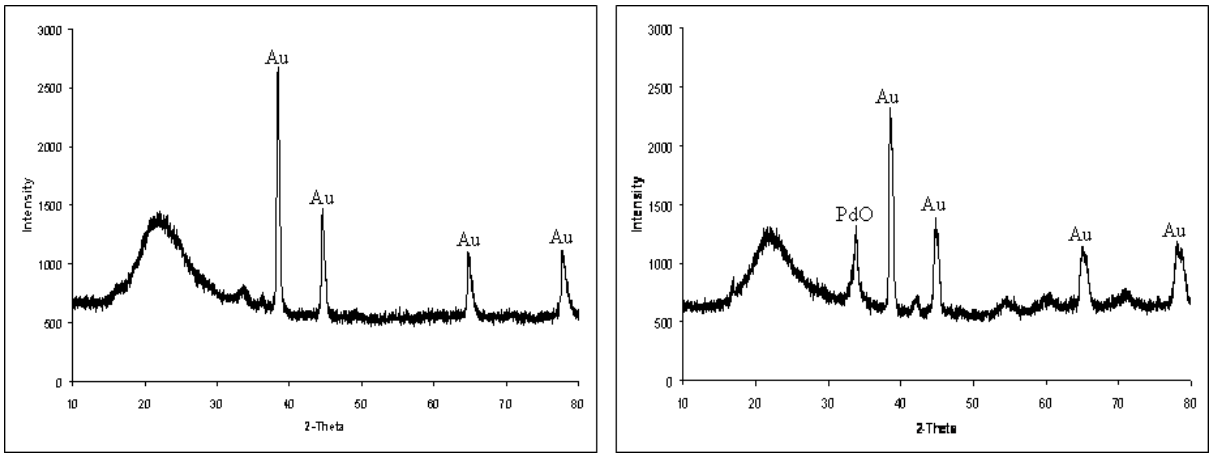

Figure 6.18 Powder XRD diffractograms of 5 wt% Au-Pd/CPI-SiO_2 catalysts comparing 80 µm (left) and 500 µm (right) supports.

The effect of decreasing the particulate size of the SiO_2 supports was also identified as leading to an enhancement in the rate of H_2O_2 formation over Au-Pd catalysts supported on Acros silica from 46 $mol_{H2O2}kg_{cat}^{-1}h^{-1}$ (200-500 μm) to 91 $mol_{H2O2}kg_{cat}^{-1}h^{-1}$ (35-75 μm). However, simultaneously the pore size of this support has increased from 60 to 90 angstroms in diameter and could represent a secondary effect in improving metal dispersion, leading to catalysts also significantly more active for the hydrogenation of H_2O_2 (>350 $mol_{H2O2}kg_{cat}^{-1}h^{-1}$) and possibly related to the mechanism proposed by Strukul *et al.*[21], as reviewed in section 6.1.

Support	**Productivity / $mol_{H2O2}kg_{cat}^{-1}h^{-1}$**	
	1st Use	**2nd Use**
Silicalite	74	62
CPI-SiO_2 (80μm)	49	31
Acros (35-75μm / 90A^o)	91	60
ZSM-5 (280)	83	23

Table 6.7 Comparison of the H_2O_2 productivities for bimetallic 2.5 wt% Au-2.5 wt% Pd catalysts supported on different Si-type/SiO_2 supports after first and second use in the direct synthesis reaction. All catalysts were dried and calcined in static air (400 ^oC, 3 h).

The impregnation of Au and Pd metals onto Si:Al framework structures and SiO_2 supports of different particulate and pore size dimensions does not resolve the stability issue raised in section 6.3, with loss of activity on re-use for all catalysts investigated in Table 6.7. As such the preparation technique must be addressed in future studies and improved relative to conventional wet impregnation, deposition precipitation and colloidal immobilization routes. Ntainjua *et al.*[36] have investigated the use of heteropolyacid acid structures for the direct synthesis reaction, employing ion-exchange methodology to exchange Au and Pd metal into Cs containing Heteropolyacids with the Keggin structure, $Cs_{2.8}H_{0.2}PW_{12}O_{40}$, to form solid acid catalysts. These materials contained on average 0.15 wt% Au-Pd to balance the charge within the Keggin structure, and are highly active for the synthesis of hydrogen peroxide and its subsequent hydrogenation/decomposition despite such low metal content.

The high activities of heteropolyacid exchanged Keggin materials could be of some interest for in-situ capture processes (the hydrogen peroxide is produced and then used to oxidise an organic substrate also present in the reactor vessel) based on phenomenal turnover frequencies due to the low metal contents used, retention of high activity on repeat use and improved H_2O_2 productivities on increasing reaction temperature from 2 to 20 ^oC for $Pd_{0.1}Au_{0.0333}Cs_{2.5}H_{0.2}PW_{12}O_{40}$ and $Pd_{0.075}Au_{0.05}Cs_{2.5}H_{0.2}PW_{12}O_{40}$ catalysts (107 and 168 $mol_{H2O2}kg_{cat}^{-1}h^{-1}$ respectively). While ion-exchange might be applicable to Silicalite, ZSM-5 and mesoporous materials and form a stable Au-Pd catalyst, it is not appropriate for disordered, amorphous SiO_2 supports and therefore an electroless deposition procedure is reviewed as a possible alternative in section 6.7.

6.7 Discussion

The reason behind the synergistic effect manifested by the Au-Pd catalyst on acid pre-treated SiO_2 (JM) cannot be rationalised from the electron microscopy characterisation as the overall morphology for the two samples appears identical. XPS analysis does however conclusively show that acid pre-treatment increases the degree of Au dispersion on SiO_2 and in addition clear differences in the nature of the hydroxyl groups using INS and TPD methods are identified between supports which might be associated with the onset of synergy and increase in activity for Au-Pd catalysts prepared using the acid pre-treated support. With respect to the enhanced catalytic activity that is observed for all Pd-containing catalysts prepared using the acid pre-treated silica, the enhanced hydroxyl functionality on the silica surface is considered to aid the dispersion of Pd metal and it is this effect that constitutes the enhanced activity.

There could be an extremely small amount of Au contained within the 2-5 nm Pd nanoparticles which is below the detection limits of the STEM-XEDS microscope (a mass fraction sensitivity of the order ~1 atom%), which is possible to detect using XPS, however, as the Au signal is observed in the acid pre-treated catalyst, but not in the untreated counterpart. For a series of 1 wt% Au+Pd/C catalysts prepared by sol-immobilisation in chapter 5, the addition of small amounts of Au to Pd significantly improved H_2O_2 activity and therefore it is plausible that this effect is observed with very small numbers of Au atoms in these small clusters, where one or two Au atoms constitute a significant volume fraction of the particle.

Theoretical modelling of the inclusion of Au atoms into a Pd surface by Ishihara *et al.* [37] has established that Au atoms can induce a marked synergistic effect on catalytic activity for the direct synthesis reaction through the blocking of O-O scission pathways by Pd ensembles and weakening of interactions between H_2O_2 molecules and the Au@Pd surface, suppressing the hydrogenation/decomposition of H_2O_2 and favouring product release away from the catalyst, resulting in higher H_2 selectivities. It is understood that catalysts comprising solely of small nanoparticles of either Pd or Au-Pd are highly active when supported on carbon. It is therefore unlikely that changing the support surface would switch of the activity of such a large population of the very small nanoparticles adding strength to the conclusion that synergy arises from a slightly enhanced dispersion of Au that arises from the presence of an enhanced population of surface hydroxyl functionalities on the surface of the silica due to the acid pre-treatment.

It is obvious from this study that silica is not an optimal support for the dispersion of Au-containing catalysts using wet impregnation. However, for Pd only catalysts, silica has been found to be effective. In addition, other catalysts preparation method including the deposition precipitation procedure are also unsuitable for the preparation of SiO_2-supported Au-Pd catalysts, given the isoelectric point of the silica support is too low to effectively stabilise the $HAuCl_4$ precursor, resulting in the formation of large and inadequately stabilized Au-rich particles. Evidence of large Au particles has also been observed for Au-Pd/SiO_2 catalysts prepared by colloidal immobilization and therefore in future other preparation methods such as ion-exchange and electroless deposition could serve as viable alternatives.

The Hutchings[36] and Park[10] groups have applied the ion-exchange method to introduce Au and Pd metals into the Keggin structure, $Cs_{2.8}H_{0.2}PW_{12}O_{40}$, to form solid acid catalysts exhibiting high H_2O_2 productivities based on moderate H_2 selectivity. The total amount of Au and Pd in these catalysts is very low (0.15% by weight) and required to maintain the overall electric charge of the Keggin structure, however, in terms of turnover frequency (mol_{H2O2}/mol_{Au+Pd}) the heteropolyacid materials are exceptional and far superior to values reported for Au-Pd catalysts prepared by wet impregnation and colloidal immobilization. The rate of H_2O_2 hydrogenation using batch conditions is elevated over Au-Pd exchanged catalysts (200-400 $mol_{H2O2}kg_{cat}^{-1}h^{-1}$ range) and unfortunately these materials cannot be imaging under an electron beam as this results in their degradation. Studies directed at optimising the preparation

of solid acid catalysts by ion-exchange and the possible introduction of alternative metals are currently underway.

Finally, Monnier *et al.* have successfully developed an electroless deposition method[38] to introduce a second metal (i.e. Au) onto a stable, monometallic 2 wt% Pd/SiO_2 catalyst with control over the specific coverage of Pd sites with Au. This preparation entails the development of an electroless bath that is thermodynamically unstable but kinetically stable, and consisting of a metal source (potassium dicyanoaurate, $KAu(CN)_2$), reducing agent (hydrazine) and solvent (water). Multiple variables including the concentration of the metal ion source, reducing agent, pH and temperature must be carefully controlled during the deposition of Au onto Pd.

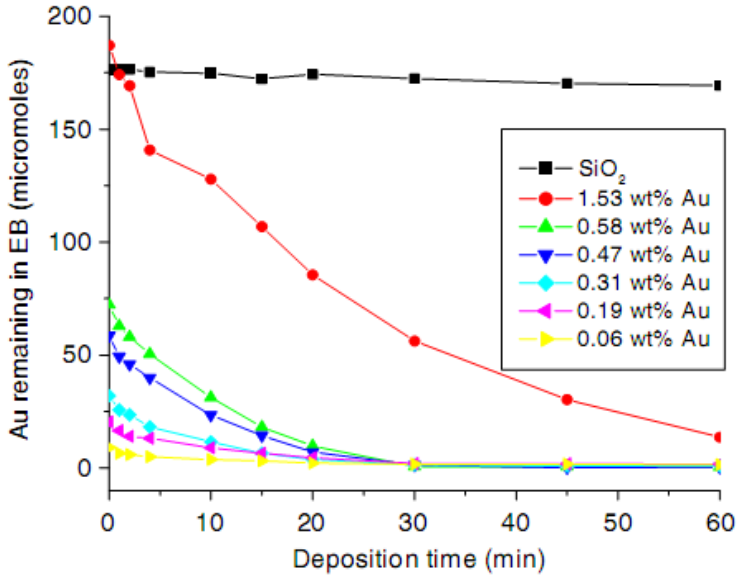

Figure 6.19 Deposition profile of Au metal (of different wt% loadings) onto a 2 wt% Pd/SiO_2 catalyst over a 60 minute period using the electroless deposition (ED) procedure[38].

The negative standard reduction potential of the metal ion source ($E^o_{Au(CN)2^-}$ = -0.60 V) is required for the formation of kinetically stable electroless solutions of long lifetime and prevention of galvanic deposition of Au onto Pd. The deposition of Au was facilitated over a period of 60 minutes period as shown in Figure 6.19, and characterisation of catalysts with loadings up to 2.01 wt% Au on Pd/SiO_2 suggested that Au was deposited on all types of Pd surface sites in a non-discriminative manner, with XPS indicating a net electron transfer from Pd to Au. The ED synthesised catalysts were evaluated for propylene hydrogenation activity

and exhibited significantly enhanced turnover frequencies for Au-Pd/SiO_2 catalysts in which the fractional coverage (θ) of Au on Pd exceeded 0.60. Hydrogen chemisorption measurements showed that Au deposition disrupted Pd ensembles on the catalyst, favouring the formation of propylene and preventing formation of the less reactive, propylidyne product[38]. The ED method has also been used by Okada *et al.*[39] in the preparation of Pd/SiO_2 catalysts, resulting in enhanced activities for both the hyrogenation of nitrobenzene and the direct synthesis of hydrogen peroxide reactions compared to impregnated Pd/SiO_2 catalysts, due to the formation of spherical, uniform Pd particles (6-12 nm size distribution) by the electroless deposition route. For hydrogen peroxide synthesis, the concencentration of H_2O_2 produced after 60 minutes (ambient conditions in 0.01 M HCl) amounted to 15 mM - 2.3 times greater than that achieved using impregnated Pd/SiO_2 catalysts.

6.8 Conclusion

From the study undertaken in chapter 6, the reason behind the observed synergy displayed by the Au-Pd catalyst on acid pre-treated SiO_2 cannot be rationalised from electron microscopy characterisation as the overall morphology for the two samples appears identical. XPS analysis does however conclusively show that acid pre-treatment increases the degree of Au dispersion on SiO_2 and in addition clear differences both in the bulk concentration and nature of the hydroxyl groups using inelastic neutron scattering and temperature programmed desorption techniques are identified between supports which might be associated with the onset of synergy and increase in activity for Au-Pd catalysts prepared using the acid pre-treated support. With respect to the enhanced catalytic activity that is observed for all Pd-containing catalysts prepared using the acid pre-treated silica, the enhanced hydroxyl functionality on the silica surface is suggested to aid the dispersion of Pd metal and it is this effect that constitutes the enhanced activity. There could be an extremely small amount of Au contained within the 2-5 nm Pd nanoparticles which is below the detection limits of the STEM-XEDS microscope (a mass fraction sensitivity of the order ~1 atom%), which is possible to detect using XPS, however, as the Au signal is observed in the acid pre-treated catalyst, but not in the untreated counterpart.

6.9 References

1. J. K. Edwards, G. J. Hutchings, *Angew. Chem. Int. Ed.*, **2008**, 47, 2.
2. J. K. Edwards, E. Ntainjua N, A. F. Carley, A. A. Herzing, C. J. Kiely, G. J. Hutchings, *Angew. Chem. Int. Ed.*, **2009**, 48, 8512.
3. J. K. Edwards, B. Solsona, E. Ntainjua N, A. F. Carley, A. A. Herzing, C. J. Kiely, G. J. Hutchings, *Science*, **2009**, 323, 1037.
4. Q. Liu, J. C. Bauer, R. E. Schaak, J. H. Lunsford, *App. Catal. A.*, **2008**, 339, 130.
5. Q. Liu, K. K. Gath, J. C. Bauer, R. E. Schaak, J. H. Lunsford, *Catal. Lett.*, **2009**, 132, 342.
6. V. R. Choudhary, C. Samanta, *Catalysis Lett.*, **2005**, 99, 79.
7. T. Ishihara, Y. Ohura, S. Yoshida, Y. Hata, H. Nishiguchi, Y. Takita, *App. Catal. A.*, **2005**, 291, 215.
8. M. Okumura, Y. Kitagawa, K. Yamagcuhi, T. Akita, S. Tsubota, M. Haruta, *Chem. Lett.*, **2003**, 32, 822.
9. H. Lee, S. Kim, D. W. Lee, K. Y. Lee, *Catal. Comm.*, **2011**, 12, 968.
10. S. Park, S. H. Lee, S. H. Song, D. R. Park, S. Baeck, T. J. Kim, Y. Chung, S. Oh, I. K. Song, *Catal. Comm.*, **2009**, 10, 391.
11. S. Park, K. M. Cho, M. H. Youn, J. G. Seo, J. C. Jung, S. Baeck, T. J. Kim, Y. Chung, S. Oh, K. Song, *Catal. Comm.*, **2008**, 9, 2485.
12. S. Park, J. C. Jung, J. G. Seo, T. J. Kim, Y. Chung, S. Oh, I. K. Song, *Catal. Lett.*, **2009**, 130, 296.
13. S. Park, J. G. Seo, J. C. Jung, S. Baeck, T. J. Kim, Y. Chung, S. Oh, I. K. Song, *Catal. Comm.*, **2009**, 10, 1762.
14. S. Park, S. Baeck, T. J. Kim, Y. Chung, S. Oh, I. K. Song, *J. Mol. Catal. A. Chem.*, **2010**, 319, 98.
15. S. Park, D. R. Park, J. H. Choi, T. J. Kim, Y. Chung, S. Oh, I. K. Song, *J. Mol. Catal. A. Chem.*, **2010**, 332, 76.
16. S. Park, K. M. Cho, M. H. Youn, J. G. Seo, J. C. Jung, S. Baeck, T. J. Jim, Y. Chung, S. Oh, I. K. Song, *J. Mol. Catal. A. Gen.*, **2011**, 336, 78.
17. S. Park, J. H. Choi, T. J. Kim, Y. Chung, S. Oh, I. K. Song, *J. Mol. Catal. A. Chem.*, **2012**, 353, 37.

18. F. Menegazzo, M. Signoretto, G. Frison, F. Pinna, G. Strukul, M. Manzoli, F. Boccuzzi, *J. Catal.*, **2012**, 290, 143.
19. S. Abate, S. Perathoner, G. Centi, *Catalysis Today*, **2012**, 179, 170.
20. S. Abate, P. Lanzafame, S. Perathoner, G. Centi, *Catalysis Today*, **2011**, 169, 167.
21. E. Ghedini, F. Menegazoo, M. Signoretto, M. Manzoli, F. Pinna, G. Strukul, *J. Catal.*, **2010**, 273, 266.
22. L. Ren, H. Zhang, A. Lu, Y. Hao, W. Li, *Micro. Meso. Mater.*, **2012**, 158, 7.
23. A. Thomas, Q. He, J. K. Edwards, *Faraday Discuss.*, **2011**, 152, 381.
24. Q. Fu, W. Deng, H. Saltsburg, M. Flytzani-Stephanopoulos, *App. Catal. B. Env.*, **2005**, 56, 57.
25. M. T. Kim, *Thin Solid Films*, **2000**, 360, 60.
26. A. Ramirez, B. L. Lopez, L. Sierra, *J. Phys. Chem. B.*, **2003**, 107, 9275.
27. E. C. Spencer, A. A. Levchenko, N. L. Ross, A. I. Kolesnikov, J. Boerio-Goates, B. F. Woodfield, A. Navrotsky, G. Li, *J. Phys. Chem. A.*, **2009**, 113, 2796.
28. J. Jobic, *J. Catal.*, **1991**, 131, 289.
29. W. P. J. H. Jacobs, J. H. M. C. Van Wolput, R. A. Van Santen, H. Jobic, *Zeolites*, **1994**, 14, 117.
30 C. Hammond, Selective Oxidation of Methane using Zeolites, PhD Thesis, *Cardiff University*, **2011**.
31. A. F. Combariza, G. Sastre, A. Corma, *J. Phys. Chem. C.*, **2009**, 113, 11246.
32. G. Li, J. K. Edwards, A. F. Carley, G. J. Hutchings, *Catalysis Today*, **2007**, 122, 361.
33. W. Kleist, F. Jutz, M. Maciejewski, A. Baiker, *Euro. J. Inorg. Chem.*, **2009**, 24, 3552.
34. S. Hermes, M. K. Schroter, R. Schmid, L. Khodeir, M. Muhler, A. Tissler, R. W. Fischer, R. A. Fischer, *Angew. Chem. Int. Ed.*, **2005**, 44, 6237.
35. C. Schmoger, A. Stolle, W. Bonrath, B. Ondrushka, T. Keller, K. D. Jandt, *ChemSusChem*, **2008**, 1, 1.
36. E. Ntainjua N., M. Piccinini, J. C. Pritchard, J. K. Edwards, A. F. Carley, C. J. Kiely, G. J. Hutchings, *Catalysis Today*, **2011**, 178, 47.
37. T. Ishihara, K. Yoshizawa, *J. Phys. Chem. C.*, **2011**, 115, 25359.
38. J. Rebelli, M. Detwiler, S. Ma, C. T. Williams, J. R. Monnier, *J. Catal.*, **2010**, 270, 224.
39. S. Okada, S. Ikurumi, T. Kamegawa, K. Mori, H. Yamashita, *Catalysis Today*, **2012**, 185, 109.

Chapter 7

7.1 Introduction

In previous chapters, it was demonstrated that the addition of Au to Pd significantly enhanced the activity and selectivity of catalysts applied to the direct synthesis reaction, with Au recognised as playing a critical role in limiting the sequential hydrogenation/decomposition of hydrogen peroxide. By comparing the activities of monometallic Au and Pd catalysts and bimetallic Au-Pd catalysts, the existence of a synergistic effect between Au and Pd has been identified when using carbon, TiO_2, Al_2O_3 or Fe_2O_3 as the catalyst support[1]. The origin of this synergistic effect in relation to catalyst structure is still not fully understood but is known to result from alloy formation leading to an electronic enhancement that increases the catalyst activity. With respect to gold catalysis there has been considerable interest in the use of ceria as a catalyst support, which has been identified as a very active support for gold nanoparticles across a range of reactions including alcohol oxidation and carbon monoxide oxidation[2-7].

Regarding selection of this support, cerium is a lanthanide element characterised as having two valence states, +3 and +4. As such, oxygen is adsorbed irreversibly on ceria due to the small electric potential that exists between the Ce^{3+} and Ce^{4+} redox couple and is considered to serve as an oxygen reservoir with the ability to adjust the oxygen concentration at the catalyst surface under reaction conditions[8]. It has been recognised that increasing the pKa or the temperature of depositon precipitation and co-precipitation procedures used to synthesise ceria particles can siginifcantly the activity of resulting catalysts, due to a decrease in surface oxygen content on increasing the pKa or temperature[9]. This is improtant for reaction such as CO oxidation for example, where it is widely accepted that the mechanism involves the lattice oxygen of the support. An important property of ceria is that is has the ability to undergo the transformation from $2CeO_2 \rightarrow Ce_2O_3 + ½\ O_2$, forming oxygen vacancies without loss of the face centred cubic ‘fluorite’ crystal structure (Figure 7.1).

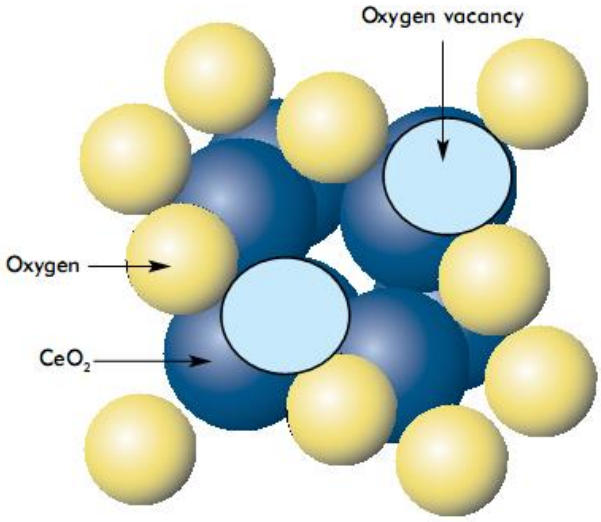

Figure 7.1 Fluorite structure of cerium oxide containing oxygen vacancies.

In term of catalysis, CeO_2-supported monometallic Pd catalysts have been evaluated for methanol oxidation by Matsumura *et al.* [10, 11] and for the water gas shift reaction in addition to being used as a monolithic component in modern catalytic converters and as a fuel cell electrolyte due to the high oxygen storage properties of ceria. For Pd/CeO_2 catalysts reduced at low temperature, the interface between Pd and the ceria surface is proposed as the active site for the methanation of carbon dioxide[12] and is characterised as a strong metal support interaction, SMSI.

Both the morphology and oxidation state of Pd supported on ceria are highly dependent on the synthesis procedure and heat treatment step(s) with strong interactions between Pd and ceria capable of stabilising cationic Pd species. Preparation of Pd/CeO_2 catalysts by deposition precipitation highlighted a surface Pd oxidation state of approximately +1, resulting from the formation of $Pd(OH)_2$ at basics sites on ceria that are converted into Pd-O-Ce bonds at the metal-support interface under calcination conditions[13]. Theoretical studies have also indicated the importance of Pd-O-Ce linkages and ideally dispersed cationic Pd species as critical to the catalytic activity of Pd/CeO_2 catalysts in addition to determining PdO_x cluster edge sites as potential active sites, with the boundary between PdO_x particles and CeO_2 support providing similar activity to simulations performed for incorporated $Pd_xCe_{1-x}O_2$ [111] catalysts with respect to hydrocarbon oxidation[14].

CeO_2-supported Au-Pd catalysts have been applied as catalysts for methanol synthesis and for other reactions including the selective oxidation of arabinose to arabinoic acid[15], with pre-treatment steps performed in hydrogen at T >300 ^oC and room temperature reduction in formaldehyde respectively resulting in higher catalytic activity relative to Au and Pd/CeO_2 counterparts. Activity was found to be dependent on the sample pre-treatment and nature of the support used, with reduction of $Au\text{-}Pd/CeO_2$ in formaldehyde giving the highest activity and selectivity towards arabinoic acid[15].

Matsamura *et al.* [10] investigated the effect of adding *X* wt% Au to a 5 wt% Pd/CeO_2 catalyst on the activity exhibited toward the decomposition of methanol at 180 ^oC. For 3 wt% $Au\text{-}Pd/CeO_2$, a large fraction of the gold component was determined by XRD analysis to be excluded from the nano-sized Pd-Au clusters, although it was predicted that the concentration of Au in the Pd-Au clusters should rise as a function of increasing Au content, becoming saturated at higher concentrations[10]. The activity was found to be highly promoted by addition of a small quanitity of Au, leading to the proposal that Au atoms and/or clusters incorporated into Pd-rich particles induce a synergistic effect between Au and Pd (Figure 7.2).

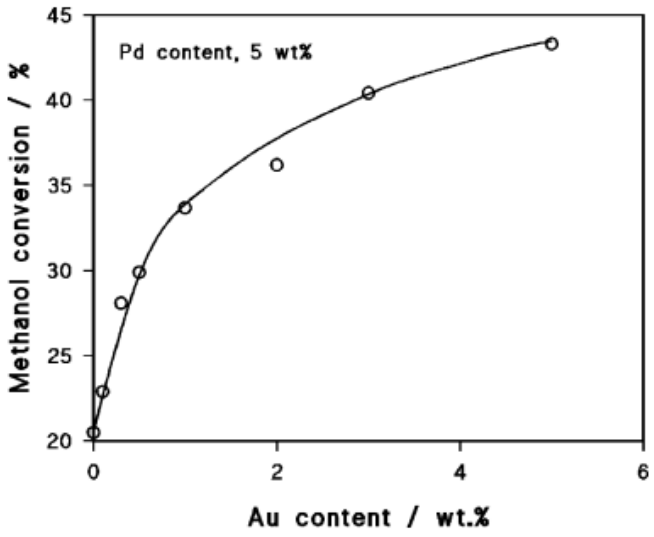

Figure 7.2 Au addition to 5 wt% Pd/CeO_2 catalysts for methanol decomposition reaction[10].

XPS analysis of the samples showed no change in the electronic state of Pd or Au components, and the authors concluded that the catalytic function of Pd is assisted by the presence of Au atoms, with the rate determining step estimated as being the interaction between methoxyl groups and surface hydrogen, formed by the dissociative adsorption of methanol.

The aim of chapter 7 is to investigate the effect of the addition of Au to Pd/CeO_2 catalysts on the rates of H_2O_2 synthesis and hydrogenation, prior to extending the study to CeO_2-supported bimetallic Au-Pt, Pd-Pt and trimetallic Au-Pd-Pt compositions, with reference to carbon and TiO_2-supported catalysts. XPS characterisation is undertaken for CeO_2- and TiO_2-supported catalysts, while STEM-HAADF images are presented for TiO_2-supported catalysts only, due to the difficulty in achieving contrast between Au, Pd and Pt and ceria particles of comparable dimension (Aldrich-sourced CeO_2 is composed of disordered, irregular structure ceria particles in the range 20-50 nm) using advanced aberration corrected electron microscopy techniques.

In addition, representative STEM-HAADF images and XEDS analysis of both TiO_2-supported bi and trimetallic catalysts are included in chapter 7 to assist in understanding the effect of a third metal on structure and activity, specifically the addition of Pt to Au-Pd and the role of Pt in bimetallic Au-Pt and Pd-Pt compositions on catalytic activity for direct H_2O_2 synthesis.

7.2 CeO_2-supported monometallic Pd catalysts for direct H_2O_2 synthesis

For this initial part of study, the activities of supported 5 wt% Pd catalysts for the direct synthesis of hydrogen peroxide were compared and these results are presented below in Table 7.1. The 5 wt% Pd/CeO_2 catalyst was determined to the most active with respect to H_2O_2 synthesis by a considerable margin (97 $mol_{H2O2}kg_{cat}^{-1}h^{-1}$), highlighting that ceria may represent an important choice of support for direct H_2O_2 synthesis.

Catalyst	**Productivity / $mol_{H2O2}kg_{cat}^{-1}h^{-1}$**	**Hydrogenation / $mol_{H2O2}kg_{cat}^{-1}h^{-1}$**
5% Pd/Fe_2O_3 [16]	4	832
5% Pd/Al_2O_3 [17]	12	200
5% Pd/TiO_2	31	288
5% Pd/C	55	135
5% Pd/CeO_2	97	329

Table 7.1 Summary of the H_2O_2 synthesis and hydrogenation activities using supported monometallic 5 wt% Pd catalysts.

It is possible that the defective nature of ceria aids in the dispersion of Pd nanoparticles and theoretical modelling has added support to this concept, including for example the work of Catlow *et al.* [18], where DFT simulations predicated that Rh^{3+}, Pd^{2+} and Pt^{2+} metal ions could segregate together at oxygen vacancies at the low index, [111] and [110] surface faces of ceria, the former of which is the most stable index face and it is expected that the presence of noble metals in this manner can influence catalytic activity. The commercial grade ceria supports are predominantly composed of disordered, irregular phases as oppose to controlled and ordered morphologies that can be synthesised by precipitation routes[19]. However, highly ordered phases of ceria obtained by supercritical anti-solvent precipitation and used as a support for bimetallic Au-Pd catalysts and tested for benzyl alcohol oxidation at 160 ^oC were shown to collapse and tend toward becoming disordered in nature after multiple reactions[20]. This lead to a decline in activity by third use, in comparison to high turnover frequencies that are achieved using Au-Pd catalysts supported on commercial grade ceria that are maintained on repeat use.

7.2.1 Effect of Au addition to CeO_2-supported Pd catalyst for the direct synthesis and hydrogenation of H_2O_2

The addition of Au to Pd catalysts supported on carbon, TiO_2, Al_2O_3 and Fe_2O_3 is understood to lead to a significant increase in H_2O_2 productivity with Au serving to limit the sequential hydrogenation/decomposition of H_2O_2, and a marked synergistic effect is observed between Au and Pd for H_2O_2 formation over these catalysts. The direct synthesis and hydrogenation of H_2O_2 over CeO_2-supported 5 wt% Au, Pd and 2.5 wt% Au-2.5 wt% Pd catalysts is shown in Table 7.2. The addition of Au to Pd resulted in a decrease in H_2O_2 hydrogenation activity, which is in agreement with previous studies of Au and Pd catalysts. However, in contrast to the synergy observed between Au and Pd on other supports, the addition of Au to Pd supported on CeO_2 resulted in a considerable decrease in both the rates of H_2O_2 synthesis and hydrogenation over the catalyst respectively.

CeO_2 Untreated	**Productivity / $mol_{H2O2}kg_{cat}^{-1}h^{-1}$**	**Hydrogenation / $mol_{H2O2}kg_{cat}^{-1}h^{-1}$**	**C_{H2} (%)**	**S_{H2} (%)**
CeO_2	0	88	n.d	
5% Au	1	118		
5% Pd	97	329	31	43
2.5% Au-2.5% Pd	68	145	31	30

Table 7.2 Direct synthesis of H_2O_2 over CeO_2-supported (untreated) Pd, Au and Au-Pd catalysts, dried in air (110 ^oC, 16 h) and calcined in static air (400 ^oC, 3 h). n.d = not determined due to yields being very low.

7.2.2 Effect of acid pre-treatment of the CeO_2 support on the direct synthesis and hydrogenation of H_2O_2

It was previously demonstrated that the pre-treatment of carbon or TiO_2 supports in 2 vol% nitric acid prior to the impregnation of Au and Pd precursors resulted in significant enhancement in the H_2O_2 synthesis activity and H_2 selectivity of bimetallic Au-Pd catalysts. Table 7.3 shows the effect of acid pre-treatment of the CeO_2 support on the activity and H_2 selectivity of supported 5 wt% Au, Pd and 2.5 wt% Au-2.5 wt% Pd catalysts. Although acid pre-treating the CeO_2 support did not influence the rates of H_2O_2 production and H_2 selectivity over 5 wt% Pd/CeO_2 catalysts, both the 5 wt% Au and Au-Pd catalysts exhibited improved H_2O_2 synthesis activities, increasing from 68 to 85 $mol_{H2O2}kg_{cat}^{-1}h^{-1}$ for the latter catalyst. This improvement can be attributed to a decrease in H_2O_2 hydrogenation activity over acid pre-treated 5 wt% Au/CeO_2 (decreasing from 118 to 63 $mol_{H2O2}kg_{cat}^{-1}h^{-1}$). However, this is not applicable to 2.5 wt% Au-2.5 wt% Pd/CeO_2, where the rate of H_2O_2 hydrogenation is also increased after acid-pretreatment from 145 to 198 $mol_{H2O2}kg_{cat}^{-1}h^{-1}$.

CeO_2 Acid Treated	**Productivity / $mol_{H2O2}kg_{cat}^{-1}h^{-1}$**	**Hydrogenation / $mol_{H2O2}kg_{cat}^{-1}h^{-1}$**	**C_{H2} (%)**	**S_{H2} (%)**
CeO_2	0	37	n.d	
5% Au	7	63		
5% Pd	97	329	30	45
2.5% Au-2.5% Pd	85	198	31	38

Table 7.3 Direct synthesis of H_2O_2 over CeO_2-supported (2% HNO_3 pre-treated) Pd, Au and Au-Pd catalysts, dried in air (110 ^oC, 16 h) and calcined in static air (400 ^oC, 3 h). n.d = not determined due to yields being very low.

For acid pre-treated SiO_2, TiO_2 and carbon-supported Au-Pd catalysts, an enhanced Au dispersion in supported bimetallic Au-Pd catalysts was concluded as a contributing factor in the promotional effect observed for the direct synthesis reaction. However, in the case of CeO_2-supported catalysts, while acid pre-treatment of the support prior to impregnation of Au and Pd metals does partially improve the H_2O_2 synthesis activity of 5 wt% Au-Pd/CeO_2 from 68 to 85 $mol_{H2O2}kg_{cat}^{-1}h^{-1}$, it does not raise the activity of bimetallic Au-Pd catalysts above the activity demonstrated by 5 wt% Pd/CeO_2 catalysts (97 $mol_{H2O2}kg_{cat}^{-1}h^{-1}$).

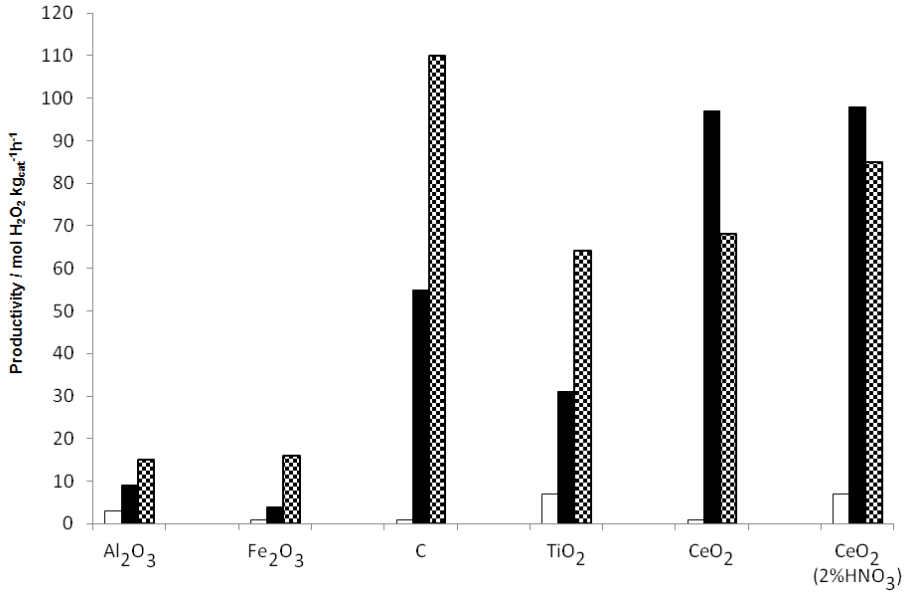

Figure 7.3 Plot showing synergy versus no synergy for supported Au and Pd catalysts for the direct synthesis of H_2O_2, comparing Al_2O_3, Fe_2O_3, Carbon, TiO_2 and CeO_2 (untreated and acid pre-treated) supports. All samples were calcined in static air at 400 ^oC for 3h. **Key** - 5%Au □, 5%Pd ■, and 2.5%Au-2.5%Pd ⬕

However, synergy between Au and Pd is observed for materials calcined at lower temperatures (uncalcined and calcined 200 ^oC) as shown in Table 7.4, representing the first time that this effect has been observed on ceria. Figure 7.3 summarises that while synergy is observed between Au and Pd for H_2O_2 synthesis over Al_2O_3, Fe_2O_3, carbon and TiO_2-supported 2.5 wt% Au-2.5 wt% Pd catalysts after 400 ^oC calcination (denoted using diagonal black and white bars), both untreated and acid pre-treated CeO_2-supported catalysts did not show evidence of synergy between Au and Pd metals for direct H_2O_2 synthesis.

7.2.3 Effect of calcination temperature on the activity of CeO_2-supported catalysts

The effect of calcination temperature on rates of H_2O_2 synthesis and hydrogenation over 5 wt% Pd and 2.5 wt% Au-2.5 wt% Pd/CeO_2 catalysts is compared in Table 7.4. While the H_2O_2 synthesis activity of Pd/CeO_2 initially decreased after calcination at 200 ^oC before rising from 46 to 97 $mol_{H2O2}kg_{cat}^{-1}h^{-1}$ on increasing calcination temperature to 400 ^oC, a minor decrease in the synthesis activity of 2.5 wt% Au-2.5 wt% Pd/CeO_2 with calcination temperature was observed. This was accompanied by a large decrease in H_2O_2 hydrogenation activity (from 433 to 145 $mol_{H2O2}kg_{cat}^{-1}h^{-1}$) indicating that different sites on the catalyst surface are responsible for H_2O_2 synthesis and hydrogenation on the catalyst surface, and are affected to different extents by calcination. On comparing the H_2O_2 synthesis activities of 5 wt% Pd and 2.5 wt% Au-2.5 wt% Pd catalysts, both uncalcined and calcined 200 ^oC, a synergistic effect on addition of Au to Pd (58 vs. 72 $mol_{H2O2}kg_{cat}^{-1}h^{-1}$) is observed and subsequently lost after calcination at 400 ^oC.

Calcination Temperature / ^oC	**Productivity / $mol_{H2O2}kg_{cat}^{-1}h^{-1}$**	**Hydrogenation / $mol_{H2O2}kg_{cat}^{-1}h^{-1}$**
5% Pd		
Uncalcined	58	639
200	46	624
400	97	329
2.5% Au-2.5% Pd		
Uncalcined	72	433
200	76	333
400	68	145

Table 7.4 Effect of calcination temperature on direct H_2O_2 synthesis for CeO_2-supported 5 wt% Pd and 2.5 wt% Au-2.5 wt% Pd bimetallic catalysts.

Analysis of the XPS-derived surface compositions for uncalcined and calcined 400 ^{o}C 5 wt% Pd/CeO_2 catalysts showed that calcination in static air increased the concentration of surface exposed Pd approximately 3 fold (Table 7.5). Simultaneously the surface chloride content decreased on calcination and this is attributed to the decomposition of the $PdCl_2$ precursor, while surface oxygen content increased by 8.9%. It is acknowledged that ceria is hygroscopic and will absorb carbon dioxide present in the atmosphere, which in some cases can constitute a significant portion of the measured surface oxygen content, and therefore a contribution to the observed catalytic activity however small, cannot be excluded.

Calcination Temperature / ^{o}C	**Surface atom %**				
	Pd	**Cl**	**O**	**Ce**	**C**
Uncalcined	3.19	2.75	34.92	12.87	46.27
400	10.35	1.94	43.81	7.77	36.13

Table 7.5 XPS-derived surface atom concentrations for uncalcined and calcined (400 ^{o}C, 3 h) 5 wt% Pd/CeO_2 catalysts as determined by XPS.

The H_2O_2 productivities determined for CeO_2-supported 5 wt% Au, Pd and Au-Pd catalysts prepared by wet impregnation can be accurately reproduced and therefore any contribution from carbon is either consistent and/or negligible. Inspection of Ce (3d) spectra shows Ce to be in the +4 state entirely, with no evidence of a +3 contribution. Although calculation of the Ce/O atom ratio gives a stoichiometry deviating from the nominal value of 0.5, this effect is anticipated and suggested to be a consequence of surface hydroxylation effects, with an increase in oxygen content associated with development of PdO/Pd-O-Ce surface species upon calcination.

XPS-derived surface Pd^{2+} concentrations in both uncalcined and calcined 400 ^{o}C samples are 100% and as illustrated by repeat scans in Figure 7.4 (b), the calcined sample solely underwent reduction to Pd^{0} on continued exposure to the X-ray beam. This could be brought about by reduction of Pd-O-Ce bonds formed during the calcination step in comparison to a higher fraction of Pd^{2+} associated with the Pd-Cl bonds in the $PdCl_2$ precursor, present to a greater extent in the uncalcined material.

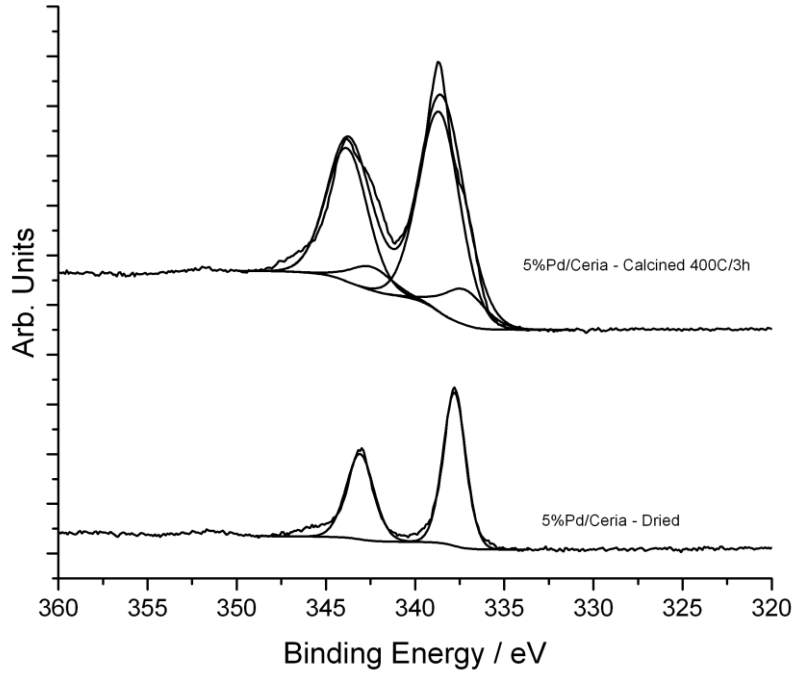

Figure 7.4 (a) XPS analysis of 5 wt% Pd/CeO_2 catalysts – moderate exposure to X-ray beam.

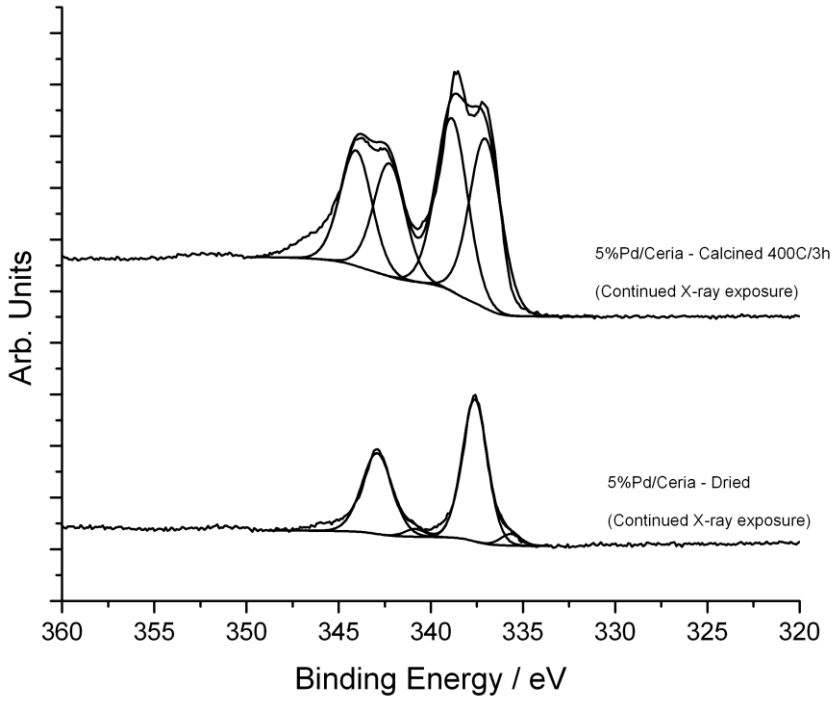

Figure 7.4 (b) XPS analysis of 5 wt% Pd/CeO_2 catalysts - prolonged exposure to X-ray beam.

7.2.4 Reusability of CeO_2-supported catalysts

Reusability experiments for CeO_2-supported 5 wt% Pd and 2.5 wt% Au-2.5 wt% Pd (both untreated and acid pre-treated) catalysts calcined at 400 ^oC confirmed that all catalysts prepared by wet impregnation were completely reusable (Figure 7.5). In contrast, uncalcined counterparts showed a considerable decrease in H_2O_2 synthesis activity on second use (with the activity of uncalcined 5 wt% Pd/CeO_2 declining from 58 to 38 $mol_{H2O2}kg_{cat}^{-1}h^{-1}$), and therefore as stated in chapters 3 and 4, the calcination step of the catalyst preparation method is critical to forming a stable and reusable material.

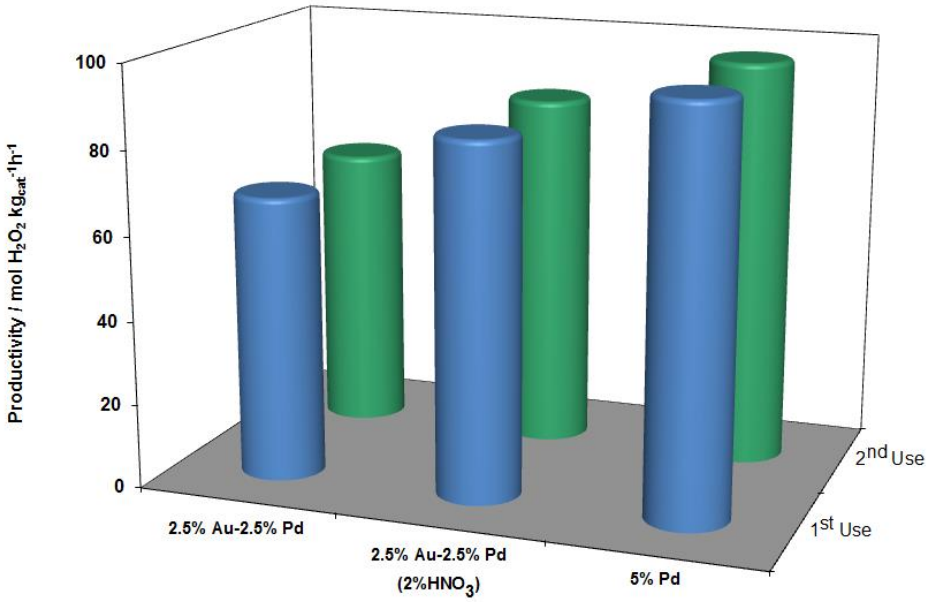

Figure 7.5 Effect of catalyst reuse on the direct synthesis of hydrogen peroxide over 5 wt% Pd/CeO_2 and bimetallic 2.5 wt% Au-2.5 wt% Pd/CeO_2 (untreated and acid pre-treated) catalysts, calcined in static air at 400 ^oC for 3 h.

7.2.5 Comparison of Au and Pd surface states as a function of calcination

The role of surface oxidation state has been investigated throughout chapters 3 to 6 and is continued in this chapter, where the effect of treating bimetallic Au-Pd catalysts under different atmospheres on the rates of H_2O_2 synthesis and hydrogenation (expressed as percentage H_2O_2 consumption) is compared. Analysis of the Pd(3d) region of Au-Pd/CeO_2 catalysts treated under different atmospheres is included in Figure 7.6 alongside their corresponding activities for direct H_2O_2 synthesis, where in the absence of STEM-HAADF imaging to determine particle size, it is implied that Pd oxidation state influences both the rates of H_2O_2 synthesis and hydrogenation over catalysts.

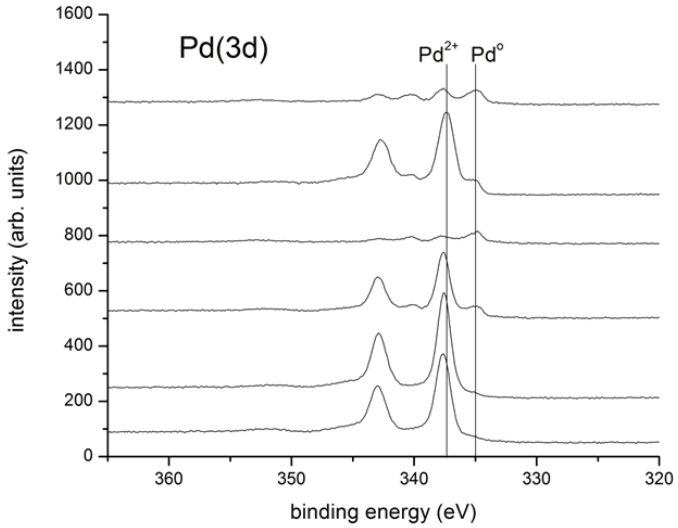

	Productivity / $mol_{H2O2}kg_{cat}^{-1}h^{-1}$	% Hydrogenation
5% H_2/Ar + H_2O_2	64	20
Static air + H_2O_2	66	9
5% H_2/Ar	68	19
Nitrogen	74	3
Flowing Air	99	4
Static Air	68	7

Figure 7.6 Pd(3d) XP spectra for bimetallic 2.5 wt% Au-2.5 wt% Pd/CeO_2 catalysts treated at 400 ^oC for 3 h under different atmospheres - Select catalysts were post-treated in aqueous 50 wt% H_2O_2 for 3 h. Respective H_2O_2 productivities and percentage H_2O_2 hydrogenation are listed adjacent to the spectra.

In general, catalysts comprising a high surface Pd^{2+} concentration hydrogenated the least hydrogen peroxide, while all of the catalysts demonstrated high activity toward H_2O_2 synthesis, in particular when calcining in flowing air (the Pd(3d) spectra of which is similar to that obtained when calcining in static air, and therefore the difference in activity is likely associated with differences in Pd surface exposure). Treatment of 2.5 wt% Au-2.5 wt% Pd/CeO_2 catalysts in aqueous 50 wt% H_2O_2 after calcination/reduction did not dramatically alter either the rates of H_2O_2 synthesis and hydrogenation over Au-Pd/CeO_2 reduced in 5% H_2/Ar

(H_2O_2 productivities: 64 vs. 68 $mol_{H2O2}kg_{cat}^{-1}h^{-1}$, and 19 vs. 20% H_2O_2 hydrogenation respectively), while identical H_2O_2-treatment of Au-Pd/CeO_2 after calcination in static air increased the amount of H_2O_2 hydrogenated over the catalyst from approximately 7 to 9%. Simultaneous to this, a partial increase in the Pd^0 signal intensity was noted alongside the dominant Pd^{2+} signal, with surface Pd^{2+} concentration 50 wt% H_2O_2 post-treatment. Atomic absorption spectroscopy of H_2O_2-treated catalysts showed no evidence of Au or Pd leaching, suggesting that for **5% H_2/Ar reduced Au-Pd/CeO_2** catalysts, particle sintering has proceeded to greater extent relative to other heat treatment conditions, forming larger nanoparticles that constitute the reduced signal intensities witnessed in Pd(3d) and Au(4f) spectral regions.

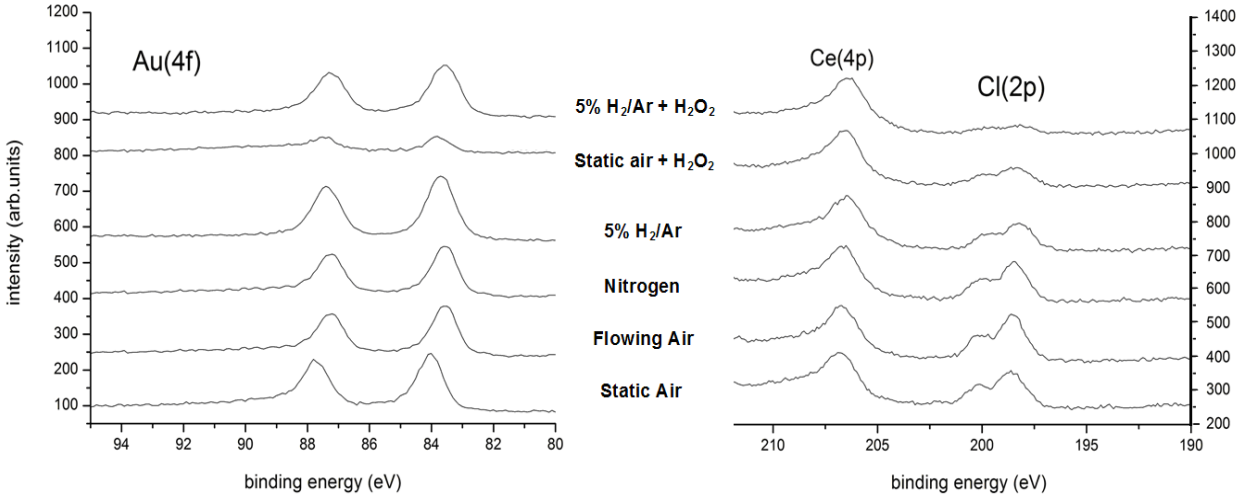

Figure 7.7 Au(4f), Ce(4p) and Cl(2p) XP spectra for bimetallic 2.5 wt% Au-2.5 wt% Pd/CeO_2 catalysts treated at 400 ^oC for 3 h under different atmospheres - Select catalysts were post-treated in 50 wt% H_2O_2 for 3 h. Respective H_2O_2 synthesis activities and percentage H_2O_2 hydrogenation values listed adjacent to spectra.

Furthermore, from comparison of the Au(4f), Ce(4p) and Cl(2p) regions shown in Figure 7.7, solely metallic Au^0 species are present for all 2.5 wt% Au-2.5 wt% Pd/CeO_2 catalysts, the binding energies of which fall in the range 83.5-84.2 eV. A high variation of 0.7 eV across this series may be related to particle size and the degree of Au-Pd alloying depending on the heat treatment conditions applied[21]. The chloride content of Au-Pd/CeO_2 catalysts after calcination in static or flowing air is comparable and indicative of at least two different chloride species situated in the binding energy range 197-202 eV. This is similar to

findings reported for carbon-supported Au-Pd catalysts in chapter 4, and attributed to interaction of residual chloride species with Au and Pd nanoparticles and the ceria surface, and chloride associated with $PdCl_2$ retained after heat treatment (the decomposition temperature of palladium chloride is stated as 679 ^oC)[22].

7.3 Discussion

The initial findings of this chapter highlight that ceria could be a suitable support for Au and Pd nanoparticles active for the direct synthesis of hydrogen peroxide, due in part to very high H_2O_2 synthesis activities over 5 wt% Pd/CeO_2 (97 $mol_{H2O2}kg_{cat}^{-1}h^{-1}$) catalysts, which are also superior to the activities reported for carbon and metal-oxide supported 5 wt% Pd catalysts. However, the addition of Au to Pd/CeO_2 catalysts does not result in an enhanced synthesis activity, although it does influence the rate of H_2O_2 hydrogenation. The origin of this effect is most likely to be due to lack of alloy formation under the heat treatment conditions applied, *i.e.* calcination in static air.

This is suggested by a large variation in binding energy of 0.7 eV observed in the Au(4f) region, corresponding to Au^0 species ranging from 83.5-84.2 eV and depending on the heat treatment atmosphere applied to 2.5 wt% Au-2.5 wt% Pd/CeO_2 catalysts. Unfortunately, ceria is a difficult support on which to observe Au nanoparticles using aberration corrected electron microscopy techniques due to the difficulty in achieving sufficient Z-contrast for this system. The determination of whether alloying is observed using more advanced techniques will represent the subject of a subsequent and more detailed investigation.

Other studies have indicated that the interactions of Au and Pd with reducible ceria can co-exist with the mutual interactions between these metals implying that not all of the metal present is alloyed[15]. For the selective oxidation of arabinose to arabinoic in particular, non-alloyed Au^0 species are considered as responsible for the activation of arabinose while transformation of Pd^0/Pd^{2+} species can provoke oxygen interaction[15], with the proposal that Au or Au-Pd alloys covered with a thin PdO film consititue the synergistic effect observed.

It is also interesting to note that the method used to synthesize ceria nanoparticles can have a profound effect on structure and activity. For Au/CeO_2 catalysts where the support was synthesized using a solvothermal approach[23], Au particles were identified as being larger in size than the ceria crystallites (~3-8 nm) they were supported on, whereas the crystallite size of commercial grade supports are quoted in the range 20-50 nm, with some sources stating the average crystallite size as 54 nm which is similar to the value of 51-52 nm, determined using the Scherrer equation). The orientation and size of CeO_2 crystallites has also been suggested to influence catalytic activity.

For example, Rh deposited on cubic [110] and rod [110]/[100] shaped nanocrystalline CeO_2 formed catalysts that demonstrated improved H_2 selectivity for ethanol reforming compared to catalysts prepared using disordered/irregular CeO_2 nanoparticles, suggesting that the ratio of surface planes could play a key role in enhancing ethanol reforming activity[24]. The quantity of exposed Pd atoms on CeO_2-supported catalysts synthesized by co-precipitation were shown to depend mainly on the surface areas of the catalysts, and is supported in part by Miedziak and co-workers[20], who studied the solvent free oxidation of benzyl alcohol using cerium oxide prepared by supercritical precipitation to host Au and Pd. The resulting catalyst gave improved activity relative to supports derived *via* a non-supercritical synthesis route and showed evidence of synergy between Au and Pd. Microscopy of supercritically precipitated CeO_2-supported Au-Pd catalysts showed homogeneous alloy particles 50 to 150 nm in size (found to be Au-rich) with a low number density of highly dispersed Pd species associated with the CeO_2 support and present as Au^0 and Pd^{2+} respectively.

Most importantly the non-supercritically prepared $Au-Pd/CeO_2$ catalyst showed a loss of activity on second use compared to a significant increase in activity for the supercritically prepared $Au-Pd/CeO_2$ catalyst. However, activity did then decrease on third use given the spherical morphology of nanocrystalline supercritical CeO_2 started to break down, to resemble the morphology CeO_2 prepared by the non-supercritical route and was accompanied by phase separation of Au and Pd. To conclude, this finding implies that use of a non-ordered ceria supports may not necessarily be disadvantageous to catalytic activity.

7.4 Development and optimisation of supported Au-Pd-Pt catalysts

Monometallic Pd has so far qualified as the most active composition in chapter 7, however, it is appreciated that alloying or combining two metals can lead to materials with specific chemical properties due to an interplay of ensemble and electronic effects, and that a bimetallic surface can exhibit catalytic properties that are very different from those of the surfaces of the individual metals. It has been demonstrated that the combination of Pd with Au, Ir, Ag and Pt metal can improve both the activity and selectivity of catalysts active for the direct synthesis of hydrogen peroxide[25]. The addition of a second metal to Pd has been claimed to improve the H_2 selectivity, favouring selective formation H_2O_2 as oppose to the non-selective formation of water. Specifically, the effect of doping Pd with Pt was found to enhance the selectivity of catalysts, with a maximum activity exhibited at a Pd:Pt ratio of 18, before further increasing Pt content leads to a decrease in selectivity[26]. For TS-1 supported catalysts, addition of Pt to Pd resulted in the stabilization of surface Pd^{2+} species, with the optimum level of Pt determined to represent a balance between the increase of surface Pd^{2+} concentration and variation in the morphology of Pd nanoparticles[27].

Okada and co-workers[28] have synthesised Pd-Pt and Pd-Au/ZrO_2-SO_4 catalysts and compared their activity for the direct synthesis of hydrogen peroxide using mild conditions outside of the explosion region. The effect of adding Pt to Pd with respect to increasing the yield of hydrogen peroxide is critically sensitive to Pt amount, and using only a low Pt content, it is possible to improve the H_2 selectivity from 55 to 70% and subsequent H_2O_2 productivity with respect to the Pd-only catalysts. The addition of Au to Pd (1:1 weight) also improved both the H_2O_2 productivity and H_2 selectivity, maintaining a stable 62% selectivity after 12 h.

The aim of the second part of chapter 7 is to investigate the effect of addition of Pt to Au, Pd, Au-Pd/CeO_2 catalysts on rates of H_2O_2 synthesis and hydrogenation, in addition to understanding the role of Pt in supported Pd-Pt catalysts already found to be highly active by Lunsford *et al.* [29].

7.4.1 Comparison of carbon-supported Au-Pd-Pt catalysts

Platinum is facile at decomposing hydrogen peroxide as was first reported by Faraday and has been applied extensive to a range of selective and total hydrogenation reactions of major industrial importance, including ethylene and propylene hydrogenation, and represents a component of both the three-way catalytic converter and polymer electrolyte fuel cells[30]. Many commercially available Pt-based hydrogenation catalysts[31] are supported on carbon and therefore for direct H_2O_2 synthesis, the activity of Au-Pt, Pd-Pt and Au-Pd-Pt/C (Darco G60) catalysts were evaluated in advance of Au-Pd-Pt/CeO_2 catalysts for comparative purposes.

	Carbon Composition / wt%	**Productivity / $mol_{H2O2}kg_{cat}^{-1}h^{-1}$**	**Hydrogenation / $mol_{H2O2}kg_{cat}^{-1}h^{-1}$**
1	2.50% Au-2.50% Pd	120	117
2	2.50% Au-2.50% Pt	30	1038
3	2.50% Pd-2.50% Pt	154	504
4	2.45% Au-2.45% Pd-0.05% Pt	120	294
5	2.40% Au-2.40% Pd-0.10% Pt	137	324
6	2.35% Au-2.35% Pd-0.20% Pt	179	301
7	2.28% Au-2.28% Pd-0.45% Pt	142	58
8	0.20% Au-4.60% Pd-0.20% Pt	145	409

Table 7.6 Effect of catalyst composition on the direct H_2O_2 synthesis - Carbon supported catalysts.

While high rates of H_2O_2 production can be achieved, the H_2O_2 hydrogenation rates are exceptionally high over all catalysts (except 2.28 wt% Au-2.28 wt% Pd-0.45 wt% Pt/C), and unique to the carbon. This will be demonstrated in the results obtained for CeO_2 and TiO_2-supported Au-Pd-Pt catalysts, and though using carbon as a support is not an aim of chapter 7, it is likely differences in the morphology of Au-Pd nanoparticles as recognised for reducible (TiO_2 - $Au_{core}Pd_{shell}$) and non-reducible (carbon - homogeneous alloys) supported 2.5 wt% Au-2.5 wt% Pd catalysts may apply to Au-Pt, Pd-Pt and Au-Pd-Pt compositions.

7.4.2 CeO_2-supported mono and bimetallic Pt catalysts.

Comparison of the activities of CeO_2-supported mono and bimetallic Pt catalysts in Table 7.7 indicated that while 5 wt% Pt is not a highly active catalyst for H_2O_2 synthesis compared to 5 wt% Pd (97 $mol_{H2O2}kg_{cat}^{-1}h^{-1}$), it did hydrogenate 2-3 times less hydrogen peroxide (126 $mol_{H2O2}kg_{cat}^{-1}h^{-1}$). The synthesis activity of 2.5 wt% Pd-2.5 wt% Pt/CeO_2 is 138 $mol_{H2O2}kg_{cat}^{-1}h^{-1}$, confirming that a synergistic effect is manifested on the addition of Pt to Pd, compared to no synergy on the addition of Au to Pd, and is accompanied by a decrease in hydrogenation activity relative to 5 wt% Pd.

CeO_2 Composition / wt%	**Productivity / $mol_{H2O2}kg_{cat}^{-1}h^{-1}$**		**Hydrogenation / $mol_{H2O2}kg_{cat}^{-1}h^{-1}$**
	2 min	**30 min**	
5% Pt	46	8	126
5% Pd	354	97	329
2.5% Au-2.5% Pt	120	20	109
2.5% Au-2.5% Pd	281	68	145
2.5% Pd-2.5% Pt	392	138	182
4.8% Pd-0.2% Pt	441	125	192
4.8% Pd-0.2% Au	198	79	178

Table 7.7 Effect of catalyst composition on the direct synthesis of H_2O_2 over 5 wt% Pt, Pd and 2.5 wt% Au/Pd-2.5 wt% Pt/CeO_2 catalysts including 2 minute / initial rate measurements.

Further compositions are included in Table 7.7 to assess the effect of a minor addition of Pt/Au to Pd, where it was determined that addition of 0.2 wt% Pt induced a synergistic effect close to the extent achieved in 2.5 wt% Pd-2.5 wt% Pd. In comparison, addition of 0.2 wt% Au to Pd decreased the rate of H_2O_2 synthesis from 97 to 79 $mol_{H2O2}kg_{cat}^{-1}h^{-1}$, but did simultaneously reduce the hydrogenation activity of the catalyst. These two observations are a

useful guide to directing the design of further compositions (maintaining 5 wt% loading) including trimetallic Au-Pd-Pt catalysts, since it is now understood that even low loadings of secondary and tertiary metals can induce a significant synergistic effect.

Calcination Temperature / ^{o}C	**Productivity / $mol_{H2O2}kg_{cat}^{-1}h^{-1}$**	**Hydrogenation / $mol_{H2O2}kg_{cat}^{-1}h^{-1}$**
2.5% Au-2.5% Pd		
Uncalcined	72	433
200	76	333
400	68	145
500	34	136
2.5% Pd-2.5% Pt		
Uncalcined	16	351
200	23	286
400	138	182
500	18	575

Table 7.8 Effect of calcination temperature on the direct synthesis of H_2O_2 over bimetallic 2.5 wt% Au-2.5 wt% Pd and 2.5 wt% Pd-2.5 wt% Pt/CeO_2 catalysts.

Before discussing the screening of 42 CeO_2-supported Au-Pd-Pt compositions, the effect of calcination temperature in static air on the direct synthesis of hydrogen peroxide was compared for CeO_2-supported Au-Pd and Pd-Pt catalysts to determine if 400 ^{o}C represented the optimum temperature for Pd-Pt in terms of catalyst activity and reusability (Table 7.8). These requirements are fulfilled at 400 ^{o}C. However, the variation in H_2O_2 synthesis and hydrogenation over Pd-Pt is different to that of Au-Pd, with H_2O_2 synthesis activity rising from 16 to 138 $mol_{H2O2}kg_{cat}^{-1}h^{-1}$ on increasing the calcination temperature to 400 ^{o}C, before decreasing to 18 $mol_{H2O2}kg_{cat}^{-1}h^{-1}$ at 500 ^{o}C (Table 7.8). Simultaneously the rate of H_2O_2 hydrogenation over Pd-Pt becomes elevated and reference to the literature[32] suggests this could result from an elevated surface Pt exposure *via* Pt-O bond formation.

7.4.3 CeO_2-supported trimetallic Au-Pd-Pt catalyst screening

In this section, the preparation of trimetallic 5 wt% Au-Pd-Pt/CeO_2 catalysts based on a gradual addition of Pt, maintaining equivalent Au and Pd loadings is initially investigated. Referring to Table 7.9, addition of Pt to Au-Pd induced a significant promotional effect with respect to H_2O_2 synthesis, with an initial decrease in hydrogenation activity at both 0.05 and 0.10 wt% Pt loadings compared to 2.5 wt% Au-2.5 wt% Pd/CeO_2. Addition of 0.45 wt% Pt gave the highest rates of H_2O_2 synthesis (2 min) and hydrogenation for catalyst series **1-7**, implying that the addition of Pt to Au-Pd/CeO_2 catalysts resulted in modification of surface Au-Pd-Pt composition, which is supported by catalyst characterisation in section 7.5.

	CeO_2 Composition / wt%	**Productivity / $mol_{H2O2}kg_{cat}^{-1}h^{-1}$**		**Hydrogenation / $mol_{H2O2}kg_{cat}^{-1}h^{-1}$**
		2 min	**30 min**	**30 min**
1	2.50% Au-2.50% Pd	281	68	145
2	2.48% Au-2.48% Pd-0.05% Pt	308	63	46
3	2.45% Au-2.45% Pd-0.10% Pt	171	109	76
4	2.40% Au-2.40% Pd-0.20% Pt	436	170	145
5	2.35% Au-2.35% Pd-0.30% Pt	389	159	177
6	2.28% Au-2.28% Pd-0.45% Pt	670	100	459
7	2.00% Au-2.00% Pd-1.00% Pt	194	115	93
8	2.50% Au-2.30% Pd-0.20% Pt	260	86	11

Table 7.9 Effect of catalyst composition on the direct synthesis of H_2O_2 using trimetallic Au-Pd-Pt/ CeO_2 catalysts.

The most active catalyst composition with respect to H_2O_2 productivity was determined as 2.40 wt% Au-2.40 wt% Pd-0.20 wt% Pt - which also exhibited a hydrogenation activity identical to 2.5 wt% Au-2.5 wt% Pd (145 $mol_{H2O2}kg_{cat}^{-1}h^{-1}$), indicating that addition of Pt at specific loadings could improve the H_2O_2 synthesis activity for a given catalyst without modifying the hydrogenation activity. For catalyst **8**, a minor variation in Au and Pd metal loadings from equivalency (2.50 wt% Au-2.30 wt% Pd-0.20 wt% Pt) significantly reduced the H_2O_2 hydrogenation activity of the catalyst to the extent that it was almost switched-off (11 $mol_{H2O2}kg_{cat}^{-1}h^{-1}$), demonstrating that minor variation in the loading of any metal present in trimetallic Au-Pd-Pt catalyst can significantly influence activity.

The results presented in sections 7.4.2 and 7.4.3 respectively serve as the basis of a larger catalyst screening study to determine the optimum Au-Pd-Pt catalyst composition with respect to both H_2O_2 synthesis and hydrogenation activity. While no synergy was observed between Au and Pd for bimetallic 2.5 wt% Au-2.5 wt% Pd/CeO_2 catalysts, addition of Pt to Au, Pd and Au-Pd/CeO_2 catalysts has induced synergy, and therefore the aim of upcoming sections is to gain an understanding of the possible promotional effect(s) on addition of Pt in terms of catalyst structure, *i.e.* evidence of Au-Pt / Pd-Pt / Au-Pd-Pt alloys.

7.4.4 The effect of 5 wt% Au-Pd-Pt/CeO_2 catalyst composition on both the rates of H_2O_2 synthesis and hydrogenation

In section 7.4.4, results from previous sections comparing the effect of addition of Pt to CeO_2-supported Au, Pd and Au-Pd catalysts are extended to a full Au-Pd-Pt compositional study, encompassing a total of 42 catalysts. All catalysts were prepared by wet-impregnation, air dried and calcined in static air (400 ^oC, 3 h) as standard. For convenience, changes in the activity and composition of catalysts are presented in the form of 2D (Figures 7.8 and 7.9) and 3D (Figure 7.10, Appendix A7.1 and A7.2) ternary diagrams, plotted using Origin 8.5 software. In addition, the H_2O_2 synthesis and hydrogenation activities obtained using Au-Pd-Pt/CeO_2 are plotted on separate diagrams and therefore will be discussed in sequence, and will be used to better highlight optimum catalyst composition(s) using a colour assignment scheme. For all ternary diagrams, the top of the diagram represents Pd-rich compositions, followed by Pt-rich compositions on the bottom-left and Au-rich compositions on the bottom-right of the diagram respectively, with the Au/Pd/Pt loading for all catalysts fixed at 5 wt%.

Referring to Figure 7.8, the H_2O_2 synthesis activities obtained using different CeO_2-supported Au, Pd, Pt, Au-Pt, Pd-Pt and Au-Pd-Pt catalysts are summarised in 2D form. It is observed that in general, the highest rates of H_2O_2 synthesis are obtained using Pd-Pt and Au-Pd-Pt catalysts in which the Pd loading exceeds 2 wt% (corresponding to the upper half of the ternary diagram), while moderate to low synthesis activities are obtained using Au-Pt and Au-Pd-Pt catalysts in which the Au or Pt loading exceeds 2.5 wt%.

The investigation of Pd-rich catalyst compositions showed that partial addition of Pt and Au-Pt to Pd resulted in the highest rates of H_2O_2 synthesis, the maximum of which was obtained using 0.20 wt% Au-4.60 wt% Pd-0.20 wt% Pt (185 $mol_{H2O2}kg_{cat}^{-1}h^{-1}$).

The reasons as to why this catalyst composition is the most active will be discussed in section 7.5, but briefly it is understood that high Pd surface exposure is crucial. The second highest H_2O_2 synthesis activity was obtained using 2.40 wt% Au-2.40 wt% Pd-0.20 wt% Pt (170 $mol_{H2O2}kg_{cat}^{-1}h^{-1}$), indicated that partial addition of Pt to Au-Pd catalysts also serves as a viable route to achieving high rates of H_2O_2 synthesis.

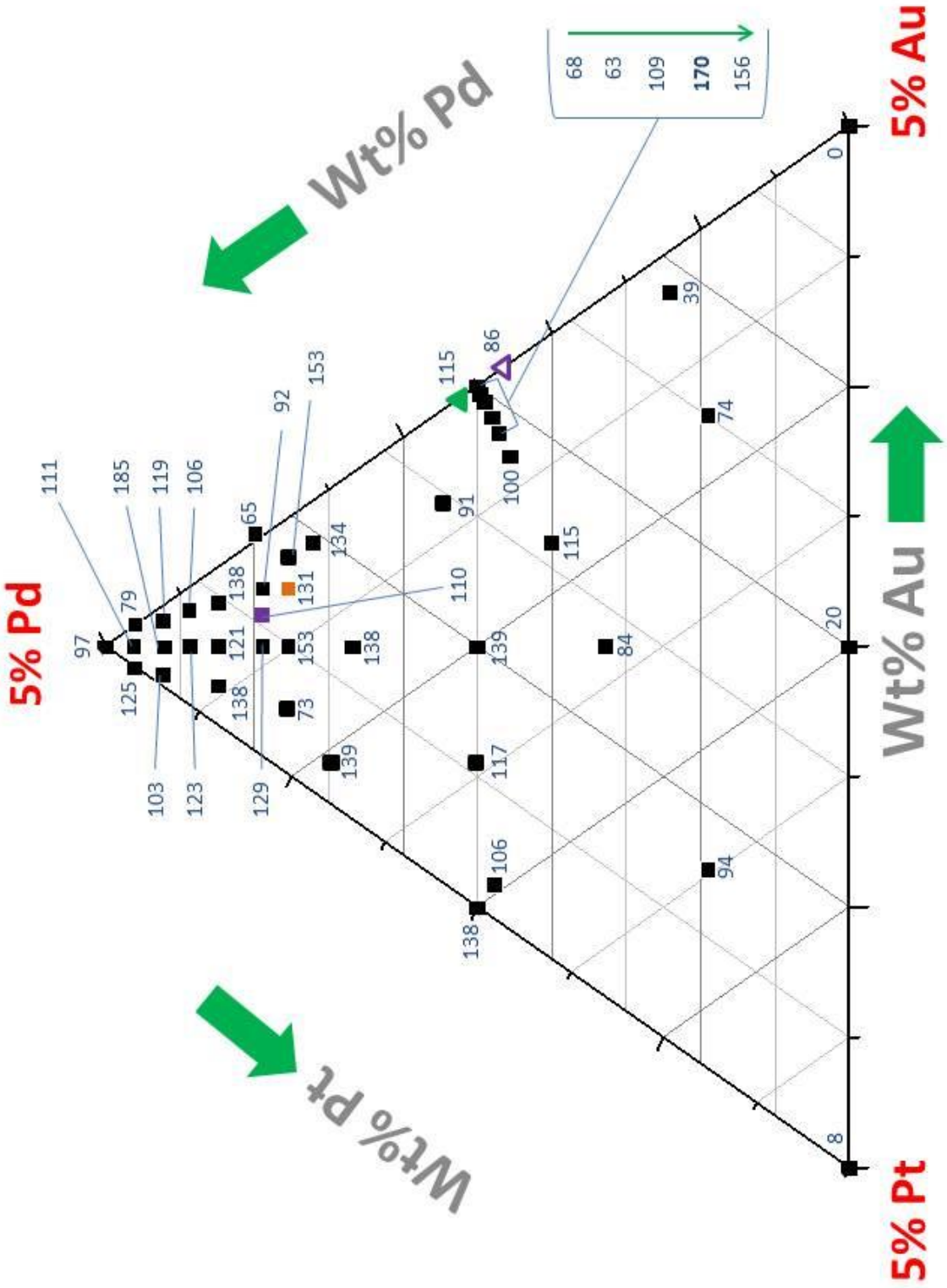

Figure 7.8 Summary of the H_2O_2 synthesis activities for 5 wt% Au-Pd-Pt/CeO_2 catalysts. Numbers presented in the 2D ternary diagram are H_2O_2 productivities ($mol_{H2O2}kg_{cat}^{-1}h^{-1}$).

Referring to Figure 7.9, the corresponding H_2O_2 hydrogenation activities obtained for different CeO_2-supported Au, Pd, Pt, Au-Pt, Pd-Pt and Au-Pd-Pt catalysts are summarised in 2D form. A different scenario is evident for H_2O_2 hydrogenation activity as a function of Au-Pd-Pt composition, with high rates of hydrogenation observed in all parts of the diagram, indicating that the H_2O_2 synthesis and hydrogenation pathways, as anticipated, are affected to different extents with on varying catalyst composition.

The most active catalyst for H_2O_2 synthesis: 0.20 wt% Au-4.60 wt% Pd-0.20 wt% Pt, is also an efficient H_2O_2 hydrogenation catalyst (385 $mol_{H2O2}kg_{cat}^{-1}h^{-1}$) as are many of the surrounding compositions. However, on close inspection of Pd-rich, Au-Pd-Pt compositions at the top of the diagram, low rates of H_2O_2 hydrogenation are observed for 2 Au-Pd-Pt catalysts both containing 4.20 wt% Pd. The presence of such isolated low hydrogenation activities suggests that 'zones' exist on descending the diagram / increasing Au, Pt content, resulting in several Pd-rich, Au-Pd-Pt catalysts highly active for H_2O_2 synthesis and exhibiting low rates of H_2O_2 hydrogenation (in the range 30-70 $mol_{H2O2}kg_{cat}^{-1}h^{-1}$).

Several moderate to low H_2O_2 hydrogenation activities were also identified on addition of Pt to Au-Pd catalysts (of equal loading) and for 2.40 wt% Au-2.40 wt% Pd-0.20 wt% Pt in particular, addition of Pt significantly increased the H_2O_2 synthesis activity of the catalyst relative to 2.50 wt% Au-2.50 wt% Pd without modifying H_2O_2 hydrogenation activity (which is maintained at 145 $mol_{H2O2}kg_{cat}^{-1}h^{-1}$). This catalyst and 2.5 wt% Pd-2.5 wt% Pt represent important examples where H_2O_2 synthesis activity is improved relative to 5 wt% Pd and 2.5 wt% Au-2.5 wt% Pd catalysts, without increasing the rate of H_2O_2 hydrogenation - evidence of a promotional effect induced by Pt in bimetallic and trimetallic catalysts.

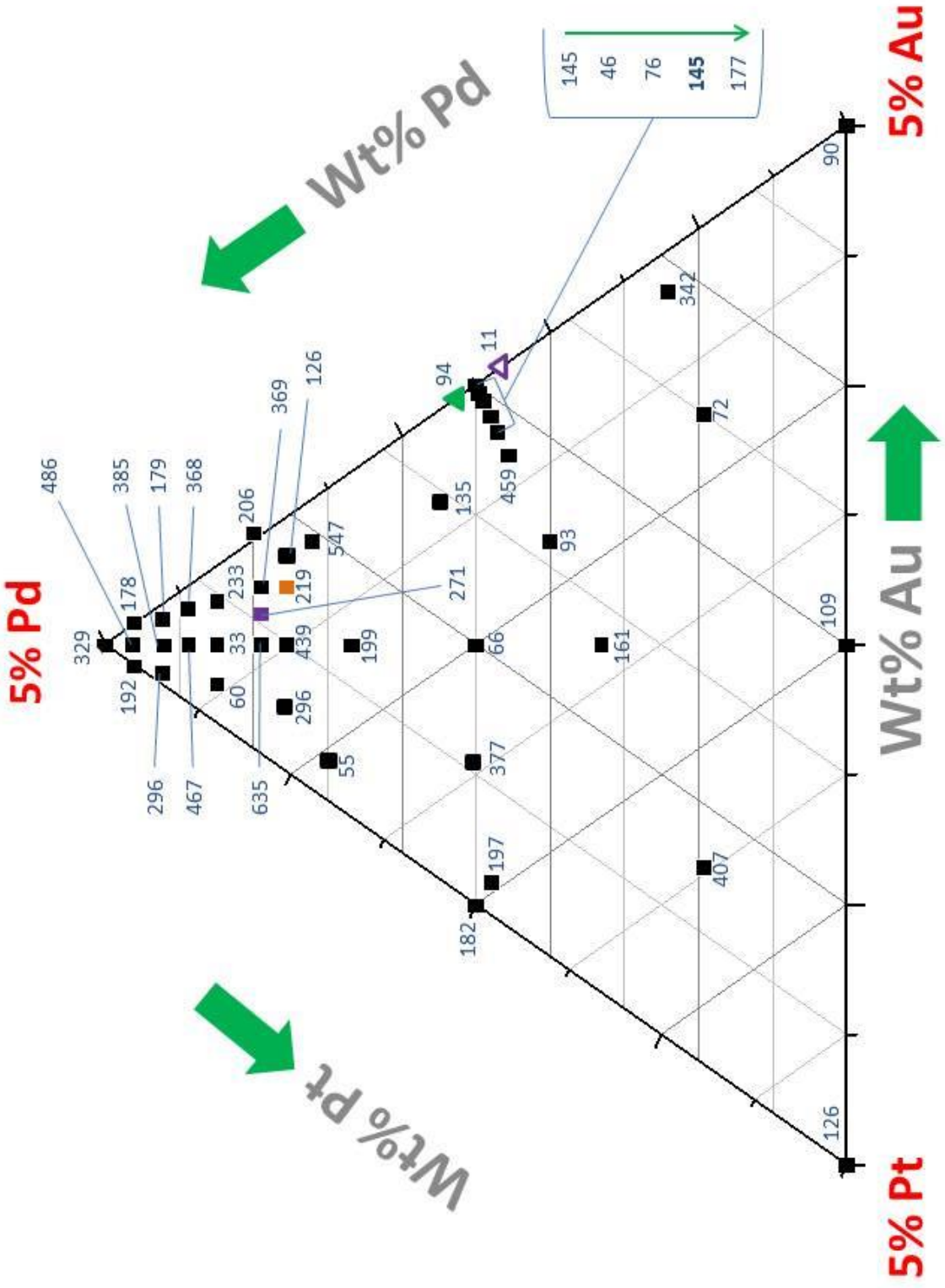

Figure 7.9 Summary of the H_2O_2 hydrogenation activities for 5 wt% Au-Pd-Pt/CeO_2 catalysts. Numbers presented in the 2D ternary diagram are H_2O_2 hydrogenation activities ($mol_{H2O2}kg_{cat}^{-1}h^{-1}$).

In order to simplify the relationship between H_2O_2 synthesis and hydrogenation activity with Au-Pd-Pt composition, 3D ternary diagrams were plotted using Origin software. Colour assignments are used to represent hydrogen peroxide synthesis (Appendix A7.1) and hydrogenation (Appendix A7.2) activities respectively, with highly active H_2O_2 synthesis/ hydrogenation catalysts represented using red and grey colours. For H_2O_2 synthesis, two red regions corresponding to CeO_2-supported 2.40 wt% Au-2.40 wt% Pd-0.20 wt% Pt and 0.20 wt% Au-4.60 wt% Pd- 0.20 wt% Pt catalysts exist, whereas only one red region exists for H_2O_2 hydrogenation, corresponding to 0.50 wt% Au-4.00 wt% Pd-0.50 wt% Pt/CeO_2.

In Figure 7.10, the H_2O_2 synthesis and hydrogenation activities determined for Au-Pd-Pt/CeO_2 catalysts were combined in a composite diagram (synthesis – hydrogenation) to show optimum catalyst compositions in red, where H_2O_2 synthesis > H_2O_2 hydrogenation, to give a positive value. Using this approach, trimetallic Au-Pd-Pt/CeO_2 catalysts comprising metal loadings (highest to lowest): Pd > Pt > Au, were proposed to represent the optimum compositions. More specifically, Pd loading is >2.5 wt%, Pt loading is 0.2-1.9 wt% and Au loading is distributed over two regions: 0.2-0.7 wt% and 1.2-1.9 wt% respectively.

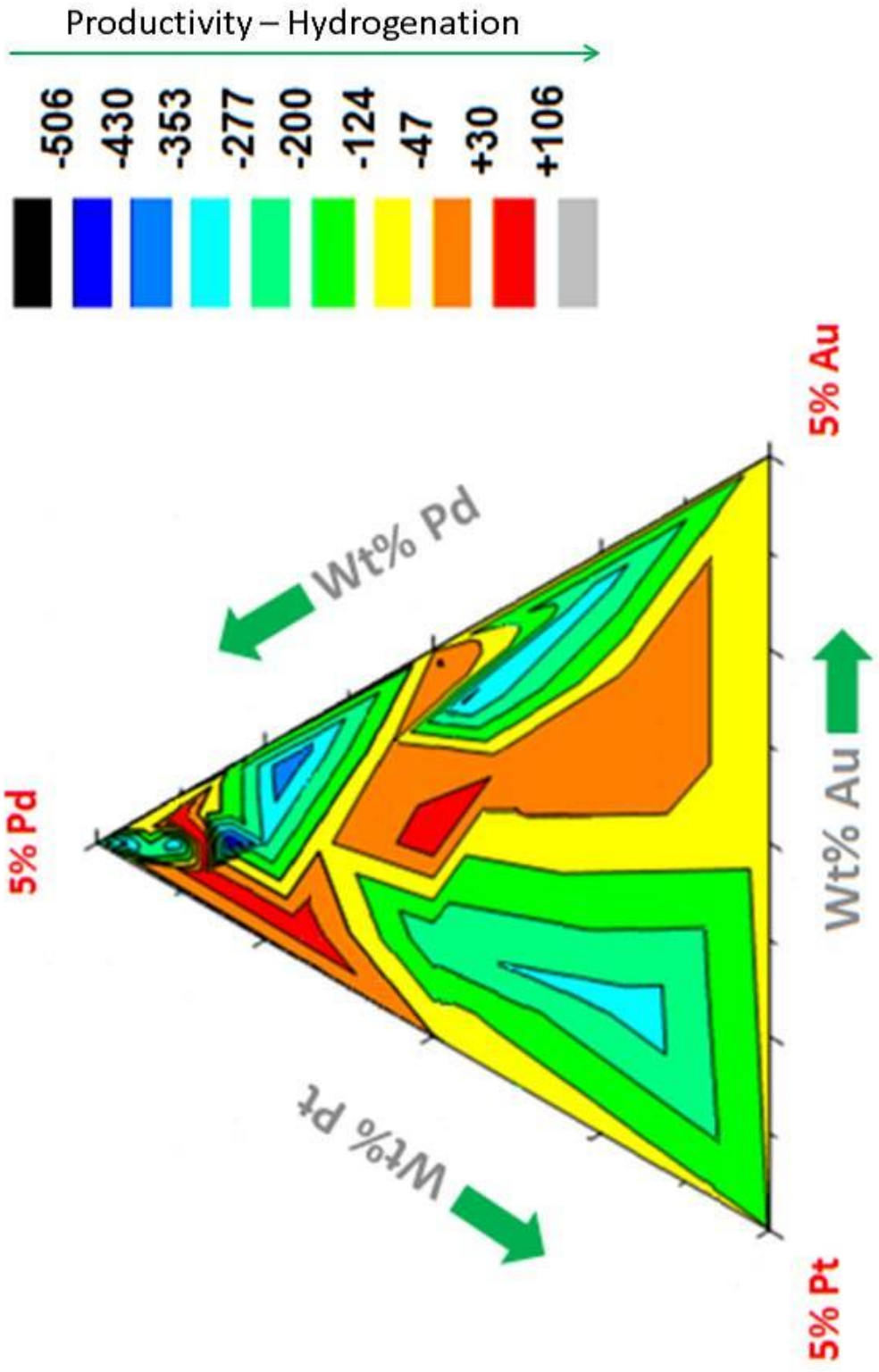

Figure 7.10 Composite values (synthesis – hydrogenation) values for CeO_2-supported 5 wt% Au-Pd-Pt catalysts presented as a 3D diagram.

It is appreciated that while this approach is not an absolute indicator in terms of what constitutes optimum/favourable catalyst compositions as it is specific to the reaction conditions used (*e.g.* batch operation, pressure, solvent, temperature, time), it does serve as a useful guideline in directing further development of Au-Pd-Pt/CeO_2 catalysts for application in other systems. Examples include: (i) flow reactors, where the residence time is dramatically shorter (seconds) compared to batch reactors (30 minutes, inside sealed autoclave containing a finite concentration of H_2/O_2 gases), and (ii) use of immiscible solvent mixtures.

Piccinini[33] demonstrated that performing the direct synthesis reaction in an immiscible two-phase, decanol-1-ol/water solvent and using a 0.63 wt% Au-3.75 wt% Pd-0.63 wt% Pt/CeO_2 catalyst and semi-batch conditions that a 3.5 wt% H_2O_2 concentration could be formed in the water phase. This concentration is at the lower end of the industrial target (3-8 wt% H_2O_2) and as represents a highly significant result as no acid/halide promoters or distillation steps were required, with high yield achieved *via* in-situ extraction of hydrogen peroxide formed in the organic, decanol-1-ol phase.

The H_2O_2 synthesis (2 and 30 min) and hydrogenation activities for all Au-Pd-Pt/CeO_2 catalysts in this study are tabulated in Appendix Table A7.1. In addition, results for Pd-Pt and Au-Pd/CeO_2 catalysts where Au or Pt loading was systematically increased are shown in Appendix Table A7.2, as results for bimetallic catalysts plotted along the perimeter of ternary diagrams and therefore are difficult to distinguish from each other. Briefly, partial Au or Pt addition to Pd/CeO_2 was found to influence H_2O_2 synthesis and hydrogenation activities in a somewhat complex manner on systematically increasing Au or Pt content. These findings will be investigated in a future study, separate to the development Au-Pd-Pt/CeO_2 catalysts. In section 7.5, XPS characterisation for a selection of highly active trimetallic Au-Pd-Pt catalysts is presented.

7.5 XPS Characterisation

The surface composition for select CeO_2-supported catalysts was investigated by XPS, with results for Pd-Pt and three highly active Au-Pd-Pt catalysts summarised in Table 7.10. Firstly for catalyst **2**, which exhibited high rates of H_2O_2 synthesis (185 $mol_{H2O2}kg_{cat}^{-1}h^{-1}$) and hydrogenation (385 $mol_{H2O2}kg_{cat}^{-1}h^{-1}$) respectively, a high surface Pd exposure consisting of >90% Pd^{2+} species was identified. Referring to Figure 7.11 (top), the high Pd^{2+} signal intensity in the Pd(3d) region indicates formation of a 'film-like' dispersion of PdO alongside a minor Pt contribution. Interestingly, no Au(4f) signal was detected despite a 0.20 wt% Au loading, implying sub-surface reduction and/or coverage of Au by cationic Pd and Pt species (Pt^{2+} detected at 72.5 eV binding energy).

	CeO_2 Composition / wt%	**Surface atom %**			
		Au	**Pd**	**Pt**	**Cl**
1.	2.50% Pd-2.50% Pt	-	6.05	1.51	3.73
2.	0.20% Au-4.60% Pd-0.20% Pt	0.00	19.38	0.26	9.21
3.	0.63% Au-3.75% Pd-0.63% Pt	0.07	3.73	0.28	3.62
4.	2.40% Au-2.40% Pd-0.20% Pt	0.08	7.12	0.17	3.74

Table 7.10 Summary of surface atomic composition for select CeO_2-supported catalysts.

The surface Cl concentration for catalysts **1-4** is moderate to high, which may affect the H_2O_2 synthesis/hydrogenation activities of catalysts with respect to controlling the degree of particle dispersion during the calcination step, and by minimising H_2O_2 hydrogenation *via* selective blocking of surface sites active for O-O bond scission.

Comparison of Pd(3d) spectra for catalysts **2** and **3** in Figure 7.11 supports the development of a thin-film PdO dispersion on ceria for catalyst **2**, based on the unexpectedly high difference in signal intensity observed between samples, which exceeds the difference in wt% Pd loading, Secondly the Pd oxidation state is influenced by composition, with transition from Pd^{2+} to Pd^{0} exclusively on increasing both Au and Pt loadings from 0.20 to 0.63 wt%.

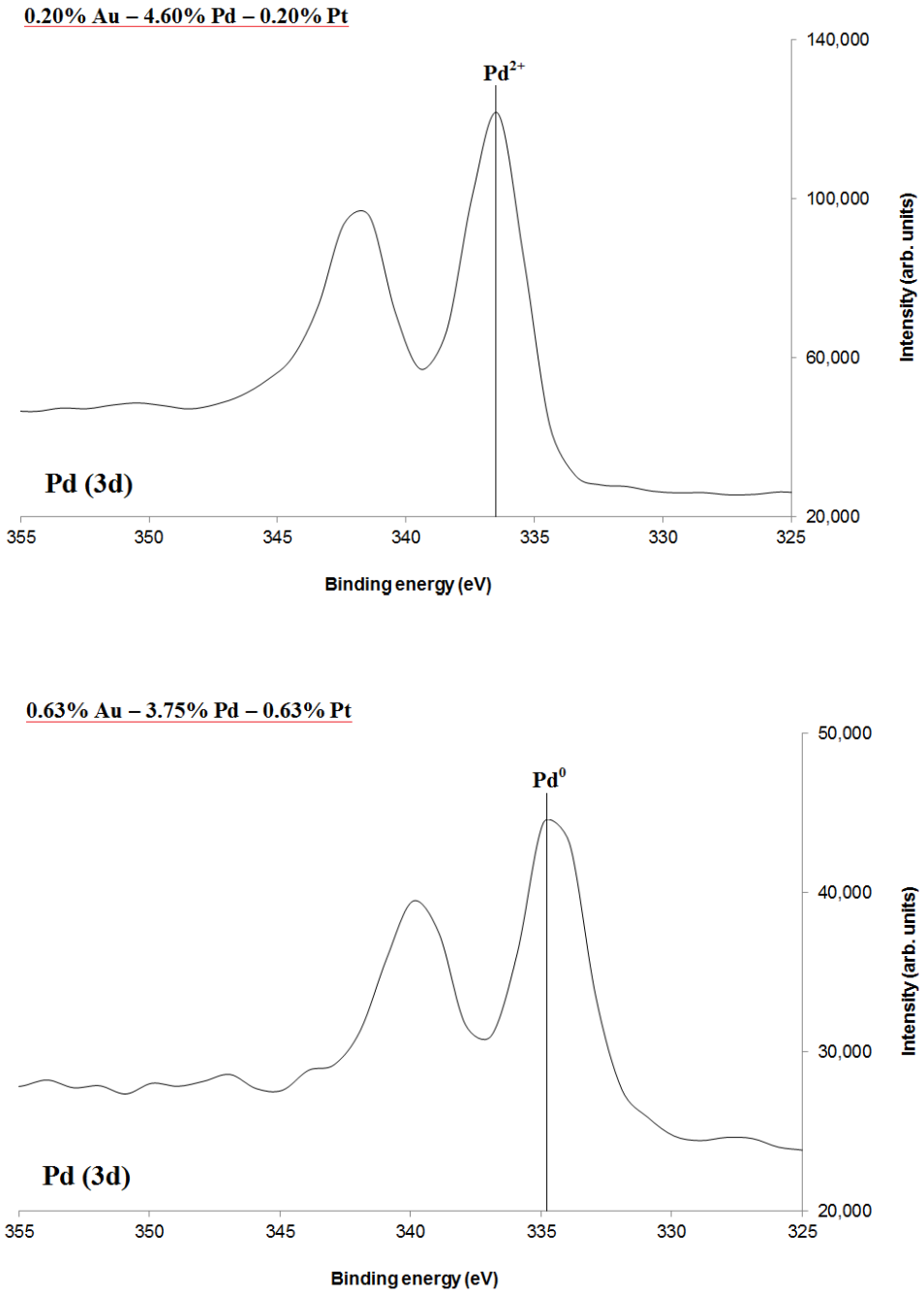

Figure 7.11 Pd(3d) spectra for CeO_2-supported 0.20 wt% Au-4.60 wt% Pd-0.20 wt% Pt (top), and 0.63 wt% Au-3.75 wt% Pd-0.63 wt% Pt (bottom) catalysts.

With respect to differences in Pd oxdaition state, a previous Au-Pd-Pt/CeO_2 catalyst optimisation study by Fierro *et al.* [34] also indicated the suppression of cationic Pd^{2+} species in trimetal compositions, and on evaluating catalysts for methane activation recognised an optimum ratio between surface Pd^{2+}/Pd^0 species (leading to formation Pd^0-PdO ensemble sites) and stabilization of a high Pd dispersion were required for methane activation.

7.6 Effect of calcination temperature on 2.28% Au-2.28% Pd-0.45% Pt/CeO_2

The effect of calcination in static air at different temperatures was previously investigated in sections 7.2.3 and 7.4.2 for 5 wt% Pd, Au-Pd and Pd-Pt/CeO_2 catalysts respectively. Briefly, results showed that the H_2O_2 synthesis activity for Pd and Pd-Pt catalysts overall increased on calcination up to temperatures of 400 ^oC, compared to only a minor difference in activity for Au-Pd. This was suggested to result from differences in alloying behaviour and interactions with the ceria surface between bimetallic Pd-Pt and Au-Pd catalysts, with the latter catalyst displaying no evidence of synergy.

Calcination Temperature / ^oC	**Productivity / $mol_{H2O2}kg_{cat}^{-1}h^{-1}$**	**Hydrogenation / $mol_{H2O2}kg_{cat}^{-1}h^{-1}$**
Uncalcined	73	619
200	82	553
400	100	459

Table 7.11 Effect of calcination temperature on the direct synthesis of hydrogen peroxide for 2.28 wt% Au-2.28 wt% Pd-0.45 wt% Pt/CeO_2.

The H_2O_2 synthesis activity of 2.28 wt% Au-2.28 wt% Pd-0.45 wt% Pt/CeO_2 increased from 73 to 100 $mol_{H2O2}kg_{cat}^{-1}h^{-1}$ after 400 ^oC calcination and was accompanied by a decrease in subsequent H_2O_2 hydrogenation activity (Table 7.11). The effect of calcination temperature on surface composition was tracked using XPS. Referring to Table 7.12, the surface Pd concentration increased by <1% after 200 ^oC calcination before a four-fold increase to 5.64% after 400 ^oC calcination. This corresponded to a pronounced decrease in the surface Au concentrations which was accompanied by minimal, inconsistent variation for both Pt and Cl content respectively.

Calcination Temperature / ^{o}C	Surface atom %			
	Au	Pd	Pt	Cl
Uncalcined	0.82	0.30	0.01	1.86
200	0.16	1.06	0.20	2.31
400	0.11	5.64	0.04	1.71

Table 7.12 Surface atom compositions for 2.28 wt% Au-2.28 wt% Pd-0.45 wt% Pt/CeO_2 catalysts calcined in static air (3 h) at the temperatures indicated.

Similar to previous XPS analysis of 0.20 wt% Au-4.60 wt% Pd-0.20 wt% Pt/CeO_2, inspection of the Pd(3d) and Au(4d) regions in Figure 7.12 indicated that calcination at 400 ^{o}C resulted in simultaneous reduction of Au^{3+} to Au^{0} and oxidation to Pd^{0} to Pd^{2+} at 354.1 and 335.0 eV binding energies respectively, forming a catalyst comprising Au^{0}, Pd^{2+} and Pt^{2+} oxidation states. However, any change in Pt oxidation state on calcination is very difficult to observe due to detection of weak signals in Pt(3d) and Pt(4f) regions, which in the absence of high resolution microscopy is suggested to arise from an elevated Pt dispersion on ceria relative to Au and Pd.

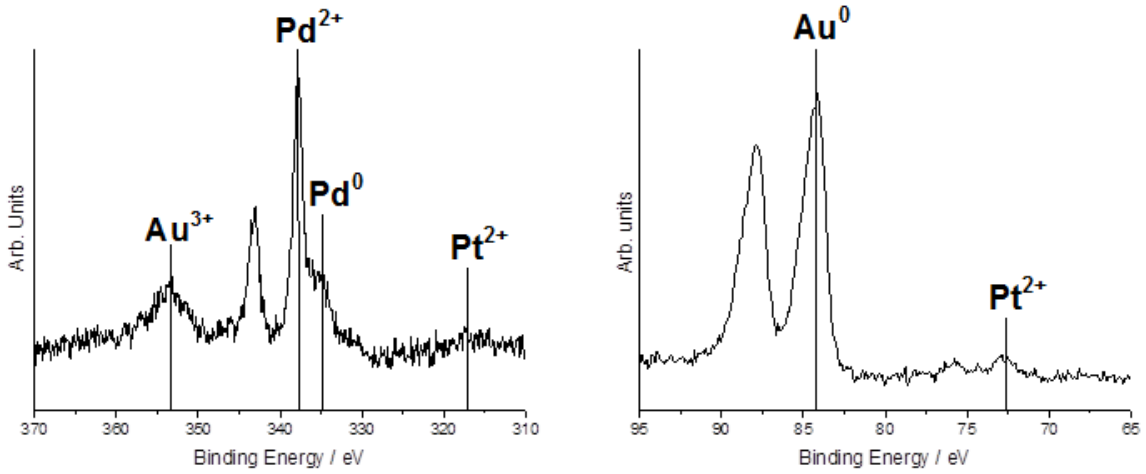

Figure 7.12 XPS spectra of 2.28 wt% Au-2.28 wt% Pd-0.45 wt% Pt/CeO_2 (uncalcined), showing Pd(3d), Au(4d), Pt(3d) spectra **(left)**, and Au(4f), Pt(4f) spectra **(right)** respectively.

In addition, Thermo-gravimetric analysis (TGA) performed in static air showed that catalyst mass increased by 1.1% on heating to 400 ^{o}C (Appendix Figure A7.3 (d)), which is attributed to the uptake of oxygen by Pd and Pt specifically, *via* formation of cationic/ surface oxide surface species, supported by a minimal oxygen uptake on ceria under the same conditions (Appendix Figure A7.3 (a)). Catalyst reusability experiments for a several Au-Pd-Pt/CeO_2 catalysts concluded that similar to 5 wt% Pd and 2.5 wt% Au-2.5 wt% Pd/CeO_2, calcination in static air at 400 ^{o}C is required to form a stable, reusable catalyst for direct H_2O_2 synthesis (Appendix Table A7.3). To conclude the trimetallic investigation in chapter 7, a comparative study with TiO_2-supported Au-Pd-Pt catalysts and using STEM microscopy was undertaken to assist in understanding the effect of Pt addition to Au, Pt and Au-Pd catalysts.

7.7 Comparison of TiO_2-Supported Au-Pd-Pt Catalysts

In this section, the preparation of trimetallic 5 wt% Au-Pd-Pt/TiO_2 catalysts based on a gradual addition of Pt, maintaining equivalent Au and Pd loadings is initially investigated. Referring to Table 7.13, addition of Pt to Au-Pd induced a significant promotional effect with respect to H_2O_2 synthesis, with an initial decrease in the hydrogenation activity after 0.05 wt% Pt addition relative to 2.5 wt% Au-2.5 wt% Pd/TiO_2. Similar to CeO_2-supported Au-Pd-Pt catalysts, addition of Pt to Au-Pd (catalysts **4-8)** resulted in high H_2O_2 synthesis activities, specifically for 0.05-0.20% Pt loadings and followed by a decrease thereafter, implying that the addition of Pt to Au, Pd and Au-Pd/TiO_2 catalysts has modified surface Au-Pd-Pt composition.

	TiO_2 Composition / wt%	**Productivity / $mol_{H2O2}kg_{cat}^{-1}h^{-1}$**	**Hydrogenation / $mol_{H2O2}kg_{cat}^{-1}h^{-1}$**
1	2.50% Au-2.50% Pd	64	235
2	2.50% Au-2.50% Pt	65	103
3	2.50% Pd-2.50% Pt	124	129
4	2.45% Au-2.45% Pd-0.05% Pt	154	135
5	2.45% Au-2.45% Pd-0.10% Pt	159	283
6	2.40% Au-2.40% Pd-0.20% Pt	156	318
7	2.28% Au-2.28% Pd-0.45% Pt	106	263
8	0.20% Au-4.60% Pd-0.20% Pt	184	382

Table 7.13 Effect of catalyst composition on direct H_2O_2 synthesis: TiO_2-supported catalysts.

Surprisingly for bimetallic catalysts **1-3**, addition to Pt to Au resulted in a catalyst exhibiting comparable H_2O_2 synthesis activity to 2.5 wt% Au-2.5 wt% Pd/TiO_2. While activity enhancement was anticipated and subsequently demonstrated on addition of Pt to Pd/TiO_2 for carbon and CeO_2-supported counterparts, the beneficial improvement in both H_2O_2 synthesis and hydrogenation activities on addition of Pt to Au/TiO_2 is an unexpected

result given the poor synthesis activities obtained for monometallic Au and Pt/TiO_2 catalysts (7 and 15 $mol_{H2O2}kg_{cat}^{-1}h^{-1}$) respectively, and shows that high activities can be obtained without Pd metal. STEM-HAADF images of $Au\text{-}Pt/TiO_2$ (Figure 7.13) highlight a trimodal particle size distribution similar to the features reported for $Au\text{-}Pd/TiO_2$, with small 1-5 nm Pd-rich particles, intermediate 10-20 nm Au-Pt alloyed particles, and large Au-rich >20 nm particles identified in corresponding XEDS analysis (Figure 7.14).

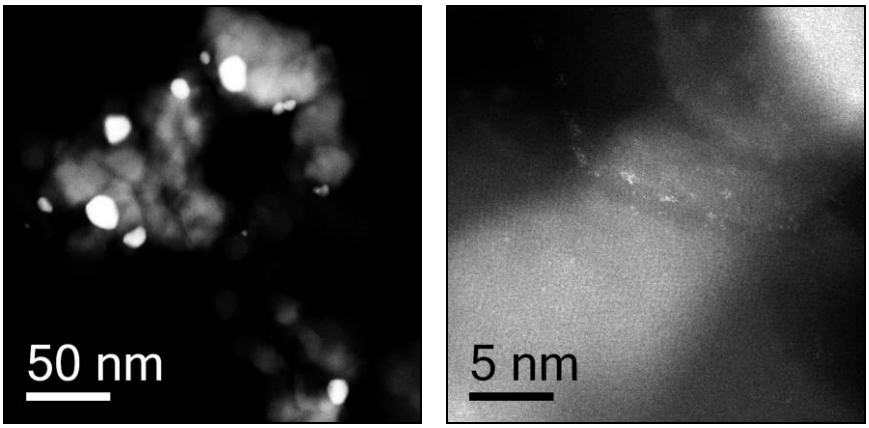

Figure 7.13 Representative STEM-HAADF images of 2.50 wt% Au-2.50 wt% Pt/TiO_2.

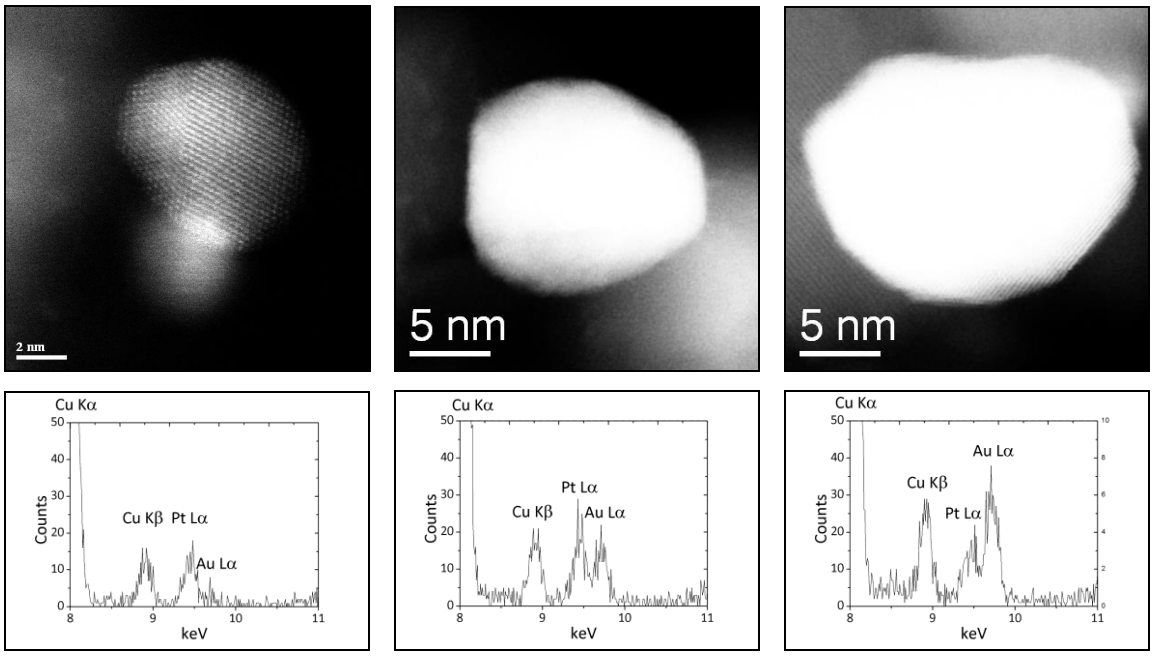

Figure 7.14 STEM-XEDS analyses of 2.50 wt% Au-2.50 wt% Pt/TiO_2, highlighting the composition of small (left), intermediate (middle) and large (right) particles. Note the presence of Cu signal(s) in XEDS represent an artefact of the JEOL FS2200 microscope and are not characteristic of catalyst samples.

STEM-HAADF images of Pd-Pt/TiO_2 (Figure 7.15) again highlight a trimodal particle size distribution similar to the features reported for Au-Pd/TiO_2, with small 1-5 nm Pd-rich particles, intermediate 10-20 nm Pd-Pt alloyed particles, and large Au-rich >20 nm particles identified in corresponding XEDS analysis (Figure 7.16). Referring to XPS analysis of Au-Pt and Pd-Pt/TiO_2 catalysts in Table 7.14, the formation of homogeneous Au-Pt particles and Pt-core Pd-shell nanoparticles is implied by the calculated surface Au/Pt and Pd/Pt ratios of 1.0 and 6.0 respectively, indicating preferential surface segregation of Pd in the latter sample, attributed to the formation of Pd-O bonds, and corresponding to high Pd^{2+} signal intensity.

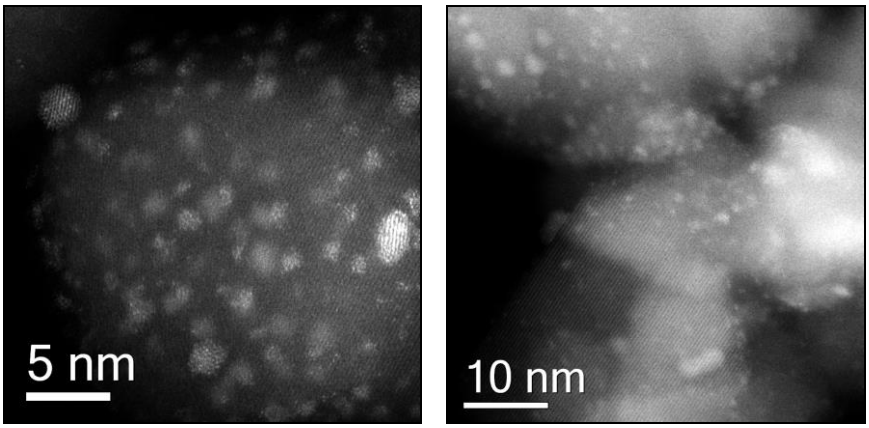

Figure 7.15 Representative STEM-HAADF images of 2.50 wt% Pd-2.50 wt% Pt/TiO_2.

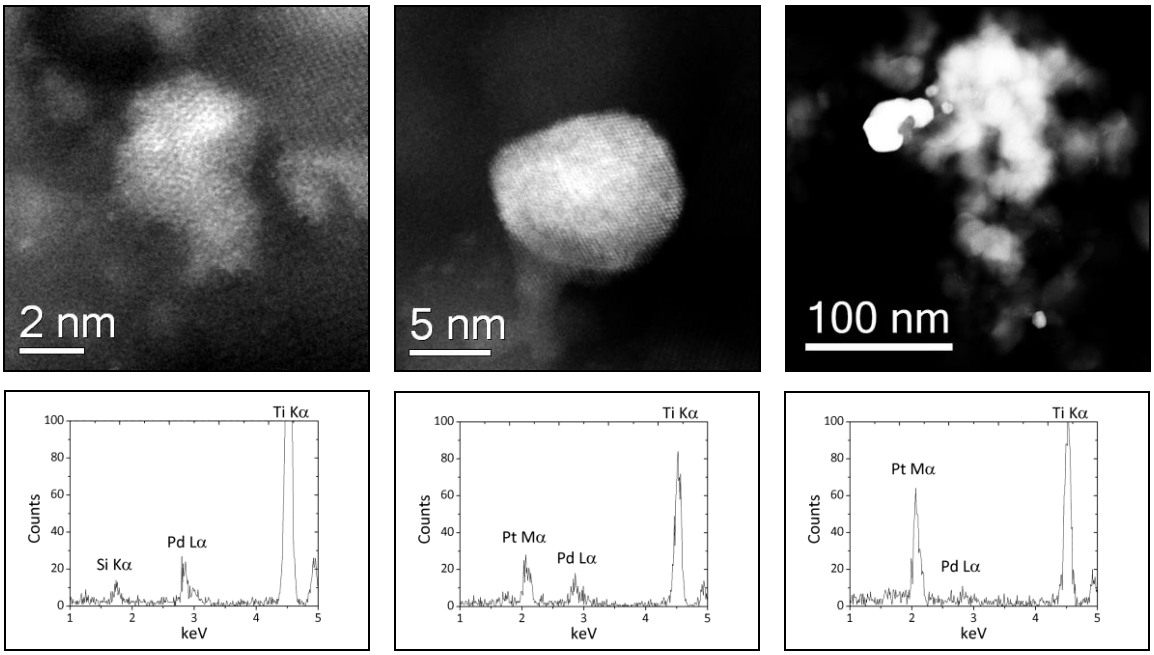

Figure 7.16 STEM-XEDS analyses of 2.50 wt% Pd-2.50 wt% Pt/TiO_2, highlighting the composition of small (left), intermediate (middle) and large (right) particles.

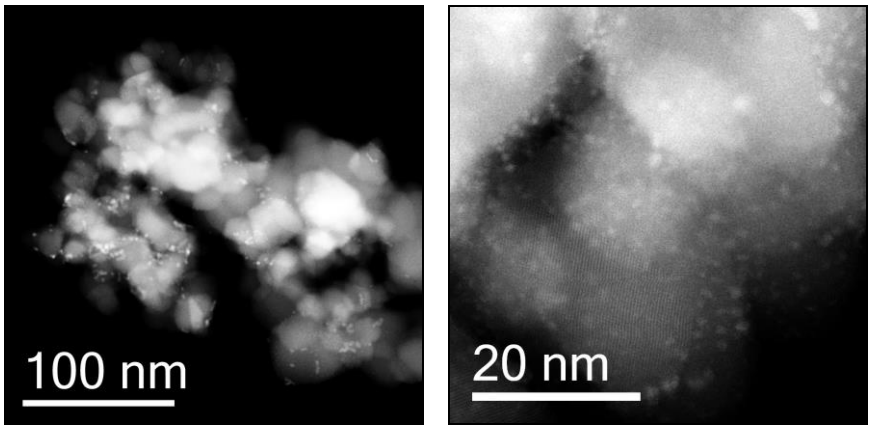

Figure 7.17 Representative STEM-HAADF images of 2.40 wt% Au-2.40 wt% Pd-0.20 wt% Pt/TiO_2.

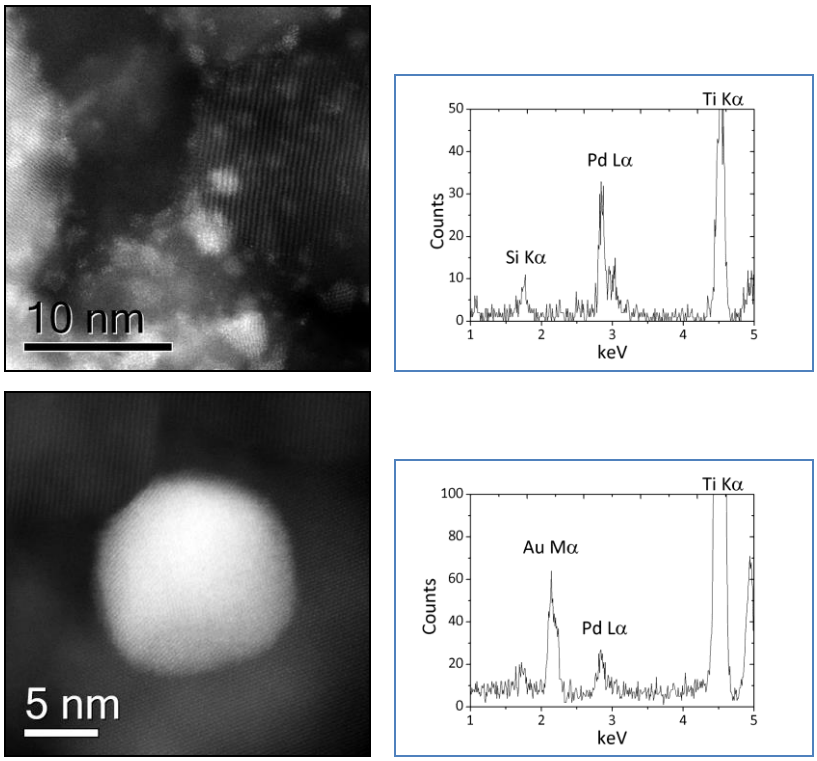

Figure 7.18 STEM-XEDS analyses of 2.40 wt% Au-2.40 wt% Pd-0.20 wt% Pt/TiO_2.

Interestingly, STEM-HAADF images of the 2.40% Au-2.40% Pd-0.20% Pt/TiO_2 catalyst (Figure 7.17) now reported a bimodal particle size distribution, consisting of small 1-5 nm Pd-only particles, and large Au-rich particles >10nm. Both XEDS (Figure 7.18) and XPS (Table 7.14) analysis of this did not detect the presence of Pt in nanoparticles on the catalyst surface. The Pt loading in this catalyst is very low and it is probable that highly dispersed Pt species (1-2 atoms) are present below the detection limit of XEDS and XPS techniques. The presence of a bimodal particle size distribution that is significantly different

compared to bimetallic Au-Pd, Au-Pt and Pd-Pt analogues may represent an effect of minor Pt addition, specifically a particle size redistribution and elevated surface Pd/Au ratio of ~25, explaining the high H_2O_2 synthesis activity (156 $mol_{H2O2}kg_{cat}^{-1}h^{-1}$) observed over this catalyst.

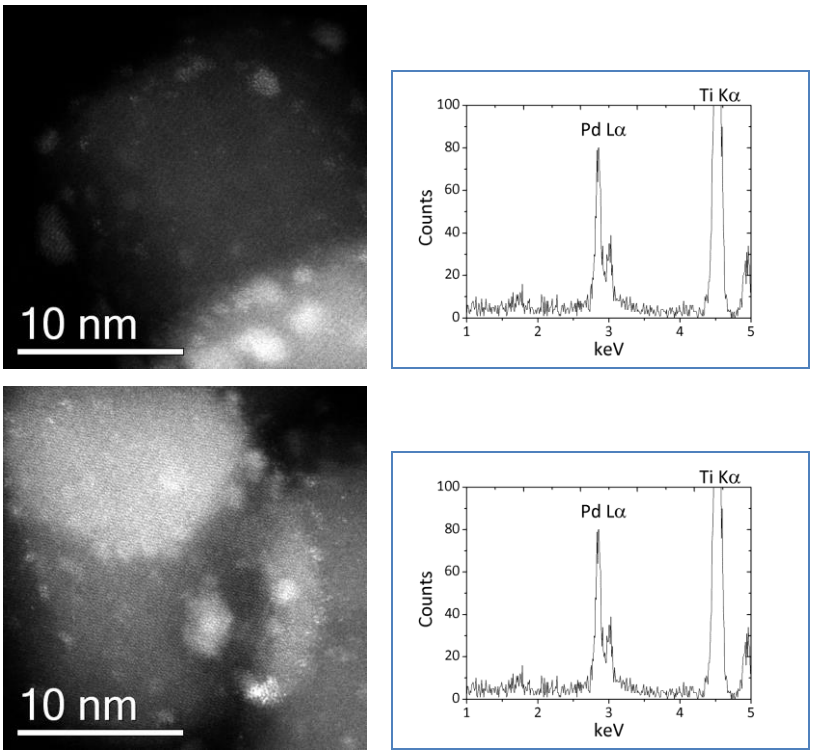

Figure 7.19 Representative STEM-HAADF images of 0.20 wt% Au-4.60 wt% Pd-0.20 wt% Pt/TiO_2 and corresponding XEDS spectra.

STEM-HAADF images of 0.20% Au-2.40% Pd-0.20% Pt/TiO_2 (Figure 7.19) show a uniform particle size distribution, consisting of <5 nm Pd-only particles, with no detection of either Au or Pt using either XEDS or XPS (Table 7.14) techniques. Both Au and Pt loading in this catalyst are fixed at 0.20 wt%, implying that highly dispersed Au and Pt species (1-2 atoms) are present below the detection limit of XEDS/XPS. The presence of an atomic dispersion of Au and Pt and high surface Pd exposure, partly related to the 4.60 wt% Pd loading (in addition to moderate surface chloride content), may explain why both substantial H_2O_2 synthesis (184 $mol_{H2O2}kg_{cat}^{-1}h^{-1}$) and hydrogenation (382 $mol_{H2O2}kg_{cat}^{-1}h^{-1}$) activities are observed over the catalyst.

TiO_2 Composition / wt%	**Surface atom %**			
	Au	**Pd**	**Pt**	**Cl**
2.28% Au-2.28% Pd-0.45% Pt	0.04	0.98	0.06	0.98
2.40% Au-2.40% Pd-0.20% Pt	0.06	1.52	0.00	1.13
0.20% Au-4.60% Pd-0.20% Pt	0.00	3.14	0.00	2.49
2.50% Pd-2.50% Pt		0.72	0.12	0.93
2.50% Au-2.50% Pt	0.12		0.12	0.00

Table 7.14 Summary of the XPS-derived surface atomic concentrations for Au-Pt, Pd-Pt and trimetallic Au-Pd-Pt/TiO_2 catalysts.

To conclude, XPS analysis of a 2.28 w% Au-2.28 wt% Pd-0.45 wt% Pt/TiO_2 catalyst (Figure 7.20) indicated the presence of Pd^{2+}, Pt^{2+} and Au^0 oxidation states at binding energies respectively (Referring to Table 7.14, surface Au, Pd and Pt content was detected on this catalyst). The same oxidation states were identified for 2.28 wt% Au-2.28 wt% Pd-0.45 wt% Pt/CeO_2 and imply a degree of crossover may exist between different metal oxide supports with respect to activity and surface composition. Both Au(4f) and Pt(4f) signals were of relatively weak intensity, corresponding to low surface Au and Pt concentrations of 0.04 and 0.06 atom%.

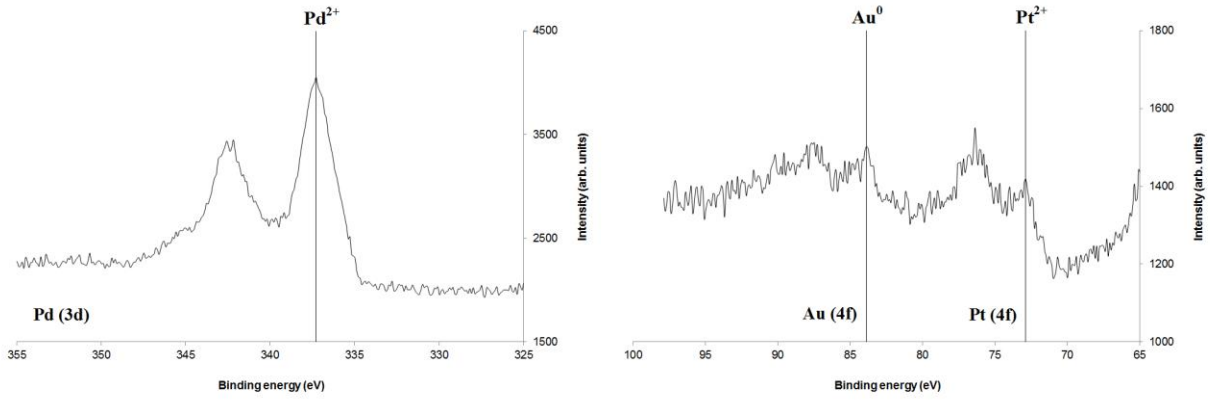

Figure 7.20 Pd(3d) spectra **(left)**, and Au(4f) and Pt(4f) spectra **(right)** obtained for 2.28 wt% Au-2.28 wt% Pd-0.45 wt% Pt/TiO_2.

7.8 Discussion

In the second part of chapter 7 (section 7.4 onward) the effect of Pt addition to Au, Pd, and Au-Pd/CeO_2 catalysts was studied, concluding ceria as a suitable support with respect to achieving high rates of H_2O_2 synthesis and moderate/low rates of H_2O_2 hydrogenation respectively. Low rates of H_2O_2 synthesis were obtained using Au, Pt and Au-Pt/CeO_2 catalysts, while subsequent evaluation of Au-Pt/TiO_2 revealed a H_2O_2 synthesis activity comparable to that of the previously studied and well characterised Au-Pd/TiO_2 catalyst (64 $mol_{H2O2}kg_{cat}^{-1}h^{-1}$) - a surprise result and demonstrating the potential of catalysts prepared without using Pd, which has represented the primary catalyst composition in most of the previous studies reported in the literature.

Following these observations, a series of bimetallic Pd-Pt/CeO_2 catalysts were prepared leading up to the development of trimetallic Au-Pd-Pt catalysts. While the addition of Au to Pd/CeO_2 did not induce synergy with respect to H_2O_2 synthesis, addition of Pt to Pd did induce a synergistic effect, with H_2O_2 synthesis activity increasing from 97 $mol_{H2O2}kg_{cat}^{-1}h^{-1}$ (5% Pd) to 138 $mol_{H2O2}kg_{cat}^{-1}h^{-1}$ (2.5% Pt-2.5% Pd). Even addition of small amounts of Pt resulted in enhanced synthesis activity (0.2% Pt-4.8% Pd = 125 $mol_{H2O2}kg_{cat}^{-1}h^{-1}$), with another study[35] suggesting that the nature of the promotional effect achieved on addition of Pt to Pd is different to the behaviour observed on addition of Au to Pd, specifically by the tuning of Pd electronic structure by the small addition of Pt (*i.e.* weakening of surface Pd-O bonds), leading to improved stabilization of O_2 molecules on Pd sites and subsequent formation of hydroperoxy, OOH intermediates.

Clear differences are highlighted between Au-Pd and Pd-Pt catalysts after 400 ^oC calcination in static air, however, specific differences between Pd-Pt and Au-Pd interactions on ceria have not been determined in this study due to the effective Z-contrast than can be achieved between Au, Pd and Ce elements using the JEOL FS2200 microscope. Future studies on next generation instruments are planned are intended and are approximately 1-2 years away based on recent developments in aberration corrected electron microscopy[36], to permit imaging of multiple elements in a specimen where effective Z-contrasting can be achieved based on differences in atomic number as low as 1-2, an improvement on the current which stands at ~4.

Regarding the nature of Pd-Pt interaction, theoretical work[37] has indicated that strong surface segregation of Pd atoms is facile in surface [100] and [111] planes of Pd-Pt alloys as a result of the lower surface energy of Pd and greater cohesive energy of Pt, while the addition of a single Pt atom into a Pd cluster was determined as being sufficient to modify the geometrical structure of Pd-Pt clusters[37]. Toshima and co-workers[38] reported that for a range of Pd-Pt nanoparticles synthesised *via* colloidal development (using different Pd/Pt molar ratios), both geometric structure and the degree of disorder of Pd-Pt nanoparticles varied substantially with alloy composition. It was also identified that minimization of the surface-free energy of Pd-Pt cluster particles, corresponding to maximization in the number of Pd-Pt bonds, resulting in surface segregation of Pd relative to the Pt component in Pd-Pt clusters. These previous studies add support to findings reported in this chapter, with respect to 5 wt% Pd-Pt/CeO_2 catalysts and likely play an important role in trimetallic Au-Pd-Pt/CeO_2 catalyst compositions, which will be concluded next, in terms of both structure and activity.

Important experimental observations were made when evaluating Au-Pd-Pt/CeO_2 catalysts for direct H_2O_2 synthesis reaction specifically that the application of trimetallic catalysts resulted in the highest rates of H_2O_2 synthesis reported to date (for 5 wt% catalysts prepared by wet-impregnation and calcined in static air at 400 ^oC for 3 h). The most active trimetallic catalyst compositions for H_2O_2 synthesis were:

(1) 0.20 wt% Au - 4.60 wt% Pd - 0.20 wt% Pt - 185 $mol_{H2O2}kg_{cat}^{-1}h^{-1}$

(2) 2.40 wt% Au - 2.40 wt% Pd - 0.20 wt% Pt - 170 $mol_{H2O2}kg_{cat}^{-1}h^{-1}$

Although catalysts **1** and **2** both contained a 0.20 wt% Pt loading, the Au and Pd wt% loadings were simultaneously varied, making direct comparison between structure and activity particularly difficult for trimetallic systems. In order to identify/better understand the possible relationship(s) between catalyst composition and H_2O_2 synthesis/hydrogenation activity, a series of ternary diagrams were plotted (Figures 7.9-7.11) to triangulate activity as a function of Au/Pd/Pt loading. The close inspection of Pd-rich, Au-Pd-Pt compositions at the top of the ternary diagram evaluating H_2O_2 hydrogenation (Figure 7.9) revealed low rates of hydrogenation for two Au-Pd-Pt/CeO_2 catalysts, both comprising 4.20 wt% Pd.

The presence of such isolated, low activities indicates the existence of 'zones' on simultaneous increasing Au and Pt content in trimetallic catalysts, resulting in several Pd-rich, Au-Pd-Pt catalysts that are both highly active for H_2O_2 synthesis and exhibit low rates of H_2O_2 hydrogenation (in the range 30-70 $mol_{H2O2}kg_{cat}^{-1}h^{-1}$).

On moving from 5 wt% Pd and 2.5 wt% Au-2.5 wt% Pd/CeO_2 to select trimetallic 5 wt% Pd-Pt and Au-Pd-Pt/CeO_2 catalysts, it was demonstrated that Pt addition could specifically improve the H_2O_2 synthesis activity, without increasing the rate of subsequent H_2O_2 hydrogenation over the catalyst (with hydrogenation activity in many cases actually being considerably reduced), providing evidence of a synergistic effect induced by Pt in bimetallic and trimetallic catalysts. H_2O_2 synthesis and hydrogenation activities obtained for Au-Pd-Pt/CeO_2 catalysts were combined in a composite diagram (synthesis - hydrogenation) to show optimum catalyst compositions in red, where H_2O_2 synthesis > H_2O_2 hydrogenation, to give a positive value (Figure 7.10). Using this approach, trimetallic Au-Pd-Pt/CeO_2 catalysts comprising metal loadings (highest to lowest): Pd > Pt > Au, were proposed to represent optimum catalyst compositions. More specifically, Pd loading is >2.5 wt%, Pt loading is 0.20-1.9 wt%, and the Au loading is distributed over two regions: 0.2-0.7 wt% and 1.2-1.9 wt% respectively.

DFT calculations performed by Meyer and Todorovich[39] for direct H_2O_2 synthesis on Pd [111], Pt [111], PdH [211] and $Au_{0.89}Pd_{0.11}$ [221], compared three formation steps and their competing reactions on all model surfaces:

(1)	O_2 hydrogenation	vs.	O_2 dissociation
(2)	OOH hydrogenation	vs.	OOH dissocation
(3)	H_2O_2 desorption	vs.	H_2O_2 dissociation

Results showed that as the surface structure of the catalyst is changed form Pd to Pt to Au, the step that governs the non-selective formation of H_2O was shifted from O_2 dissociation to OOH dissociation to H_2O_2 decomposition respectively. Based on the composite values presented in Figure 7.10, it is highly likely interplay exists between these three steps in trimetallic Au-Pd-Pt/CeO_2 catalysts depending on the amount of Au, Pd and Pt present and alloying effect(s).

X-ray photoelectron spectroscopy (XPS) analysis for select catalysts implied that a thin surface Pd^0/PdO film was formed on ceria, based on extremely high signal intensities observed in Pd(3d) spectra. A previous catalyst screening study by Fierro *et al*, also recognised a high surface Pd exposure, and suggested that formation Pd^0-PdO ensemble sites responsible for methane activation[34] were regulated (*e.g.* changes in Pd^0/PdO ratio, dispersion) by Au and Pt metals, which too is implied in our XPS studies. It is appreciated that further investigation into trimetallic Au-Pd-Pt catalysts is required, and will be continued using ceria - a suitable support with respect to achieving high rates of H_2O_2 synthesis and moderate/low rates of H_2O_2 hydrogenation respectively. In particular, experiments are required to determine the nature of the metal support interactions in CeO_2-supported catalysts, comparing both strong metal support interactions (M-O-Ce, where M = Au, Pd, Pt) and the possible interactions operating between Au, Pd and Pt metals.

7.9 Conclusion

The work presented in this chapter shows that ceria could be a suitable support for Au and Pd nanoparticles active for the direct synthesis of hydrogen peroxide. This is due in part to the very high H_2O_2 synthesis activities achieved over 5 wt% Pd/CeO_2 (97 $mol_{H2O2}kg_{cat}^{-1}h^{-1}$) catalysts, which are superior to the activities reported for carbon and metal-oxide supported 5 wt% Pd catalysts[1]. However, the addition of Au to Pd/CeO_2 catalysts did not improve the rate of H_2O_2 synthesis, although it did influence the rate of H_2O_2 hydrogenation. The origin of this effect is considered likely due to insufficient alloy formation under the heat treatment conditions applied. On moving from 5 wt% Pd and 2.5 wt% Au-2.5 wt% Pd/CeO_2 to select 5 wt% Pd-Pt and Au-Pd-Pt/CeO_2 catalyst compositions, it was demonstrated that Pt addition could improve the rate of H_2O_2 synthesis by a factor of 2 without increasing the rate of subsequent H_2O_2 hydrogenation over the catalyst (with the hydrogenation activity in many cases actually being considerably reduced), providing evidence of a synergistic effect induced by Pt in bimetallic and trimetallic CeO_2-supported catalysts. Characterisation of Pd-Pt and Au-Pd-Pd/CeO_2 catalysts by X-ray photoelectron spectroscopy indicated that the Pd surface concentration and oxidation state (Pd^{2+}/Pd^0) were critically sensitive to Au/Pd/Pt composition.

7.10 References

1. J. K. Edwards, G. J. Hutchings, *Angew. Chem. Int. Ed.*, **2008**, 47, 9192.
2. A. Abad, P. Conception, A. Corma, H. Garcia, *Angew. Chem. Int. Ed.*, **2005**, 44, 4066.
3. S. Carrettin, A. Corma, M. Iglesias, F. Sanchez, *App. Catal. A. Gen.*, **2005**, 291, 247.
4. A. Corma, M. E. Domine, *Chem. Comm.*, **2005**, 32, 4042.
5. A. Abad, C. Almela, A. Corma, H. Garcia, *Chem. Comm.*, **2006**, 30, 3178.
6. A. Abad, A. Corma, H. Garcia, *Chem-A. Euro. J.*, **2008**, 14, 212.
7. O. Casanova, S. Iborra, A. Corma, *ChemSusChem*, **2009**, 2, 1138.
8. P. Patnaik, Handbook of Inorganic Chemicals, *McGraw-Hill Publishing*, *New York*, **2003**.
9. W. Shen, Y. Ichihashi, H. Ando, Y. Matsumura, M. Okumura, M. Haruta, *App. Catal. A. Gen.*, **2001**, 217, 231.
10. M. P. Kapoor, Y. Ichihashi, T. Makamori, Y. Matsumura, *J. Mol. Catal. A. Gen.*, **2004**, 213, 251.
11. W. Shen, A. Kobayashi, Y. Ichihashi, Y. Matsumura, M. Haruta, *Catal. Lett.*, **2001**, 73, 2.
12. N. Tsubaki, K. Fujimoto, *Top Catal.*, **2003**, 22, 3.
13. W. Shen, Y. Ichihashi, H. Ando, Y. Matsumura, M. Okumura, M. Haruta, *App. Catal. A. Gen.*, **2001**, 217, 231.
14. S. Sharma, B. D. Mukri, M. S. Hedge, *Dalton Trans.*, **2011**, 40, 11480.
15. E. Smolentseva, B. T. Kusema, S. Beloshapkin, M. Estrada, E. Vargas, D. Y. Murzin, F. Castillon, S. Fuentes, A. Simakov, *App. Catal. A. Gen.*, **2011**, 392 ,69.
16. J. K. Edwards, B. E. Solsona, P. Landon, A. F. Carley, A. A. Herzing, M. Watanabe, C. J. Kiely, G. J. Hutchings, *Chem. Mater.*, **2005**, 15, 4595.
17. B. E. Solsona, J. K. Edwards, P. Landon, A. F. Carley, A. A. Herzing, C. J. Kiely, G. J. Hutchings, *Chem. Mater.*, **2006**, 18, 2689.
18. T. X. T. Sayle, S. C. Parker, R. A. Catlow, *J. Phys. Chem.*, **1994**, 98, 13625.
19. W.-I. Hsaio, Y.-S. Lin, Y.-C. Chen, C.-S. Lee, *Chem. Phys. Lett.*, **2007**, 441, 294.
20. P. J. Miedziak, Z. Tang, T. E. Davies, D. I. Enache, J. K. Bartley, A. F. Carley, A. A. Herzing, C. J. Kiely, S. H. Taylor, G. J. Hutchings, *J. Mater. Chem.*, **2009**, 19, 8619.
21. M. P. Seah, G. C. Smith, M. T. Anthony, *Surf. Interface Anal.*, **1990**, 15, 293.

22. N. N. Greenwood, A. Earnshaw, Chemistry of the Elements, *Butterworth-Heinemann Limited, Oxford*, Second Edition, **1997**.
23. S. A. C. Carabineiro, A. M. T. Silva, G. Drazix, P. B. Tavares, J. L. Figueiredo, *Catalysis Today*, **2010**, 154, 21.
24. W.-I. Hsaio, Y.-S. Lin, Y.-C. Chen, C.-S. Lee, *Chem. Phys. Lett.*, **2007**, 441, 294.
25. S. Abate, G. Centi, S. Perathoner, S. Melada, F. Pinna, G. Strukul, *Top. Catal.*, **2006**, 38, 181.
26. B. Coq, F. Figueras, *J. Mol. Catal. A. Chem.*, **2001**, 173, 117.
27. R. Meiers, U. Dingerdissen, W. F. Holderich, *J. Catal.*, **1998**, 176, 376.
28. G. Bernardotto, F. Menegazzo, F. Pinna, M. Signoretto, G. Cruciani, G. Strukul, *App. Catal. A. Gen.*, **2009**, 358, 129.
29. Q. Liu, J. C. Bauer, R. E. Schaak, J. H. Lunsford, *App. Catal. A. Gen.*, **2008**, 339, 130.
30. S. L. Hudson, S. C. Ball, K. B. Blaney, G. H. Chouchelamane, S. G. Fiddy, I. Harvey, P. Sivasubramaniam, B. C. Tessier, B. R. C. Theobald, D. Thompsett, *ECS Trans.*, **2008**, 16, 1395.
31. G. J. Acres, A. J. Bird, P. J. Davidson, *Chem. Eng.*, **1974**, 283, 157.
32. M. Hatanaka, N. Takahashi, T. Tanabe, N. Takahashi, Y. Nagai, A. Suda, H. Shinjoh, *J. Catal.*, **2009**, 266, 182.
33. M. Piccinini, The direct synthesis of hydrogen peroxide using gold and palladium based catalysts, PhD Thesis, *Cardiff University*, **2011**.
34. A. Tompos, J. L. Margitfalvi, M. Hegedus, A. Szegedi, J. L. G. Fierro, S. Rojas, *Combinatorial Chemistry and High Throughput Screening*, **2007**, 10, 71.
35. J. Xu, L. Ouyang, G.-J. Da, Q.-Q. Song, X.-J. Yang, Y.-F. Han, *J. Catal.*, **2012**, 285, 74.
36. Q. He, Study of Heterogeneous Gold and Gold Alloy Catalysts *via* Analytical Electron Microscopy, PhD Thesis, *Lehigh University*, *Pennsylvania*, USA, **2012**.
37. C. Massen, T. V. Mortimer-Jones, R. L. Johnston, *J. Chem. Soc., Dalton Trans.*, **2002**, 23, 4375.
38. N. Toshima, M. Harada, T. Yonezawa, K. Kushihashi, K. Asakura, *J. Phys. Chem.*, **1991**, 95, 7448.
39. R. Todorovic, R. J. Meyer, *Catalysis Today*, **2011**, 160, 242.

Chapter 8

8.1 Conclusions

The study was undertaken in collaboration with Solvay®, the largest manufacturer of H_2O_2 using the anthraquinone auto-oxidation (AO) process. This represents an indirect process based on sequential hydrogenation and oxidation of an R-alkyl anthraquinone to produce hydrogen peroxide at high concentrations with H_2 selectivity >95%. However, the degradation of anthraquinone components and organic solvents, which must be extracted and regenerated/replaced on a regular basis, and the fact that this process is only viable on an industrial scale whereas small scale and widespread processes are desired has generated much interest in developing of alternative technologies. A major research area is the direct synthesis of H_2O_2 from H_2 and O_2. For commercial applications to be realised in the future, this process must meet safety criteria, be economically viable and meet industrial targets set by Solvay, *i.e.* production of 8 wt% H_2O_2 (without acid and halide promoters), H_2 selectivity >90%, using a catalyst that is stable over extended reaction times.

Using an autoclave reactor (a three-phase, stirred autoclave, operating under batch conditions), a range of Au, Pd, Au-Pd, Au-Pt, Pd-Pt and Au-Pd-Pt catalysts supported on carbon, ceria, silica and titania were prepared, characterised and evaluated for the direct synthesis of hydrogen peroxide in the absence of acid and halide promoters. Because this study adheres to using batch conditions, the maximum hydrogen peroxide yield that can be produced in a single reaction (based on 100% H_2 conversion and selectivity) is 1.1 wt%.

These conditions are employed because this thesis is aimed at catalyst development, and the optimized batch conditions described in chapter 2 are appropriate for high throughput catalyst screening studies. A selection of the most active H_2O_2 synthesis catalysts identified across chapters 3-7 have been evaluated in separate studies using biphasic systems and semi-

batch/flow conditions and indeed in principle it has been demonstrated that >3 wt% H_2O_2 solutions in the water phase can be produced. The objectives previously outlined in chapter 1 were:

1 Optimisation of the wet-impregnation catalyst preparation method for carbon and TiO_2 supported Au-Pd catalysts for the direct synthesis of hydrogen peroxide, with insight into the preparation of halide-free catalysts **(chapter 3)**.

2 Achieving an improved understanding as to how the acid pre-treatment of carbon supports prior to Au-Pd impregnation generates highly active catalysts for the direct synthesis of hydrogen peroxide in which the non-selective H_2O_2 hydrogenation/ decomposition pathways are completely switched-off **(chapter 4)**.

3 Development of the colloidal "sol" immobilisation methodology to prepare Au-Pd/C and TiO_2 catalysts with application of aberration corrected electron microscopy techniques to investigate the origin of the high activity exhibited by these catalysts for the direct synthesis of hydrogen peroxide **(chapter 5)**.

4 Investigation into the origin of synergistic effect(s) between Au and Pd supported on SiO_2 as a function of acid-pretreatment, using multiple characterisation techniques including Inelastic Neutron Scattering (INS) measurements **(chapter 6)**.

5 Development of trimetallic Au-Pd-Pt catalysts for the direct synthesis of hydrogen peroxide, with catalyst screening undertaken for Au-Pd-Pt/CeO_2 **(chapter 7)**.

In chapter 3, it was shown that for 5 wt% Au-Pd/TiO_2 catalysts prepared *via* wet impregnation, the addition of minimal amounts of water to form a catalyst slurry, which subsequently was not heated to form a thick, viscous gel (*i.e.* still contains 2 ml of H_2O) prior to drying (110 ^oC) and calcination in static air (400 ^oC), resulted in highly active H_2O_2 synthesis catalysts (*ca.* 120 $mol_{H2O2}kg_{cat}^{-1}h^{-1}$) of activity comparable to 5 wt% Au-Pd/C catalysts (120 $mol_{H2O2}kg_{cat}^{-1}h^{-1}$). The addition of more water (*ca.* 2-30 ml) during the catalyst

impregnation step prior to drying leads to a significant change in the particle size distribution, with a modified bimodal distribution now observed for Au-Pd/TiO_2 catalysts.

Specifically a bimodal distribution of Au and Pd nanoparticles with larger particles (20-80 nm) containing Au and small particles (1-10 nm) containing Pd was reported, with no detectable Au-Pd alloy formation in either the smaller or larger particles. The larger Au-only particles are ineffective in limiting H_2O_2 hydrogenation and as a result a reduced synergistic effect of Au is observed, and therefore the higher H_2O_2 synthesis and hydrogenation activities observed over Pd-only and Au-Pd catalysts prepared using this modified methodology are related to an enhanced Pd dispersion. Unfortunately, TiO_2-supported catalysts prepared in this manner are not stable on re-use. However, catalysts prepared using a similar method, but with the removal of *ca.* 75% of the initial H_2O ensuring that a viscous, gel consistency is formed prior to drying, were determined as stable and fully reusable (and comprised intermediate, $Au_{core}Pd_{shell}$ alloyed nanoparticles).

In contrast, for Au-Pd/C catalysts, addition of water during the catalyst impregnation step (*ca.* 2-30 ml) did not affect either structure or activity and these catalysts could be re-used without loss of catalyst performance. A major difference was established in the rate of Au and Pd uptake onto TiO_2 and carbon supports, with instant adsorption of Au and Pd precursors onto carbon irrespective of water addition/concentration, compared to negligible uptake onto TiO_2, which was determined as being influenced by surface iso-electric point.

Additional experiments presented in the latter half of chapter 3 conclude that reduced halide content/halide free catalysts can be synthesized using deposition precipitation routes and mild reduction treatments, leading to moderately active H_2O_2 synthesis and hydrogenation catalysts. A possible drawback with using deposition precipitation methodology to co-deposit $Au(OH)_3$ and $Pd(OH)_2$ species onto TiO_2 and carbon supports is that control over the fraction of each metal deposited onto a given support is limited, since $AuCl_4$ and $PdCl_2$ precursors are hydrolysed at different pH values and may deposit at different rates onto the support, with a higher Pd content detected in the final catalysts. The use of co-deposition techniques will therefore be investigated in future given that halide free catalysts can already be produced allowing further studies aimed at optimising Au/Pd particle composition and weight ratio.

In chapter 4, the H_2O_2 synthesis and hydrogenation activities over non-acid and acid treated Au-Pd/C catalysts were compared and contrasted as a function of calcination temperature. A minimum temperature of 400 ^oC was required to form a highly active, stable and fully reusable catalyst, simultaneously decreasing the H_2O_2 hydrogenation activity to the extent that for acid treated Au-Pd/C it was switched-off. Characterisation of non-acid and acid treated carbons by FT-IR ATR spectroscopy and in particular TPD showed an increase in the amount of carboxylic acid groups.

The surface composition and structure of non-acid and acid treated Au-Pd/C catalysts was studied using XPS and STEM-HAADF imaging techniques. Aberration corrected electron microscopy showed that both non-acid treated and acid-treated Au-Pd/C samples calcined at 400 °C consisted of Au-rich nanoparticles and a highly dispersed coverage of atomic and cluster-like Pd species, intermixed with a small amount of atomically dispersed Au. Calcination appears to improve the overall metal dispersion, although acid pre-treatment of the support does not seem to affect the catalyst morphology or the dispersion of metallic species; suggesting the enhancement in observed activity for acid treated Au-Pd/C samples could be related to changes in metal oxidation state and residual surface species.

Indeed XPS analysis showed the most important distinguishing feature between non-acid treated and acid treated Au-Pd/C catalysts as being the concentration of surface Pd^{2+} species associated with O^{2-} and/or Cl^- electronic modification, with >90% Pd^{2+} present in all acid treated catalysts. The stability of surface Pd^{2+} species was however found to be dependent on calcination temperature (Table 4.11). For all catalysts calcined in static air at temperatures below 400 ^oC, reduction to Pd^0 during hydrogen peroxide synthesis occurred (alongside possible leaching of Au and Pd from the catalyst), corresponding to a significant decrease in the rates of H_2O_2 synthesis observed on second use.

A subtle variation in dispersion of Au and Pd species cannot be excluded as a reason for improved catalytic activity and surface Pd^{2+} concentration after acid pre-treating carbon, given the inability to directly determine the chemical identity of sub-nm species and isolated atoms in bimetallic Au-Pd/C catalysts using atomic level Z-contrast measurements due to the rough nature of the support.

Microscopy for monometallic Au and Pd samples implies that a small concentration of atomically dispersed Au atoms is intermixed within atomically dispersed Pd species in bimetallic alloys, and XPS analysis reported higher than anticipated Pd/Au ratios on acid treated Au-Pd/C catalysts. The critical role of surface Pd^{2+} species with respect to H_2O_2 yield was further demonstration by redox cycle experiments, showing post-treatment in mild reducing/ oxidising condition can reversibly modify the surface Pd oxidation state of acid-treated Au-Pd/C and switch on/off corresponding H_2O_2 hydrogenation. A theoretical study of Au@Pd surfaces by Ishihara and co-workers[1] has led to a mechanistic proposal, illustrating the importance of the Au present in Au-Pd surfaces with respect to the binding energies of adsorbed reactants/ products. The presence of Au in Au-Pd surfaces significantly increases the activation energy barriers for competing OOH hydrogenation and decomposition processes (Figure 8.1), which could possibly explain the role of the improved atomic dispersion of Au, intermixed with sub-nm Pd clusters in acid treated Au-Pd/C catalysts.

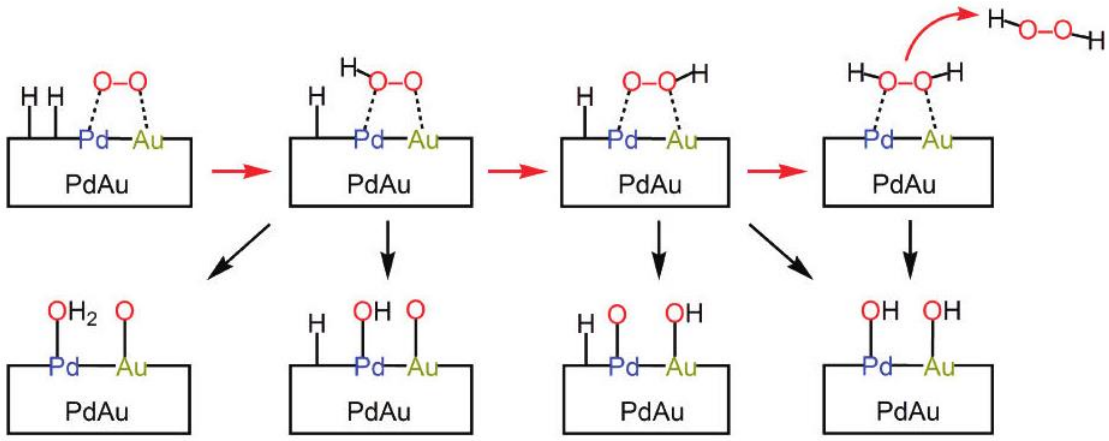

Figure 8.1 Schematic of the adsorption configuration of O_2 on the H atoms co-adsorbed on the Au@Pd [111] surface, showing reactions possible involved in each H_2O_2 synthesis steps[1]. The reaction cycle indicated by red arrows is thermodynamically favoured when Au atoms are presented on the Pd [111] surface, with the black arrows corresponding to competing H_2O_2 hydrogenation/ pathways in which the activation energy barrier for a reaction to proceed has been significantly increased by the presence of Au.

Regarding the choice of calcination conditions applied in preparation of acid treated Au-Pd/C catalysts, calcination in static air at 400 ^{o}C is mandatory to form a stable catalyst that can be reused for the direct synthesis reaction. This is not afforded *via* heat treatment in

reducing, inert or oxygen rich atmospheres and is likely due to the sensitivity of the activated carbon material toward these environments. Chapter 4 has permitted a better understanding of the effect of nitric acid pre-treatment, highlighting that functional groups present on the non-acid treated support are enhanced. Currently, the phenomenon in which the rate of sequential H_2O_2 hydrogenation over a catalyst is switched-off is specific to Au-Pd/C, and therefore further experiments are planned to ascertain if the H_2O_2 hydrogenation activity of other catalyst compositions can be eliminated.

In chapter 5, it was concluded from investigation into the preparation of Au+Pd, Au{Pd} and Pd{Au} colloidal nanoparticles that the order of Au and Pd metal reduction during colloid synthesis and prior to immobilization on carbon and TiO_2 supports can affect the resulting activity of catalysts active toward both the synthesis and hydrogenation of hydrogen peroxide as summarised for the carbon-supported series in Figure 8.2. The initial rates of H_2O_2 synthesis over sol-immobilized catalysts are exceptionally high and in some instances as much as 0.19 wt% H_2O_2 can be produced after 2 minutes, which is higher than many of the yields reported for 5 wt% catalysts prepared by wet-impregnation after 30 minutes. This also represents a 7-8 fold improvement in terms of turnover frequency given sol-immobilisation catalysts are prepared using 5 times less Au and Pd metal relative to impregnation (5 wt%).

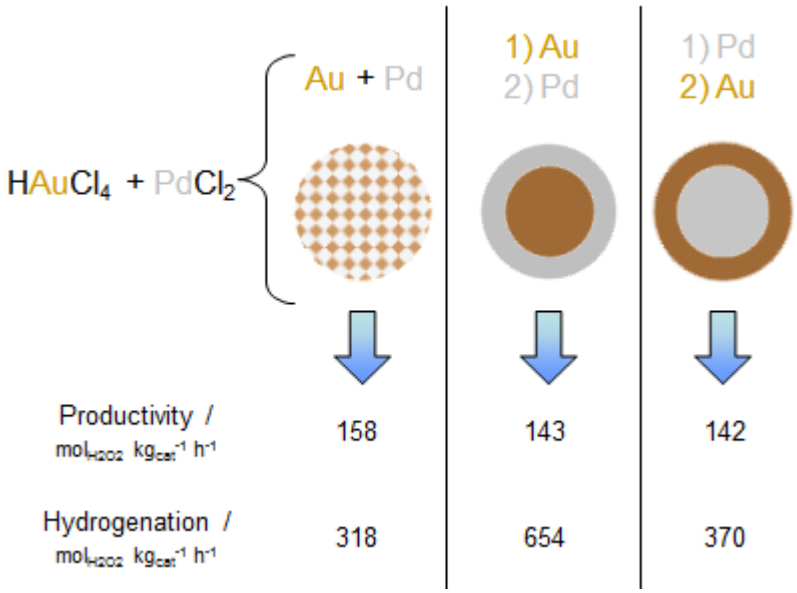

Figure 8.2 Summary of the H_2O_2 synthesis and hydrogenation activities of Au+Pd, Pd{Au} and Au{Pd} nanoparticles immobilized on carbon.

The H_2O_2 synthesis activities of sol-immobilized Au+Pd, Pd{Au} and Au{Pd)/C catalysts are approximately 5-6 times higher than their TiO_2-supported counterparts and characterisation of catalysts by advanced aberration corrected electron microscopy concludes a dramatically different particle structure and metal-support interaction manifests depending on the choice of support.

Specifically, high resolution images of immobilized Au+Pd particles identified a non-wetting interaction between 'rounded' Au+Pd particles and activated carbon, compared to formation of an extended flat interface was between mainly 'faceted' Au+Pd particles and TiO_2. The latter observation is evidence of surface wetting behavior and is independent of the order Au and Pd reduction during nanoparticle synthesis and is attributed to the development of strong metal-support interactions and consequently the displacement of PVA ligands in close proximity to metal-support interfaces.

Although the preparation of Au-Pd nanoparticles by sol-immobilisation was undertaken in order to generate catalysts of improved particle size and composition, microscopic analysis of nanoparticles before and after immobilisation onto carbon and TiO_2 did detect some off-centre cores, particles with incomplete shell coverage and those simply lacking the core-shell structure with respect to Pd{Au} and Au{Pd} colloids. The variation and non-uniformity in the Au-shell coverage of Pd-core particles is likely the result of insufficient 'shell' material being provided during nanoparticle formation.

In addition, a series of Au+Pd alloy colloidal nanoparticles having a range of Au:Pd ratios were immobilized on carbon and evaluated for hydrogen peroxide synthesis. In all cases the Au-Pd nanoparticles were homogeneous alloys, with the optimum H_2O_2 synthesis activity attained using a catalyst with Au:Pd molar ratio of 1:2. Activity in terms of both H_2O_2 synthesis and hydrogenation obeyed a distorted 'volcano' relationship with increasing Pd molar content. Referring to XPS studies, the hydrogenation activity of Au+Pd/C catalysts was suggested to increasing with rising Pd content due to systematic variation in the quantity of surface exposed Pd and Pd^0/Pd^{2+} ratio, which as a result cancels out the positive effect of adding Pd to the Au nanoparticles.

Further experiments will be aimed at addressing the catalysts stability parameter to determine if a stable colloidal catalyst can be applied to the direct H_2O_2 synthesis reaction. However, 1 wt% Au+Pd/C was recognised as the only catalyst tested to date that is capable of forming hydrogen peroxide in a gas phase reactor over a period of 76 h (albeit at low concentration in pilot experiments)[2], and is most probably related to the exceptionally initial rates exhibited by sol-immobilisation catalysts at short reaction times (<2 min). The use of low residence times, such as those encountered in gas phase and liquid flow reactors (seconds) may provide a way forward for a potentially promising catalyst series.

Referring to chapter 6, the reason behind the observed synergy displayed by the Au-Pd catalyst on acid pre-treated SiO_2 cannot be rationalised from electron microscopy characterisation as the overall morphology for the two samples appears identical. XPS analysis does however conclusively show that acid pre-treatment increases the degree of Au dispersion on SiO_2 and in addition clear differences in the nature of the hydroxyl groups using Inelastic Neutron Scattering and TPD methods are identified between supports which might be associated with the onset of synergy and increase in activity for Au-Pd catalysts prepared using the acid pre-treated support. With respect to the enhanced catalytic activity that is observed for all Pd-containing catalysts prepared using the acid pre-treated silica, the enhanced hydroxyl functionality on the silica surface is suggested to aid the dispersion of Pd metal and it is this effect that constitutes the enhanced activity.

There could be an extremely small amount of Au contained within the 2-5 nm Pd nanoparticles which is below the detection limits of the STEM-XEDS microscope (a mass fraction sensitivity of the order ~1 atom%), which is possible to detect using XPS, however, as the Au signal is observed in the acid pre-treated catalyst, but not in the untreated counterpart. For a series of 1 wt% Au+Pd/C catalysts prepared by sol-immobilisation in chapter 5, the addition of small amounts of Au to Pd significantly improved H_2O_2 activity and therefore it is plausible that this effect is observed with very small numbers of Au atoms in these small clusters, where one or two Au atoms constitute a significant volume fraction of the particle.

It has been demonstrated in both chapters 4 and 5 that catalysts comprising solely of small nanoparticles of either Pd or Au-Pd are highly active when supported on carbon. It is therefore unlikely changing the support surface would switch-off the activity of such a large population of the very small nanoparticles adding strength to the conclusion that on silica, Au-Pd synergy is derived from a slightly enhanced dispersion of Au that arises from the presence of an enhanced population of surface hydroxyl functionalities on the surface of the silica due to the acid pre-treatment. It is obvious from this study that silica is not an optimal support for the dispersion of Au-containing catalysts using wet impregnation and colloidal immobilization, and so further studies would be directed at synthesizing Au@Pd/SiO_2 *via* an electroless deposition route, with a metal-support interaction proceeding through Pd nanoparticles (*i.e.* Au-Pd-O-Si).

Chapter 7 shows that ceria could be a suitable support for Au and Pd nanoparticles active for the direct synthesis of hydrogen peroxide, due in part to very high H_2O_2 synthesis activities over 5 wt% Pd/CeO_2 (97 $mol_{H2O2}kg_{cat}^{-1}h^{-1}$) catalysts, which are also superior to the activities reported for carbon and metal-oxide supported 5 wt% Pd catalysts. However, the addition of Au to Pd/CeO_2 catalysts does not result in an enhanced synthesis activity, although it does influence the rate of H_2O_2 hydrogenation. The origin of this effect is most likely to be due to lack of alloy formation under the heat treatment conditions applied.

On moving from 5 wt% Pd and 2.5 wt% Au-2.5 wt% Pd/CeO_2 to select trimetallic 5 wt% Pd-Pt and Au-Pd-Pt/CeO_2 catalysts, it was demonstrated that Pt addition could specifically improve the H_2O_2 synthesis activity, without increasing the rate of subsequent H_2O_2 hydrogenation over the catalyst (with hydrogenation activity in many cases actually being considerably reduced), providing evidence of a synergistic effect induced by Pt in bimetallic and trimetallic catalysts.

H_2O_2 synthesis and hydrogenation activities obtained for Au-Pd-Pt/CeO_2 catalysts were combined in a composite diagram (synthesis – hydrogenation) to show optimum catalyst where H_2O_2 synthesis > H_2O_2 hydrogenation, to give a positive value. Using this approach, trimetallic Au-Pd-Pt/CeO_2 catalysts comprising metal loadings, Pd > Pt > Au, were proposed to represent optimum catalyst compositions. Specifically, Pd loading is >2.5 wt%, Pt loading is 0.2-1.9 wt%, and Au loading is distributed over two regions, 0.2-0.7 wt% and 1.2-1.9 wt% respectively.

Although this approach is not an absolute indicator in terms of what constitutes optimum/favourable catalyst compositions as it is specific to the reaction conditions used (*e.g.* batch operation, pressure, solvent, temperature, time), it does serve as a useful guideline in directing further development of Au-Pd-Pt/CeO_2 catalysts for application in other systems. Examples include: (i) flow reactors, where the residence time is dramatically shorter (seconds) compared to batch reactors (30 minutes, inside sealed autoclave containing a finite concentration of H_2/O_2 gases), and (ii) use of immiscible solvent mixtures.

Piccinini[2] demonstrated that performing the direct synthesis reaction in an immiscible two-phase, decanol-1-ol/water solvent and using a 0.63 wt% Au-3.75 wt% Pd-0.63 wt% Pt/ CeO_2 catalyst and semi-batch conditions that a 3.5 wt% H_2O_2 concentration could be formed in the water phase. This result is highly significant since no acid/halide promoters or distillation steps were required, with the setup enabling high yields to be attained *via* in-situ extraction of hydrogen peroxide formed in the organic, decanol-1-ol phase. As part of future work, the development of highly active catalysts (determined using standard, batch conditions) will be applied to semi-batch/flow experiments in order to ascertain if the [H_2O_2] = 8 wt% target can be reached using direct synthesis technology in the near future.

The initial results from the trimetallic study are promising when using CeO_2 as the support. Catalysts up until now only been prepared using relatively simple preparation techniques, primarily to cover a broad research objective and to favour potential industrial scale-up, since both sol-immobilisation and deposition precipitation methodologies would be difficult, although not impossible to control on a large scale. While studies using the wet impregnation method to prepare mono, bi and trimetallic Au, Pd, Pt catalysts (in addition to searching for other potential metal candidates) will continue, other methods will be addressed.

8.2 References

1. T. Ishihara, K. Yoshizawa, *J. Phys. Chem. C.*, **2011**, 115, 25359.
2. M. Piccinini, The direct synthesis of hydrogen peroxide using gold and palladium based catalysts, PhD Thesis, *Cardiff University*, **2011**.

Chapter 4 - Appendices

Measurement of the water and functional group loss by thermo-gravimetric analysis for untreated and 2% HNO_3 treated G60 carbon supports.

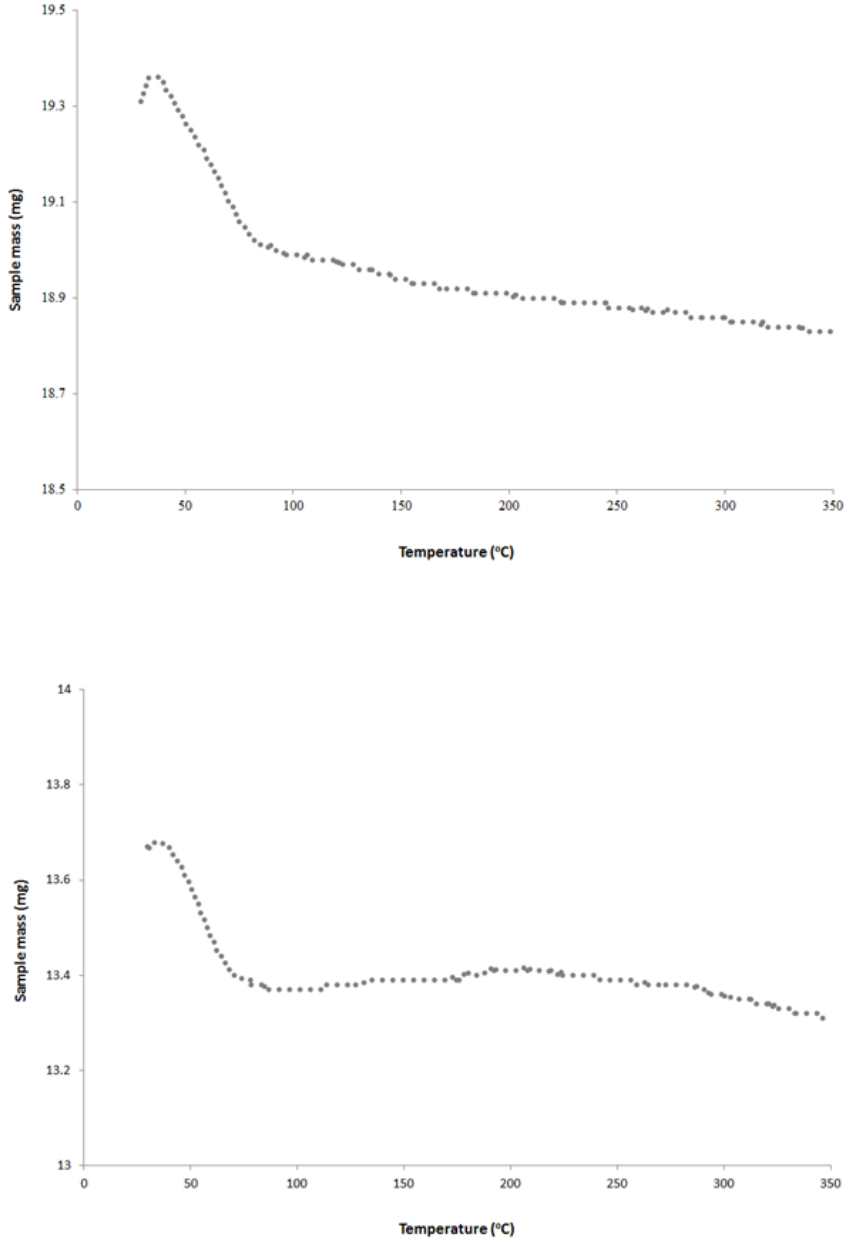

Figure A4.1 Thermo-gravimetric analysis of non-acid treated (top) and 2% HNO_3 pre-treated (bottom) G60 carbon supports heated to 350 ^{o}C under a nitrogen atmosphere.

A mass decrease of 2.7% was recorded for the non-acid treated carbon, with mass variation below 100 ^{o}C attributed to water loss. A progressive decrease is observed from 100 to 350 ^{o}C, which is in agreement with TPD experiments (Chapter 3, Figure 4.4) and suggested to arise from carboxylic acid groups. A comparable decrease in sample mass (2.6%) was observed for 2% HNO_3 treated carbon with more subtle variation above 100 ^{o}C. Small percentage variations were measured in these experiments and despite the simple identification of water evolution, changes in surface functionality are more subjective (a lower signal variation for functionalities other than H_2O) since introduction of carboxylic acid groups *via* the acid pre-treatment constituted less than 1% of activated carbon support by weight.

wt% H_2O_2	**Heat Treatment**			
	Dried 120 ^{o}C	**200 ^{o}C**	**300 ^{o}C**	**400 ^{o}C**
Initial	4.05	4.05	4.08	4.00
Final	3.55	3.48	3.49	4.04

Table A4.1 Summary of Pseudo-Synthesis experiments (H_2O_2 synthesis performed in the presence of 4 wt% H_2O_2) for acid treated 2.5 wt% Au-2.5 wt% Pd/C catalysts, calcined in static air for 3 h at temperatures indicated.

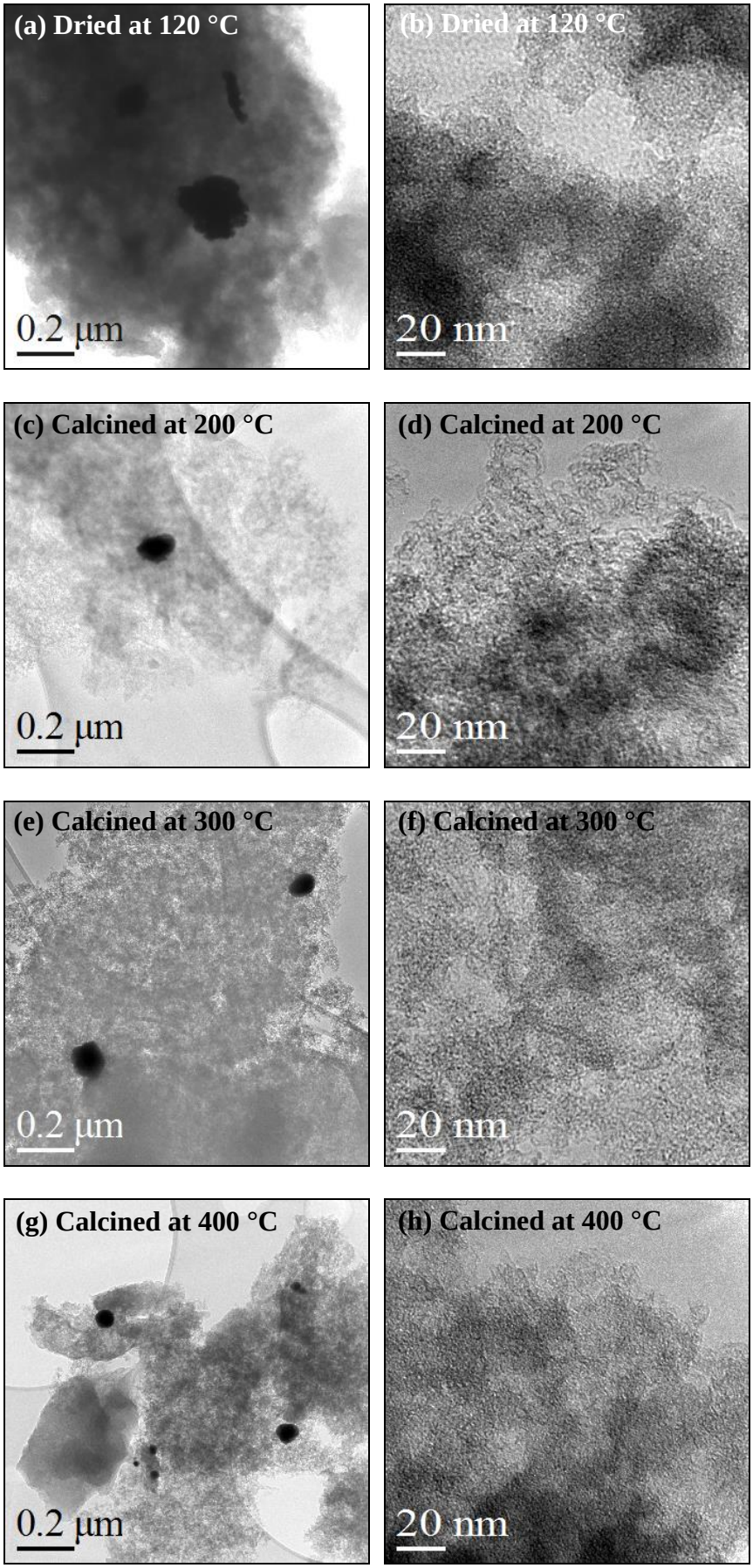

Figure A4.2

Representative BF-TEM images of acid pre-treated AuPd/C catalysts calcined at different temperatures.

(a, b) Dried 120 °C
(c, d) Calcined 200 °C
(e, f) Calcined 300 °C
(g, h) Calcined 400 °C

Images illustrate the larger metallic nanoparticles on the carbon support.

2.5% Au-2.5% Pd/C	**Productivity / $mol_{H2O2}kg_{cat}^{-1}h^{-1}$**	**Hydrogenation / $mol_{H2O2}kg_{cat}^{-1}h^{-1}$**
Untreated	21	118
2% HNO_3 Treated	27	105

Table A4.2 Evaluation of the rates of H_2O_2 synthesis and hydrogenation for non-acid treated and 2% HNO_3 pre-treated 2.5 wt% Au-2.5 wt% Pd/C catalysts, prepared by standard wet impregnation and using BNFL, nuclear grade carbon (particulate size = 90µm). The samples were dried (110 ^oC, 16 h) and calcined in static air, 400 ^oC/3h/20 $^oCmin^{-1}$.

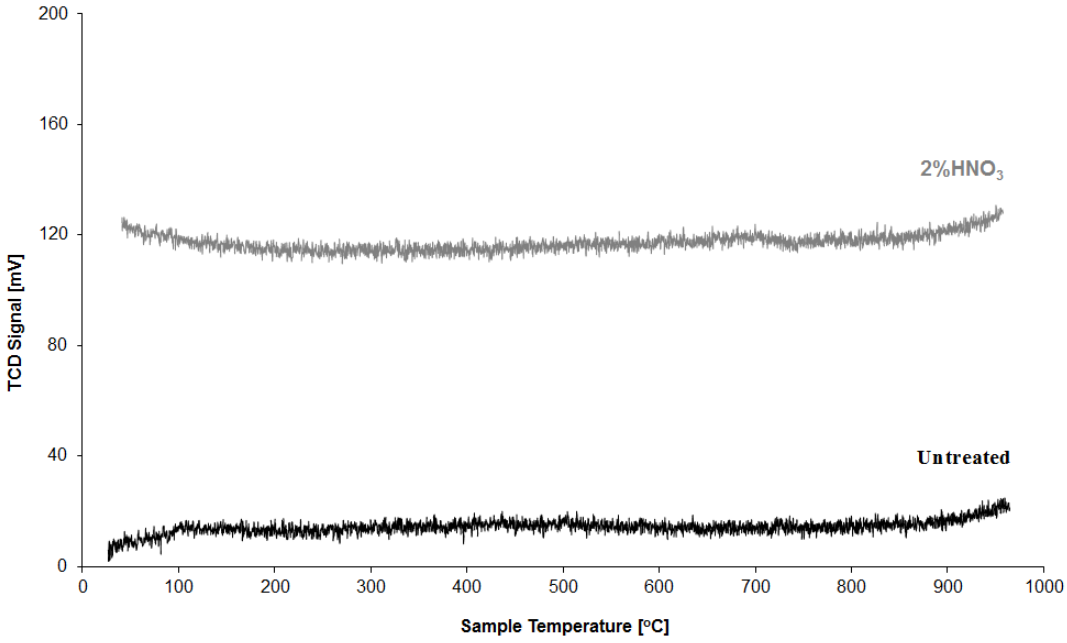

Figure A4.3 TPD profiles recorded for 2.5 wt% Au-2.5 wt%Pd/C (BNFL nuclear grade) comparing untreated (bottom) and 2%HNO_3 treated (top) carbon supports respectively.

Chapter 5 - Appendices

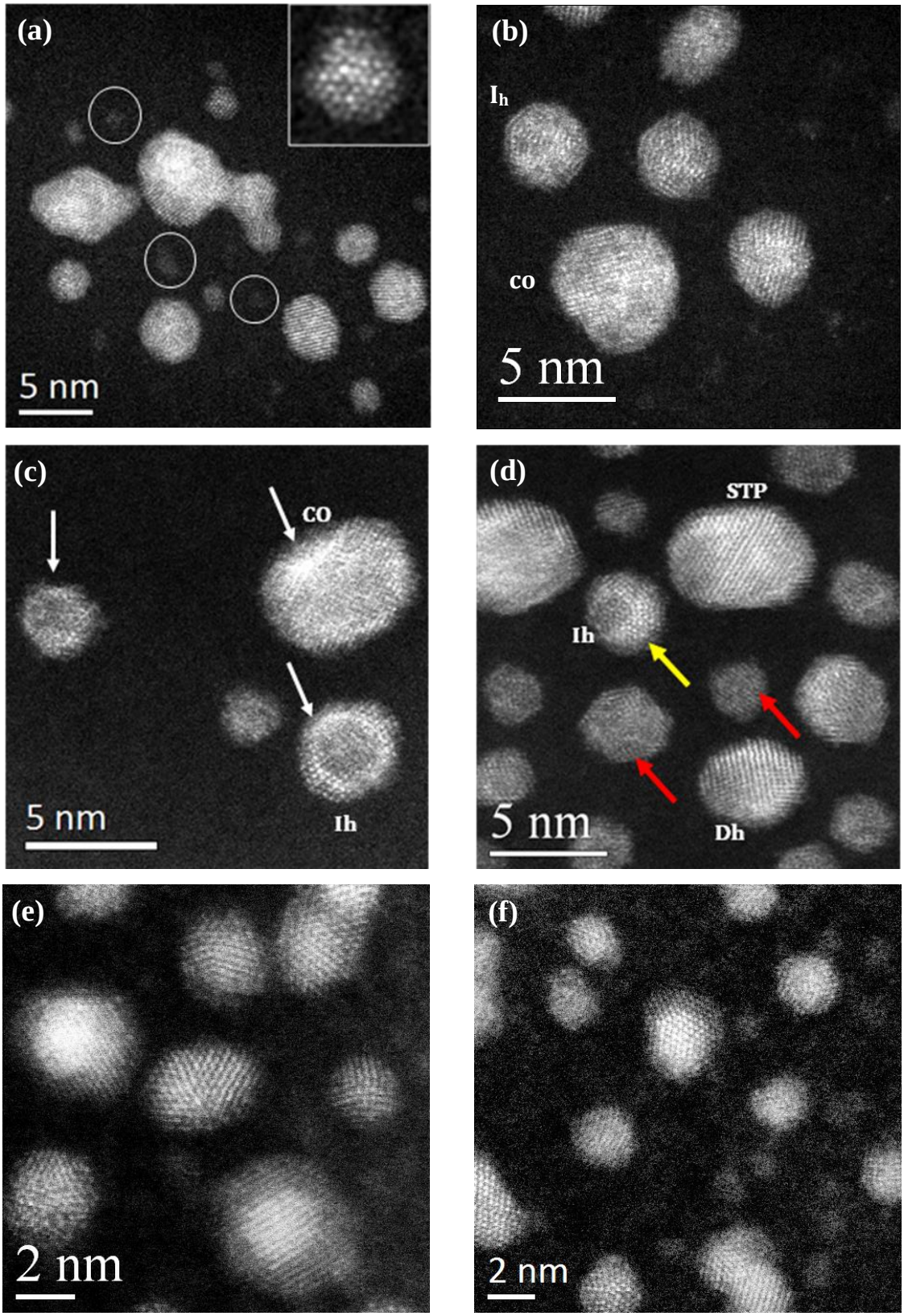

Figure A5.1 STEM-HAADF images of the starting colloids dispersed onto a continuous carbon thin film: **(a, b)** Au+Pd colloids, **(c, d)** Au{Pd} colloids, and **(e, f,)** Pd{Au} colloids.

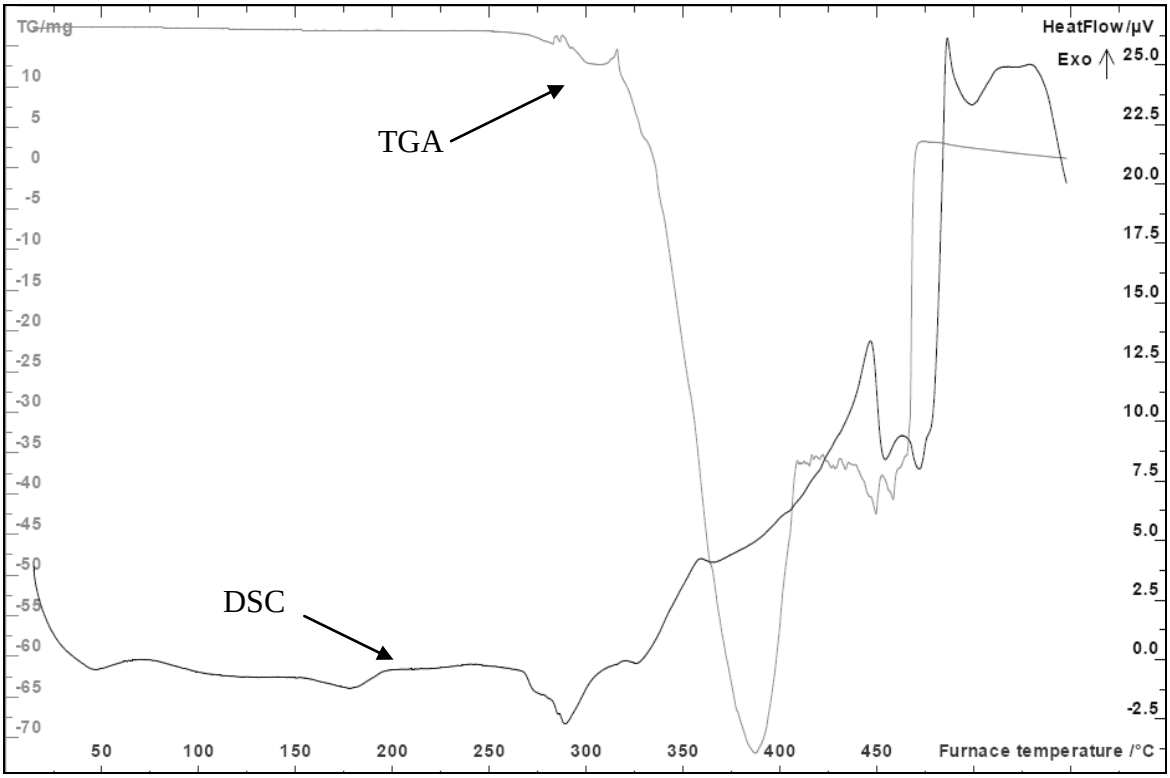

Figure A5.2 TGA and DSC curves of a PVA sample. Thermal decomposition of PVA occurs in the 300-400 ºC temperature range.

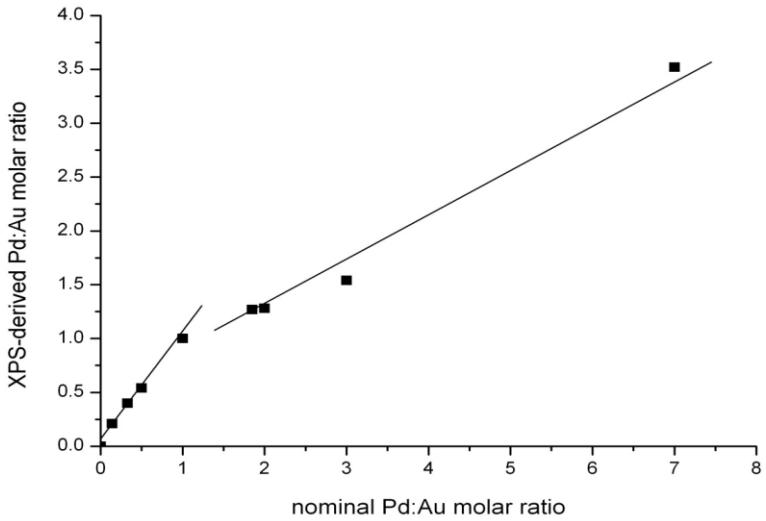

Figure A5.3 XPS derived corrected Pd:Au molar ratios plotted as a function of nominal (expected) Au:Pd ratios

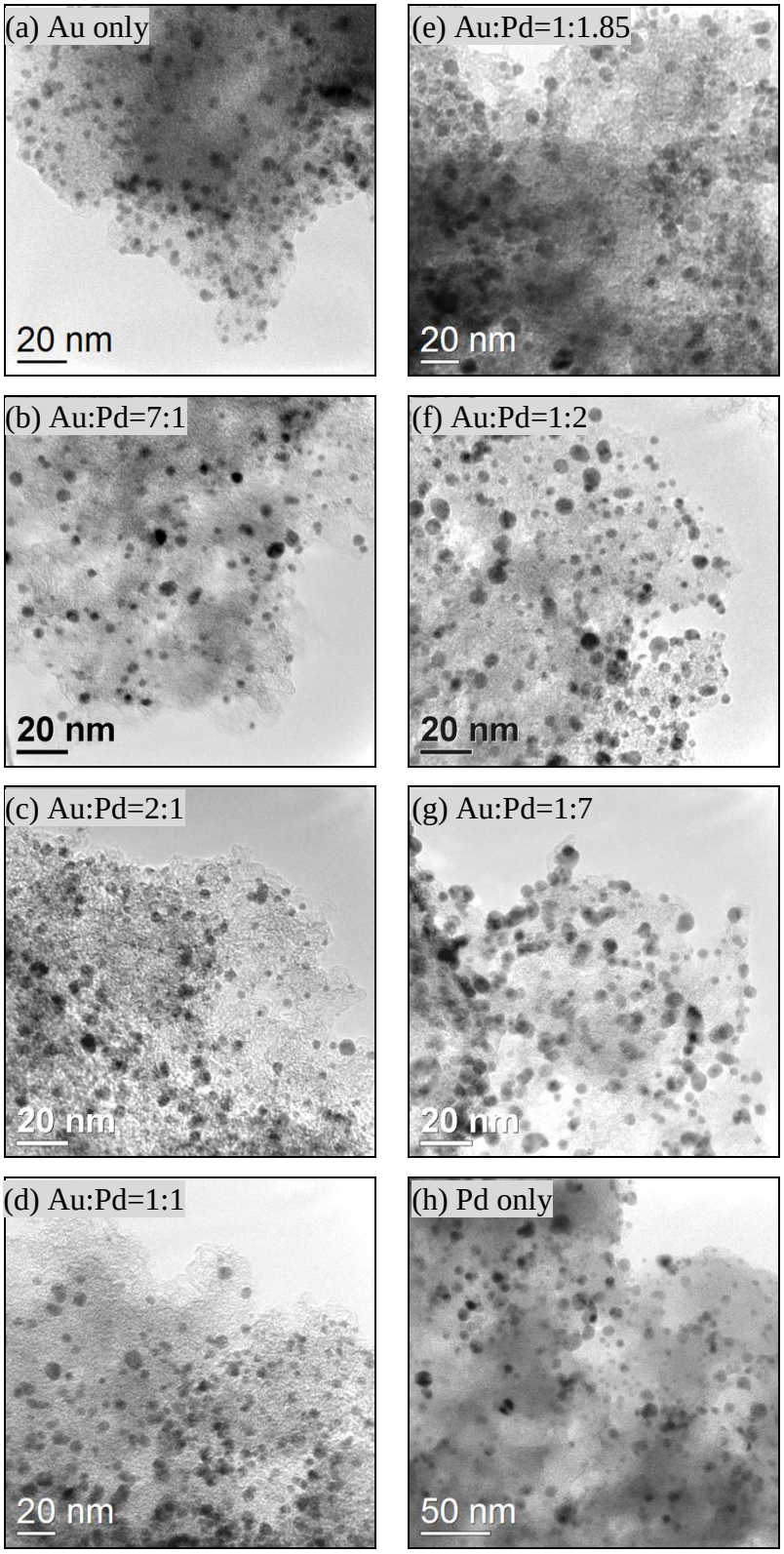

Figure A5.4 Bright field TEM micrographs showing Au-Pd particles immobilised on the activated carbon support and their respective particle size distribution: (a) Au only, (b) Au:Pd=7:1, (c) Au:Pd=2:1, (d) Au:Pd=1:1.

Chapter 6 - Appendices

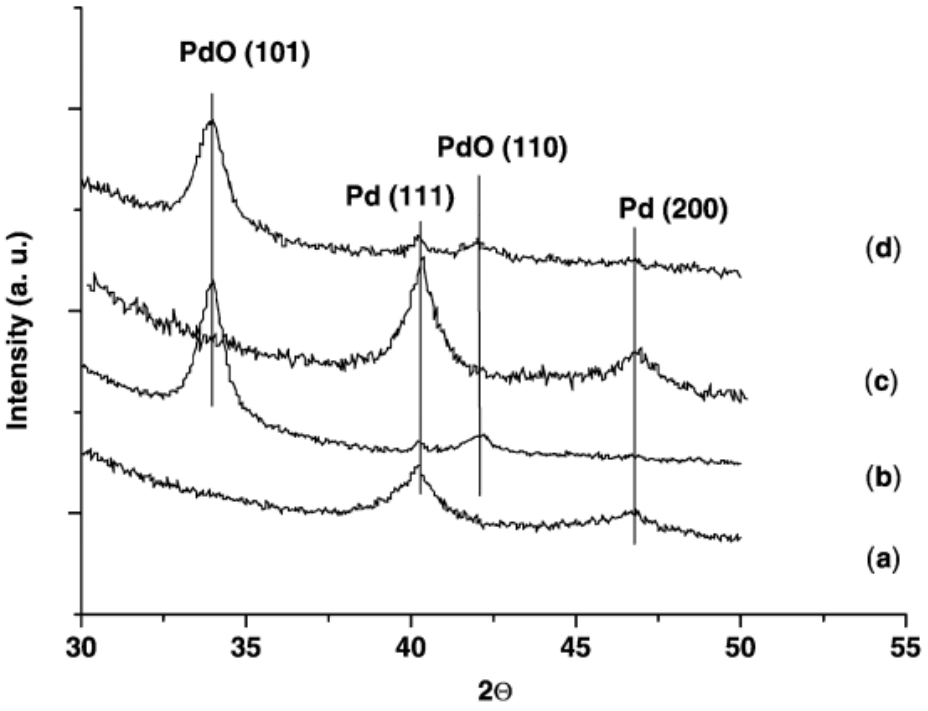

Figure A6.1 XRD profiles of 2 wt% Pd/SiO_2 prepared by sol-immobilization after different treatments: (a) as prepared, (b) after calcination at 673K, (c) after reduction at 473K, (d) after oxidation of CO reaction[1].

Precursor (5 wt% equiv)	**Productivity / $mol_{H2O2}\ Kg_{cat}^{-1}\ h^{-1}$**	**Hydrogenation / $mol_{H2O2}\ Kg_{cat}^{-1}\ h^{-1}$**
1. $Pd(NO_3)_2$	45	516
2. $H_2PdCl_4^{2-}$	80	499
3. $HAuCl_4.3H_2O$	5	32
4. Pd **(2)** + Au **(3)**	61	399

Table A6.1 Summary of the H_2O_2 synthesis and hydrogenation activities for Au and Pd precursors only performed under standard reaction conditions. The amount of precursor added was equivalent to the content (5 wt% metal) present in 10 mg of solid catalyst.

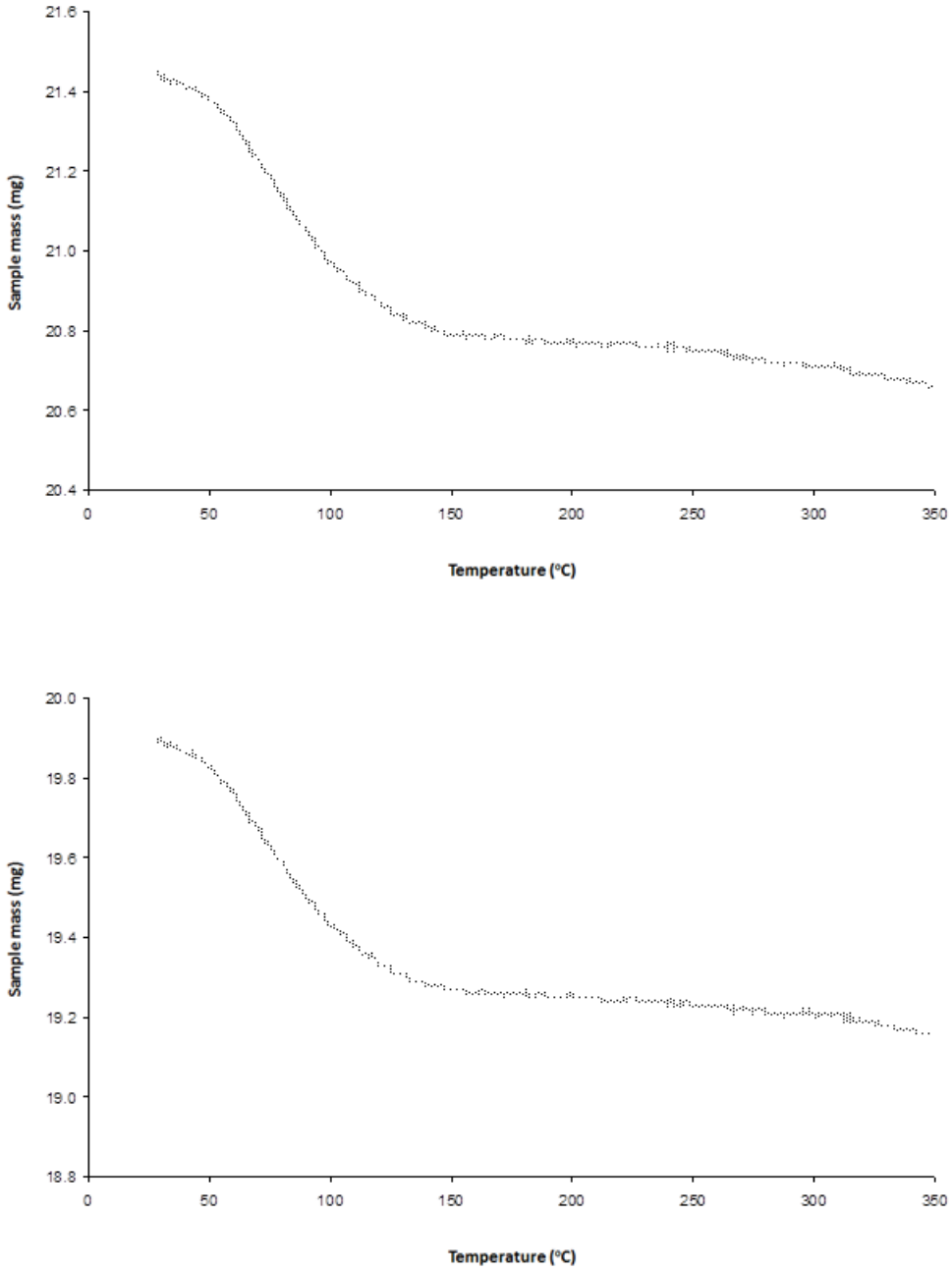

Figure A6.2 Thermo-gravimetric analysis of untreated (top) and 2% HNO_3 pre-treated SiO_2 (bottom) supports heated to 350 ^{o}C under a nitrogen atmosphere.

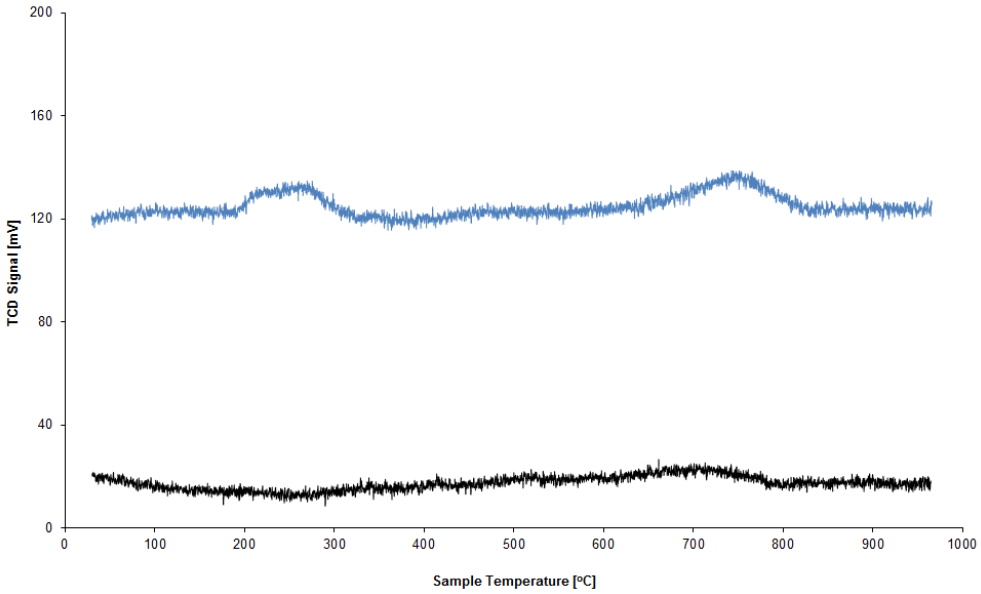

Figure A6.3 TPD profiles recorded for untreated (black) and 2%HNO_3 treated (blue) P25 TiO_2 supports respectively.

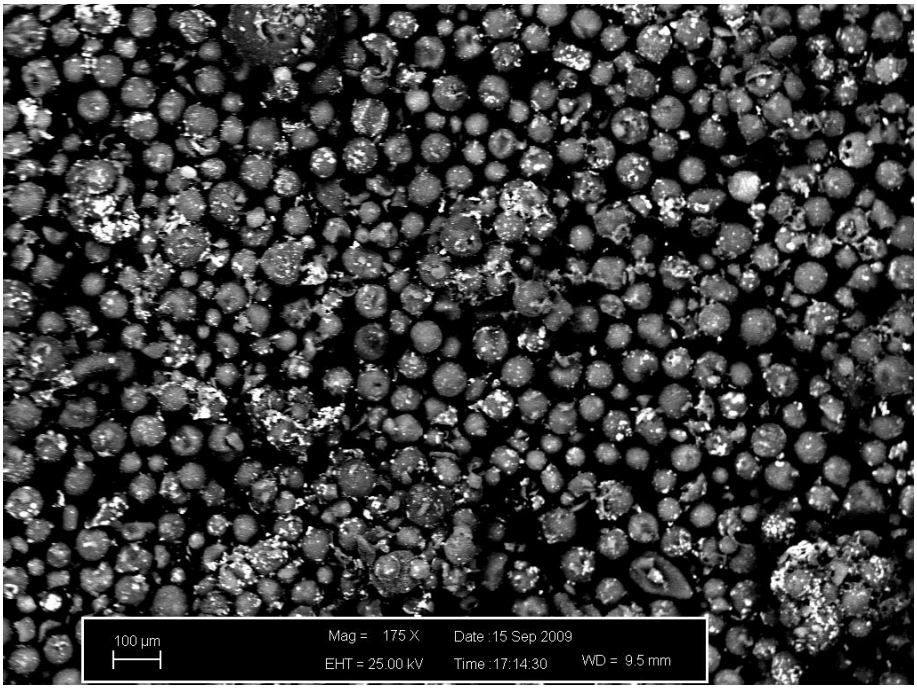

Figure A6.4 SEM-BSD image of 2.5 wt% Au-2.5 wt% Pd/CPI-SiO_2 (80µm) prepared by standard wet impregnation and calcined in static air (400 ^{o}C, 3 h). Working distance = 9.5 mm.

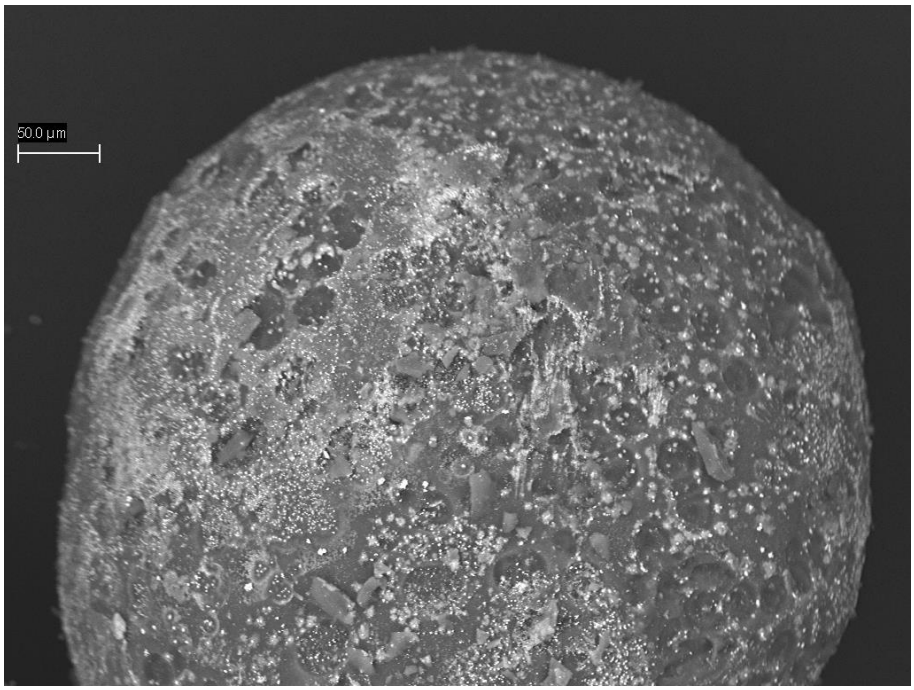

Figure A6.5 SEM-BSD image of 2.5 wt% Au-2.5 wt% Pd/CPI-SiO_2 (500µm) prepared by standard wet impregnation and calcined in static air (400 ^{o}C, 3 h). Working distance = 9.5 mm.

Chapter 7 – Appendices

Catalyst (1-38)	Productivity / $mol_{H2O2}kg_{cat}^{-1}h^{-1}$		Hydrogenation / $mol_{H2O2}kg_{cat}^{-1}h^{-1}$
	2 min / wt% H_2O_2	30 min	30 min
5.00% Pt	46 / 0.01	8	126
2.50% Au-2.50% Pd	281 / 0.09	68	145
2.50% Au-2.50% Pt	120 / 0.02	20	109
2.50% Pd-2.50% Pt	392 / 0.05	138	182
4.80% Pd-0.20% Pt	441 / 0.06	125	192
0.20% Au-4.80% Pd	198 / 0.03	79	178
0.20% Au-4.60% Pd-0.20% Pt	630 / 0.08	185	385
0.83% Au-3.33% Pd-0.83% Pt	399 / 0.06	138	66
1.25% Au-2.50% Pd-1.25% Pt	436 / 0.06	139	199
2.475% Au-2.475% Pd-0.05% Pt	308 / 0.04	63	46
2.45% Au-2.45% Pd-0.10% Pt	171 / 0.02	109	76
2.40% Au-2.40% Pd-0.20% Pt	436 / 0.06	170	145
1.20% Au-3.60% Pd-0.20% Pt	394 / 0.05	134	547
3.60% Au-1.20% Pd-0.20% Pt	59 / 0.01	39	342
2.35% Au-2.35% Pd-0.30% Pt	389 / 0.06	159	177
2.275% Au-2.275% Pd-0.45% Pt	670 / 0.09	100	459
2.00% Au-2.00% Pd-1.00% Pt	194 / 0.03	115	93
0.455% Au-0.455% Pd-0.09% Pt	95 / 0.01	21	8

0.10% Au-4.80% Pd-0.10% Pt	477 / 0.06	111	486
0.20% Au-3.50% Pd-1.30% Pt	845 / 0.11	139	55
0.20% Au-2.40% Pd-2.40% Pt	532 / 0.06	106	197
0.25% Au-3.75% Pd-1.00% Pt	308 / 0.04	73	296
0.30% Au-4.40% Pd-0.30% Pt	696 / 0.09	123	467
0.40% Au-4.20% Pd-0.40% Pt	419 / 0.06	121	33
0.45% Au-4.40% Pd-0.15% Pt	425 / 0.06	106	368
0.50% Au-4.00% Pd-0.50% Pt	602 / 0.08	129	635
0.60% Au-4.00% Pd-0.40% Pt	516 / 0.07	110	271
0.625% Au-3.75% Pd-0.625% Pt	470 / 0.06	153	439
0.625% Au-2.5% Pd-1.875% Pt	773 / 0.10	117	377
0.70% Au-4.00% Pd-0.30% Pt	425 / 0.06	92	369
0.75% Au-3.75% Pd-0.50% Pt	617 / 0.08	131	219
0.925% Au-0.95% Pd-3.125% Pt	489 / 0.06	94	407
0.95% Au-3.75% Pd-0.30% Pt	681 / 0.09	129	126
1.33% Au-1.33% Pd-1.33% Pt	403 / 0.05	84	161
1.712% Au-2.812% Pd-0.475% Pt	325 / 0.04	91	135
2.3% Au-2.5% Pd-0.2% Pt	458 / 0.06	155	94
2.5% Au-2.3% Pd-0.2% Pt	260 / 0.03	86	11
3.125% Au-0.95% Pd-0.925% Pt	276 / 0.04	74	72

Table A7.1 Summary of the H_2O_2 synthesis and hydrogenation activities obtained using CeO_2-supported Au, Pd and/or Pt catalysts.

CeO_2 Composition / wt%	**Productivity / $mol_{H2O2}kg_{cat}^{-1}h^{-1}$**	**Hydrogenation / $mol_{H2O2}kg_{cat}^{-1}h^{-1}$**	**Surface Pd / atom %**
5% Pd	**97**	**329**	**10.4**
4.80% Pd	85	216	10.4
4.60% Pd	68	349	12.7
4.40% Pd	92	71	10.2
0.20% Pt-4.80% Pd	125	192	10.7
0.40% Pt-4.60% Pd	68	616	5.8
0.60% Pt-4.40% Pd	51	560	5.5
0.20% Au-4.80% Pd	79	178	7.4
0.40% Au-4.60% Pd	98	318	2.9
0.60% Au-4.40% Pd	56	414	10.1

Table A7.2 Effect of catalyst composition on H_2O_2 synthesis and hydrogenation activities For bimetallic catalysts supported on CeO_2 - progressive variation of either Au or Pt content.

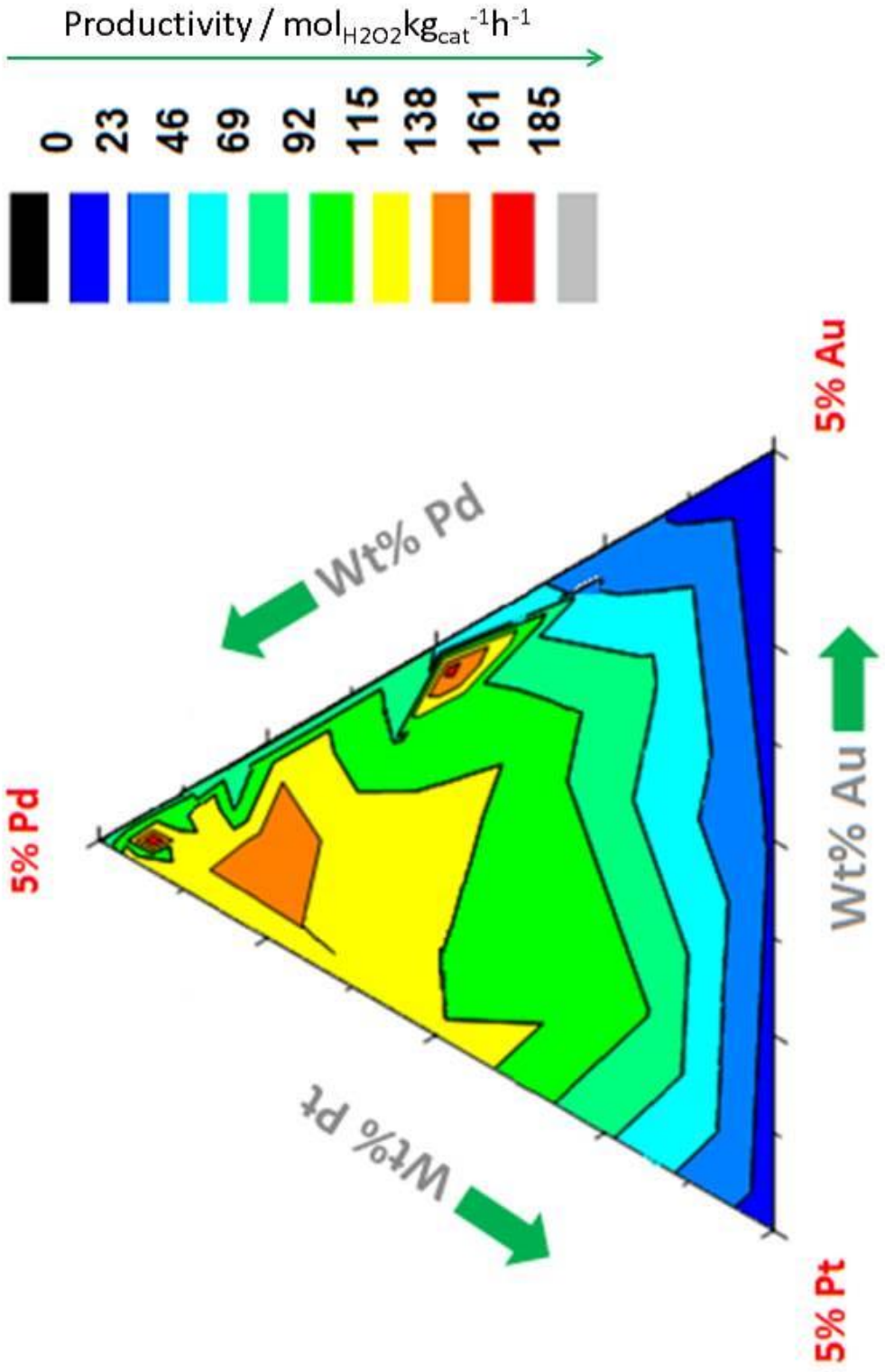

Figure A7.1 H_2O_2 productivities for CeO_2-supported 5 wt% Au-Pd-Pt catalysts presented as a 3D diagram.

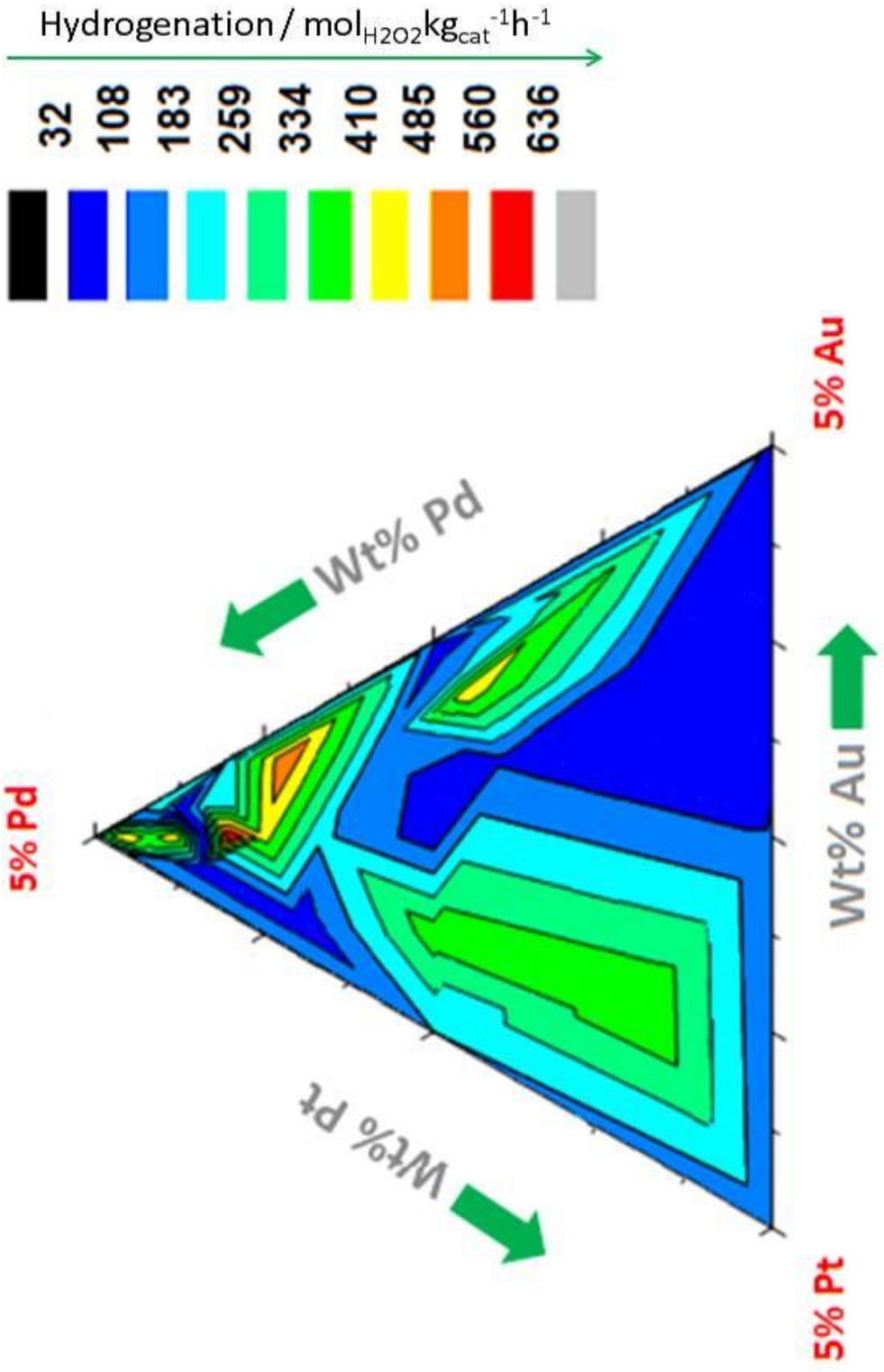

Figure A7.2 H_2O_2 hydrogenation rates for CeO_2-supported 5 wt% Au-Pd-Pt catalysts presented as a 3D ternary diagram.

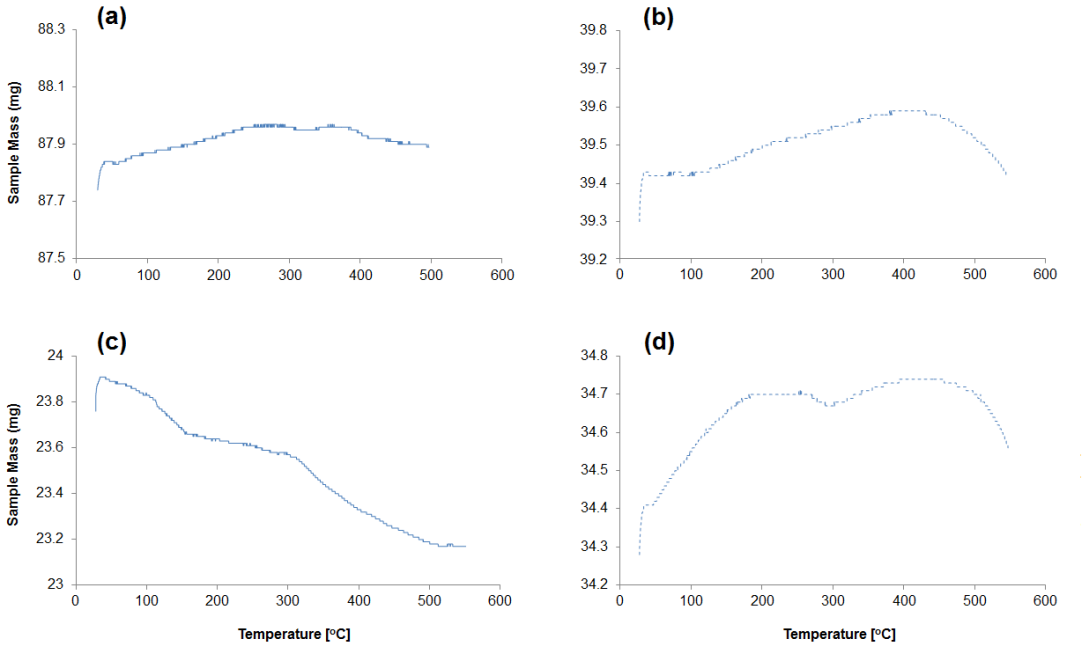

Figure A7.3 TGA profiles recorded in static air using a 5 °C min^{-1} heating ramp for samples, **(a)** CeO_2 only, **(b)** 2.5 wt% Au-2.5 wt% Pd/CeO_2, **(c)** 2.5 wt% Pt-2.5 wt% Pd/CeO_2, and **(d)** 2.28 wt% Au-2.28 wt% Pd-0.45 wt% Pt/CeO_2.

CeO_2 Composition / wt%	**Productivity / $mol_{H2O2}kg_{cat}^{-1}h^{-1}$**	
	1st Use	**2nd Use**
2.50% Au-2.50 wt% Pt	20	20
2.50% Pt-2.50 wt% Pd	138	138
2.40% Au-2.40% Pd-0.20% Pt	170	170
0.63% Au-3.75% Pd-0.63% Pt	153	153
2.28% Au-2.28% Pd-0.45% Pt	100	100

Table A7.3 Reusability studies (H_2O_2 synthesis) for CeO_2-supported Au-Pt, Pt-Pd and Au-Pd-Pt catalysts calcined in static air (400 °C, 3 h).

References

1. K. Qian, W. Huang, *Catalysis Today*, **2011**, 164, 320.

List of Publications

(1) Effect of Halide and Acid Additives on the Direct Synthesis of Hydrogen Peroxide using Supported Gold-Palladium Catalysts

Edwin Ntainjua N., Marco Piccinini, James C. Pritchard, Jennifer K. Edwards, Albert F. Carley, Jacob A. Moulijn and Graham J. Hutchings.

ChemSusChem: Volume 2, Issue 6, Pages 575-580, 2009

---

(2) Effect of Halide and Acid Additives on the Direct Synthesis of Hydrogen Peroxide using Supported Gold-Palladium Catalysts

Edwin Ntainjua N., Marco Piccinini, James C. Pritchard, Qian He, Jennifer K. Edwards, Albert F. Carley, Jacob A. Moulijn, Christopher J. Kiely and Graham J. Hutchings.

ChemCatChem: Volume 1, Issue 4, Pages 479-484, 2009

---

(3) The effect of catalyst preparation method on the performance of supported Au-Pd catalysts for the direct synthesis of hydrogen peroxide

James C. Pritchard, Qian He, Edwin Ntainjua N., Marco Piccinini, Jennifer K. Edwards, Andrew A. Herzing, Albert F. Carley, Jacob A. Moulijn, Christopher J. Kiely and Graham J. Hutchings.

Green Chemistry: Volume 12, Pages 915-921, 2010

---

(4) Direct Synthesis of Hydrogen Peroxide and Benzyl Alcohol Oxidation Using Au-Pd Catalysts Prepared by Sol Immobilization

James C. Pritchard, Lokesh Kesavan, Marco Piccinini, Qian He, Ramchandra Tiruvalam, Nikolaos Dimitratos, Jose A. Lopez-Sanchez, Albert F. Carley, Jennifer K. Edwards, Christopher J. Kiely and Graham J. Hutchings.

Langmuir: Volume 26, Issue 21, Pages 16568-16577, 2010

(5) Direct synthesis of hydrogen peroxide using ceria-supported gold and palladium catalysts

Edwin Ntainjua N., Marco Piccinini, James C. Pritchard, Jennifer K. Edwards, Albert F. Carley, Christopher J. Kiely and Graham J. Hutchings.

Catalysis Today: Volume 178, Issue 1, Pages 47-50, 2011

---

(6) Aberration corrected analytical electron microscopy studies of sol-immobilized Au + Pd, Au{Pd} and Pd{Au} catalysts used for benzyl alcohol oxidation and hydrogen peroxide production

Ramchandra Tiruvalam, James C. Pritchard, Nikolaos Dimitratos, Jose A. Lopez-Sanchez, Jennifer K. Edwards, Albert F. Carley, Graham J. Hutchings and Christopher J. Kiely.

Faraday Discussions: Volume 152, Pages 63-86, 2011

---

(7) Direct synthesis of hydrogen peroxide using Au-Pd exchanged and supported Heteropolyacid catalysts at ambient temperature using water as solvent

Edwin Ntainjua N., Marco Piccinini, Simon J. Freakley, James C. Pritchard, Jennifer K. Edwards, Albert F. Carley and Graham J. Hutchings.

Green Chemistry: Volume 14, Issue 1, Pages 170-181, 2012

---

(8) Some recent advances in gold-based catalysis facilitated by aberration corrected analytical electron microscopy

Ramchandra Tiruvalam, Qian He, Andrew A. Herzing, James C. Pritchard, Nikolaos Dimitratos, Jose A. Lopez-Sanchez, Jennifer K. Edwards, Albert F. Carley, Graham J. Hutchings and Christopher J. Kiely.

IOP EMAG (Electron Microscopy and Analysis Group): Conference Proceedings, Birmingham, UK, 6-9th September, 2011

(9) Effect of acid treatment on $AuPd/SiO_2$ catalysts for the direct synthesis of hydrogen peroxide

Jennifer K. Edwards, Stewart F. Parker, James C. Pritchard, Simon J. Freakley, Qian He, Albert F. Carley, Christopher J. Kiely and Graham J. Hutchings.

Catalysis Science and Technology: Volume 3, Issue 3, Pages 812-818, 2013

---

(10) The effect of heat treatment on the performance and structure of carbon-supported Au-Pd carbon catalysts for the direct synthesis of hydrogen peroxide

Jennifer K. Edwards, James C. Pritchard, Marco Piccinini, Greg Shaw, Qian He, Albert F. Carley, Christopher J. Kiely and Graham J. Hutchings.

Journal of Catalysis: Volume 292, Pages 227-238, 2012

---

(11) Effect of heat treatment on Au-Pd catalysts synthesized by sol-immobilization for the direct synthesis of hydrogen peroxide and benzyl alcohol

James C. Pritchard, Marco Piccinini, Ramchandra Tiruvalam, Qian He, Nikolaos Dimitratos, Jose A. Lopez-Sanchez, David J. Morgan, Albert F. Carley, Jennifer K. Edwards, Christopher J. Kiely and Graham J. Hutchings.

Catalysis Science and Technology: Volume 3, Issue 2, Pages 307-317, 2013

---

(12) Synthesis of stable ligand-free gold-palladium nanoparticles using a simple excess anion method

Sankar Meenakshisundaram, Qian He, Moataz Morad, James C. Pritchard, Simon J. Freakley, Jennifer K. Edwards, Stuart H. Taylor, David J. Morgan, Albert. F. Carley, David W. Knight, Christopher J. Kiely and Graham J. Hutchings.

ACS Nano: Volume 8, Issue 6, Pages 6600-6606, 2012